Digital-Rock-Physics Modelling of Carbonates and Sandstones

A Thesis Submitted to the
College of Graduate and Postdoctoral Studies
in Partial Fulfillment of the Requirements
for the degree of Master of Science
in the Department of Geological Sciences
University of Saskatchewan
Saskatoon

By
SOMTOCHUKWU OGOCHUKWU UFONDU

©SOMTOCHUKWU OGOCHUKWU UFONDU, June 2020. All rights reserved.

Permission to Use

In presenting this thesis in partial fulfilment of the requirements for a Postgraduate degree from the University of Saskatchewan, I agree that the Libraries of this University may make it freely available for inspection. I further agree that permission for copying of this thesis in any manner, in whole or in part, for scholarly purposes may be granted by the professor or professors who supervised my thesis work or, in their absence, by the Head of the Department or the Dean of the College in which my thesis work was done. It is understood that any copying or publication or use of this thesis or parts thereof for financial gain shall not be allowed without my written permission. It is also understood that due recognition shall be given to me and to the University of Saskatchewan in any scholarly use which may be made of any material in my thesis.

Reference in this thesis/dissertation to any specific commercial products, process, or service by trade name, trademark, manufacturer, or otherwise, does not constitute or imply its endorsement, recommendation, or favoring by the University of Saskatchewan. The views and opinions of the author expressed herein do not state or reflect those of the University of Saskatchewan, and shall not be used for advertising or product endorsement purposes.

Requests for permission to copy or to make other use of material in this thesis in whole or part should be addressed to:

Head of the Department of Geological Sciences
114 Science Place
University of Saskatchewan
Saskatoon, Saskatchewan
Canada
S7N 5E2

OR

Dean

College of Graduate and Postdoctoral Studies

University of Saskatchewan

116 Thorvaldson Building, 110 Science Place

Saskatoon, Saskatchewan S7N 5C9

Canada

Abstract

This thesis seeks to investigate the influence of porosity and pore geometry on the macroscopic parameters of a porous rock saturated with fluid. These macroscopic parameters, also known as Biot's parameters, include the drained and undrained bulk moduli which characterize the rock's resistance to compression (or expansion), the pressure parameter needed to increase the fluid content by a unit value at constant total dilatation, and the so-called Biot-Willis coefficient. This study also seeks to examine the effects of porosity and pore geometry on the stored solid elastic energy in the rock. To achieve these goals, I develop numerical simulations of compression tests of digital rock models. These simulations allow me to calculate Biot's parameters for samples with known pore geometries. The numerical model results are shown to be in good agreement with an analytical model for a spherical rock sample with a single spherical pore. I investigate the variation of the macroscopic parameters as a function of the porosity and of the solid and fluid material properties. In particular, I show that, apart from the Biot-Willis coefficient, the other macroscopic parameters, as well as the total and compression solid energy densities, decrease with an increase in porosity. Whereas Biot's parameters are generally influenced by both porosity and pore geometry, the pressure parameter is only influenced by porosity but remains the same regardless of changes in pore geometry. Also, the results reveal that the carbonate pore geometries have some similarity to the simple pore geometries but are generally softer, while sandstone pore geometries are even softer than carbonate ones.

Acknowledgements

First of all, my sincere and hearty thanks goes to my supervisor, Dr. Sam Butler, who tirelessly reviewed this thesis and had an immense contribution to the entire process. His positive guidance helped get me through some difficult moments in the course of this research.

Thank you to Dr. Igor Morozov for his feedback. His wealth of knowledge and experience was crucial in my understanding of parts of poroelasticity. I also wish to thank Dr. James Merriam for his tutorship on Geophysical Inversion. The course helped make me comfortable in the use of MATLAB® which was initially entirely new to me at first. Dr. Chris Hawkes' input was also immensely helpful to this project. He showed me the triaxial test machine in the rock physics laboratory and explained how it works. He further sent me some publications for my written thesis.

Thank you to Rafael Gonzalez, Jim Rosen, Jared Tisserand, and Ryan Olynuk for their tireless efforts in helping me troubleshoot and solve problems with any of my computer software, parts and printers. They also helped me with remote desktop, both on my Windows and Linux machines.

I am also grateful to the University of Saskatchewan for allowing me use their cluster computing for this work.

I also want to thank all my family members for their HUGE support and prayers throughout my time at the university. Special among them are my mum, who is my first and biggest role model, for her enduring prayers and wisdom; my eldest brother, Dr Nonso Ufondu, who paid for my initial flight ticket to Canada; my big brother, Engr Lotanna Ufondu and his lovely wife, Doris, who both housed me free-of-charge for my first year in Saskatoon; and my fiancee, Sandra Ifejika, who helps keep me balanced and focused, even from far-away Nigeria.

Finally, my greatest thanks goes to my Lord and personal Saviour, Jesus Christ, who has

never ceased to flood my heart with peace, even in the midst of storms. He is the one who keeps me going and has pulled me out of the 'valley of depression' many times. His words always fill my mind with the grace to thrive. I am so grateful that He met me when He did.

I would like to dedicate this thesis to all graduate students out there who might be struggling in their thesis work. You will come out stronger, if you never give up.

Contents

List of Tables

List of Figures

1 INTRODUCTION

In this thesis, Chapter One contains a general introduction to the research, including the purpose of the study, author's contribution, theories guiding this research, and the different ways to do rock physics experiments related to this study. Chapter Two covers the methodology used, including the model set-up and the numerical and analytical studies. Further, Chapters three and four show the results for the simple 3D models and the complex ones, respectively. Each of these latter chapters contains in-depth discussions of the results. The conclusions and recommendations for future studies are presented in Chapter Five. Finally, Appendix A and B show further results that were not discussed in the results chapters, while Appendix C shows the analytical proof that the total drained solid elastic potential is equal to the total undrained solid elastic potential, as shown in Chapters Three and Four.

Note that, in COMSOL Multiphysics®, 1 m represents 1 voxel (0.78 x $10^{-}6$ m). And all the dimensions of the models given in this thesis are as generated from COMSOL Multiphysics®.

1.1 Purpose of the Study

In numerous applications to soil mechanics, hydrology, and seismology, porous fluid-saturated rock is commonly described by the classical model proposed by Biot (1956). Biot's theory of poroelasticity has applications that cut across the fields of geophysics and geomechanics. Biot's macroscopic parameters (explained further in this chapter) aid geoscientists in the interpretation of actual measurements and for modeling various experiments. An example of such measurements is in the estimation of accurate effective stress for various subsurface engineering applications, which require the calculation of the Biot-Willis coefficient (Reza Saberi & Jenson, 2018). This thesis provides both a theoretical and visual understanding of how Biot's parameters can be evaluated for a given microstructure, using analytical (for a

single spherical pore in a spherical rock) and numerical studies. Such understanding is needed to prove that the Biot-Gassmann model is correct. A further relevance of this research is that it can provide geoscientists/engineers with a visual understanding of how the porosity and pore geometry of rocks influence how such rocks behave under loading.

In this research, I use the finite-element method to solve force balance equations on microscopic digital rock models with specified boundary conditions. Further, I calculate the drained and bulk moduli, K_d & K_u, the pressure, M, and the Biot-coefficient, α, (all terms are explained further in this chapter) for several rock porosities and pore geometries. For my numerical simulations, I use of COMSOL Multiphysics® software. The results are compared with some analytical cases and found to be in good agreement.

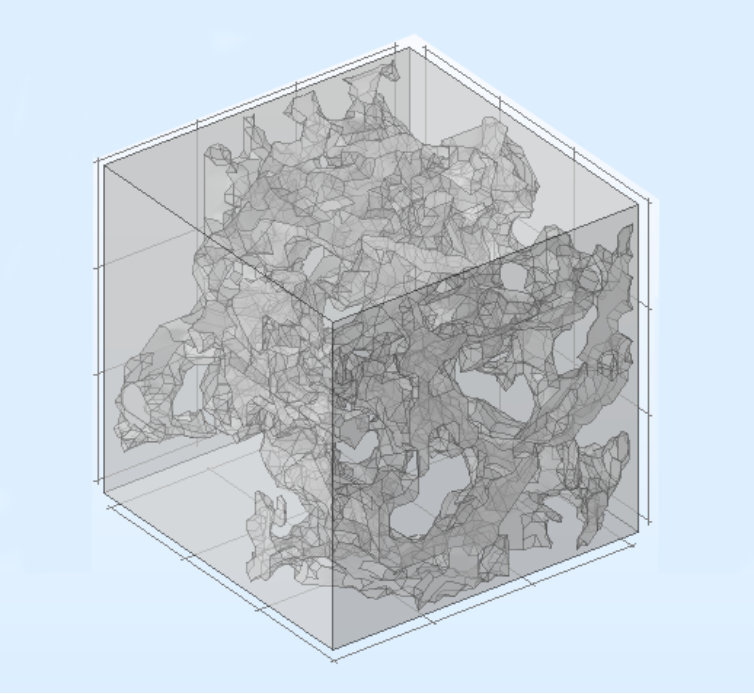

Figure 1.1: An image from this study showing the bulk matrix with pore space

1.2 Author's Contribution

During the course of this research, I was fully involved both in the numerical simulations and the analytical considerations. I started out by simulating simple 2D cases involving squares

or circles with one or more disconnected square or circular pores. These were done in order to achieve efficient computation allowing variation of multiple parameters, and each case took only a few minutes (between 2 and 10 minutes) to run each time. In December 2017, I presented some of the results from these simulations at the Saskatchewan Geological Survey Open House. Afterwards, I and Dr. Butler consulted with Dr. Morozov to get his input before moving on to trying out some simple 3D cases involving either a cube or a sphere with one or more disconnected spheres or cubes as pores. Again, these did not usually take a lot of time to run (between 5 minutes and 1.5 hours) and I presented some results from them at the Saskatchewan Geological Survey Open House in December 2018. Then, after further consultations, I moved on to slightly more complex 3D structures involving interconnected cylindrical pores contained in various solid shapes as the solid regions. Finally, I tried the simulations on X-ray tomography of actual rock samples, and these took significantly larger solution times (between 2 and 100 hours) and computer memory (between 200 and 700 GB).

1.3 Theory Review

In this section I review some basic concepts guiding this thesis which include the stress-strain relations in solids and fluids, continuum theory and the theory of poroelasticity. The elastic theory subsection describes the application of the *microscopic* theory as used in this thesis, while the continuum mechanics subsection describe the *macroscopic* theory. Then, the theory of poroelasticity subsection describes what the microscopic and macroscopic theories mean in the context of this study. Note that these subsections are not intended as exhaustive descriptions of the physical and mathematical concepts discussed in them but only summarize the notations and methods related to the present study.

1.3.1 Stress-Strain Relations in Solids and Fluids

The theory of elasticity describes how solids deform under static (time-independent) forces of stress. In the next following subsections, I describe these forces and the deformations they cause as they relate to this thesis.

To begin, I list the continuum-mechanics notation of microscopic-scale models used in this work and their meanings in Table 1.1.

Table 1.1: Continuum-Mechanics Notation of Microscopic-Scale Models

Term	Definition
σ_{ij} (Pa)	components of the stress tensor
ε_{ij}	components of the strain tensor
$\dot{\varepsilon}_{ij}$	components of the strain-rate tensor; a dot denotes a time derivative
$e_{ii} = \Delta$	fractional change in volume of the element known as the *cubical dilatation*; it is positive if the rock expands
K_s & K_f (Pa)	microscopic bulk moduli (of the solid and the fluid, respectively)
λ (Pa)	Lamé's parameter
μ (Pa)	shear modulus (also called modulus of rigidity)
η (Pa s)	shear viscosity
η_κ (Pa s)	bulk viscosity
$i, j = 1, 2(3)$	indices of a 2D or 3D Cartesian tensor
u_i (m)	displacement in the i direction
δ_{ij}	Kronecker delta, a unit tensor which equals 1 for $i = j$ and 0 everywhere else. It is equivalent to the identity matrix as illustrated below
E (Pa)	Young's modulus (also called modulus of elasticity)

Note that repeated indices "ii" mean summation, or trace of the tensor.

1.3.1.1 Stress

The stress on a material is the force acting on any infinitesimal area in the material. It has the unit of pressure - Nm^{-2}. If the force is acting perpendicular to the surface, it is a normal stress; if parallel to the surface, it is a shear stress. There are two types of forces acting on an element of a material solid - the body forces which penetrate the entire volume of the material and the surface forces which act on the boundaries of the solid (Turcotte & Schubert, 2002).

In 3D, there are nine components of stress necessary to fully describe the stresses on a small volume in the material. This is known as the *stress tensor* and Figure 1.2 shows these stress components on the faces of a small cube. The first subscript describes the direction normal to the surface while the second subscript describes the direction of the force applied to that surface. The normal stresses are σ_{xx}, σ_{yy}, and σ_{zz}, while the shear stresses are σ_{xy}, σ_{yx}, σ_{xz}, σ_{zx}, σ_{yz}, and σ_{zy}. However, the stress tensor is symmetric, $\sigma_{ij} = \sigma_{ji}$; hence, there will be only six independent components of stress (Turcotte & Schubert, 2002). Equation 1.1 shows the stress tensor matrix.

$$\sigma_{ij} = \begin{bmatrix} \sigma_{xx} & \sigma_{xy} & \sigma_{xz} \\ \sigma_{yx} & \sigma_{yy} & \sigma_{yz} \\ \sigma_{zx} & \sigma_{zy} & \sigma_{zz} \end{bmatrix} . \tag{1.1}$$

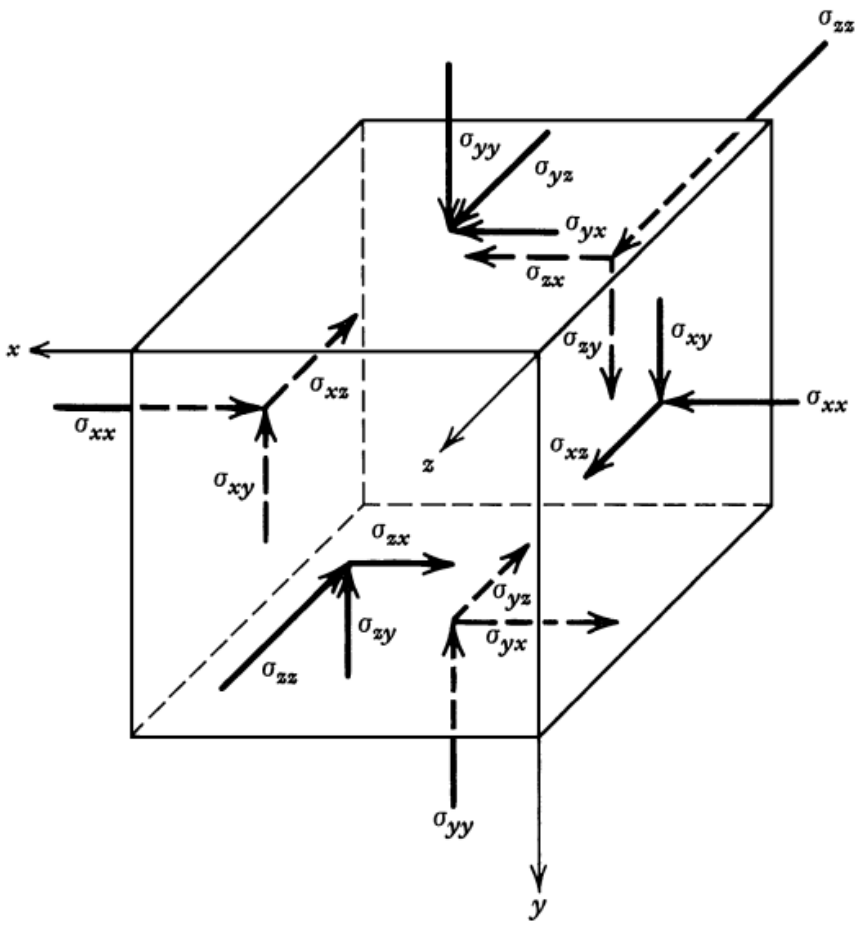

Figure 1.2: Stress components on the faces of a small cube (Turcotte & Schubert, 2002)

1.3.1.2 Strain

Strain is the deformation experienced by a material under stress. It is the ratio of the change in length of the material to its original length in the plane of the applied force. Normal strains occur when the dimensions of the solid change but the shape remains intact, while shear strains are of two types - pure shear strain, which occurs when the solid material is not allowed to rotate about any of its axes, and simple shear strain which involves rotation. An example of simple shear strain is strike-slip fault (Turcotte & Schubert, 2002). However, for the purposes of this study, we have assumed the material is under pure shear strain. It is also important to emphasize that we are considering small deformations throughout this study.

1.3.1.2.1 Normal Strain

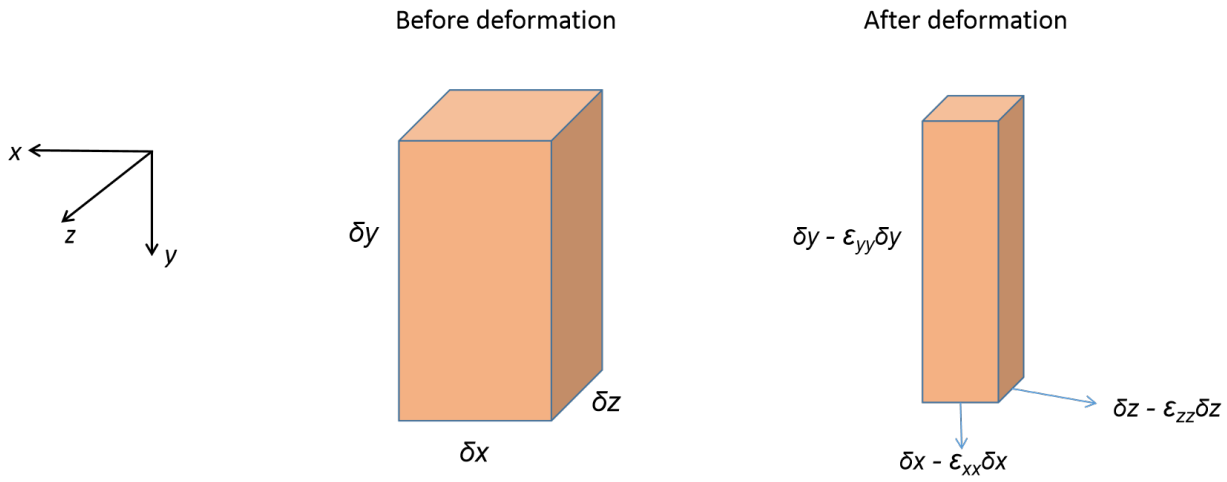

Figure 1.3: Normal strain

From Figure 1.3, the original dimensions of the cuboid were δ_x by δ_y by δ_z, corresponding to coordinates x, y, and z, respectively. However, after deformation involving only normal strains, the lengths of the sides became $\delta_x - \varepsilon_{xx}\delta_x$, $\delta_y - \varepsilon_{yy}\delta_y$, and $\delta_z - \varepsilon_{zz}\delta_z$. The normal components of strain are given by ε_{xx}, ε_{yy}, and ε_{zz}, and each of them represents the ratio of the change in length to the original length parallel to its axis. For very small strains, the fractional change in volume is determined by $\varepsilon_{xx} + \varepsilon_{yy} + \varepsilon_{zz} = \Delta$, which is also called *volumetric strain* or *dilatation* (Pan, 1999). Also, if the displacement in each direction is u_i, where the subscript i represents the component in which the displacement occurs, then

$$\Delta = \frac{\partial u_x}{\partial x} + \frac{\partial u_y}{\partial y} + \frac{\partial u_z}{\partial z} \tag{1.2}$$

1.3.1.2.2 Pure Shear Strain

As mentioned earlier, when a solid material is allowed to change shape but not allowed to rotate about an axis, it is said to be under pure shear. This is the condition assumed in this study. To attempt to explain this as it directly relates to this thesis, let us consider a condition where a rectangle is distorted into a parallelogram (see Figure 1.4).

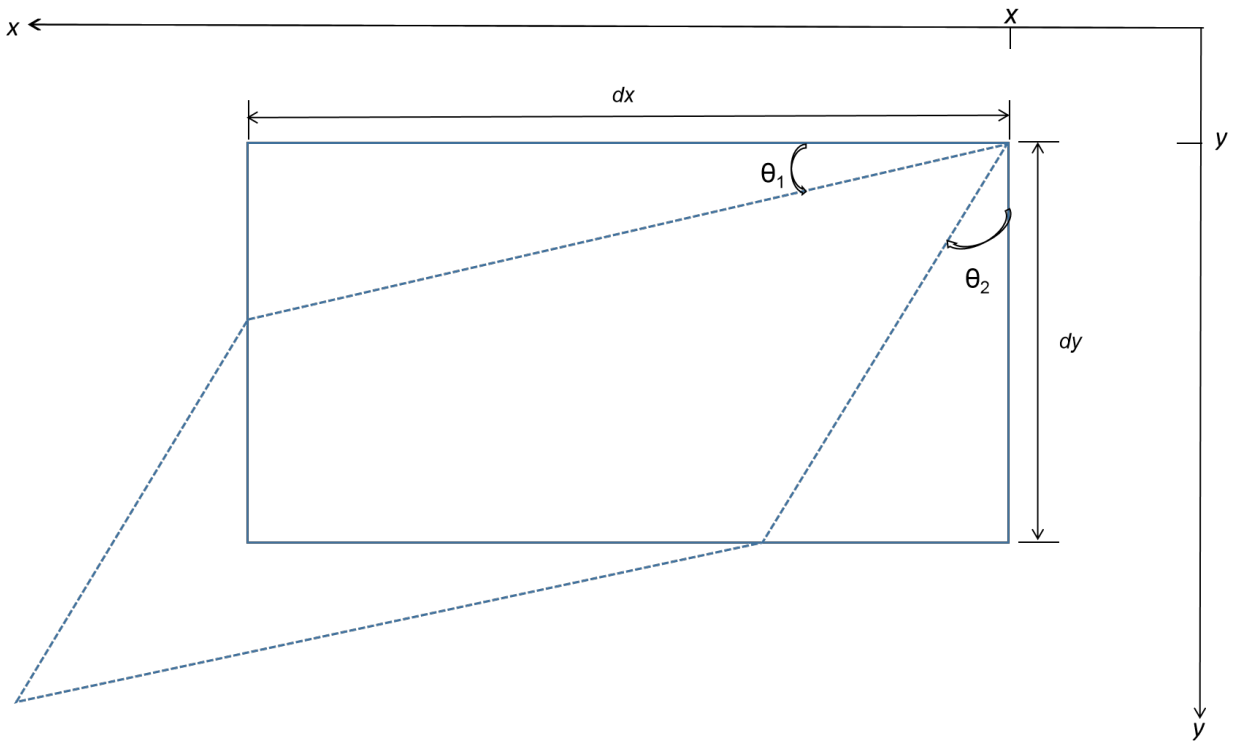

Figure 1.4: Pure shear strain ($\theta_1 = \theta_2$) with no rotation of solid-body elements

In pure shear strain, the shearing angles, θ_1 & θ_2, are equal in order to ensure that no rotation occurs. This also means that

$$\frac{\partial u_x}{\partial y} = \frac{\partial u_y}{\partial x} \tag{1.3}$$

Similar to the stress tensor, the strain tensor is symmetric, and the shear strain is related to the spatial derivatives of displacement by (Bourbie, Coussy, & Zinszner, 1987):

$$\varepsilon_{ij} = \varepsilon_{ji} = \frac{1}{2}\left(\frac{\partial u_i}{\partial x_j} + \frac{\partial u_j}{\partial x_i}\right); \qquad i, j = x, y, z. \tag{1.4}$$

Using the expressions for the normal strain and shear strain, the strain tensor matrix is given by

$$\varepsilon_{ij} = \begin{bmatrix} \frac{\partial u_x}{\partial x} & \frac{1}{2}\left(\frac{\partial u_x}{\partial y} + \frac{\partial u_y}{\partial x}\right) & \frac{1}{2}\left(\frac{\partial u_x}{\partial z} + \frac{\partial u_z}{\partial x}\right) \\ \frac{1}{2}\left(\frac{\partial u_y}{\partial x} + \frac{\partial u_x}{\partial y}\right) & \frac{\partial u_y}{\partial y} & \frac{1}{2}\left(\frac{\partial u_y}{\partial z} + \frac{\partial u_z}{\partial y}\right) \\ \frac{1}{2}\left(\frac{\partial u_z}{\partial x} + \frac{\partial u_x}{\partial z}\right) & \frac{1}{2}\left(\frac{\partial u_z}{\partial y} + \frac{\partial u_y}{\partial z}\right) & \frac{\partial u_z}{\partial z} \end{bmatrix} \tag{1.5}$$

1.3.1.2.3 Deviatoric Strain

Consider a state of isotropic strain equal to the average normal strain e_{av} (Turcotte & Schubert, 2002),

$$e_{av} = \frac{1}{3}\Big(\varepsilon_{xx} + \varepsilon_{yy} + \varepsilon_{zz}\Big) = \frac{1}{3}\Delta. \tag{1.6}$$

If the strain is not isotropic, then we can calculate the deviatoric strain as follows:

$$\tilde{\varepsilon}_{ij} = \varepsilon_{ij} - \frac{1}{3}\Delta\delta_{ij}. \tag{1.7}$$

1.3.1.3 Relationship between Stress and Strain

From Hooke's and Navier-Stokes equations for an isotropic medium, the constitutive stress-strain relationship of a porous rock is given by

$$\sigma_{ij} = \lambda\Delta\delta_{ij} + 2\mu\varepsilon_{ij} + \eta_\lambda\dot{\varepsilon}_{ii}\delta_{ij} + 2\eta\dot{\varepsilon}_{ij}, \quad i,j = 1,2,3; \tag{1.8}$$

where η and η_κ are the shear and bulk viscosities, respectively, and η_λ is the viscosity analogous to the Lame parameter in equation (1.16). And the Kronecker delta is given by

$$\delta_{ij} = \begin{bmatrix} \delta_{xx} & \delta_{xy} & \delta_{xz} \\ \delta_{yx} & \delta_{yy} & \delta_{yz} \\ \delta_{zx} & \delta_{zy} & \delta_{zz} \end{bmatrix} \equiv \begin{bmatrix} 1 & 0 & 0 \\ 0 & 1 & 0 \\ 0 & 0 & 1 \end{bmatrix}. \tag{1.9}$$

The strain tensor [as given in equation (1.4)] is given by

$$\varepsilon_{ij} = \frac{1}{2}\left(\frac{\partial u_i}{\partial x_j} + \frac{\partial u_j}{\partial x_i}\right), \tag{1.10}$$

and the dilatation,

$$e_{ii} = \sum_{i=1}^{3} \varepsilon_{ii} = \Delta. \tag{1.11}$$

A linear, isotropic, elastic material has its material orientation uniform in all directions, and the stresses and strains linearly proportional to one another. The principal strains can be written as

$$\sigma_{xx} = \lambda\Delta + 2\mu\varepsilon_{xx}, \tag{1.12}$$

$$\sigma_{yy} = \lambda\Delta + 2\mu\varepsilon_{yy}, \tag{1.13}$$

$$\sigma_{zz} = \lambda\Delta + 2\mu\varepsilon_{zz}; \tag{1.14}$$

where λ is Lame's parameter and μ is the shear modulus.

By using the fundamental moduli λ & μ, other experimentally-observed moduli are expressed. For example, to obtain the bulk modulus K, consider a cube subjected to hydrostatic stress σ, such that $\sigma_{xx} = \sigma_{yy} = \sigma_{zz} = -\sigma$. By adding equations (1.12) to (1.14), we have the trace of the stress tensor given by

$$-\sigma = \lambda\Delta + \frac{2}{3}\mu\Delta \tag{1.15}$$

Since by definition, the bulk modulus, K, is given by the expression, $\frac{-\sigma}{\Delta}$, we have that the relationship between the Lame's parameter and the bulk modulus, is

$$\lambda = K - \frac{2}{3}\mu \tag{1.16}$$

Analogously, the relationship between the viscosity parameters is

$$\eta_\lambda = \eta_\kappa - \frac{2}{3}\eta \tag{1.17}$$

These equations with the same unknowns and parameters describe the responses at any point within a two-phase medium (one with solid and fluid regions) to stress and pore fluid pressure

(Quintal, Rubino, Caspari, & Holliger, 2016).

In Chapters Three and Four, I show and discuss the results from models of two-phase rock consisting of a isotropic homogeneous solid with pores occupied by fluid. For the solid part of this rock, substituting equation (1.16) into equation (1.8) and setting all the viscosity parameters to zero, we have the equation that describes just the stress in the solid:

$$\sigma_{ij} = \left(K_s - \frac{2}{3}\mu \right) \Delta\delta_{ij} + 2\mu\varepsilon_{ij}. \tag{1.18}$$

Note that all my experiments are stationary and so the effects of viscosity are negligible.

The pore fluid is assumed to be a homogeneous Newtonian fluid in which the viscous stresses arising from its flow, at every point, are linearly proportional to the local strain rate — the rate of change of its deformation over time. Substituting equations (1.16) and (1.17) into equation (1.8), and setting the shear modulus, μ, and the bulk viscosity, η_κ, to zero, we have the equation that describes the stress in the fluid (Quintal et al., 2016):

$$\sigma_{ij} = K_f \Delta\delta_{ij} - \frac{2}{3}\eta\dot{\varepsilon}_{ij}\delta_{ij} + 2\eta\dot{\varepsilon}_{ij}. \tag{1.19}$$

1.3.1.4 Stress in the Solid Region

When equation (1.18) is expanded, the stress components in the solid region of the model becomes

$$\sigma_{xx_s} = 2\mu\big(\frac{\partial u}{\partial x}\big) + (K_s - \frac{2}{3}\mu)\big(\frac{\partial u}{\partial x} + \frac{\partial v}{\partial y} + \frac{\partial w}{\partial z}\big), \tag{1.20}$$

$$\sigma_{yy_s} = 2\mu\big(\frac{\partial v}{\partial y}\big) + (K_s - \frac{2}{3}\mu)\big(\frac{\partial u}{\partial x} + \frac{\partial v}{\partial y} + \frac{\partial w}{\partial z}\big), \tag{1.21}$$

$$\sigma_{zz_s} = 2\mu\big(\frac{\partial w}{\partial z}\big) + (K_s - \frac{2}{3}\mu)\big(\frac{\partial u}{\partial x} + \frac{\partial v}{\partial y} + \frac{\partial w}{\partial z}\big), \tag{1.22}$$

$$\sigma_{xy_s} = \mu\big(\frac{\partial u}{\partial y} + \frac{\partial v}{\partial x}\big). \tag{1.23}$$

$$\sigma_{xz_s} = \mu\big(\frac{\partial u}{\partial z} + \frac{\partial w}{\partial x}\big). \tag{1.24}$$

$$\sigma_{yz_s} = \mu\big(\frac{\partial v}{\partial z} + \frac{\partial w}{\partial y}\big). \tag{1.25}$$

For numerical calculations, it is necessary to nondimensionalize the above equations. Nondimensionalization is the complete removal of units from an equation, one that contains dimensional parameters, by substituting appropriate variables. The reason for nondimensionalization is to simplify equations and emphasize some parameters in it over the others, hence, reducing the number of parameters. This scaling also usually makes the dependent variables similar to 1, which can avoid overflow/underflow numerical errors. In the end, this may further reduce the time it would take to solve the equations numerically.

To nondimensionalize, we scale the stress with the bulk modulus of the solid region. Also, note that the displacements, $u,\ v,\ w$ (same as $u_x,\ u_y,\ \&\ u_z$ in equation 1.5) and their respective coordinates $x,\ y,\ z$, all have the same units, and we scale them with the same length scale. This makes their derivatives, $\frac{\partial u}{\partial x}, \frac{\partial v}{\partial y}, \frac{\partial w}{\partial z}$, dimensionless.

Substituting the above into equations (1.20) to (1.23), we have the dimensionless equations for the stress components in the solid region,

$$\sigma^*_{xx_s} = 2\frac{\mu}{K_s}\left(\frac{\partial u}{\partial x}\right) + \left(1 - \frac{\mu}{K_s}\right)\left(\frac{\partial u}{\partial x} + \frac{\partial v}{\partial y} + \frac{\partial w}{\partial z}\right), \tag{1.26}$$

$$\sigma^*_{yy_s} = 2\frac{\mu}{K_s}\left(\frac{\partial v}{\partial y}\right) + \left(1 - \frac{\mu}{K_s}\right)\left(\frac{\partial u}{\partial x} + \frac{\partial v}{\partial y} + \frac{\partial w}{\partial z}\right), \tag{1.27}$$

$$\sigma^*_{zz_s} = 2\frac{\mu}{K_s}\left(\frac{\partial w}{\partial z}\right) + \left(1 - \frac{\mu}{K_s}\right)\left(\frac{\partial u}{\partial x} + \frac{\partial v}{\partial y} + \frac{\partial w}{\partial z}\right), \tag{1.28}$$

$$\sigma^*_{xy_s} = \frac{\mu}{K_s}\left(\frac{\partial u}{\partial y} + \frac{\partial v}{\partial x}\right); \tag{1.29}$$

$$\sigma^*_{xz_s} = \frac{\mu}{K_s}\left(\frac{\partial u}{\partial z} + \frac{\partial w}{\partial x}\right); \tag{1.30}$$

$$\sigma^*_{yz_s} = \frac{\mu}{K_s}\left(\frac{\partial v}{\partial z} + \frac{\partial w}{\partial y}\right); \tag{1.31}$$

where $\sigma^*_{ij_s}$ is the scaled stress.

Setting up the stress tensor we have

$$\sigma^* = \begin{bmatrix} 2\frac{\mu}{K_s}\left(\frac{\partial u}{\partial x}\right) + \left(1 - \frac{2}{3}\frac{\mu}{K_s}\right)\Delta & \frac{\mu}{K_s}\left(\frac{\partial u}{\partial y} + \frac{\partial v}{\partial x}\right) & \frac{\mu}{K_s}\left(\frac{\partial u}{\partial z} + \frac{\partial w}{\partial x}\right) \\ \frac{\mu}{K_s}\left(\frac{\partial u}{\partial y} + \frac{\partial v}{\partial x}\right) & 2\frac{\mu}{K_s}\left(\frac{\partial v}{\partial y}\right) + \left(1 - \frac{2}{3}\frac{\mu}{K_s}\right)\Delta & \frac{\mu}{K_s}\left(\frac{\partial v}{\partial z} + \frac{\partial w}{\partial y}\right) \\ \frac{\mu}{K_s}\left(\frac{\partial u}{\partial z} + \frac{\partial w}{\partial x}\right) & \frac{\mu}{K_s}\left(\frac{\partial v}{\partial z} + \frac{\partial w}{\partial y}\right) & 2\frac{\mu}{K_s}\left(\frac{\partial w}{\partial z}\right) + \left(1 - \frac{2}{3}\frac{\mu}{K_s}\right)\Delta \end{bmatrix}. \tag{1.32}$$

Note that there is only one dimensionless parameter, $\frac{\mu}{K_s}$.

1.3.1.5 Stress in the Fluid Region

In the fluid region, the normal components of the strain rate tensor (in 3D) are given by

$$\dot{\varepsilon}_{xx} = \frac{\partial}{\partial x}\frac{\partial u}{\partial t}, \quad \dot{\varepsilon}_{yy} = \frac{\partial}{\partial y}\frac{\partial v}{\partial t}, \quad \dot{\varepsilon}_{zz} = \frac{\partial}{\partial z}\frac{\partial w}{\partial t}; \tag{1.33}$$

and the x-y component of the shear strain rate is given by

$$\dot{\varepsilon}_{xy} = \frac{1}{2}\left(\frac{\partial}{\partial y}\frac{\partial u}{\partial t} + \frac{\partial}{\partial x}\frac{\partial v}{\partial t}\right). \tag{1.34}$$

Then equation (1.19) for the normal component of the stress tensor in the x direction becomes

$$\sigma_{xx_f} = K_f\Delta + 2\eta\dot{\varepsilon}_{xx} - \frac{2}{3}\eta\Big(\dot{\varepsilon}_{xx} + \dot{\varepsilon}_{yy} + \dot{\varepsilon}_{zz}\Big). \tag{1.35}$$

Further, we nondimensionalize the equation as shown in the following lines.

Choosing a time scale, $T = \frac{\eta}{K_s}$, the dimensionless expressions for the normal strain rates are given by (similar for the shear strain rates)

$$\dot{\varepsilon}^*_{xx} = \dot{\varepsilon}_{xx}T, \quad \dot{\varepsilon}^*_{yy} = \dot{\varepsilon}_{yy}T, \quad \dot{\varepsilon}^*_{zz} = \dot{\varepsilon}_{zz}T. \tag{1.36}$$

Substituting these into equation (1.35), we have

$$\sigma_{xx_f} = K_f\Delta + 2\eta\frac{\varepsilon^*_{xx}}{T} - \frac{2}{3}\frac{\eta}{T}\Big(\dot{\varepsilon}^*_{xx} + \dot{\varepsilon}^*_{yy} + \dot{\varepsilon}^*_{zz}\Big). \tag{1.37}$$

Next, we introduce a variable, η^*, which is the dimensionless viscosity, such that.

$$\eta^* = \frac{\eta}{K_sT}. \tag{1.38}$$

$$=> \eta = \eta^*K_sT. \tag{1.39}$$

Further, substituting equation 1.39 into equation 1.37, we have

$$\sigma_{xx_f} = K_f\Delta + 2\eta^*K_sT\dot{\varepsilon}^*_{xx}\frac{1}{T} - \frac{2}{3}\eta^*K_sT\frac{1}{T}\Big(\dot{\varepsilon}^*_{xx} + \dot{\varepsilon}^*_{yy} + \dot{\varepsilon}^*_{zz}\Big). \tag{1.40}$$

Note that since $T = \frac{\eta}{K_s}$, then $\eta^* = 1$ in all my simulations.

Finally, we introduce $\sigma^*_{xx_f} = \frac{\sigma_{xx_f}}{K_s}$ to get the expression

$$\sigma^*_{xx_f} = K^*_f\Delta + 2\eta^*\dot{\varepsilon}^*_{xx} - \frac{2}{3}\eta^*\Big(\dot{\varepsilon}^*_{xx} + \dot{\varepsilon}^*_{yy} + \dot{\varepsilon}^*_{zz}\Big); \tag{1.41}$$

where $K^*_f = \frac{K_f}{K_s}$.

Therefore, the dimensionless equations for the stress components in the fluid region are

$$\sigma^*_{xx_f} = K^*_f\Delta + 2\eta^*\dot{\varepsilon}^*_{xx} - \frac{2}{3}\eta^*\Big(\dot{\varepsilon}^*_{xx} + \dot{\varepsilon}^*_{yy} + \dot{\varepsilon}^*_{zz}\Big), \tag{1.42}$$

$$\sigma^*_{yy_f} = K^*_f\Delta + 2\eta^*\dot{\varepsilon}^*_{yy} - \frac{2}{3}\eta^*\Big(\dot{\varepsilon}^*_{xx} + \dot{\varepsilon}^*_{yy} + \dot{\varepsilon}^*_{zz}\Big), \tag{1.43}$$

$$\sigma^*_{zz_f} = K^*_f\Delta + 2\eta^*\dot{\varepsilon}^*_{zz} - \frac{2}{3}\eta^*\Big(\dot{\varepsilon}^*_{xx} + \dot{\varepsilon}^*_{yy} + \dot{\varepsilon}^*_{zz}\Big), \tag{1.44}$$

$$\sigma^*_{xy_f} = 2\eta^*\dot{\varepsilon}^*_{xy} \tag{1.45}$$

$$\sigma^*_{xz_f} = 2\eta^*\dot{\varepsilon}^*_{xz} \tag{1.46}$$

$$\sigma^*_{yz_f} = 2\eta^*\dot{\varepsilon}^*_{yz} \tag{1.47}$$

1.3.1.6 Implementation of 2D models

In this study, we initially carried out our simulations in 2D in order to better understand the model, examine its performance, and select processing parameters. None of the results from the 2D simulations are included or discussed in Chapters Three and Four. Some of them are, however, shown in Appendix A of this thesis.

It is common to consider 2D cases with either *plane stress* (with no stress in the 3rd dimension, that is, $\sigma_{xz} = \sigma_{yz} = \sigma_{zz} = 0$, but with strain in the 3rd dimension, $u_z \neq 0$) or *plain strain* (with no displacement in the 3rd dimension, that is, $u_z = 0$, but with stress in the 3rd dimension). However, we want to consider a case with no 3rd dimension present at all. And in order to have a solution for uniform compression where $\sigma_{xx} = \sigma_{yy} = K_s\Delta$ or, alternatively, so that the trace of the stress tensor remains $K_s\Delta$, we need to modify the elastic equations

such that equation (1.16) becomes

$$\lambda = K - 2\frac{\mu}{2} = K - \mu. \tag{1.48}$$

Note that equation 1.48 will make $\lambda < 0$ for the sandstone model in 2D, and this will represent a case for auxetic materials with a negative Poisson's ratio - when some tensile stress is applied axially to the material to stretch it, the material expands transversely instead of compressing. (See Table 2.1 for the material properties of the sandstone model.)

When equation (1.18) is expanded, the stress components in the solid region of the 2D model will be

$$\sigma_{xx_s} = 2\mu\big(\frac{\partial u}{\partial x}\big) + (K_s - \mu)\big(\frac{\partial u}{\partial x} + \frac{\partial v}{\partial y}\big), \tag{1.49}$$

$$\sigma_{yy_s} = 2\mu\big(\frac{\partial v}{\partial y}\big) + (K_s - \mu)\big(\frac{\partial u}{\partial x} + \frac{\partial v}{\partial y}\big), \tag{1.50}$$

$$\sigma_{xy_s} = \mu\big(\frac{\partial u}{\partial y} + \frac{\partial v}{\partial x}\big). \tag{1.51}$$

1.3.2 Continuum Theory

In continuum mechanics, a continuum is "a compact, connected subset of a metric space" as defined by several continuum theorists (Ingram, 2006), while continuum theory is a classical physics concept premised on the postulation that matter is a continuous distribution of mass regardless of the gaps/voids between its molecules. This is captured nicely in the following lines by Fridtjov (2008):

> Regardless of how small volume elements the matter is subdivided into, every element will contain matter. The matter may have a finite number of discontinuous surfaces, for instance fracture surfaces or yield surfaces, but material curves [surfaces] that do not intersect such surfaces retain their continuity during the motion and deformation of the matter. (p. 19)

This means that, in my case, I present each rock sample by continuous functions $u(x, y, z, t)$, $v(x, y, z, t)$, and $w(x, y, z, t)$, with material properties (ρ, λ, μ) constant within the solid and fluid parts of the model.

Continuum mechanics is described by *material equations* or *constitutive equations* (Fridtjov, 2008). Hooke's law, shown in equation (1.52), represents the most basic constitutive equation (Fridtjov, 2008).

$$\sigma = E\varepsilon \tag{1.52}$$

In order to take derivatives, we are required to consider arbitrarily small length scales. However, near the atomic and molecular length scales, stress and strain become discontinuous and not well defined. To work around this, in continuum mechanics, we assume that a length scale exists which is much smaller than the length scale on which the deformation is occurring, but which is long compared to the molecular scale. The latter allows us to average within such a length scale which will then allow our stress and strain to be well-defined.

In other words, in continuum theory, we do not consider the complexity of materials on a molecular level, instead, we describe the average behaviour over volumes that are large compared to molecules within a system, but small compared to the system.

In this thesis, Figure 1.2 represents a volume that is small enough that we can take derivatives with respect to its side lengths but large compared to molecular scales.

1.3.3 Theory of Poroelasticity

The theory of poroelasticity studies how porous solids deform under applied *stress*, and the relationship between the pore fluid and the solid skeleton during the deformation. It was first introduced by Biot (1935). He went on to formulate the general theory of three-dimensional consolidation of fluid-saturated porous elastic solids (Biot, 1941), which chiefly looks at the process that porous rocks undergo when they change volume as a response to stress/pressure change, and this is the theory that gave birth to the parameters which this thesis seeks to numerically determine. The theory of poroelasticity begins with the concept of stress and *strain* on a 'continuum' level.

The theory of poroelasticity, also known as *Biot-Gassmann theory*, makes a similar approxi-

mation to the continuum theory. For instance, in our poroelastic model, using Biot's theory, we do not have to consider the complexity of the rock's pore geometry. Instead, we define a length scale that is sufficiently large that it contains a statistically representative sample of the pore geometry but small compared to the lengths over which stress and strain are changing so that we can still take derivatives. Biot's theory, which contains a few extra parameters compared with regular solid mechanics, allows us to calculate the strain on a porous rock given a certain stress when the pores are *saturated* (that is, completely filled with fluid). In other words, Biot's theory considers the whole rock as a continuum. If an additional stress parameter, representing pore pressure, and an additional strain parameter, representing fluid content, is included, Figure 1.2 can also represent a rock sample that contains saturated pores which we treat with Biot's theory. Or, on a *macroscopic* level, it would represent a sample containing a representative sample of porosity which would be considered an infinitesimal volume for Biot's theory.

1.3.3.1 Microscopic vs Macroscopic Parameters

A porous rock can be characterized by its *microscopic* structure (or microstructure) which determines how its *macroscopic* structure (or macrostructure) is strained under stress. For the purposes of this study, the microstructure considered includes two parts of the rock model - the pore space (which contains the pore fluid) and the solid region (which is the rock's skeleton) - each considered as a continuum. The macrostructure refers to the whole rock, including the pore space and the solid region, considered as a single continuum using Biot's theory. In other words, the macrostructure is a continuum made up of continuous media (the microstructures). In our model, each of the microstructures has its own elastic parameters different from those of the macrostructure, hence the name *microscopic parameters*. The *macroscopic parameters*, on the other hand, describe the elastic parameters of the rock as a whole. Once macroscopic parameters are known, calculation of a rock's response to loading does not require modeling of the detailed pore geometry. As used in this study, the microscopic parameters of a saturated single-phase porous rock (i.e. one containing only one type of fluid) include the bulk moduli of the solid region, K_s, and pore fluid, K_f, the shear modulus of the solid region, μ, and the shear viscosity of the pore fluid, η. These are

all independent parameters.

This thesis work involves carrying out calculations on the microscopic level on volumes that are big enough that they determine the macroscopic parameters. The macroscopic parameters considered are the Biot's parameters namely, the drained bulk modulus, K_d, the undrained bulk modulus, K_u, the pressure parameter, M, and the Biot-Willis coefficient, α. The parameters, K_d and K_u, characterize the bulk response of the rock to compression for drained and undrained experiments as described in Biot and Willis (1957). The pressure, M, is the pressure needed to be exerted on the pore fluid to increase its content by a unit value at constant macroscopic dilatation, and α is a quantity that describes how much apparent macroscopic dilatation there is caused by the changes in fluid content (Bourbie et al., 1987). These macroscopic parameters are all dependent parameters and the equations used to determine them are derived and explained in the following part of this thesis.

1.3.3.2 Biot's Parameters

The change in macroscopic work done per unit volume of an element is given by

$$\mathrm{d}W = \frac{\partial W}{\partial \varepsilon_{ij}}\mathrm{d}\varepsilon_{ij} + \frac{\partial W}{\partial \zeta}\mathrm{d}\zeta; \tag{1.53}$$

where, ζ, the variation in fluid content (Bourbie et al., 1987), is a quantity that describes the fluid leaving the pore.

From equation 1.53, the stress tensor and pore fluid pressure, respectively, are represented by

$$\sigma_{ij} = \frac{\partial W}{\partial \varepsilon_{ij}} \tag{1.54}$$

$$p = \frac{\partial W}{\partial \zeta} \tag{1.55}$$

In quadratic terms (Morozov & Deng, 2016; Bourbie et al., 1987), equation (1.53) can be

expanded thus:

$$W = \frac{1}{2}\big(\lambda_u + 2\mu\big)\Delta^2 + \mu\tilde{\varepsilon}_{ij}\tilde{\varepsilon}_{ij} - \alpha M\Delta\zeta + \frac{1}{2}M\zeta^2; \tag{1.56}$$

where λ_u is Lame's parameter, and the subscript u represents the undrained case.

This implies that (Bourbie et al., 1987),

$$\sigma_{ij} = \lambda_u\Delta\delta_{ij} + 2\mu\varepsilon_{ij} - \alpha M\zeta\delta_{ij}, \tag{1.57}$$

$$p = M\big(-\alpha\Delta + \zeta\big), \qquad \text{and} \tag{1.58}$$

$$\zeta = \frac{1}{M}P + \alpha\Delta. \tag{1.59}$$

Alternatively, from equation (1.58,

$$M\zeta = p + \alpha M\Delta \tag{1.60}$$

$$\sigma_{ij} = \big(\lambda_u - \alpha^2 M\big)\Delta\delta_{ij} + 2\mu\varepsilon_{ij} - \alpha p\delta_{ij}. \tag{1.61}$$

Next, two systems of deformation are considered, which are the open (drained) and closed (undrained) systems, or the jacketed and unjacketed tests (Biot & Willis, 1957; Biot, 1962).

To describe one of my experiments, let us consider a system where the fluid is allowed to drain out of the pore (the open system); that is, the pressure remains constant ($p = 0$). The bulk modulus from equation (1.16) will then be given as

$$K_d = \lambda_d + \frac{2}{3}\mu; \tag{1.62}$$

where the subscript d represents the drained case.

For another experiment where the fluid remains shut up in the pores (i.e. a closed system

with $\zeta = 0$), we have

$$K_u = \lambda_u + \frac{2}{3}\mu; \tag{1.63}$$

In equation 1.61,

$$\lambda_u - \alpha^2 M = \lambda_d. \tag{1.64}$$

From equations (1.62), (1.63), and (1.64), we have that

$$K_d = K_u - \alpha^2 M. \tag{1.65}$$

For the drained case ($p = 0$), equation (1.61) becomes

$$\sigma_{ij} = \lambda_d \Delta_d \delta_{ij} + 2\mu\varepsilon_{ij}. \tag{1.66}$$

$$\tag{1.67}$$

Further,

$$\sigma_{xx} = \sigma_{yy} = \sigma_{zz} = \sigma. \tag{1.68}$$

$$3\sigma = 3\lambda_d + 2\mu\Delta_d. \tag{1.69}$$

$$\sigma = \left(\lambda_d + \frac{2}{3}\mu\right)\Delta_d. \tag{1.70}$$

$$\sigma = K_d \Delta_d \tag{1.71}$$

Likewise, for the drained case, equation (1.59) becomes

$$\alpha = \frac{\zeta}{\Delta_d}. \tag{1.72}$$

$$1 - \alpha = 1 - \frac{\zeta}{\Delta_d}. \tag{1.73}$$

$$\big(1 - \alpha\big)\Delta_d = \Delta_d - \zeta \tag{1.74}$$

Equation (1.74) represents the dilatation of the solid (Bourbie et al., 1987) and hence gives

$$\big(1-\alpha\big)\frac{\sigma}{K_d} = \frac{\sigma}{K_s} \tag{1.75}$$

$$K_d = K_s\big(1-\alpha\big) \tag{1.76}$$

Also, the drained and undrained compressibilities (which are the inverse of their bulk moduli), respectively, can be computed from

$$J_d = \frac{\Delta_d}{\sigma_d}, \qquad \text{and} \tag{1.77}$$

$$J_u = \frac{\Delta_u}{\sigma_u}; \tag{1.78}$$

where $K_d = \frac{1}{J_d}$, while, $K_u = \frac{1}{J_u}$.

Finally, all the above parameters are related to Gassmann's (1951) equation by (for the full derivation, see Bourbie et al., 1987)

$$K_u = \frac{\phi\left[\frac{1}{K_s} - \frac{1}{K_f}\right] + \frac{1}{K_s} - \frac{1}{K_d}}{\frac{\phi}{K_d}\left[\frac{1}{K_s} - \frac{1}{K_f}\right] + \frac{1}{K_s}\left[\frac{1}{K_s} - \frac{1}{K_d}\right]} \tag{1.79}$$

The above parameters are compared to the analytical expressions in Chapter Two. They are all the Biot's parameters that this study seeks to evaluate. In Chapter Two, these parameters are determined, both by numerical and (in some special cases) analytical computations.

1.4 Laboratory Rock Physics Experiments

In rock physics, there are various laboratory experiments useful for simulating the actual in-situ tensile and compressive stresses that rocks undergo. Since my research involves numerical simulations of rock compression tests, I briefly review how experimental rock compression tests are carried out in a laboratory. One of the most common of these experiments is the

triaxial shear test (also called the triaxial compression test). Most undrained tests usually begin with a saturation phase where the rock sample is completely immersed in fluid until all the pores are completely filled with the fluid (saturated).

In triaxial testing (see Figure 1.5), the rock sample is sealed inside an impermeable latex membrane (ASTM, 2002) and placed inside a cylindrical triaxial cell. Then the test is carried out in two phases. The first phase is the consolidation phase. Consolidation, in this case, refers to the process of allowing the excess fluids in the pores of the rock sample to drain out through a drainage tube connected to a porous disc at the base of the rock sample, thereby allowing the specimen to adjust to its environment even as the pressure transfers to the rock matrix. This concept (different from the compaction of clay sediments) was first introduced by Terzaghi (1923). In the consolidation phase, the cell pressure is increased by pumping fluid into the cell through a supply tube. The cell pressure is uniform all around the rock sample ($\sigma_2 = \sigma_3$ represents the cell pressure, known as the minor principal stress). As the cell pressure increases, excess fluid (or air) also builds up inside the pores. At this point, the specimen may or may not be allowed to consolidate. The second phase is the shearing phase. Here, some load is applied to the loading cap or piston at the top of the cell causing an increase in the axial stress, σ_1, known as the major principal stress, at the top of the specimen. This vertical stress is gradually (or quickly) increased, and each time, the stress and strain data is automatically recorded on a computer running a data acquisition program.

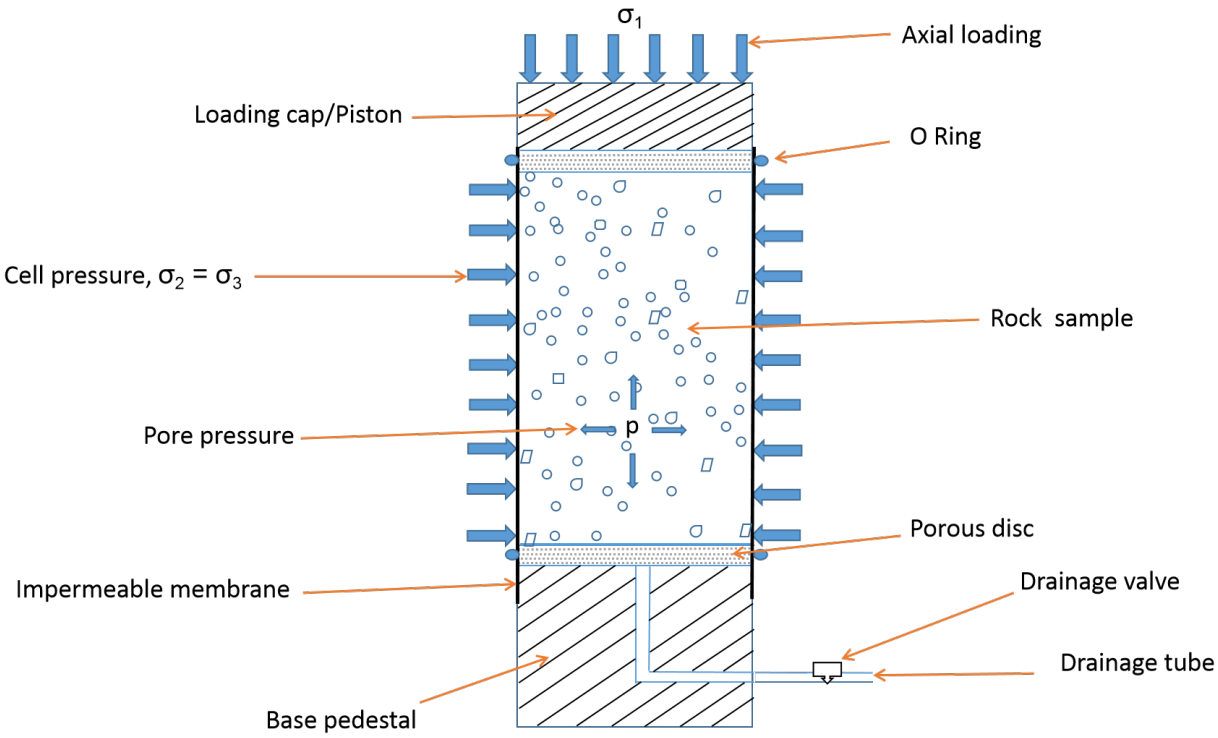

Figure 1.5: Sketch of a triaxial compression test on a cylindrical rock sample

This test is called the triaxial shear test because of the three principal stresses applied. The main difference between the triaxial test and my numerical simulations is that, in my simulations, I consider a case where the rock is completely immersed in a fluid and the hydrostatic stress is equal to the cell pressure; i.e., $\sigma_1 = \sigma_2 = \sigma_3$. And the pore space is made to interact with the outside environment through a tube (for the drained case), or no interaction with the outside environment is allowed (for the undrained case). Further, the consolidation phase in my model occurs when extra fluid is ejected out of the pore because the fluid pressure is greater than the stress on the outer boundary.

The main advantages that the triaxial compression test has over other compression tests include well-controlled drainage, both during the consolidation and shearing phases, which allows for measurement of drained or undrained parameters, and well-controlled boundary conditions which allow for determination of stresses on the outer boundaries of the rock. The volumetric strains can also be determined from the triaxial test. However, it is not without some limitations. For instance, the types of triaxial shear tests that require consolidation

must be run very slowly so that the excess pore pressure might dissipate, and this makes them difficult and time consuming. Also, the whole setup takes a lot of space and is expensive to acquire. Further, at large strains, the rock sample does not return back to its original shape, which can affect its physical measurements like the cross-sectional area. All these challenges and more are eliminated in Digital Rock Physics (DRP).

1.5 Digital Rock Physics (DRP) Experiments

Rock properties can be determined in various ways, such as "conventional (laboratory), indirect (inversion of seismic waves), and digital computation (Digital Rock Physics)" methods (Handoyo, Fatkhan, Suharno, & Fourier, 2017). In the preceding section, I described a common laboratory experiment. In DRP, the main task is to model a rock with a matrix having various pores, and then perform various simulations similar to the ones described in the previous section, albeit numerically. DRP also allows us to apply certain boundary conditions that are extremely difficult or impossible to apply in laboratory rock specimens. One of such is applying a zero displacement on the pore walls while specifying some displacement on the outer walls of the rock matrix. DRP can also make use of computerized tomography (CT) scans of rocks, showing their complex/simple pore networks and mineral geometries. In this thesis, I perform most of my experiments numerically. Also, I assume that the digital rock specimens are elastic (i.e., can return to their original shape after deformation when subjected to a load), homogeneous (i.e., of a uniform composition of minerals/rock type), isotropic (i.e., having identical properties in all directions), and single phase (i.e, having only one type of fluid in the pores). These make for convenient calculations/approximations. Moreover, it is important to point out that my numerical simulations are similar to the isotropic and static compression tests. There are no shear cases or time-dependence.

In recent years, DRP has had remarkable growth and popularity among researchers and industry because of its incredible benefits and wide application. Some rock properties/characteristics are extremely difficult (and sometimes impossible) to measure directly by experiments performed in a physical laboratory setting. For instance, it might be impossible to measure the

tortuosity of the rock matrix in a laboratory setting. Also, specifying zero displacement on the outer boundaries of an elastic rock under loading would be practically impossible. However, the scope of DRP is limitless. It opens up new intuitiveness into how reservoir rocks behave and presents new perspectives on how to look at them and study them. Exploration companies can have improved economic returns and hydrocarbon processing with the proper application of DRP to rock samples (Sungkorn et al., 2015).

2 METHODOLOGY

In this thesis, a porous rock is characterized by a detailed microscopic model which has the pore space fully saturated with fluid, and simulates an experiment where the rock is fully immersed in fluid with a mean hydrostatic pressure, σ. Equations of elasticity are used and the average stress and strain ratios are measured.

This chapter begins with a detailed explanation of the steps I followed in my numerical experiments, showing how I achieved the stress and strain simulations in my microscopic model. Next, I introduce the actual rock samples used in this research to compare the simple 3D models in COMSOL Multiphysics®. Finally, in the last section of this chapter, I show how I determined Biot's macroscopic model parameters using numerical and analytical approaches. (Note that the analytical approach is only considered for a spherical rock with one spherical pore.)

2.1 Model Description

The models are set up such that for a homogeneous sample, the stress and strain fields are isotropic (similar to an experiment where the sample is immersed in a fluid at a constant hydrostatic pressure). For the numerical modelling, this study made use of COMSOL Multiphysics® - a general finite-element solver for partial differential equations (PDEs). For the reader who is interested in carrying out similar simulations in COMSOL Multiphysics®, the implementation is described below, starting with the four main categories of COMSOL Multiphysics® which are

- Prescription of Parameters
- Component

- Study
- Results

Each of these categories will be described in detail in the next few subsections as relating to the rock model in this study, but the results will be discussed in the next two chapters.

2.1.1 Prescribing the Model Parameters

In this category, the values of the microscopic elastic parameters of the digital rock are defined. These values (see Table 2.1) were taken from those found in Quintal et al. (2016) and McLellan (1996).

Table 2.1: Material Properties of The Model

Material Parameter	Value
Bulk modulus of Carbonate	19 GPa
Shear modulus of Carbonate	11 GPa
Bulk modulus of Sandstone	36.4 GPa
Shear modulus of Sandstone	44 GPa
Fluid Bulk modulus	2.4 GPa
Shear viscosity	0.003 Pa · s

2.1.2 Components of the Model

This category describes the geometry, domain and boundary specifications, physics (PDEs and Dirichlet boundary condition), and mesh of the model.

Geometry of the Model

For the digital rock in this study and for a start, simple poroelastic models of dimensionless quantities are considered. In 2D, this consists of a circle with a radius of 1 m, and a centered circular pore of 0.1 m radius, as shown in Figure 2.1. In 3D, the model is a simple sphere

with a radius of 1 m and a centered spherical pore of 0.1 m radius (2.2). It is important to point out that these sizes were used in COMSOL Multiphysics® for convenience, but the models were dimensionless and so the sizes could be scaled arbitrarily. The pore sizes are later varied in order to obtain different porosities as will be shown in the next chapter. Also, changing the geometries to other regular shapes, like a square (for 2D) or a cube (for 3D) with similar dimensions, had varied effects on the results.

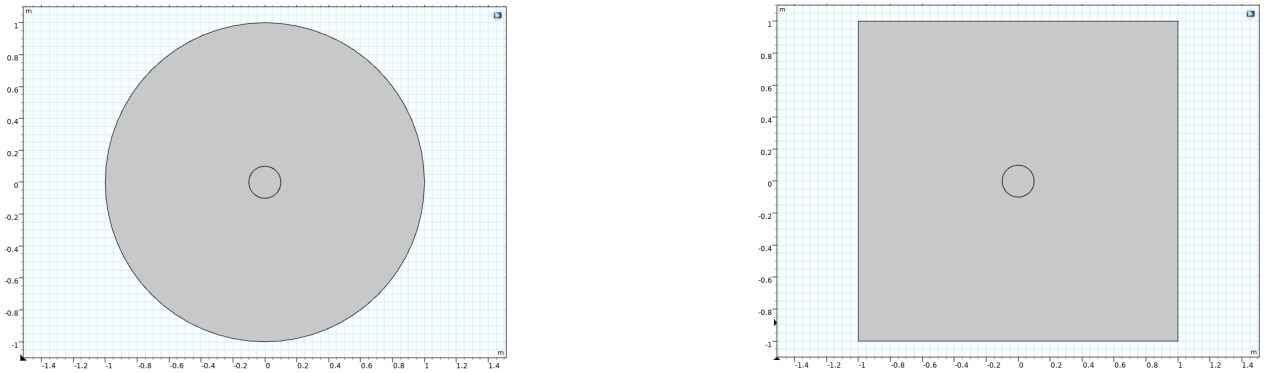

(a) **(b)**

Figure 2.1: (a) A circular rock with a circular pore at its centre (b) A square rock with a circular pore at its centre

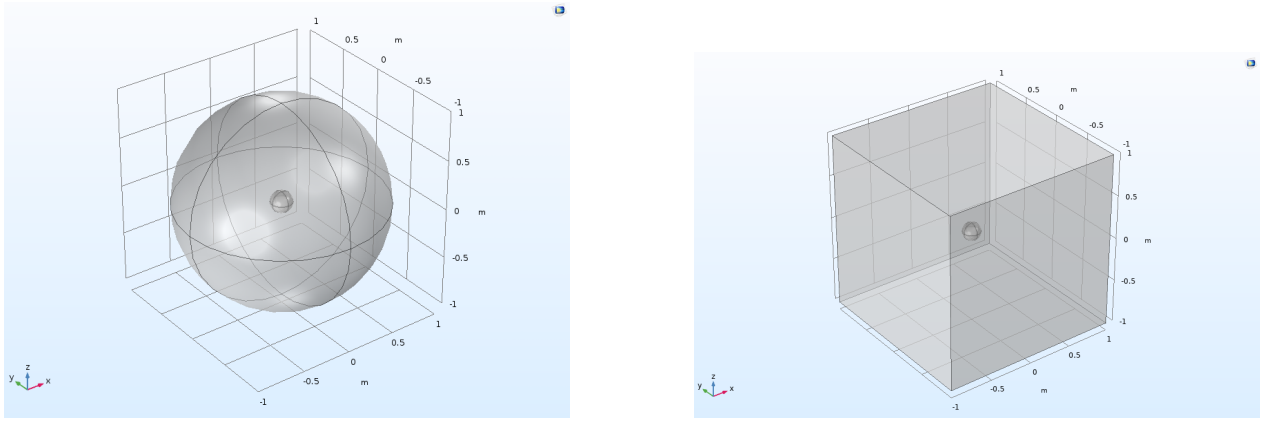

(a) **(b)**

Figure 2.2: (a) A spherical rock with a spherical pore at its centre (b) A cubical rock with a spherical pore at its centre

Domains in the Model

In DRP, PDEs are solved on domains (volumes in 3D; surfaces in 2D) bound by boundaries (surfaces in 3D; edges in 2D). The domains, in this model, are modelled as the solid

and fluid regions in the rock model (see Figures 2.3 and 2.4). The boundaries represent the outer boundaries (the outer lines/surfaces of the rock model) and the inner boundaries (pore walls) - Figures 2.5 and 2.7, respectively. The outer region is modeled as an elastic solid, and the effect of the fluid can be represented by the normal stress on the pore wall, such that simulations are only performed in the outer region. This helps the model run faster and use less memory. Some simulations did model the fluid region also and the results were found to be in good agreement with those where the fluid region was not modelled.

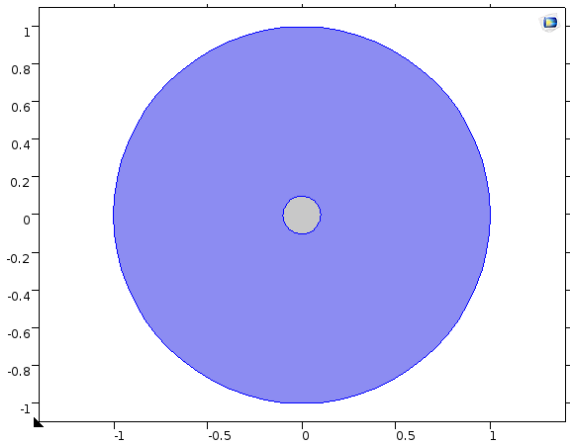

(a) A circular rock with a circular pore at its centre

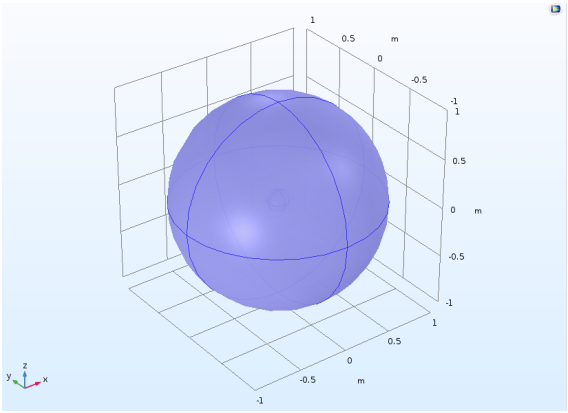

(b) A spherical rock with a spherical pore at its centre

Figure 2.3: Solid Domain (highlighted in blue)

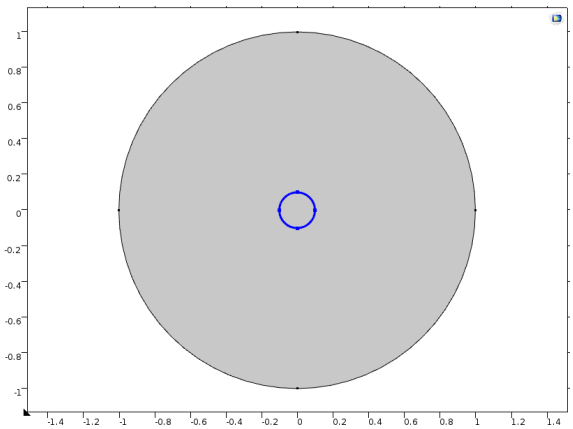

(a) A circular rock with a circular pore at its centre

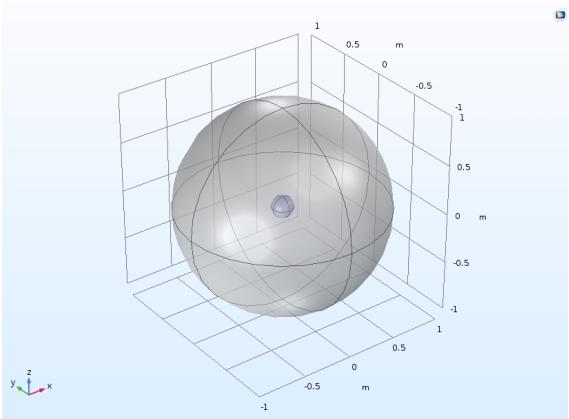

(b) A spherical rock with a spherical pore at its centre

Figure 2.4: Fluid Domain (only the boundary of the fluid domain is highlighted)

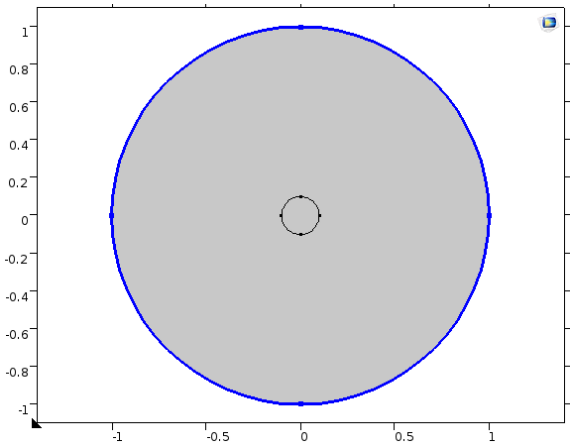

(a) A circular rock with a circular pore at its centre

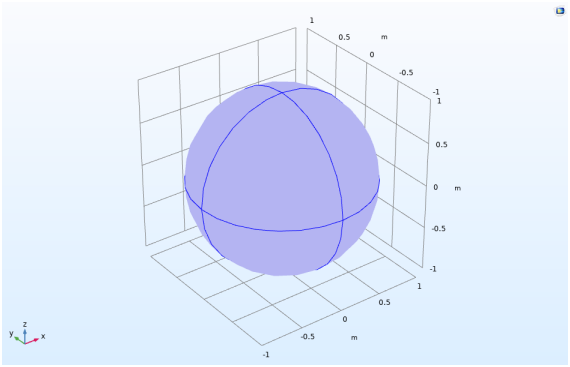

(b) A spherical rock with a spherical pore at its centre

Figure 2.5: Outer boundaries (highlighted in blue)

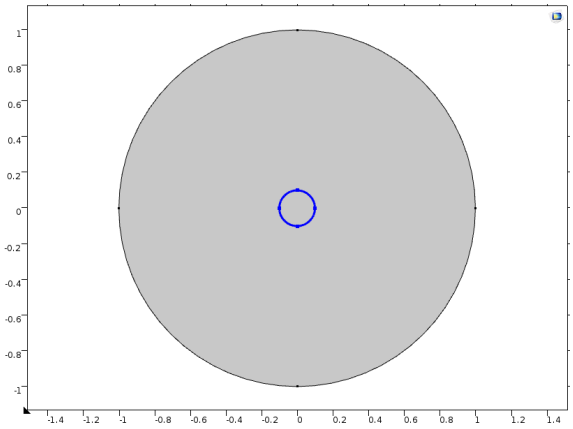

(a) A circular rock with a circular pore at its centre

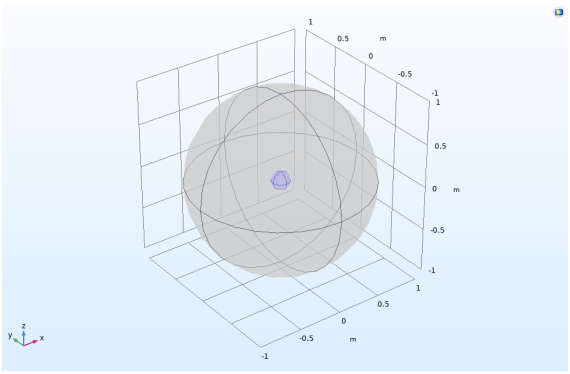

Figure 2.6: A spherical rock with a spherical pore at its centre

Figure 2.7: Pore walls (highlighted in blue)

Dirichlet Boundary Condition

The Dirichlet boundary condition specifies the values that a solution needs to take on along the boundary of the domain. The Dirichlet boundary conditions correspond to a situation where the sample is placed inside a solid and rigid structure that we can control to contract, producing uniform displacement on the outer boundaries of our sample. We refer to this as *rigid loading*. In our numerical experiment, this is done by prescribing a small normal displacement along the boundaries as shown in Figures 2.8 and 2.9 (the arrows show the direction of movement of the boundaries).

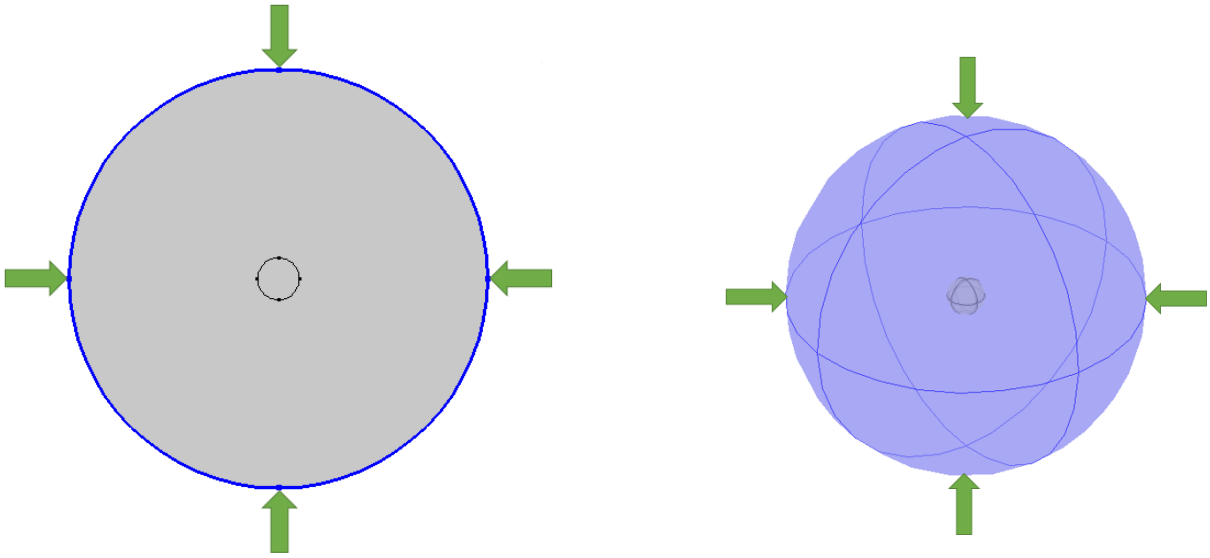

(a) A circular rock with a circular pore at its centre

(b) A spherical rock with a spherical pore at its centre

Figure 2.8: Arrows showing uniform displacement of outer boundaries

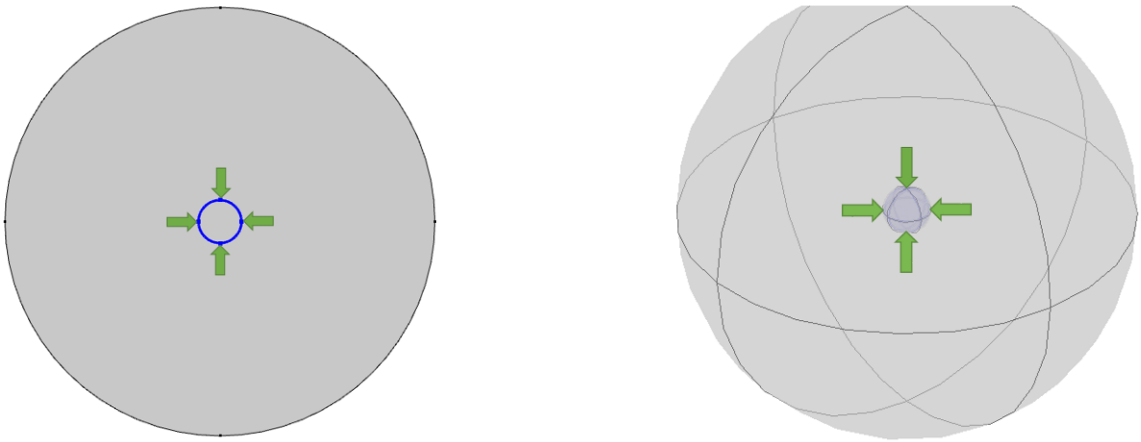

(a) A circular rock with a circular pore at its centre

(b) A spherical rock with a spherical pore at its centre

Figure 2.9: Arrows showing uniform displacement of pore walls

Neumann Boundary Condition

The Neumann boundary condition specifies the values which the derivatives of a solution need to take along the boundaries. The Neumann boundary conditions would correspond to

my sample being placed in a flexible jacket and then immersed in a fluid at high pressure. This will cause a uniform stress on the outer boundaries, whereas the displacement might not be uniform. We refer to this as *flexible loading*. In our numerical experiment, this is done by prescribing a certain normal stress on the boundaries. In this study, the Neumann boundary condition can only be used if, at least, the Dirichlet boundary condition is specified on one of the boundaries.

Note that the default boundary conditions in COMSOL Multiphysics® for when the fluid is modelled is a continuous displacement and stress across the pore boundaries.

The Mesh

For this model, the meshes used were triangular (for the 2D model) and tetrahedral (for the 3D model), using the *Finite Element Method (FEM)*. FEM starts by first detecting or identifying the PDE associated with the problem. Then it transforms the continuous functions, variables and equations into discrete (smaller) parts, known as *discretization*. As shown in Figure 2.10, each domain is divided up into a mesh of tiny finite pieces called *finite elements* (hence the name, FEM). These elements have corners called *nodes*. The discrete parts of the equation are then calculated at the nodal points and the solution estimated. This implies that a finer mesh would result in a model with higher resolution, because there are more nodal points where the equations are solved. Likewise, a coarser mesh would mean a poorly resolved model (see Figures 2.10a to 2.10d). For the simple 2D and 3D models, the degree of resolution did not affect the results so much because there were no intersecting or complex face elements. However, for the carbonate and sandstone models, the resolution of the models quickly became very important and could not be neglected.

It is important to mention that 2D axisymmetric and 1D modeling could have been done in place of the 3D modeling in COMSOL Multiphysics®. This would have further reduced the amount of time it took to carry out the 3D numerical simulations.

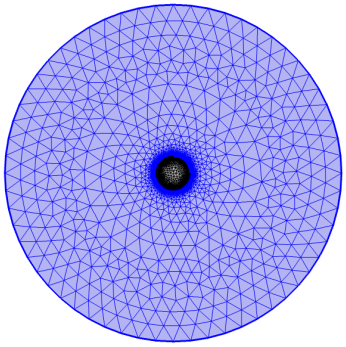

(a) 2D mesh with high resolution in the solid region

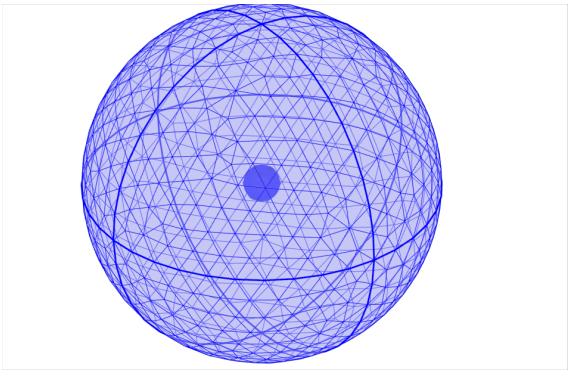

(b) 3D mesh with high resolution in the solid region

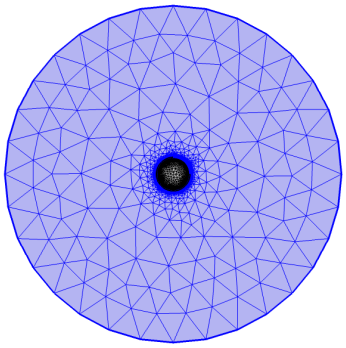

(c) 2D mesh with low resolution in the solid region

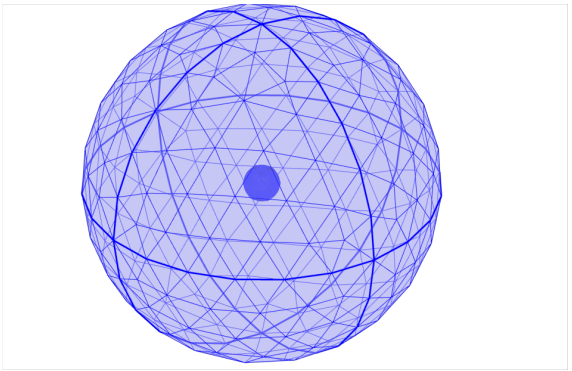

(d) 3D mesh with low resolution in the solid region

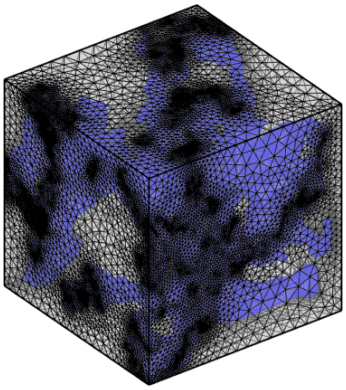

(e) Mesh for a Carbonate Sample

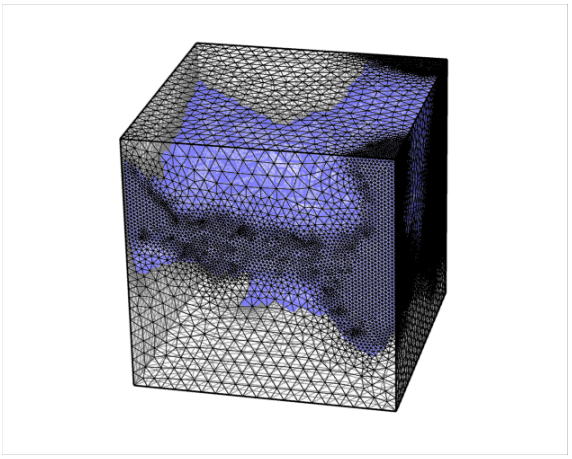

(f) Mesh for a Sandstone Sample

Figure 2.10: Model mesh

2.2 Rock Sample Methodology

For comparison with real rock samples, high resolution 3D images of reservoir rocks - carbonate (from the Weyburn oilfield) and Fontainebleau sandstone - were used. These images were obtained from a previous M.Sc. thesis project conducted by Bird (2013), and imported into COMSOL Multiphysics® as STL (Standard Tessellation or Triangle Language) files. Bird (2013) described the detail of the pore extraction methodology done in Avizo®. Only three of the carbonate samples and two of the sandstone samples (all of different porosities) were used because the other samples had highly complex pore spaces that required more computer memory than was readily available.

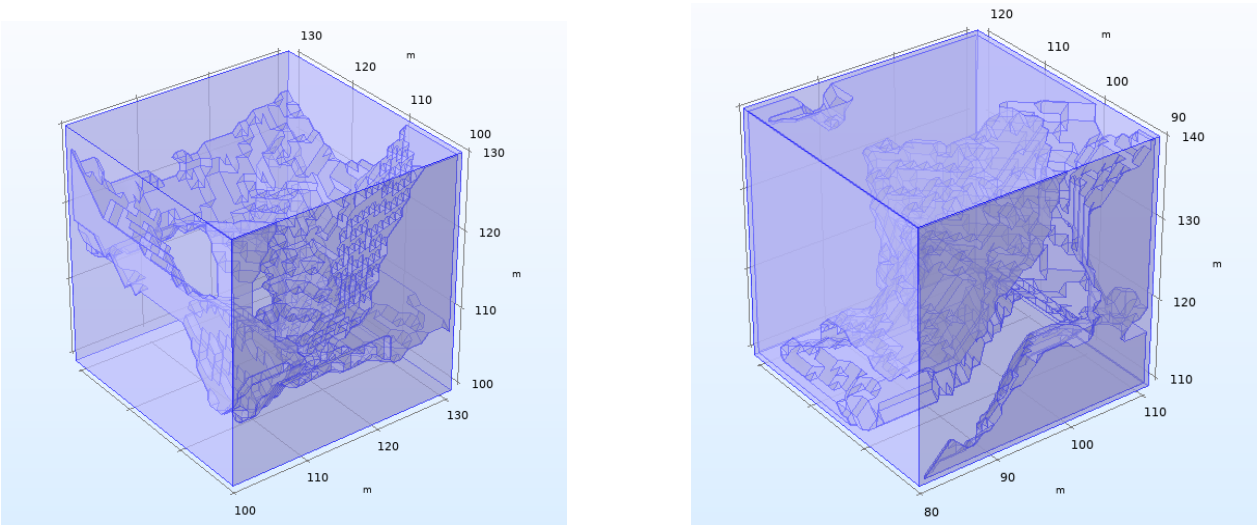

Figure 2.11: Sandstone models considered

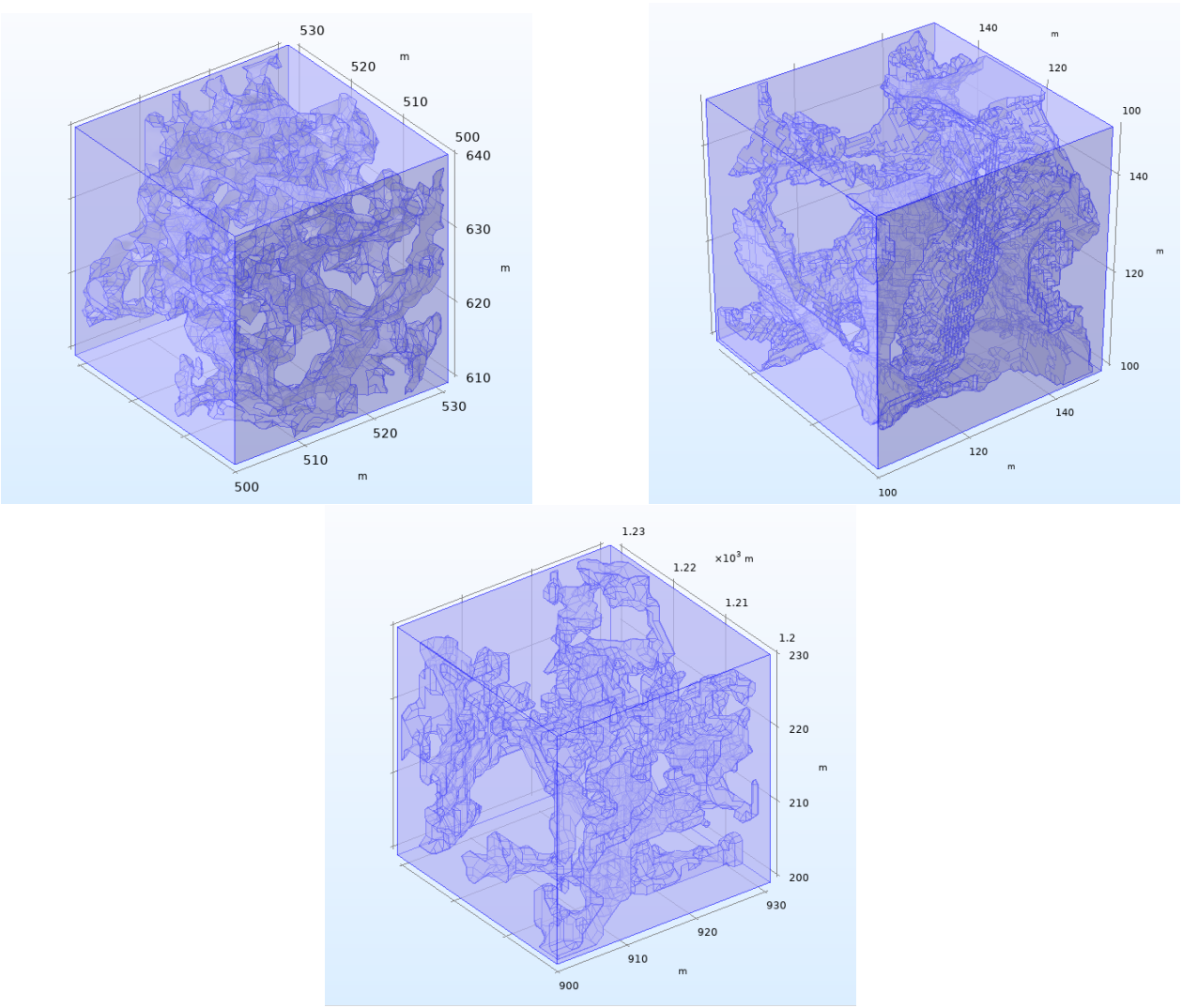

Figure 2.12: Carbonate models considered

After importing the STL images of the pore space into COMSOL Multiphysics®, the surfaces of the geometry were then built around the pore spaces as shown in Figures 2.11 to 2.12. These would serve as the outer boundaries of the rock models. Further, because of the complexity of the pore spaces, the fluid region could not be modelled as just the pore boundaries. Therefore, the simulations were carried out in all regions. Also, in order to ensure that the models were well-resolved, the mesh resolution for each model was increased to a point where further increases did not cause significant changes in the results.

Finally, except for the microscopic values of the rock parameters (as shown in Table 2.1), the

global definitions, variables, and boundary conditions were all applied to the rock samples mostly in the same way as already described in the preceding section.

2.3 Inversion for Macroscopic Parameters

Before going further into the study section, it is important to re-iterate the purpose of this study. This study seeks chiefly to numerically calculate the Biot and Willis (1957) elastic parameters (or coefficients) - $K_d,\ K_u,\ \alpha,\ M,\ \zeta$ (which will be further defined in the following subsection). In this study, special cases of analytical computations were also considered. These were all found to be in good agreement with those of Biot and Willis (1957) and Biot (1962). It is also important to emphasize that I am only considering isotropic stress.

2.3.1 Numerical Study

A stationary or time-dependent modeling may be used to numerically compute the results. The main difference between these two types of studies in solid mechanics is that stationary studies are used to compute deformations, stresses, and strains at static equilibrium. However, time-dependent studies are used to compute the time-varying deformation and motion of solids subject to transient loads. In my case, however, constant load is applied causing the deformation to immediately go to a steady state.

In this study, only isotropic compression was considered, hence, the system can be characterized by a small number of parameters. The Biot's parameters can be determined from the following equations:

$$\begin{bmatrix} \sigma \\ p \end{bmatrix} = \begin{bmatrix} K_u & \alpha M \\ \alpha M & M \end{bmatrix} \begin{bmatrix} \Delta \\ \zeta \end{bmatrix}; \tag{2.1}$$

where the symbols σ and p both represent the normal elastic stress on the outer boundary and the pressure in the fluid region, respectively.

By inverting the matrix in the above equation, it can be shown that

$$\boldsymbol{K} = \begin{bmatrix} K_u & \alpha M \\ \alpha M & M \end{bmatrix}, \tag{2.2}$$

$$\boldsymbol{K}^{-1} = \boldsymbol{J} = \frac{1}{K_d M} \begin{bmatrix} M & -\alpha M \\ -\alpha M & K_u \end{bmatrix}; \tag{2.3}$$

where the symbol K_u is the undrained bulk modulus.

Moreover, the drained bulk modulus can be determined from

$$K_d = K_u - \alpha^2 M = \frac{|\boldsymbol{K}|}{M}; \tag{2.4}$$

where $|\boldsymbol{K}|$ is the determinant of the K matrix, and $\boldsymbol{J}$ is the compressibility matrix.

The dilatation of the pore, Δ_p, and the total dilatation, Δ, can be evaluated by integrating the normal displacements over the pore walls and outer boundaries, respectively. Alternatively, Δ_p and Δ can be calculated by integrating the divergence of displacement (div $\boldsymbol{u}$) over the volume, and I calculated these quantities both ways and got the same results. Further, σ and p can be determined by averaging the normal stress over the outer boundaries and pore walls, respectively. To derive this, we have

$$\boldsymbol{\sigma} = \hat{n}\boldsymbol{\sigma}\hat{n} = \begin{bmatrix} n_x & n_y \end{bmatrix} \begin{bmatrix} \sigma_{xx} & \sigma_{xy} \\ \sigma_{xy} & \sigma_{yy} \end{bmatrix} \begin{bmatrix} n_x \\ n_y \end{bmatrix} \tag{2.5}$$

$$\sigma = \sigma_{xx_s} n_x^2 + \sigma_{yy_s} n_y^2 + 2\sigma_{xy_s} n_x n_y \tag{2.6}$$

where $\hat{n}$ is the normal vector, and $\boldsymbol{\sigma}$ is the stress tensor.

Then, σ is evaluated from

$$\sigma = \int_0^{2\pi} \frac{\left(\sigma_{xx_s} n_x^2 + \sigma_{yy_s} n_y^2 + 2\sigma_{xy_s} n_x n_y\right) r}{L}\, d\theta \qquad - \text{for 2D} \tag{2.7}$$

This contains the same stress components of equations (1.20) to (1.23) and their normal vectors $n_x,\ n_y$, evaluated over the circumference, L. Also, note that equation (2.7) is the same for p but integrated over the pore boundary. Similarly, in 3D, σ and p are evaluated over the surface area.

Numerically, the change in fluid content, ζ, is calculated from

$$\zeta = -\Delta_p + \frac{p}{K_f}\phi \tag{2.8}$$

where ϕ is the porosity of the entire rock, and Δ_p is the fractional change in the volume of the pore (the change in volume of the pore divided by the total volume), and $\frac{p}{K_f}$ is the fractional change in the volume of the fluid due to compression, such that, for a completely saturated pore in the undrained case, $\zeta = 0$:

$$\zeta = -\frac{\Delta V_p}{V_T} + \frac{\Delta V_p}{V_p}\frac{V_p}{V_T}; \tag{2.9}$$

where V_T is the total volume of the porous material.

Also,

$$\frac{\Delta V_p}{V_p} = \frac{p}{K_f}, \qquad \text{and} \tag{2.10}$$

$$K_f = \frac{V_p}{\Delta V_p} p. \tag{2.11}$$

Further, $\frac{p}{K_f}$ in equation (2.8) describes the state of the fluid, such that, if there is constant pore fluid pressure (i.e. $p = 0$), $\zeta \neq 0$. This is the drained case.

From one simulation we obtain one value each for σ and ζ, while p and Δ are prescribed under flexible and rigid loading conditions, respectively. For this reason, to solve for the K matrix numerically, two or more numerical simulations must be done to obtain different values for $\sigma,\ p,\ \Delta$ and ζ. To do this, a combination of different Dirichlet boundary condition and/or Neumann boundary condition were used in this study. Consequently, the drained experiment was achieved by setting $p = 0$ inside the pore and prescribing a fixed displacement, $u_o = 1$ x 10^{-6}, (Dirichlet boundary condition, with dimensionless units) on the outer boundaries (see figure 2.13a). Setting $p = 0$ resulted in zero normal stress on the pore walls, which mimicked the effects of allowing fluids to drain from the pore. Then, for another simulation, some normal stress value, $p \neq 0$, (Neumann boundary condition) was prescribed on the pore walls as well as some Dirichlet boundary condition on the outer walls (see figure 2.13b). Note that this latter case does not imply that there is no fluid in the pore, but that the pore pressure is zero. Also, for most simulations, the fluid regions were not included, rather, they were represented by only specifying the normal stress on the pore boundaries. Some simulations were done with the fluid region present, and they gave the same result as the ones done without the fluid region.

Figure 2.13 shows the radial normal stress field from drained and undrained cases.

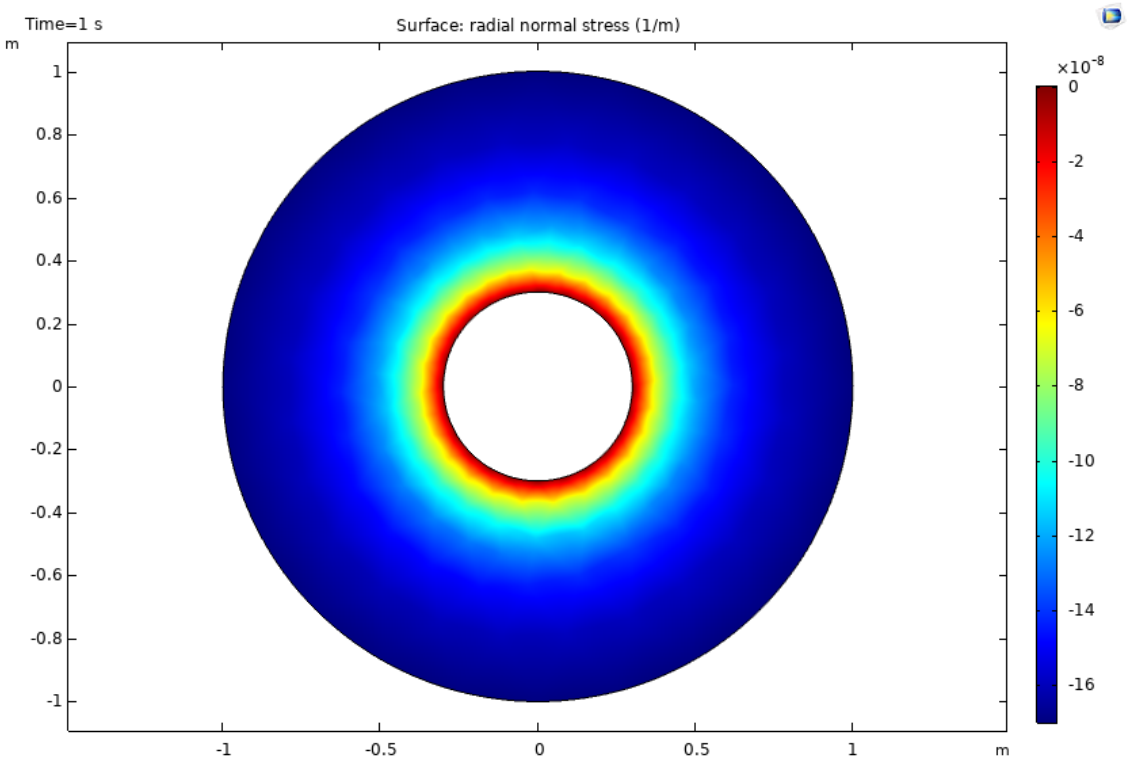

(a)

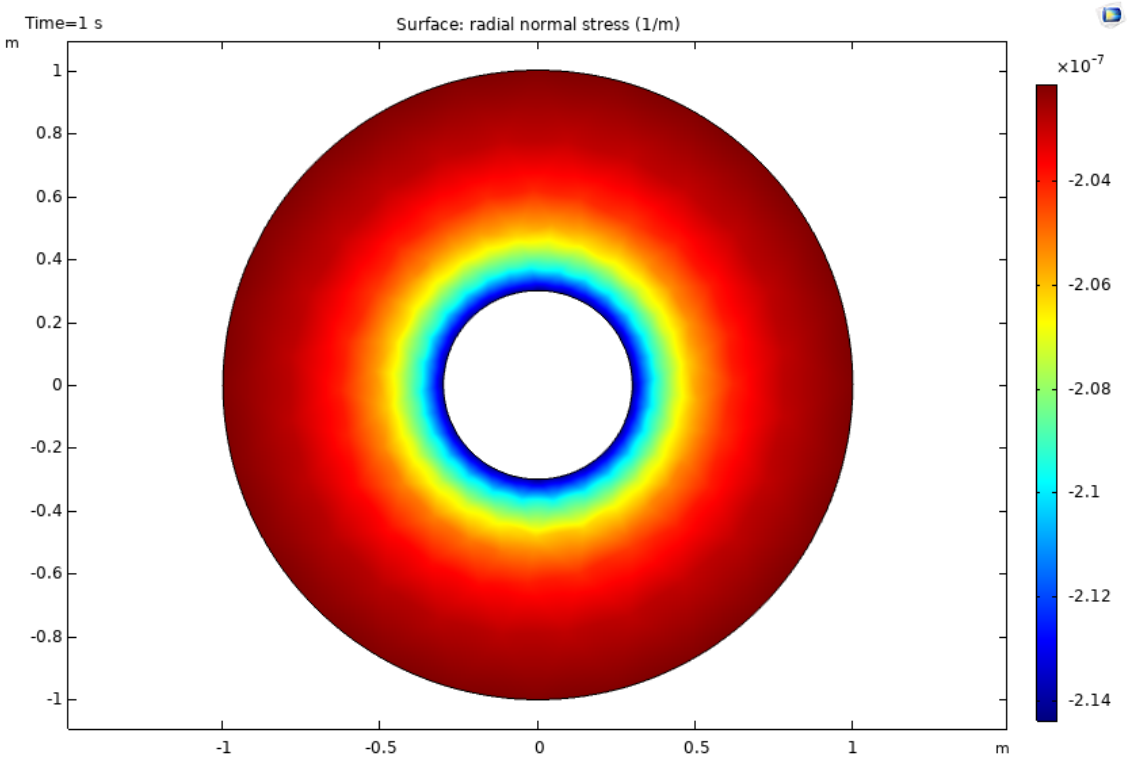

(b)

Figure 2.13: Radial normal stress field for (a) Drained Case; $p = 0$ (b) Undrained Case; $p \neq 0$ - for a circular rock of 1 m radius having a circular pore of 0.3 m radius

Numerical Evaluation of Elastic Energy

The total microscopic elastic potential is the total stored elastic energy per unit volume (total elastic energy density) which can be calculated from

$$E_{tot} = \frac{1}{2} K \Delta_s^2 + \mu \tilde{\varepsilon} : \tilde{\varepsilon}. \tag{2.12}$$

The first term is the energy due to isotropic compression, while the second term is the energy due to shear. The symbol K is the microscopic bulk modulus, and Δ_s is the value of the dilatation at a point.

The energy stored in the solid is computed numerically by replacing K with K_s, which is the bulk modulus of the solid; while, for the energy in the fluid, the shear part turns to zero, and K is substituted with K_f, the bulk modulus of the fluid.

2.3.2 Analytical Study

The numerical model for a spherical rock with one spherical pore was checked by analytical solutions to see whether the model indeed worked, and to help gain physical understanding.

An assumption of a spherical annulus with inner and outer radii, R_i and R_o, are made. In spherical coordinates, the linear elastic equations with only radial variations and no body forces can be shown to be

$$\frac{d}{dr} \frac{1}{r^2} \frac{d}{dr} \left(r^2 u_r \right) = 0; \tag{2.13}$$

where u_r is the displacement in the radial direction. This equation has solution

$$u_r = C_1 r + \frac{C_2}{r^2}; \tag{2.14}$$

where C_1 and C_2 are integration constants.

Imposing Dirichlet boundary conditions with rigid loading of displacements u_i and u_o on the inner and outer boundaries, respectively, the integration coefficients can be determined and the radial displacement can be shown to be

$$u_r = \frac{R_o^2 u_o - R_i^2 u_i}{R_o^3 - R_i^3} r + \frac{R_i^2 R_o^2 \big(R_o u_i - R_i u_o\big)}{r^2 \big(R_o^3 - R_i^3\big)}. \tag{2.15}$$

Testing equation (2.15) against the numerical solution showed the two to be in good agreement.

The radial normal stress can be shown to be related to the radial displacement by (Bower, 2009):

$$\sigma_{rr} = \frac{E}{(1-\nu)(1-2\nu)} \left[(1-\nu) \frac{du_r}{dr} + 2\nu \frac{u_r}{r} \right]. \tag{2.16}$$

For homogeneous isotropic materials, the P-wave, Lamé parameter, Young's, and bulk moduli are related as

$$P = \frac{E(1-\nu)}{(1+\nu)(1-2\nu)} = K + \frac{4}{3}\mu, \qquad \text{and} \tag{2.17}$$

$$\lambda = \frac{E\nu}{(1+\nu)(1-2\nu)} = K - \frac{2}{3}\mu; \tag{2.18}$$

where P is the P-wave modulus (M is the conventional symbol, but is already in use), λ is the Lamé parameter, E is the Young's modulus, and ν is the Poisson's ratio.

Substituting equations (2.15), (2.17), and (2.18) into equation (2.16) gives

$$\sigma_{rr} = \frac{3K\big(R_o^2 u_o - R_i^2 u_i\big)}{R_o^3 - R_i^3} - \frac{4\mu R_i^2 R_o^2 \big(R_o u_i - R_i u_o\big)}{r^3 \big(R_o^3 - R_i^3\big)}. \tag{2.19}$$

Also, testing the above against the numerical solution proved to be a good match.

Subsequently, the stress at the outer boundary (σ) and inner boundary (p) are calculated

from the following expressions

$$\sigma = \frac{3K\big(R_o^2 u_o - R_i^2 u_i\big)}{R_o^3 - R_i^3} - \frac{4\mu R_i^2\big(R_o u_i - R_i u_o\big)}{R_o\big(R_o^3 - R_i^3\big)}, \text{and} \tag{2.20}$$

$$p = \frac{3K\big(R_o^2 u_o - R_i^2 u_i\big)}{R_o^3 - R_i^3} - \frac{4\mu R_o^2\big(R_o u_i - R_i u_o\big)}{R_i\big(R_o^3 - R_i^3\big)}. \tag{2.21}$$

The total dilatation, Δ, is related to the displacement on the outer boundary by

$$\Delta = \frac{3u_o}{R_o}. \tag{2.22}$$

Also, the dilatation of the pore is related to the displacement of the inner boundary by

$$\Delta_f = \frac{3u_i R_i^2}{R_o^3}. \tag{2.23}$$

To obtain the compliance and incompressibility matrices, two independent solutions are required. Solving for two simple cases where $u_i = 0$ for one, and $u_o = 0$ for the other, and subsequently inverting the K matrix to obtain the compliance matrix, J, the following is obtained

$$\boldsymbol{J} = \frac{1}{4K\mu\big(R_o^3 - R_i^3\big)} \begin{bmatrix} 3K_s R_i^3 + 4\mu R_o^3 & -\big(3K_s + 4\mu\big)R_i^3 \\ -\big(3K_s + 4\mu\big)R_i^3 & -R_i^3 \frac{\left(4K_s\mu R_i^3 - 4K_f\mu R_i^3 - 3K_s K_f R_i^3 R_o^3 - 4K_s\mu R_i^3 R_o^3\right)}{R_o^3 K_f} \end{bmatrix}. \tag{2.24}$$

From the above, the drained bulk modulus is given by

$$K_D = \frac{4K\mu\big(R_o^3 - R_i^3\big)}{3K_s R_i^3 + 4\mu R_o^3}. \tag{2.25}$$

But porosity is given by $\phi = \left(\frac{R_i}{R_o}\right)^3$. Therefore, equation (2.25) becomes

$$K_d = \frac{4K\mu\big(1 - \phi\big)}{3K_s\phi + 4\mu}. \tag{2.26}$$

Inverting J gives back the incompressibility matrix as

$$\boldsymbol{K} = \frac{1}{3\big(K_s - K_f\big)R_i^3 + \big(3K_f + 4\mu\big)R_o^3} \begin{bmatrix} 4\big(-K_s + K_f\big)\mu R_i^3 + K\big(3K_f + 4\mu\big)R_o^3 & K_f\big(3K_s + 4\mu\big)R_o^3 \\ K_f\big(3K_s + 4\mu\big)R_o^3 & \frac{K_f R_o^3\big(3K_s R_i^3 + 4\mu R_o^3\big)}{R_i^3} \end{bmatrix}. \tag{2.27}$$

From the above, the undrained bulk modulus is given by

$$K_u = \frac{4\big(-K_s + K_f\big)\mu\phi + K\big(3K_f + 4\mu\big)}{3\big(K_s - K_f\big)\phi + \big(3K_f + 4\mu\big)}. \tag{2.28}$$

Both K_d and K_u were compared against their results from the numerical study and found to be in good agreement.

Further, from

$$\boldsymbol{K} = \begin{bmatrix} K_u & \alpha M \\ \alpha M & M \end{bmatrix}, \tag{2.29}$$

and from equation (2.27),

$$M = \frac{K_f\big(3K_s\phi + 4\mu\big)}{3\big(K_s - K_f\big)\phi^2 + \big(3K_f + 4\mu\big)\phi}, \tag{2.30}$$

$$\alpha = \frac{\phi\big(3K_s + 4\mu\big)}{3K_s\phi + 4\mu}. \tag{2.31}$$

Analytical Evaluation of Elastic Energy

This section shows the equations I used to test the numerical energy for a spherical rock with one spherical pore.

From equation 2.12,

$$E_c = \frac{1}{2}K_s\Delta_s^2, \qquad \text{and} \tag{2.32}$$

$$E_{sh} = \mu\tilde{\varepsilon} : \tilde{\varepsilon}. \tag{2.33}$$

where E_c and E_{sh} are the compression and shear energies.

When there exists a radial displacement which only varies with radius in spherical coordinates, the components of the strain tensor can be expressed as $\left[\text{substituting } \phi = \left(R_i/R_o\right)^3\right]$

$$\varepsilon_{rr} = \frac{du_r}{dr} = \frac{R_o^2 u_0 - R_i^2 u_i}{R_o^3(1-\phi)} - \frac{2(R_i^2 u_i - \phi R_o^2 u_0)}{(1-\phi)r^3}. \tag{2.34}$$

$$\varepsilon_{\theta\theta} = \frac{u_r}{r} = \frac{R_o^2 u_0 - R_i^2 u_i}{R_o^3(1-\phi)} + \frac{R_i^2 u_i - \phi R_o^2 u_0}{(1-\phi)r^3}. \tag{2.35}$$

$$\varepsilon_{\psi\psi} = \frac{u_r}{r} = \frac{R_o^2 u_0 - R_i^2 u_i}{R_o^3(1-\phi)} + \frac{R_i^2 u_i - \phi R_o^2 u_0}{(1-\phi)r^3}. \tag{2.36}$$

$$\tag{2.37}$$

Solving for Δ_s, we have that

$$\Delta_s = \varepsilon_{rr} + \varepsilon_{\theta\theta} + \varepsilon_{\psi\psi} = 3\frac{R_o^2 u_0 - R_i^2 u_i}{R_o^3(1-\phi)}. \tag{2.38}$$

and

$$\tilde{\varepsilon} = \varepsilon - \frac{\Delta_s}{3}\boldsymbol{I} = \begin{bmatrix} \varepsilon_{rr} - \frac{\Delta}{3} & 0 & 0 \\ 0 & \varepsilon_{\theta\theta} - \frac{\Delta}{3} & 0 \\ 0 & 0 & \varepsilon_{\psi\psi} - \frac{\Delta}{3} \end{bmatrix} = \begin{bmatrix} -\frac{2(R_i^2 u_i - \phi R_o^2 u_0)}{(1-\phi)r^3} & 0 & 0 \\ 0 & \frac{R_i^2 u_i - \phi R_o^2 u_0}{(1-\phi)r^3} & 0 \\ 0 & 0 & \frac{R_i^2 u_i - \phi R_o^2 u_0}{(1-\phi)r^3} \end{bmatrix} \tag{2.39}$$

Equation (2.12) further becomes

$$E_{tot} = E_c + E_{sh} = \frac{9K_s}{2}\frac{\left(R_o^2 u_0 - R_i^2 u_i\right)^2}{\left(1-\phi\right)^2 R_o^6} + \frac{6\mu\left(R_i^2 u_i - \phi R_o^2 u_0\right)^2}{\left(1-\phi\right)^2 r^6}. \tag{2.40}$$

From the above, it is obvious that when there is no pore present ($\phi = R_i = 0$), $E_{sh} = 0$ and $E_c = \frac{9Ku_o^2}{2R_o^2}$. This would mean that all of the stored energy is in the isotropic compression part. This also shows that for the energy densities of spheres of different volumes to be comparable, the value of the outer displacement, u_0, must always be a fraction of the value of the outer radius, R_o. This was shown to be consistent with the numerical model. Further, even with the presence of a pore, the isotropic compression contribution is constant in space

within the solid while the shear energy density decreases strongly the farther away you move from the centre of the pore ($E_{sh} \propto \frac{1}{r^6}$). To be able to compare with numerical simulations, the values of u_o and u_i must be known.

The total energy stored in the solid can be evaluated by integrating equation (2.40) over the volume of the solid to give

$$\overline{E_{tot}} = \frac{2\pi}{\big(1-\phi\big)R_o^3}\left[3K_s\big(R_o^2u_0 - R_i^2u_i\big)^2 + \frac{4\mu}{\phi}\big(R_i^2u_i - \phi R_o^2u_0\big)^2\right]. \tag{2.41}$$

In order to eliminate the effects of the bulk volume on the total energy, a normalized version of equation 2.41 is used, which is to divide the total energy stored in the solid when the pore is present ($\phi \neq 0$) by the total compression energy stored when the pore is absent ($\phi = 0$). And subsequently, we have

$$E_{tot_n} = \frac{\overline{E_{tot}}}{\overline{E_0}}; \tag{2.42}$$

where E_{tot_n} is the normalized average E_{tot}, $\overline{E_{tot}}$ is the total energy stored in the solid when $\phi \neq 0$, and $\overline{E_0}$ is the total energy when $\phi = 0$ (for the analytical solution of a single spherical pore in a spherical rock sample). This gives

$$E_{tot_n} = \frac{\big(R_o^2u_o - R_i^2u_i\big)^2}{\big(1-\phi\big)R_o^4u_o^2} + \frac{4}{3}\frac{\mu\big(R_i^2u_i - \phi R_o^2u_o\big)^2}{K_s\phi\big(1-\phi\big)R_o^4u_o^2}; \tag{2.43}$$

where the first part of the RHS is the normalized average compression energy density, E_{c_n}, and the second part is the normalized average shear energy density, E_{sh_n}.

Further, if p and/or σ is specified as the boundary condition, they can both be evaluated by writing equations (2.20) and (2.21) in matrix form as

$$\begin{bmatrix}\sigma\\ p\end{bmatrix} = \frac{1}{R_o^3 - R_i^3}\begin{bmatrix}3K_sR_o^2 + 4\mu\frac{R_i^3}{R_o} & -3K_sR_i^2 - 4\mu R_i^2\\ 3K_sR_o^2 + 4\mu R_o^2 & -3K_sR_i^2 - 4\mu\frac{R_o^3}{R_i}\end{bmatrix}\begin{bmatrix}u_o\\ u_i\end{bmatrix}. \tag{2.44}$$

The inverse relation is as below:

$$\begin{bmatrix} u_o \\ u_i \end{bmatrix} = \frac{-1}{12K_s\mu\left(R_o^3 - R_i^3\right)} \begin{bmatrix} -3K_sR_oR_i^3 - 4\mu R_o^4 & \big(3K_s + 4\mu\big)R_oR_i^3 \\ -\big(3K_s + 4\mu\big)R_o^3R_i & 3K_sR_o^3R_i + 4\mu R_i^4 \end{bmatrix} \begin{bmatrix} \sigma \\ p \end{bmatrix}. \tag{2.45}$$

For the drained experiment ($p = 0$), equation (2.45) becomes

$$u_o = \frac{\big(3K_s\phi + 4\mu\big)R_o}{12K_s\mu(1-\phi)}\sigma, \qquad \text{and} \tag{2.46}$$

$$u_i = \frac{\big(3K_s + 4\mu\big)R_i}{12K_s\mu(1-\phi)}\sigma. \tag{2.47}$$

For the undrained case ($\zeta = 0$) equation (2.8) becomes

$$p = \frac{\Delta_p}{\phi}K_f, \tag{2.48}$$

and the relationship between u_o and u_i is

$$u_o = \left[\frac{(3K_s\phi - 4\mu)\sigma - (3K_s + 4\mu)K_fu_i}{12K_s\mu(1-\phi)}\right]R_o. \tag{2.49}$$

The results of these considerations are shown and discussed in the next chapter.

3 RESULTS/DISCUSSION Part 1 – Simple Models

In this chapter, the results from the various simulations are shown in order to describe how some of the Biot parameters vary with porosity for the simple 3D geometries. For each numerical experiment, the drained and undrained cases are considered for the numerical solutions. Various results for simulations with different pore sizes are plotted for the simple cases. Some comparisons with the numerical model are also shown alongside the analytical results to show their agreement. The bulk compressibilities (J) and incompressibilities (K) are shown. Both dimensional and non-dimensional results are also plotted.

The parameters used are those from Table 2.1. The bulk and shear moduli for sandstone were used for the simple models. Further, the list of symbols used in this chapter and their meanings are given in Table 3.1.

Table 3.1: List of Symbols 2

Term	Definition
K_d	drained bulk modulus
K_{d_N}	drained bulk modulus for the numerical model
K_{d_A}	drained bulk modulus for the analytical model
K_u	undrained bulk modulus
K_{u_N}	undrained bulk modulus for the numerical model
K_{u_A}	undrained bulk modulus for the analytical model
J_d	drained compressibility
J_{d_N}	drained compressibility for the numerical model
J_{d_A}	drained compressibility for the analytical model
J_u	undrained compressibility
J_{u_N}	undrained compressibility for the numerical model
J_{u_A}	undrained compressibility for the analytical model
ϕ	porosity
K_f	fluid bulk modulus
K_s	bulk modulus of solid region
μ	shear modulus of solid region

3.1 Spherical 3D Cases with 1 Spherical Pore at the Centre

In this section, we discuss the results from a spherical rock model with one spherical pore under the considerations of the effects of porosity, solid incompressibility, fluid incompressibility, shear modulus, and compression, shear, and total energies.

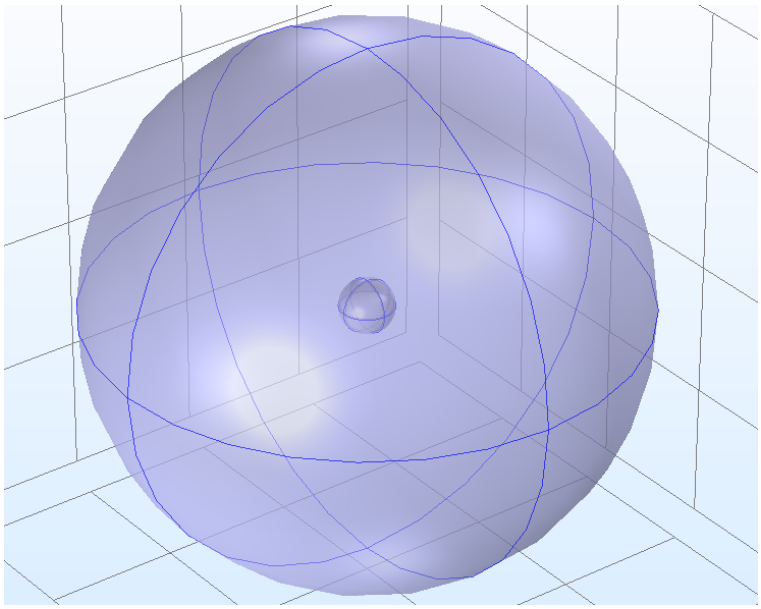

Figure 3.1: A simple 3D model with only 1 pore

3.1.1 Effect of Porosity on Macroscopic Parameters

In this subsection, the spherical model has a radius of 1 m and the pore radius ranges from 0.05 m with increments of 0.05 m up to 0.95, and then a final data point of 0.99, making 20 data points in total. Figure 3.1 shows the image of a spherical rock with one spherical pore.

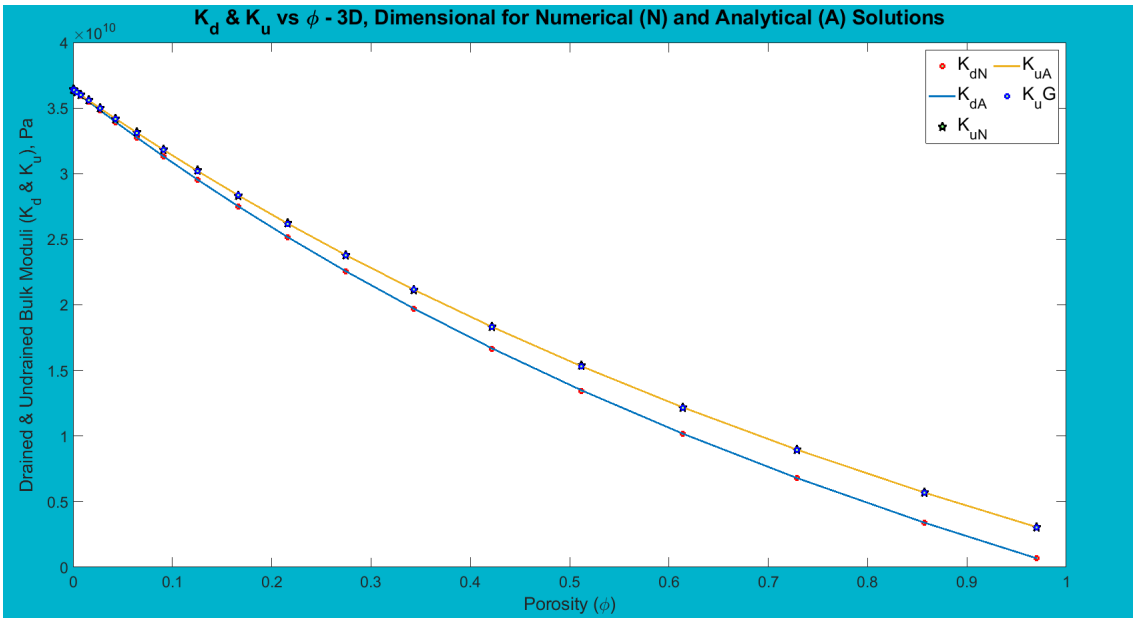

Figure 3.2: Dimensional plots showing numerical and analytical results for drained (K_d), undrained (K_u) and Gassmann-undrained (K_uG) bulk modili against porosity for a spherical rock with one spherical pore. The subscripts N and A represent the numerical and analytical experiments, respectively.

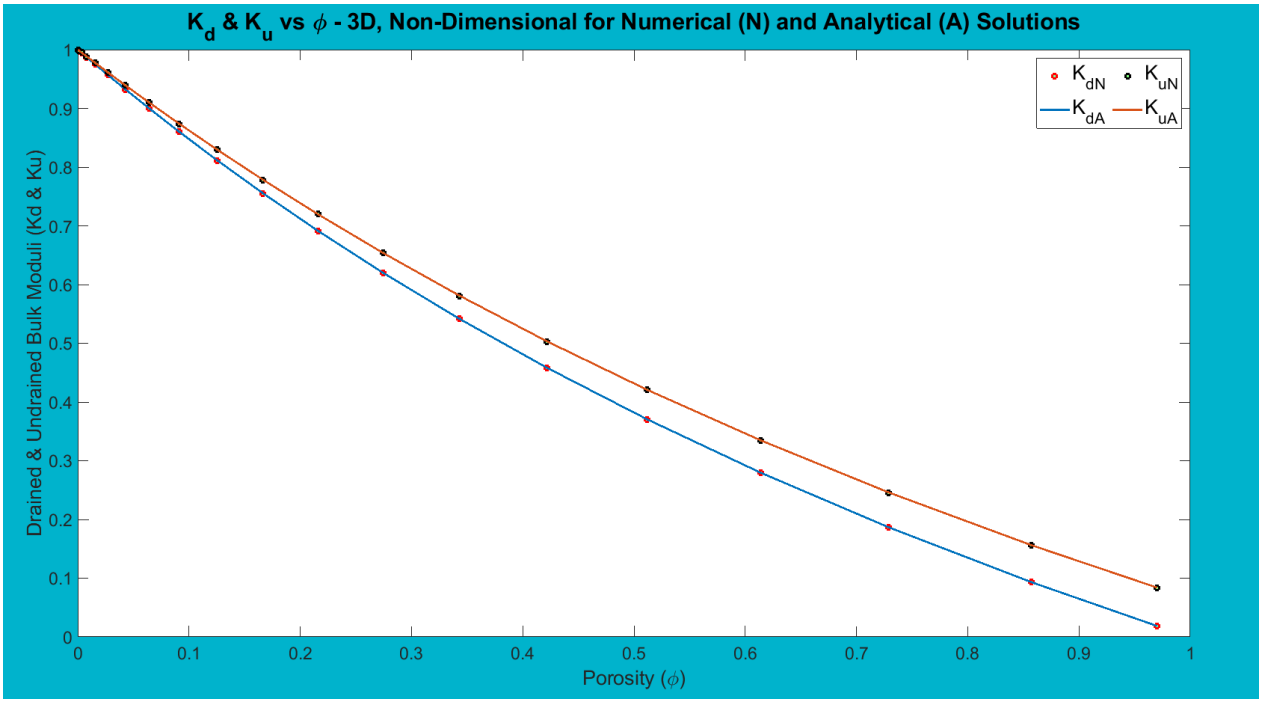

Figure 3.3: Non-Dimensional plots showing numerical and analytical results for drained (K_d) and undrained (K_u) bulk modili against porosity for a spherical rock with one spherical pore.

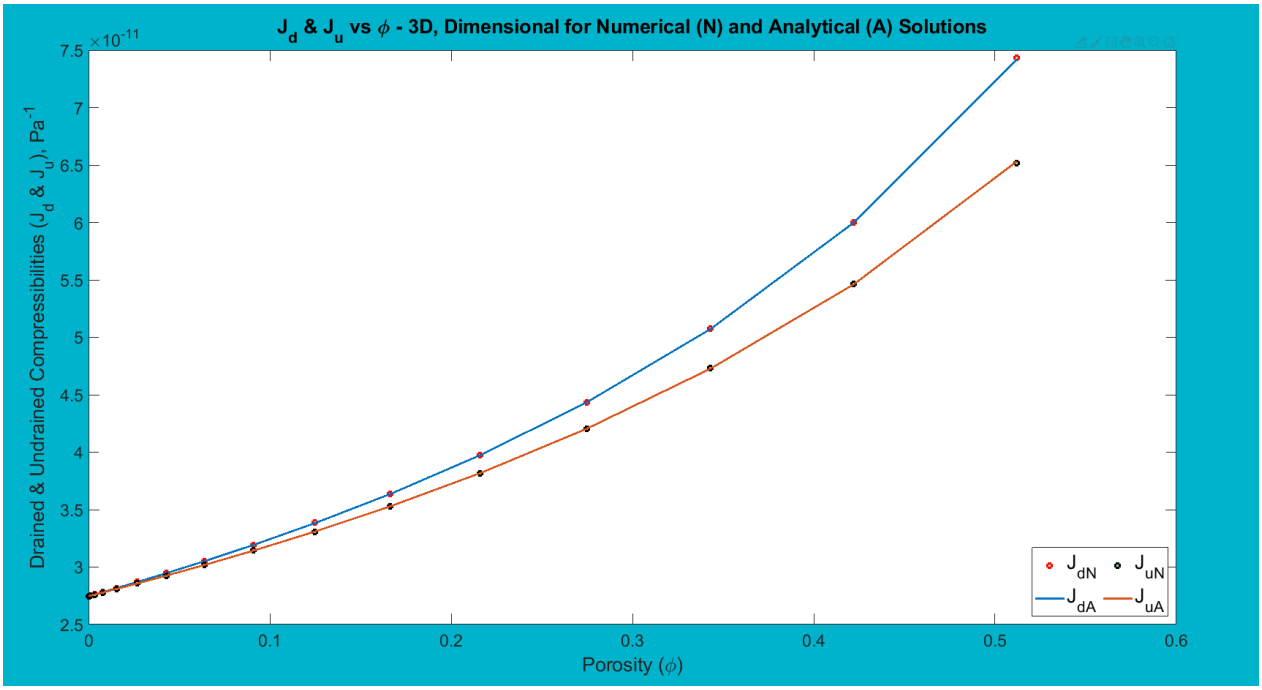

Figure 3.4: Dimensional plots showing numerical and analytical results for drained (J_d) and undrained (J_u) bulk compressibilities against porosity for a spherical rock with one spherical pore.

Figures 3.2 to 3.4 show two sets of plots for both dimensional and non-dimensional cases. The purpose of this investigation is to see how the change in porosity influences the drained and undrained bulk moduli of the rock. The porosity starts at 0.1% and goes up in increments of 10% to around 97%. In Figures 3.2 and 3.3, K_d and K_u are both plotted against ϕ, while in Figure 3.4, J_d and J_u are plotted against ϕ. The numerical and analytical results, represented by the subscripts 'A' & 'N', are also shown to be in perfect agreement. Further, Figure 3.2 shows the K_u from both my analytical and numerical models to be in perfect agreement with K_uG which is Gassmann's undrained bulk modulus (see equation 1.79). To make the comparison, I used the numerical value of K_d and the values of the microscopic parameters, K_s and K_f together with that of the porosity, ϕ to calculate K_uG. From all cases, it is obvious that the rock is less resistant to external stress as its porosity increases. That is, it becomes more compressible (softer) as the porosity increases. For the undrained case, this is because the liquid incompressibility is less than the solid one. Further, the plots show $K_d < K_u$, and as the porosity goes to zero, $K_d = K_u = K_s$. This is because, when the rock is at zero porosity, it implies that there is no pore, hence, zero fluid. And this will

cause the undrained experiment to behave as the drained case. And if there is no fluid in the rock, it implies that the entire model is rock solid, therefore, the model will assume the microscopic parameters of the solid region. Analytically, this can further be represented by the following sets of equations:

$$K_d = K_u - \alpha^2 M \tag{3.1}$$

$$K_d = K_s\big(1 - \alpha\big); \tag{3.2}$$

$0 \leq \alpha \leq 1$. Thus, for a rock with zero porosity, $\alpha = \phi = 0$ (see Figure 3.6), and $K_d = K_u = K_s$

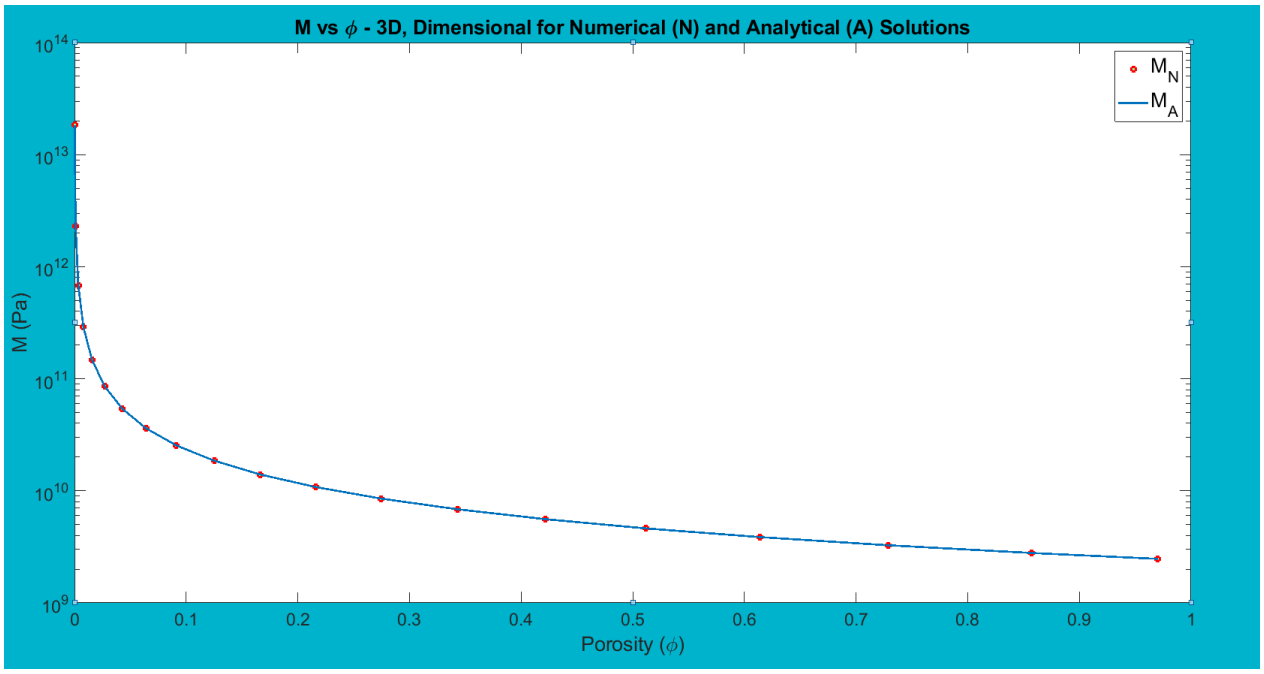

Figure 3.5: Pressure M vs porosity ϕ for a spherical rock with one spherical pore

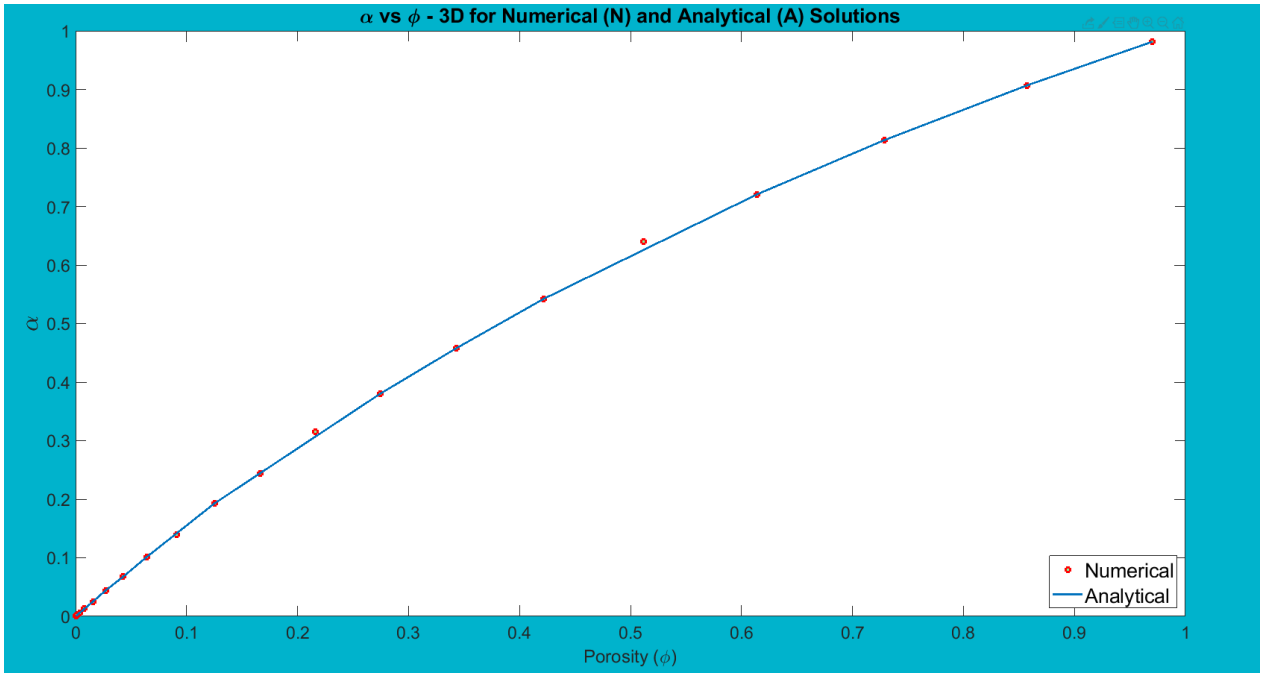

Figure 3.6: Coefficient α vs porosity for a spherical rock with one spherical pore

Figure 3.5 investigates the effect of porosity changes on M. As stated earlier, M is the pressure that causes a unit increase in fluid content when exerted on the pore fluid at constant volume. Figure 3.5 shows that, as the porosity of the rock increases, the amount of pressure needed to increase its fluid content decreases. This is because, the rock becomes softer as it

has more pore spaces to fill up with fluid. Note also that most of the reduction occurs for small values of porosity.

Figure 3.6 shows an almost linear relationship between α and ϕ at low and high porosities. To explain this intuitively, it is important to recall the physical meaning of α. Note that we can see from equation 1.76 that α is a property of the solid skeleton. It is also the amount of macroscopic dilatation for a given change in fluid content for the drained case. The coefficient α describes the magnitude of macroscopic dilatation that the rock undergoes as a result of change in the fluid content. Hence, the rock will attain minimum and maximum macroscopic dilatations when α is 0 and 1, respectively. This corresponds to solid and fluid media, respectively.

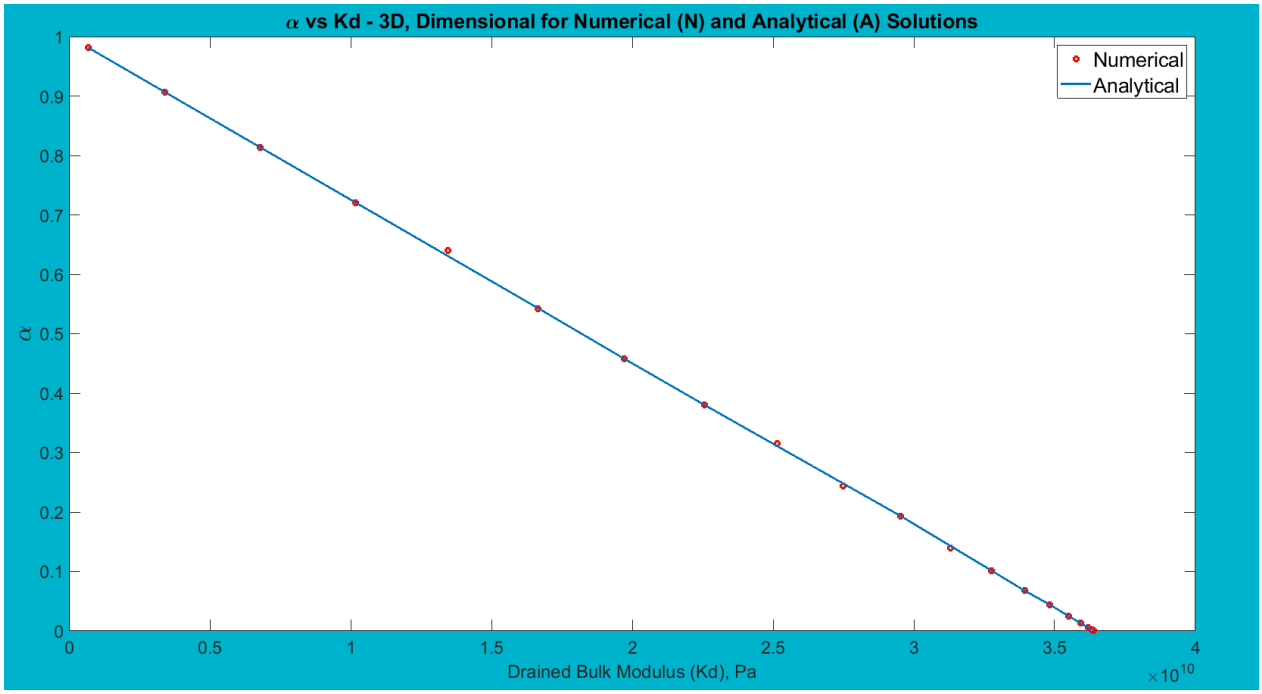

Figure 3.7: α vs dimensional K_d for spherical models with a single spherical pore

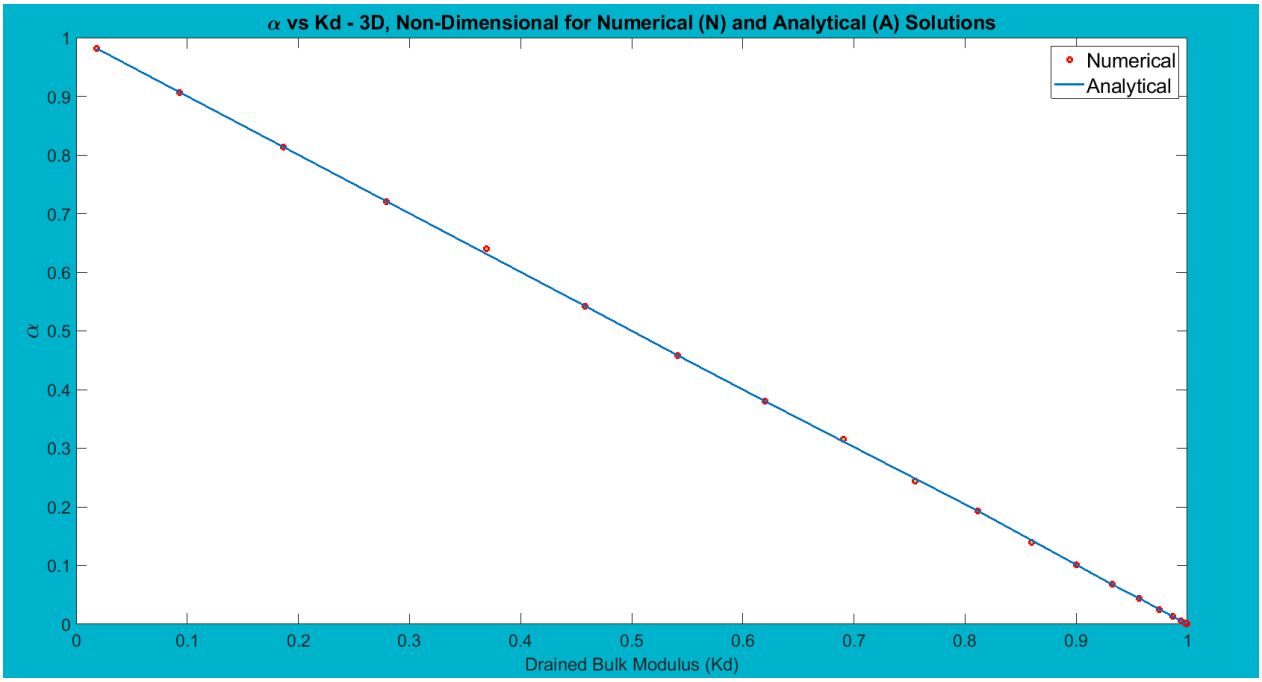

Figure 3.8: α vs non-dimensional K_d for spherical models with a single spherical pore

Figures 3.7 and 3.8 both show the following relationship:

$$\alpha = 1 - \frac{K_d}{K_s}; \tag{3.3}$$

where the slope $= -\frac{1}{K_s}$

Recall that α quantifies how much total strain the system undergoes as a result of variations in fluid content (ζ). From Figures 3.7 and 3.8, the decrease in α becomes smaller in magnitude as K_d approaches K_s ($\alpha \to \phi \to 0$). This is because, as the porosity of the rock approaches zero, the total strain caused by variations in fluid content becomes insignificant (very small).

3.1.2 Effect of Solid Incompressibility on Macroscopic Parameters

In this section, the model is at 15% porosity and the solid bulk modulus K_s is varied from 5 GPa to 50 GPa in steps of 5 GPa giving a total of 10 data points.

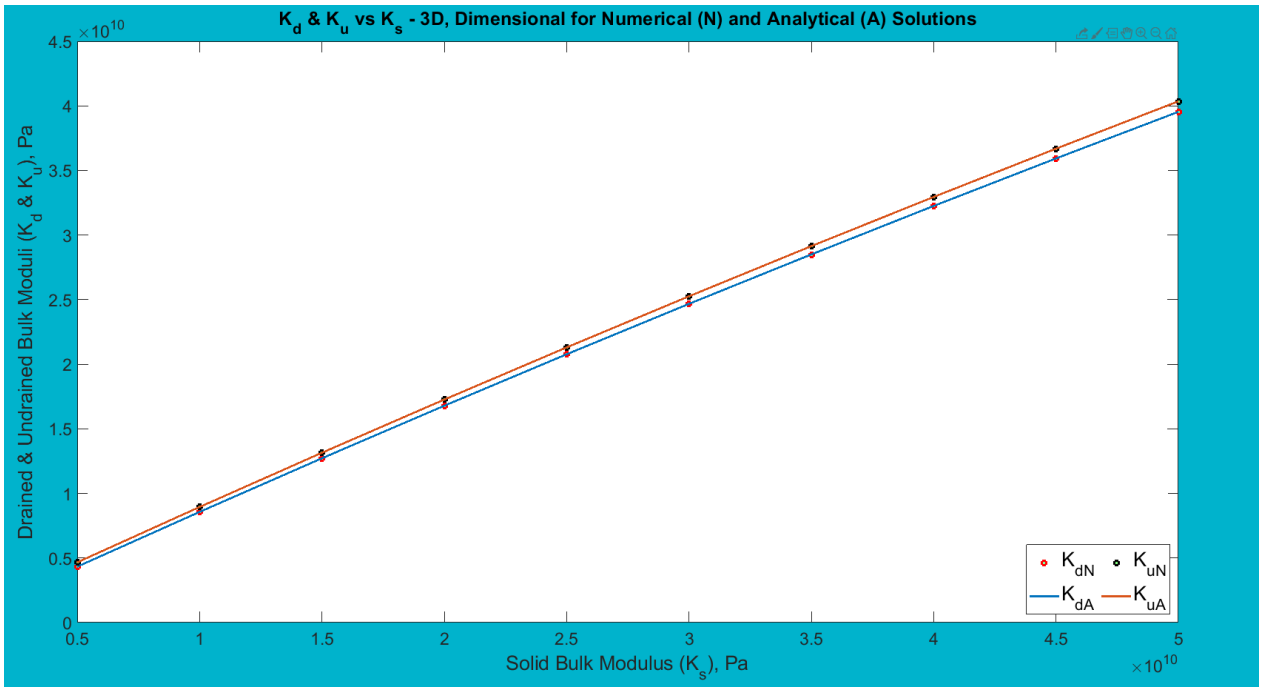

Figure 3.9: K_d and K_u vs K_s for spherical models with a single spherical pore

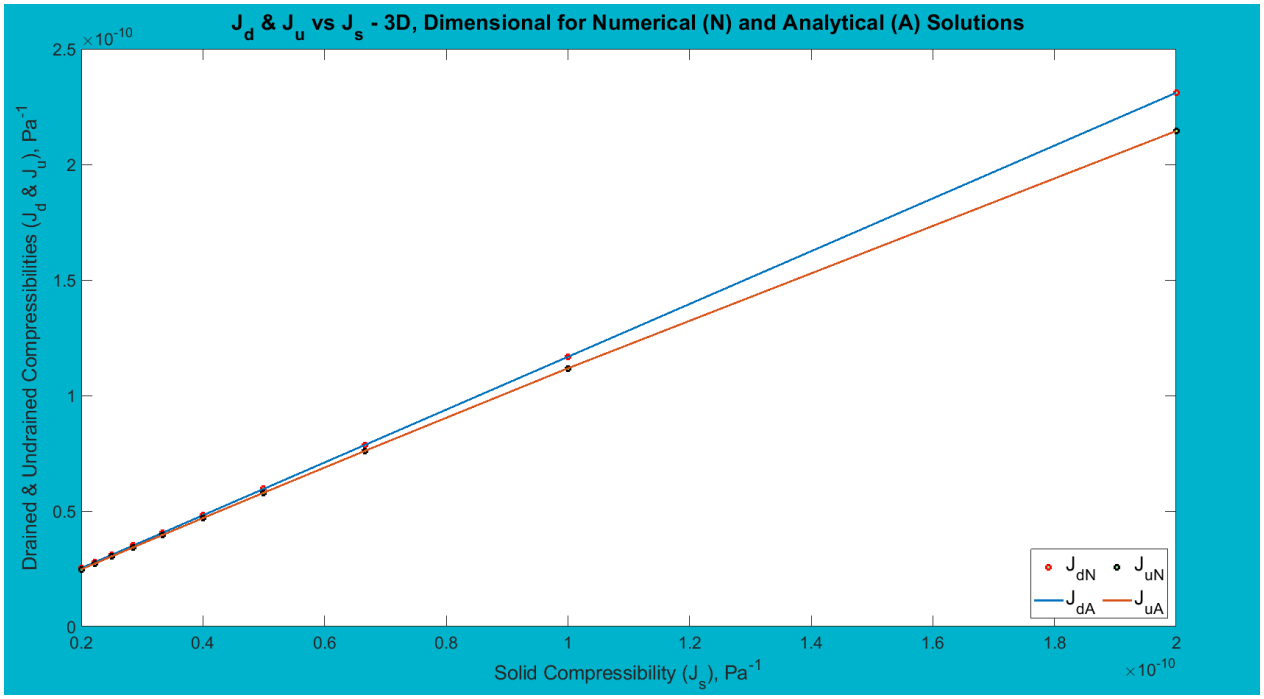

Figure 3.10: J_d and J_u vs J_s for spherical models with a single spherical pore

In Figure 3.9, K_d and K_u are both plotted against K_s, while in Figure 3.10, J_d and J_u are plotted against J_s. These simulations were carried out with constant μ and K_f (from Table 2.1), and a porosity of 12.5%. These results show how K_d and K_u vary with different solid

grain bulk moduli of rocks. From these, it is evident that, as the resistance to compression of the skeleton of the rock (microscopic - K_s) increases, the total resistance of the rock (macroscopic) also increases as a result, for both the drained and undrained cases. In simpler words, the porous rocks with smaller solid bulk modulus are softer than those with larger solid bulk modulus for the drained and undrained cases. These equations show the expected linear relationships with slopes of $1 - \alpha$:

$$K_d = K_s\big(1 - \alpha\big), \quad \text{and} \tag{3.4}$$

$$K_d = K_u - \alpha^2 M. \tag{3.5}$$

$$=> K_u = K_s\big(1 - \alpha\big) + \alpha^2 M; \tag{3.6}$$

3.1.3 Effect of Fluid Incompressibility on Macroscopic Parameters

In this section, the model is at 15% porosity and the fluid bulk modulus K_f is varied. The first three data points for K_f are 0.3 MPa, 1.82 GPa, and 3.64 GPa. Subsequently, it is increased in steps of 3.64 GP up to 54.6 GPa.

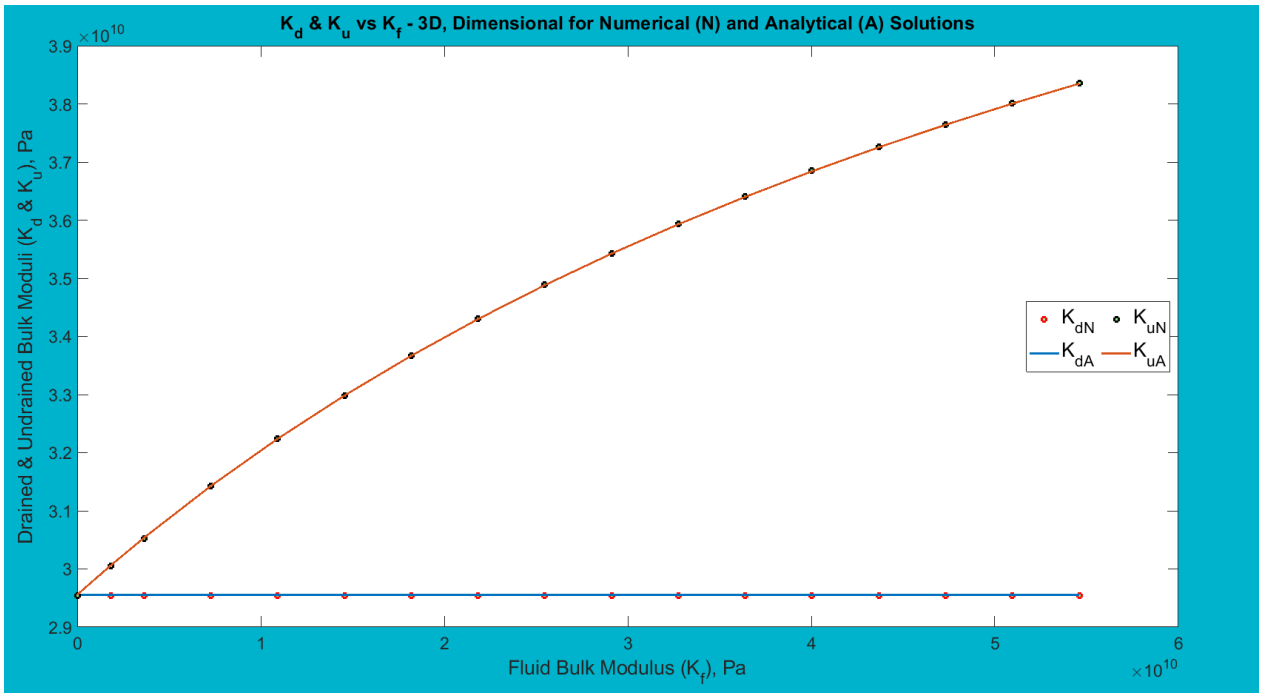

Figure 3.11: Plots showing numerical and analytical results for K_d and K_u against K_f

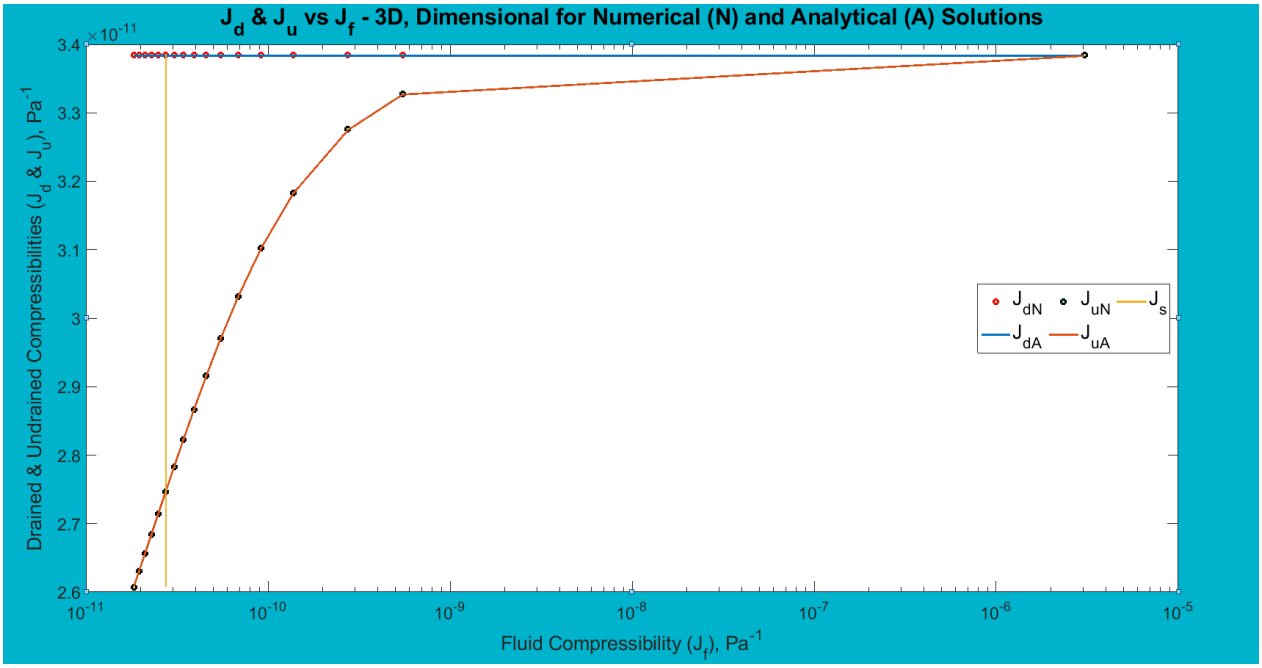

Figure 3.12: Plots showing numerical and analytical results for J_d and J_u against J_f

In Figure 3.11, K_d and K_u are both plotted against K_f, while in Figure 3.12, J_d and J_u are plotted against K_f. These simulations were carried out with constant μ and K_s (from Table 2.1), and a porosity of 12.5% (note that the plot for J_s is only for reference purpose). The results show that, for the undrained case, the entire rock becomes more compressible as the fluid compressibility becomes larger. While, for the drained case, the change in fluid compressibility does not affect the drained bulk modulus. This makes sense because, the drained case represents the case where fluid is allowed to leave the pore. This is also evident from the fact that, from the results, $K_d = K_u$ when $K_f = 0$, and J_d tends to J_u as J_f increases. Further, the curve for J_u vs J_f is changing rapidly until J_f is roughly the same as J_s. And when $J_f >> J_s$, the undrained compressibility stops changing fast.

3.1.4 Effect of Shear Modulus on Macroscopic Parameters

In this section, the model is at 15% porosity and the shear modulus μ is varied. The first two data points for K_f are 0.01 GPa, and 5 GPa. Subsequently, it is increased in steps of 5 GP up to 100 GPa.

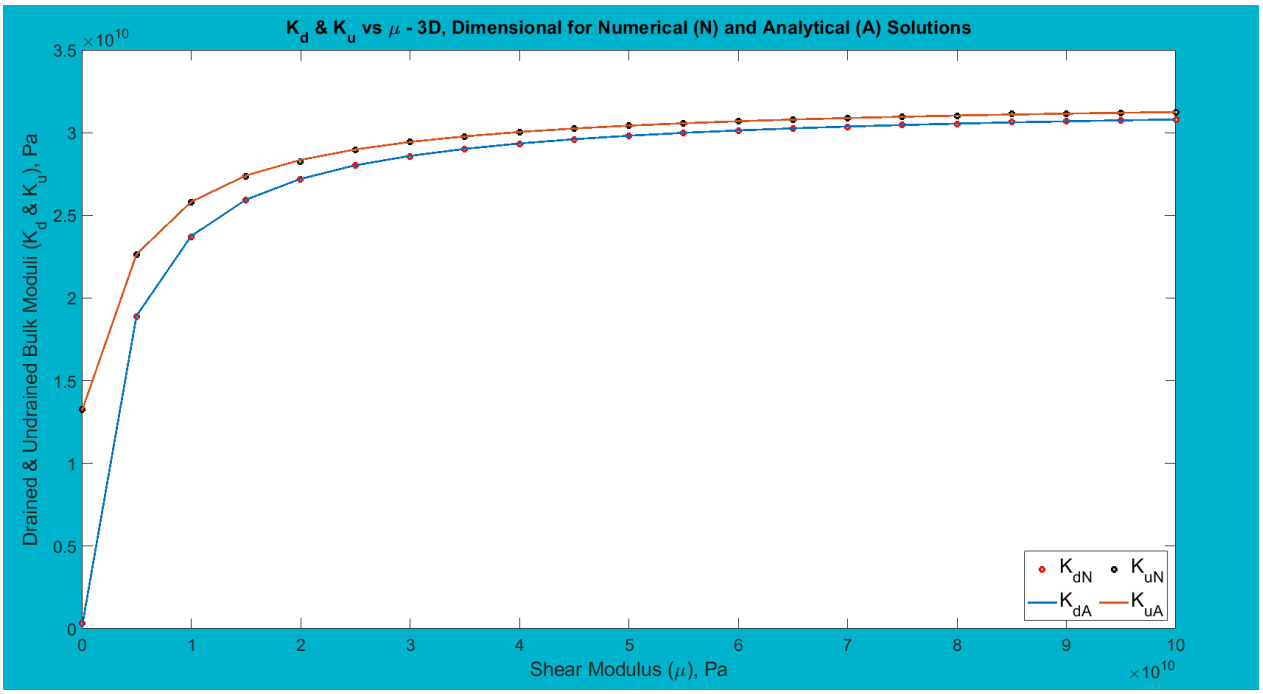

Figure 3.13: Plots showing numerical and analytical results for K_d and K_u against μ

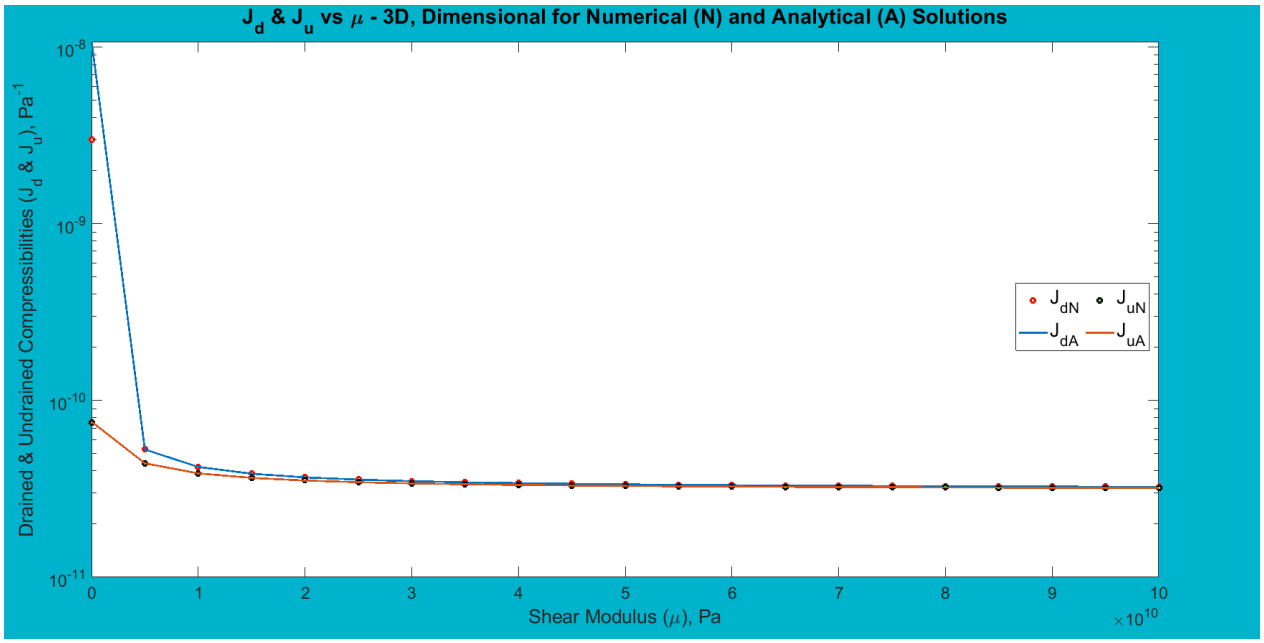

Figure 3.14: J_d and J_u vs μ - with smallest data point - for spherical models with a single spherical pore

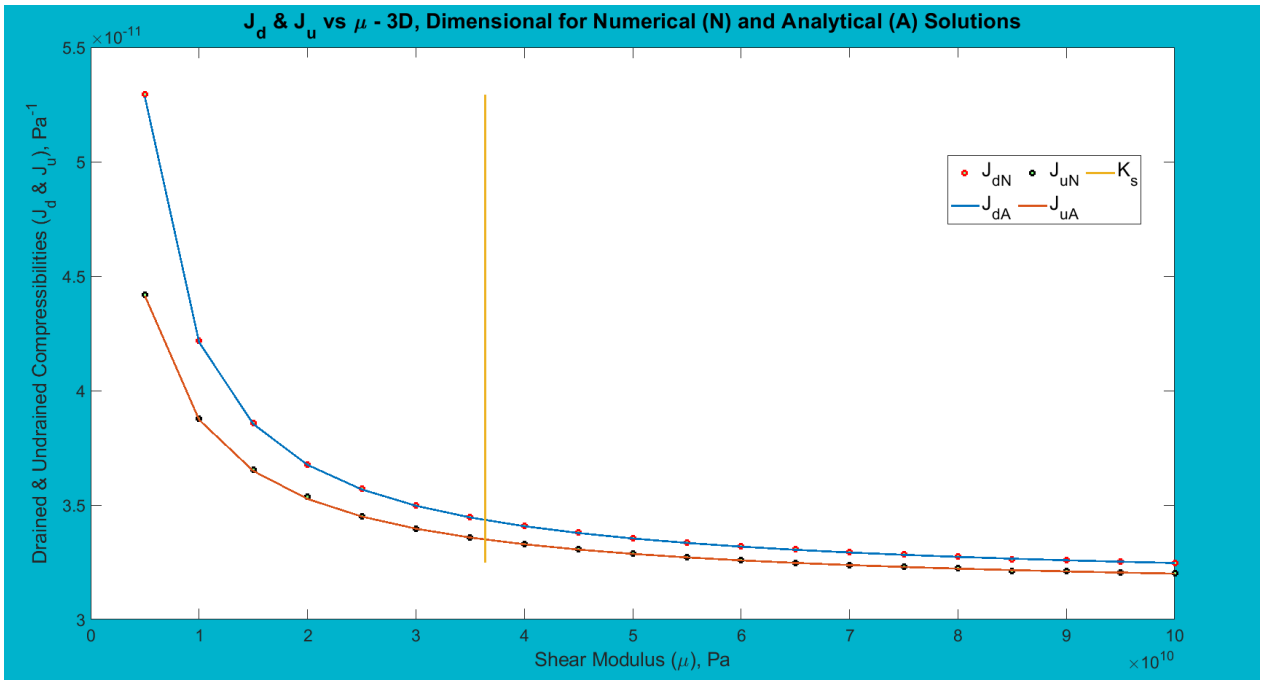

Figure 3.15: J_d and J_u vs μ - without smallest data point - for spherical models with a single spherical pore

Here, the effects of the shear modulus of the solid region are investigated. For this particular investigation, the bulk modulus of the solid region was kept constant at $K_s = 36.4$ GPa, while that of the fluid remained at $K_f = 2.4$ GPa, and the porosity of the rock was 12.5%.

Figure 3.13 shows plots of K_d and K_u against μ, while Figures 3.14 and 3.15 both show their compressibilities plotted against the shear modulus. The only difference between Figures 3.14 and 3.15 is the presence and absence (respectively) of the smallest data points; while the plot for K_s is there for reference. Since the numerical model would not run at zero shear modulus, the smallest possible value (to the nearest tens) of the shear modulus that it could run with was chosen. This smallest data point for μ was 0.01 GPa, followed by 20 larger data points in the range of 5-100 (GPa). $\mu = 0.01$ GPa resulted in a value for K_d that was significantly smaller and closer to zero than that of K_u.

It is really interesting that $K_d \to 0$ as $\mu \to 0$ but not so for K_u. This is possibly because, for the drained case, there is no resistance, whatsoever, from the pore fluid (see equation 2.26) because of the absence of fluid. However, for the undrained case, the bulk resistance from the fluid influences the outcome (see equation 2.28). This is also why the difference between K_d and K_u reduces significantly for higher values of μ, because the shear modulus is so large that the influence from K_f is almost negligible. Moreover, K_d and K_u stop changing rapidly once $\mu >> K_s$.

Finally, from the results shown in Figures 3.13 to 3.15, it is clear that the shear modulus of porous rocks must play a role in poroelasticity. This is generally because of the inhomogeneities caused by the pores which give rise to shear around the pores.

3.1.5 Comparison between Undrained Solid Stress and Pore Pressure

Here, I show results from the comparison between the stress in the solid for the undrained experiment and the pore fluid pressure.

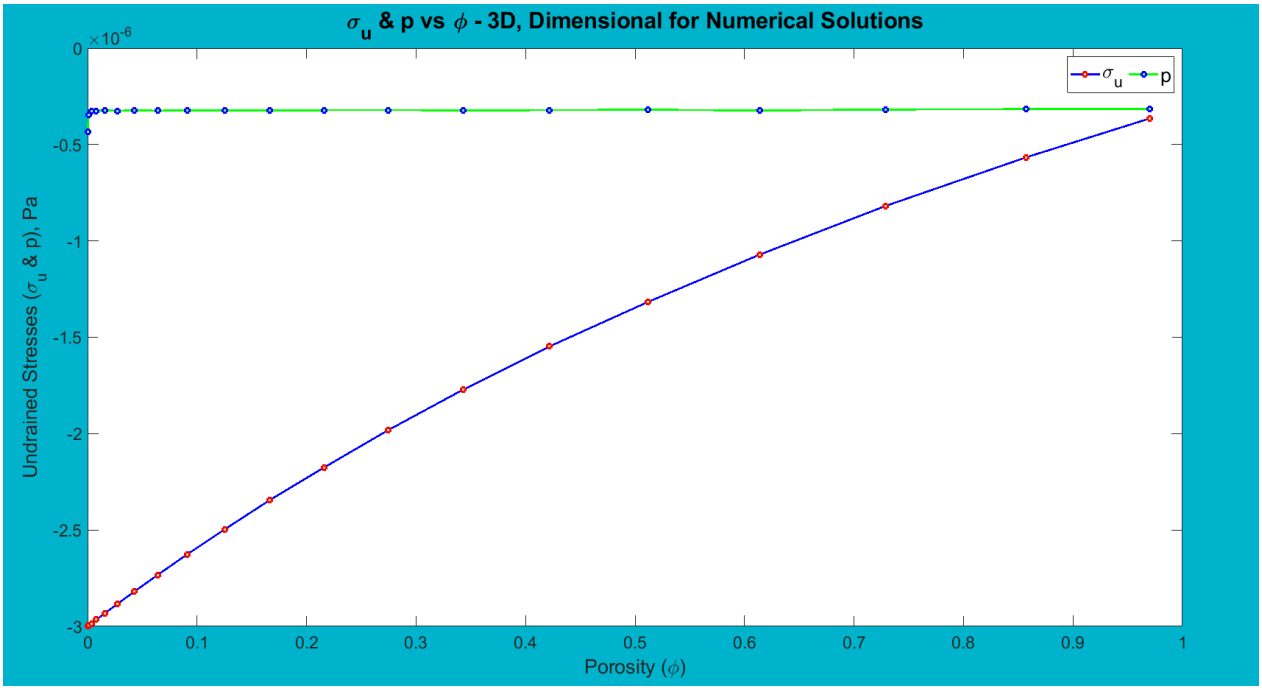

Figure 3.16: Plots showing numerical results for σ_u and p against ϕ

From Figure 3.16 it can be seen that the pore fluid pressure is greater than the solid stress. This is how consolidation is achieved in my model, where the excess pore fluid is expelled from the pore because the stress in the fluid is greater than the solid stress generated from the loading on the outer surface of the rock. Both stresses become essentially equal once 100% porosity is achieved. These stresses are also shown radially in 2D in Figure 3.17; where the negative sign indicates compression.

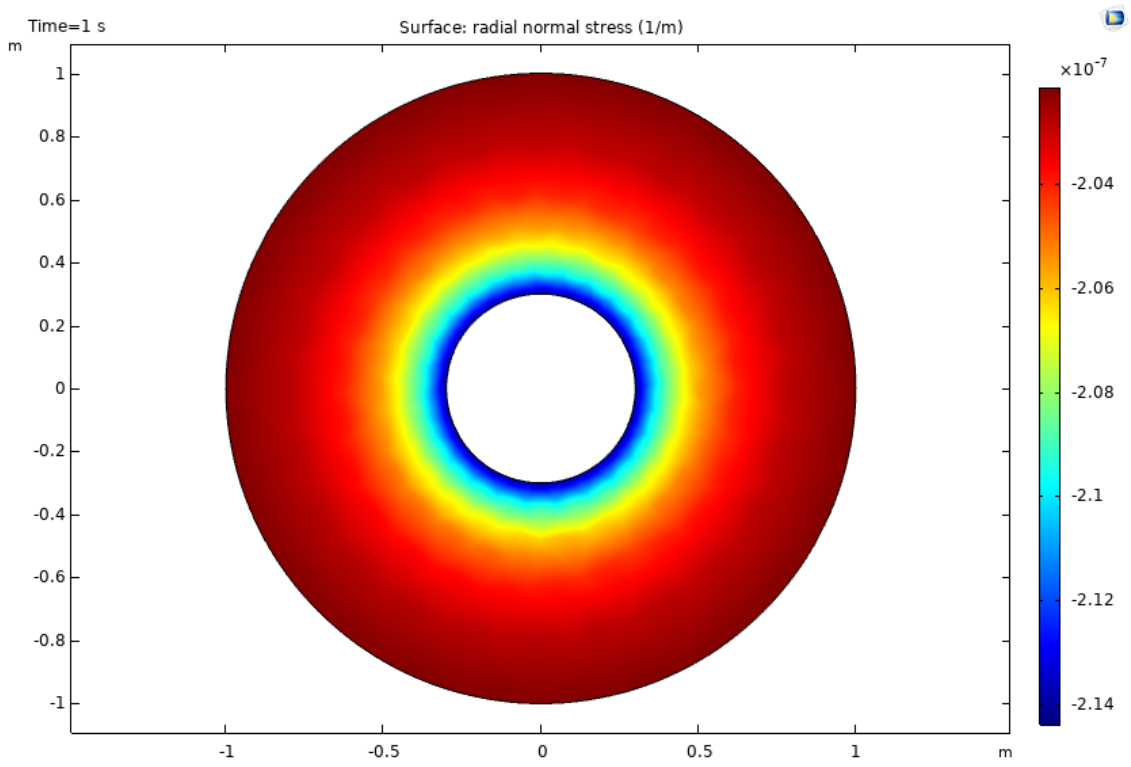

(a)

Figure 3.17: Radial normal stress field for undrained case, $p \neq 0$, for a circular rock of 1 m radius having a circular pore of 0.3 m radius

3.1.6 Energy vs Porosity

In this section, the spherical model has a radius of 1 m and the pore radius ranges from 0.05 m with increments of 0.05 m up to 0.95, and then a final data point of 0.99, making 20 data points in total.

Figures 3.18 and 3.19 show the 3D energy density plots in COMSOL Multiphysics® for shear and compression, respectively, in simulations in which the solution in the fluid domain is determined for both the drained and undrained cases. In the solid region in Figure 3.18, the shear energy increases as you approach the fluid region and reaches a maximum on the pore wall. The shear energy in the fluid region is zero since the shear modulus is 0. The reason we have shear in the matrix of a spherically symmetric sample under a spherically symmetric load is because of the presence of the pore. This has also been shown analytically

in equation (2.40). Further, the normal stresses are not all equal near the pore, causing some shear, and as shown in Figure 3.18, the shear energy is greatest around the pore walls. In Figure 3.19, however, the compression energy density is constant in the solid region, and constant with a different value in the fluid region. The difference is due to the difference in the compressibilities of the two regions.

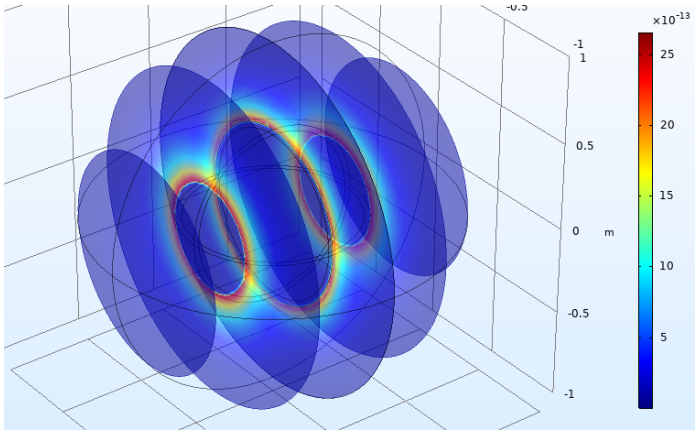

Figure 3.18: Shear Energy Density

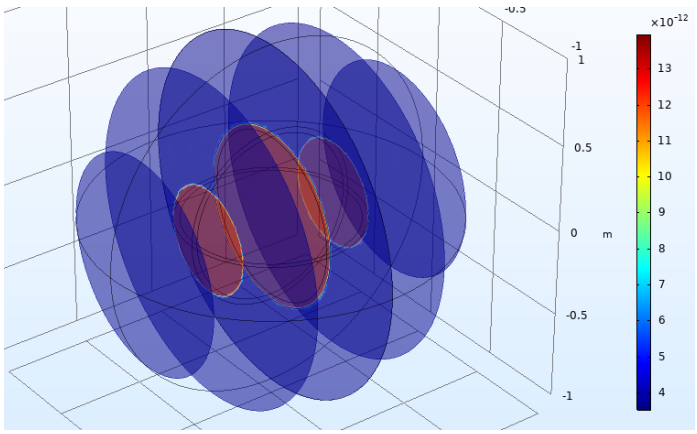

Figure 3.19: Compression Energy Density

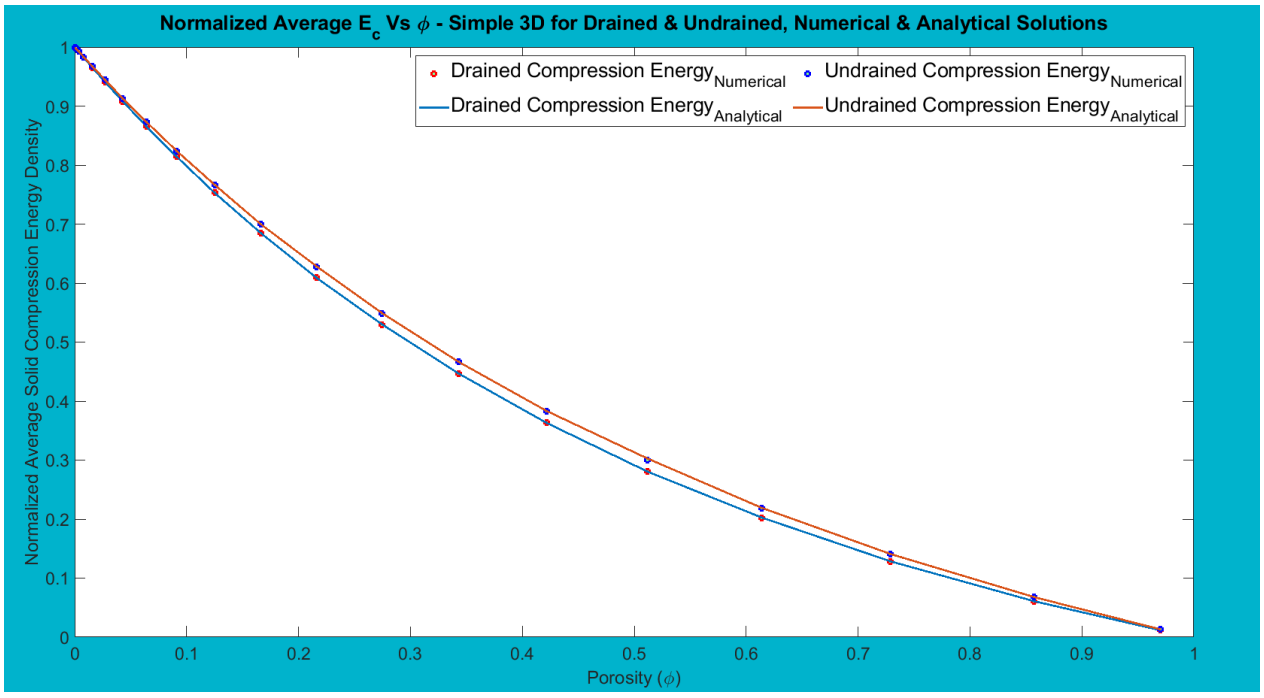

Figure 3.20: Plots showing numerical and analytical results for normalized average E_c against ϕ

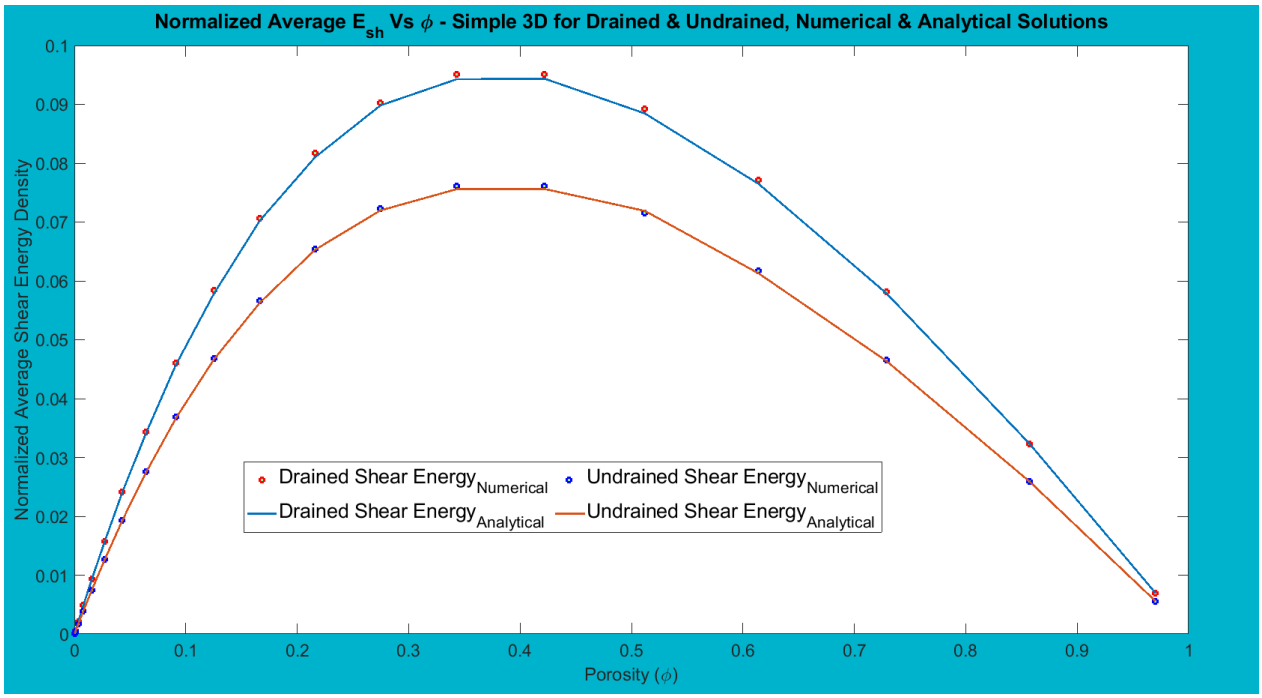

Figure 3.21: Plots showing numerical and analytical results for normalized average E_{sh} against ϕ

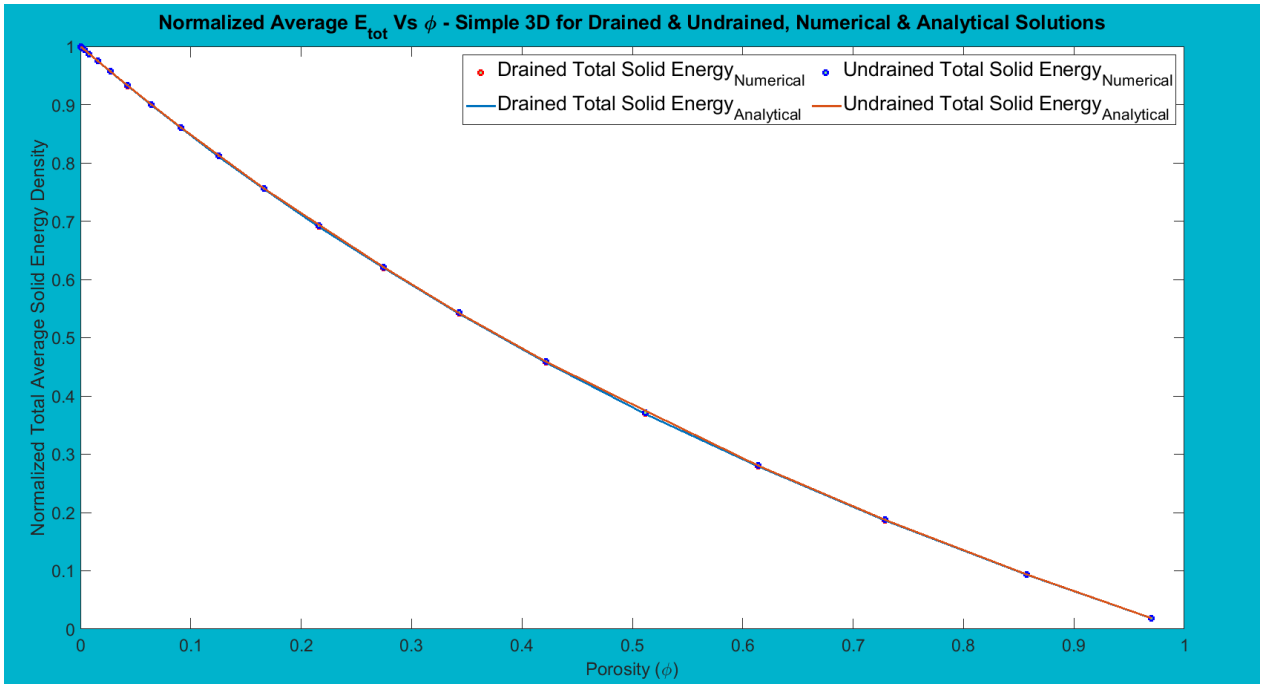

Figure 3.22: Plots showing numerical and analytical results for normalized average E_{tot} against ϕ

Figures 3.20 to 3.22 consider the effect of porosity on the normalized averages of the solid

compression energy density, shear energy density, and total solid energy density. They are averaged over the volume of the whole sample. Both the numerical and analytical studies were considered for each plot, and they were in good agreement with each case. In Figure 3.20, the normalized average solid compression energy density (E_{c_n}) is plotted against porosity. This plot shows that E_{c_n} decreases as the porosity of the rock increases. This agrees quite well with equation (2.41) for the solid compression energy,

$$E_c = 6\pi K \frac{\left(R_o^2 u_o - R_i^2 u_i\right)^2}{\left(1-\phi\right) R_o^3}. \tag{3.7}$$

Intuitively, this makes sense because, as the pore gets bigger, the volume of the fluid becomes larger relative to that of the solid, shifting more of the energy storage into the fluid region. Also, there is not a lot of difference between the drained and undrained cases for the solid compression energy since the evaluation is done only in the solid region. Although, from the plots, the undrained case generally stores more energy than the drained case. This is because of the presence of fluid.

Figure 3.21 shows that the normalized average shear energy density (E_{sh_n}) continues to increase until about 35% porosity before it sharply begins to decline. This is an interesting observation because, since shear mostly occurs around the solid-pore interface (see Figure 3.18), as the pore volume increases initially, the average shear energy on the pore boundaries increases as well. But as the pore gets a lot bigger, the average shear energy decreases because there is a smaller volume of solid in which you can have stored shear energy. Further, there is less shear in the undrained case than in the drained one since the presence of fluid reduces shear.

Finally, the normalized total average energy density (E_{tot_n}) from equation 2.41 is plotted against porosity in Figure 3.22. This result reveals that the total energy density is mostly from the contribution of the compression energy density, because the magnitude of the shear energy density is very small compared to that of the compression energy (compare Figure 3.21 with Figure 3.20). Also, whereas the results for the drained and undrained cases in Figure 3.20 vary slightly, Figure 3.22 shows an identical match for the total average energy

in both cases. This is because, while the average solid compression energy is a bit bigger for the undrained cases, the average shear energy is a bit larger for the drained cases, and the combined effects are exactly the same. Analytically, this is shown in Appendix C.

3.2 Spherical Models with Different Spherical and Cylindrical Pore Sets

In this section, the cubic model with one spherical pore has a length of 1 m and the pore size ranges from 0.1 m to 0.4 m in steps of 0.1 m. The spherical model with one spherical pore has a radius of 1 m and the pore radius ranges from 0.1 m to 0.7 m in steps of 0.1 m. The spherical model with two spherical pores has a radius of 1 m and each pore radius ranges from 0.06 m to 0.46 m in steps of 0.05 m. The spherical model with four spherical pores has a radius of 1 m and each pore radius ranges from 0.04 m to 0.32 m in steps of 0.04 m. Each of the spherical models with one, two and three cylindrical pores has a radius of 15 m and each pore has a height of 10 m with a radius that ranges from 1 m to 9 m in steps of 1 m, except for the model with the one cylindrical pore that goes up to a radius of 10 m.

Further, in this section, I show the comparison between the results from three spherical 3D models with spherical pore sets - one, two, and four pore sets - and three different cylindrical pore sets - one, two, and three pore sets. (See Figures 3.23a to 3.24c for an explanation of the geometry.)

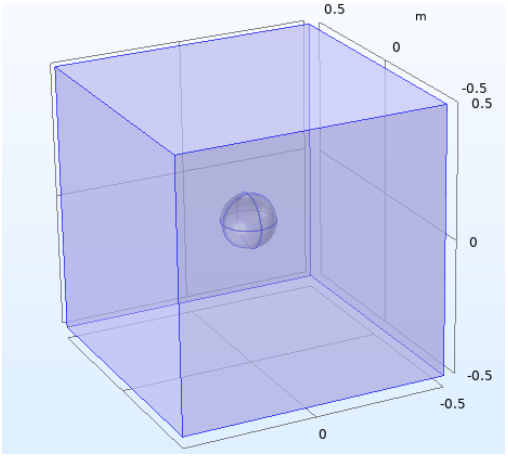

(a) 1 Spherical pore in a cube

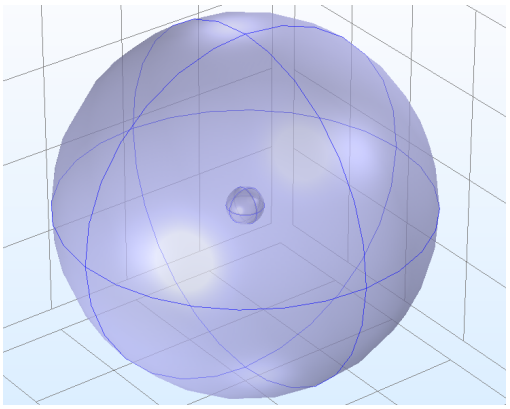

(b) 1 Spherical pore in a sphere

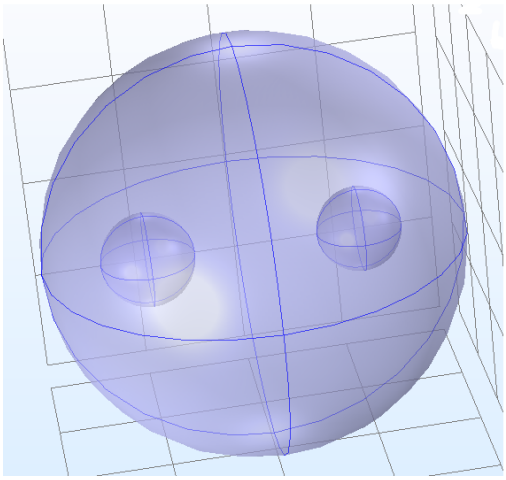

(c) 2 Spherical pores in a sphere

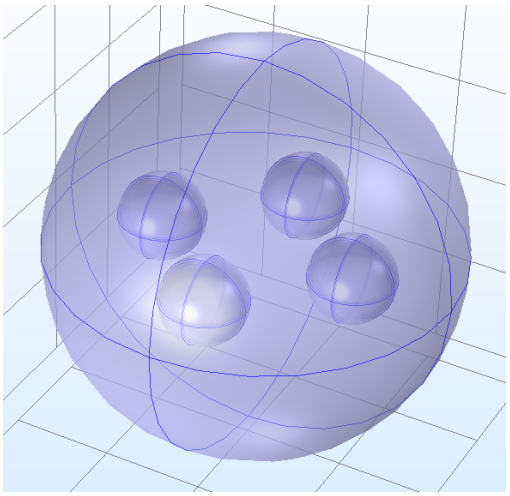

(d) 4 Spherical pores in a sphere

Figure 3.23: Simple spherical pores

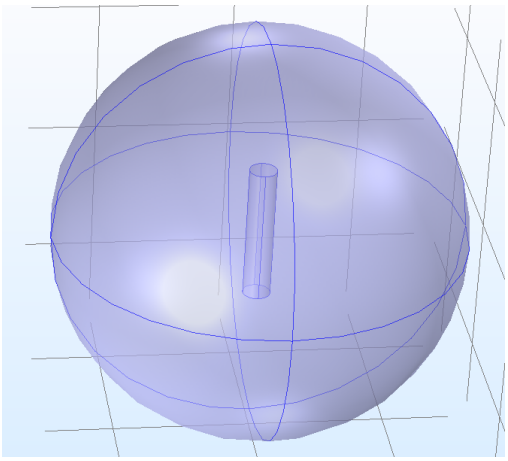

(a) 1 Cylindrical pore in a sphere

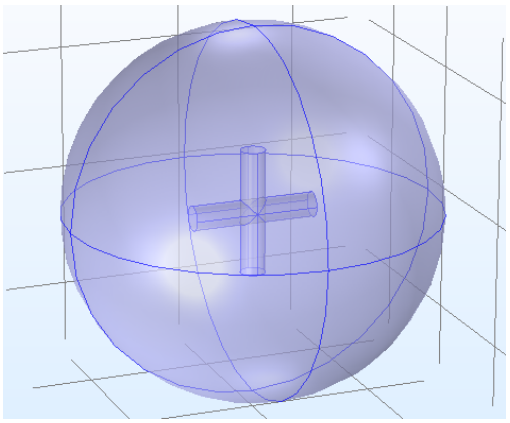

(b) 2 Cylindrical pores in a sphere

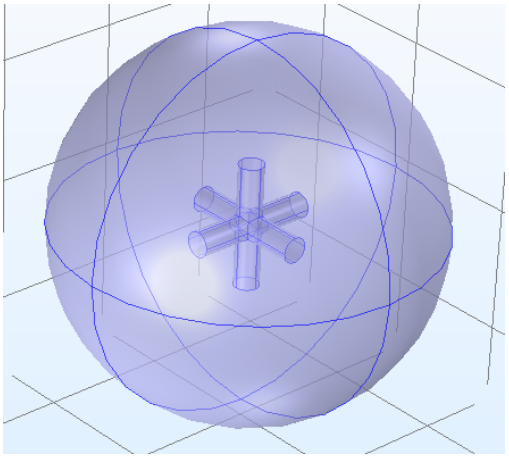

(c) 3 Cylindrical pores in a sphere

Figure 3.24: Simple cylindrical pores

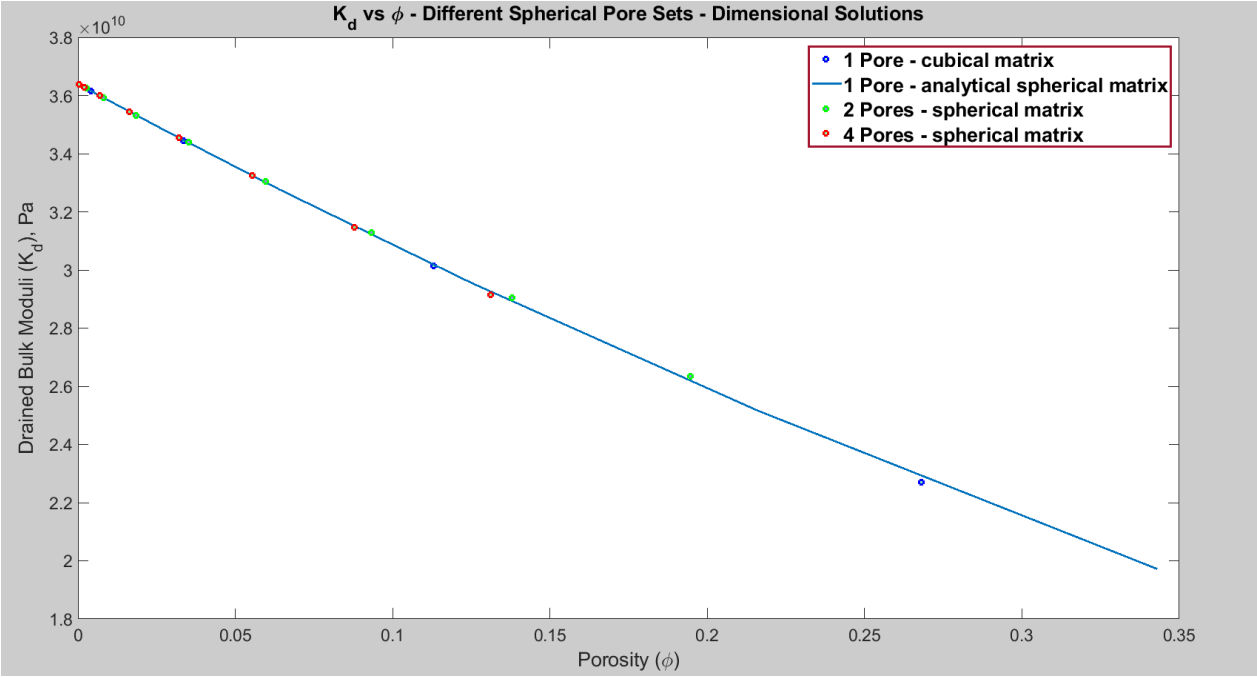

Figure 3.25: K_d against ϕ - numerical solutions for models in Figure 3.23

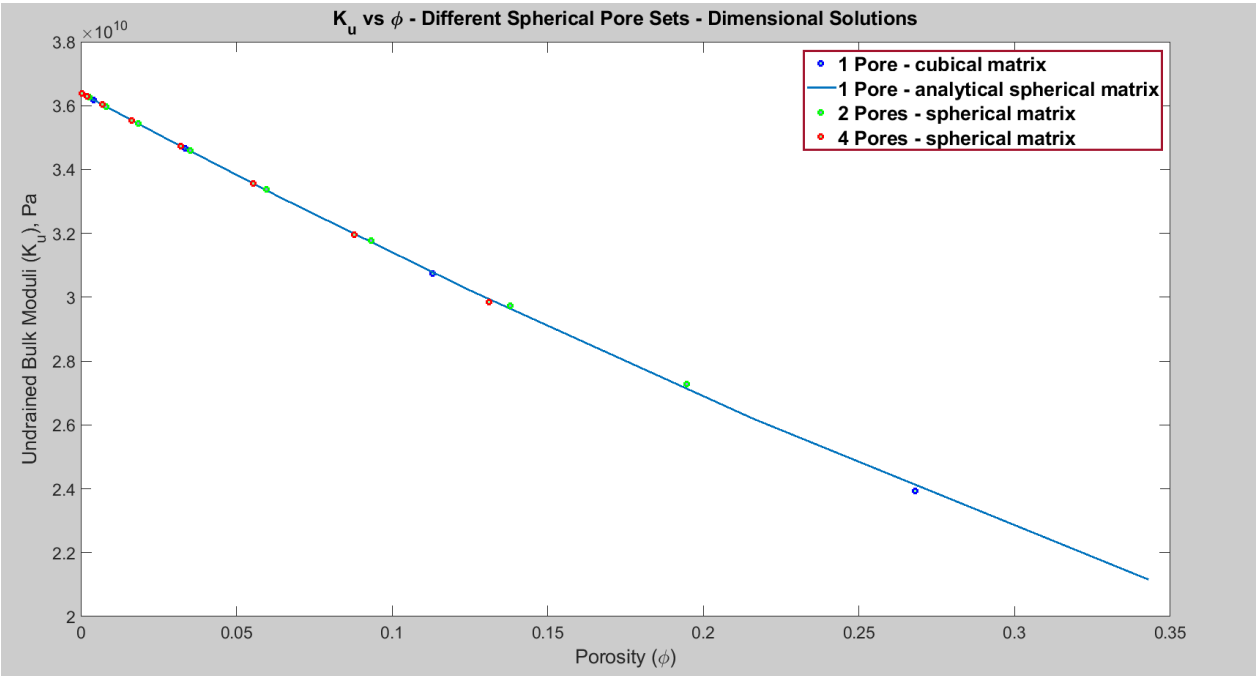

Figure 3.26: K_u against ϕ - numerical solutions for models in Figure 3.23

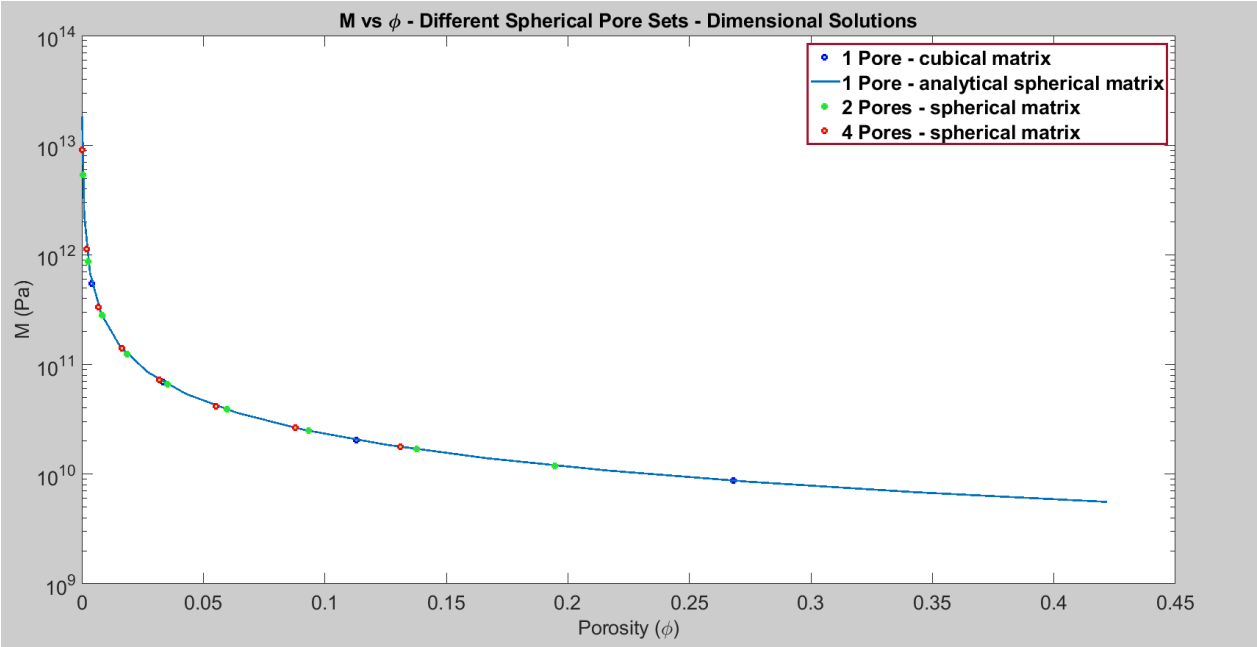

Figure 3.27: M against ϕ - numerical solutions for models in Figure 3.23

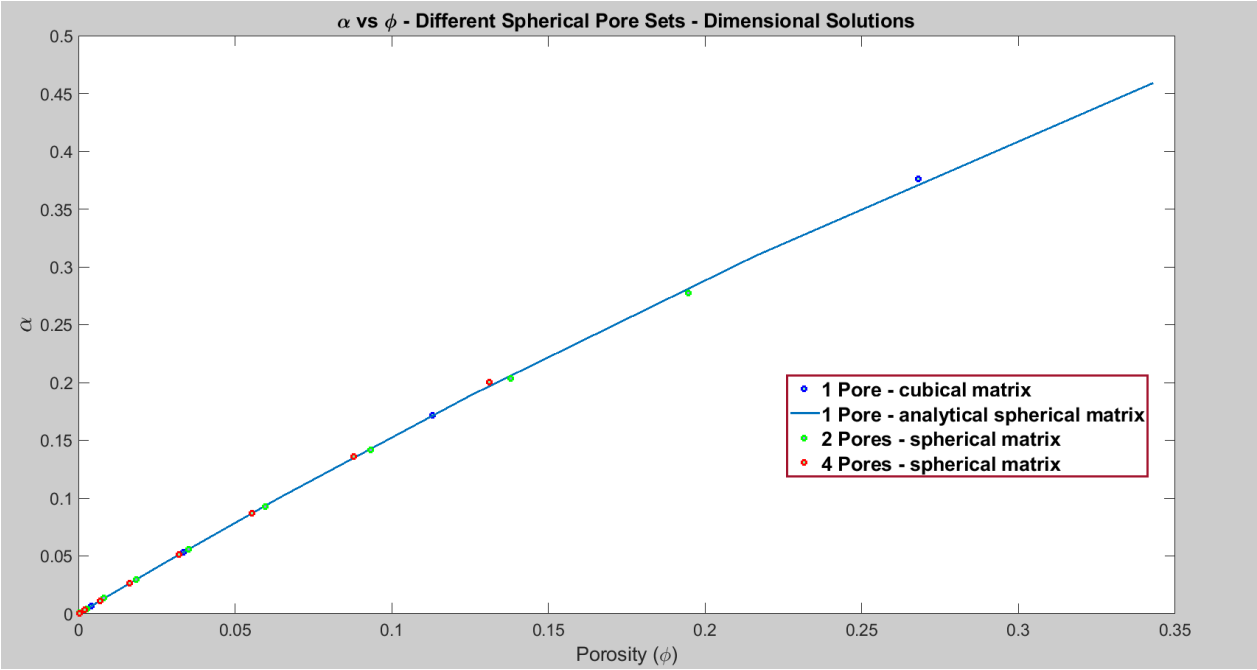

Figure 3.28: α against ϕ - numerical solutions for models in Figure 3.23

Figures 3.25 and 3.26 show the results of K_d and K_u, respectively, for three sets of spherical pores in spherical bulks, and one spherical pore in a cubical bulk. These plots show a near-perfect agreement among the pore sets, most likely because the pore sets are all spherical.

However, there are slightly varying results when the pore space is made up of cylindrical pore sets (see Figures 3.29 and 3.30). The results from the two and three cylindrical pore sets are in close agreement with each other, and both differ from the ones obtained from the single pore case. This might be because the two and three pore sets both have geometries that are aligned with more than one axis, longitudinally.

Further, I have carried out these calculations with different sample geometries to verify that the results are independent of this geometry.

Finally, Figures 3.27 and 3.31 show no difference in M for both the cylindrical and spherical pore sets. The significance of this is that the pressure required to cause a unit increase in the fluid content at constant volume does not change regardless of the geometry of the pore space. This is shown more clearly in the next section. In the same sense, the coefficient α increases with increase in porosity (see Figure 3.28). This shows that, as porosity increases, there is an decrease in the macroscopic volumetric strain caused by the variations in fluid content (in the drained case, $\alpha = \frac{\zeta}{\Delta}$).

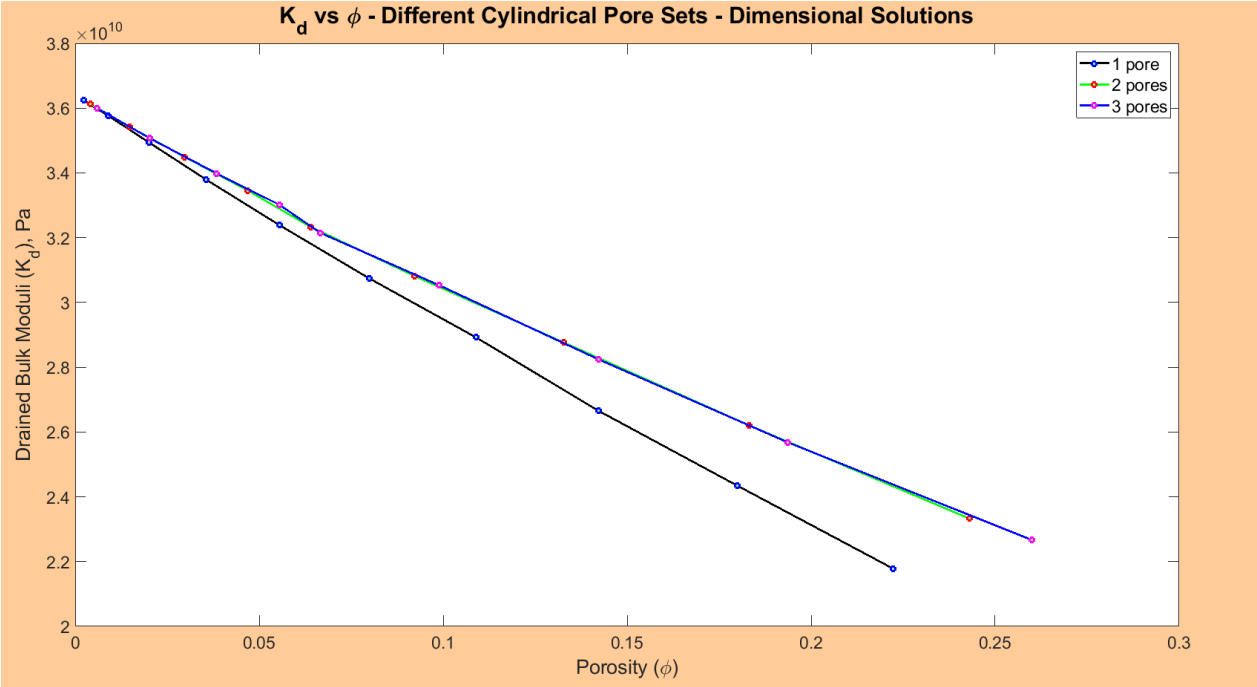

Figure 3.29: K_d against ϕ - numerical solutions for models in Figure 3.24

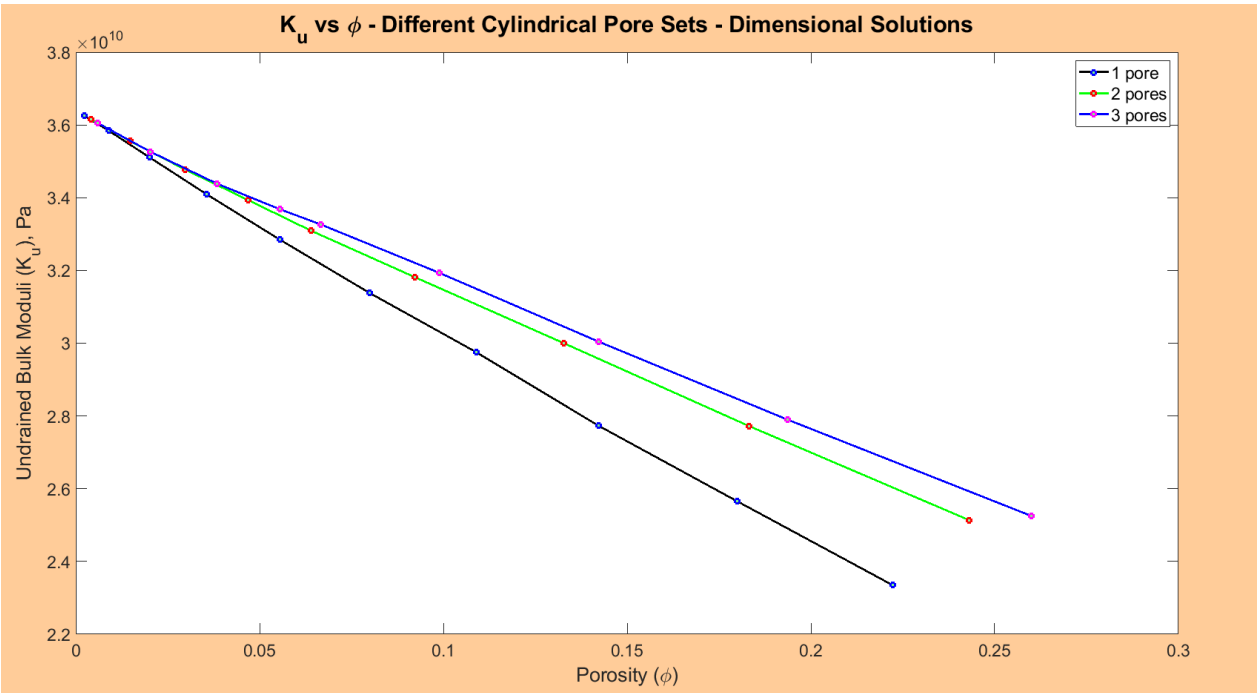

Figure 3.30: K_u against ϕ - numerical solutions for models in Figure 3.24

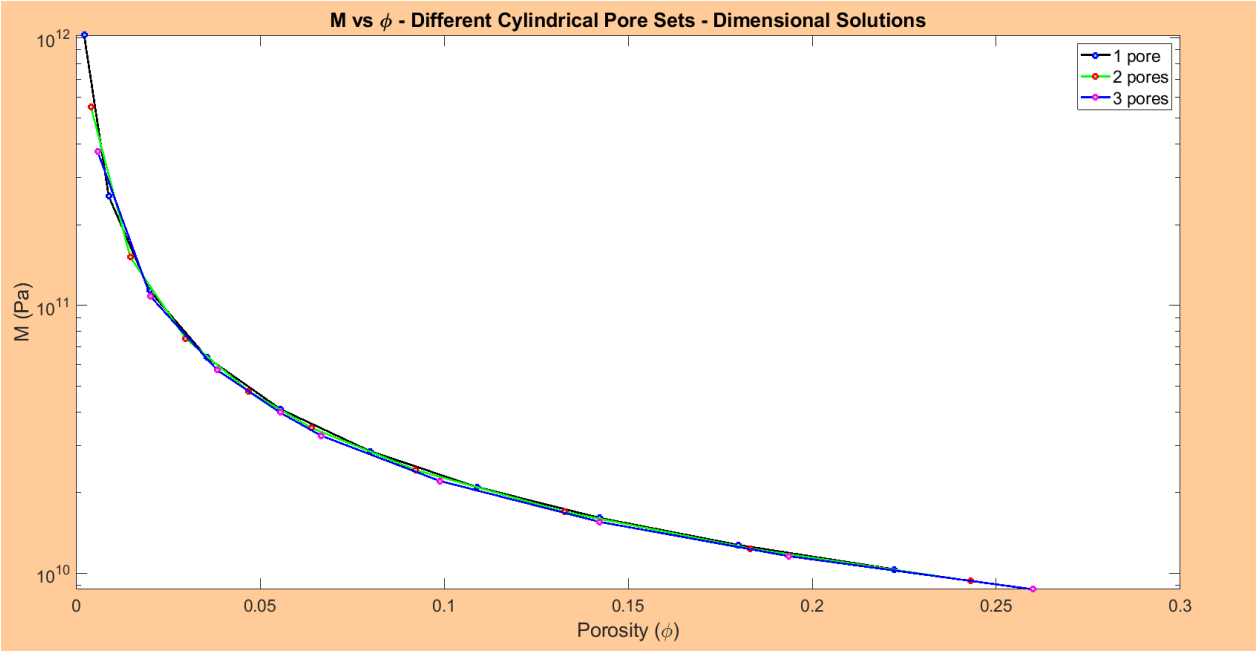

Figure 3.31: M against ϕ - numerical solutions for models in Figure 3.24

3.2.1 Energy Considerations for Models with Various Spherical Pore Sets

Next, I look at how the compression and shear energy densities are affected by the number of pores present. These were normalized over the bulk volumes in order to inspect only the contribution from the pores. They were then plotted against porosity for the various spherical pore sets shown in Figures 3.23a to 3.23d, and the results of these plots are shown in Figures 3.32 to 3.34.

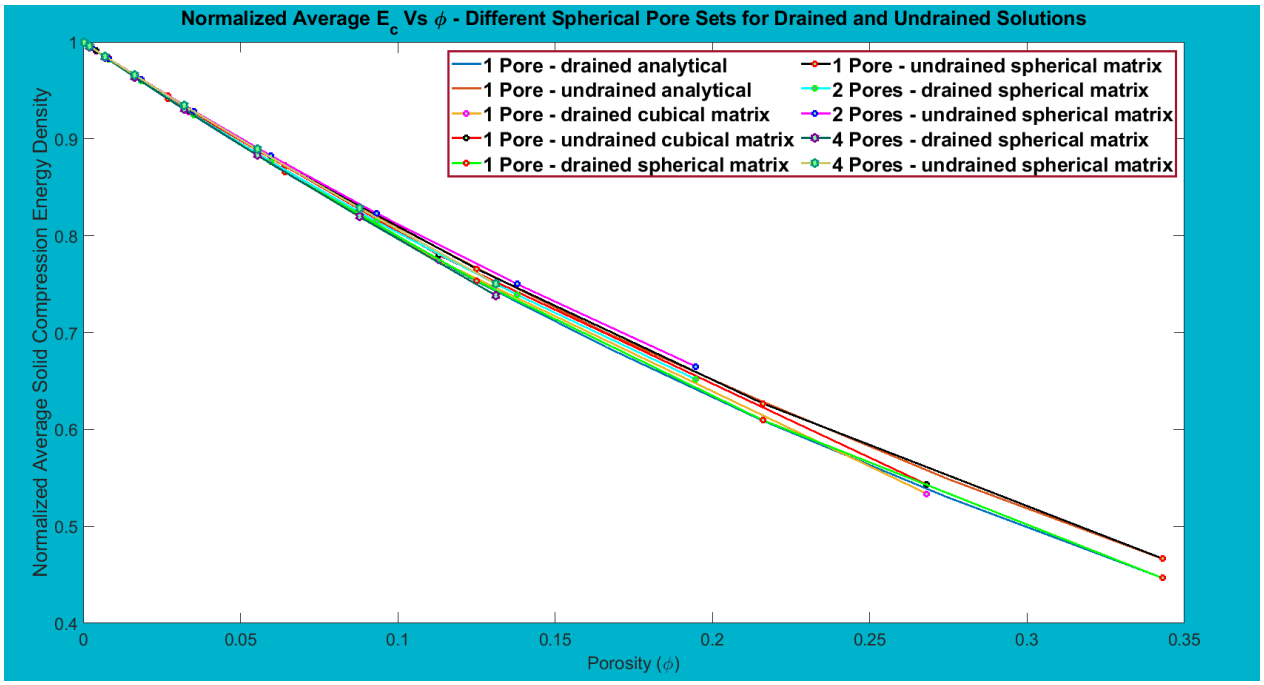

Figure 3.32: Plots showing E_{c_n} against ϕ for various spherical pore sets

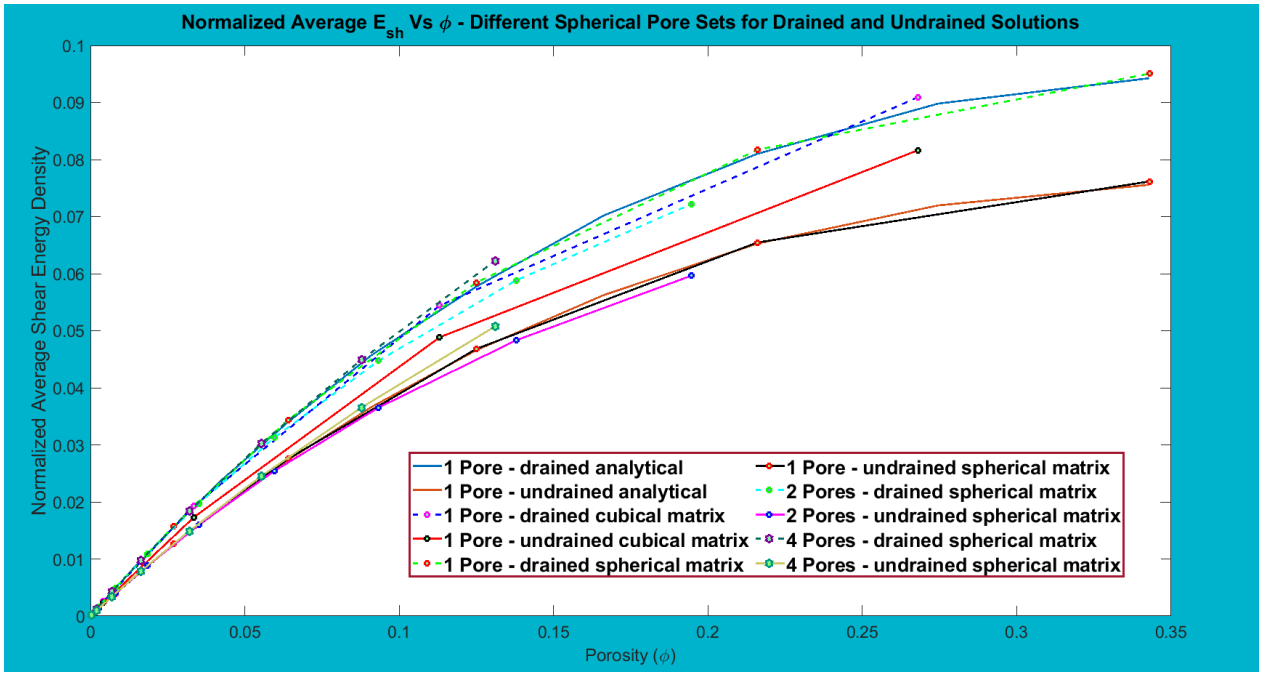

Figure 3.33: Plots showing E_{sh_n} against ϕ for various spherical pore sets

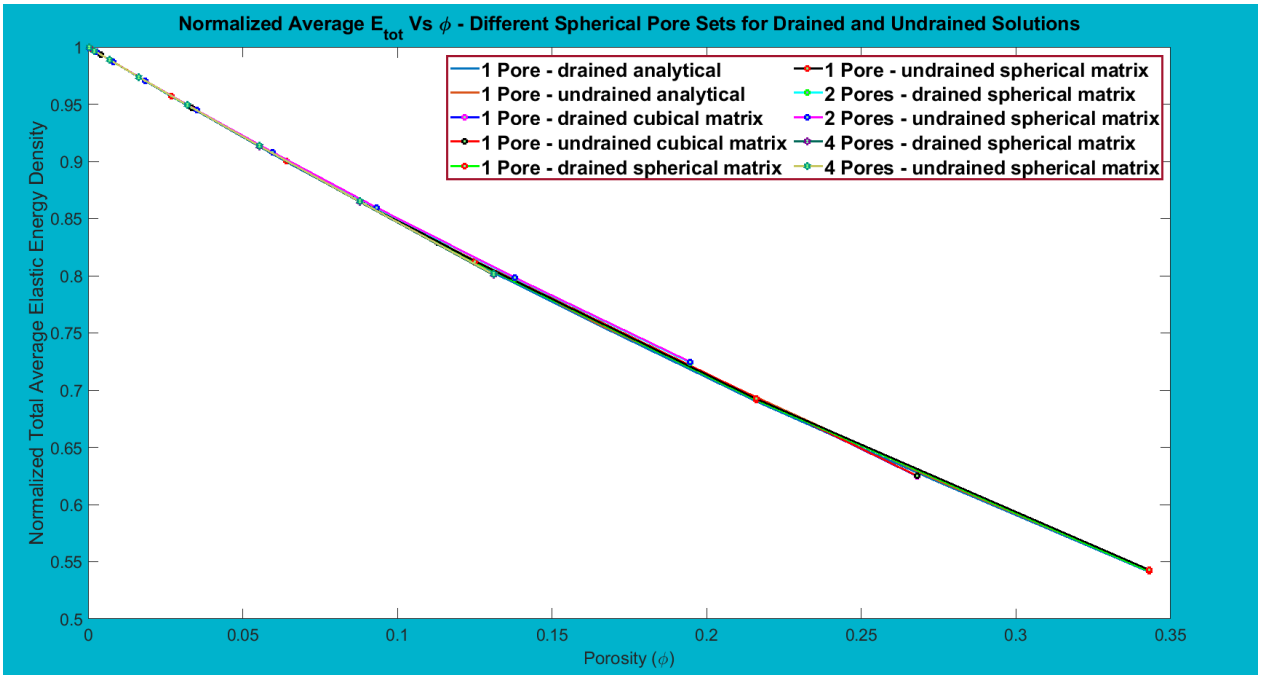

Figure 3.34: Plots showing E_{tot_n} against ϕ for various spherical pore sets

In Figure 3.32, E_{c_n} is plotted against ϕ for the various pore sets and rock matrices listed in the legend (see Figures 3.23a to 3.23d for the model set-ups). From this figure, it is interesting to see that the number of pores do not play a significant role in the average amount of energy stored in the elastic solid. This was not expected. However, E_{c_n} is decreasing with increase in porosity as expected.

Further, Figure 3.33 shows plots for E_{sh_n} against ϕ again for the various model set-ups as shown above in Figures 3.23a to 3.23d. From these plots, it is observed that, unlike the plots for E_{c_n} in Figure 3.32, the ones here are a little bit dispersed. This is because of the difference in the number of pores present in each sample. Another observation is that the shear energy is higher in the drained cases than in the undrained ones. This is because, a fluid-filled pore is harder than an empty pore (see Figure 3.2) which will reduce the amount of shear around it and so decrease the shear energy. Further, this plot shows E_{sh_n} increasing with increase in porosity. However, as shown from Figure 3.21, it is expected that, as the pore volume increases at constant total rock volume, the rock matrix volume becomes smaller for the shear energy to be stored, hence, there should be a decrease in the average shear energy.

Finally, E_{tot_n} is plotted against ϕ in Figure 3.34. Here again, just like in Figure 3.22, the combined effects of the normalized average shear and compression energies give very similar results for the total average energy in the drained and undrained cases of each model arrangement. This E_{tot_n} also has very close agreement among the models.

3.3 Spherical 3D Models - Spherical vs Cylindrical Pores

In this section, results from spherical and cylindrical pores will be shown side by side, and comparisons and/or contrasts drawn. The spherical model with two spherical pores has a radius of 1 m and the pore radius ranges from 0.05 m to 0.6 m in steps of 0.05 m. The spherical model with two cylindrical pores has a radius of 15 m and each pore has a height of 10 m with a radius that ranges from 1 m to 8 m in steps of 1 m.

3.3.1 Two-Pore Case

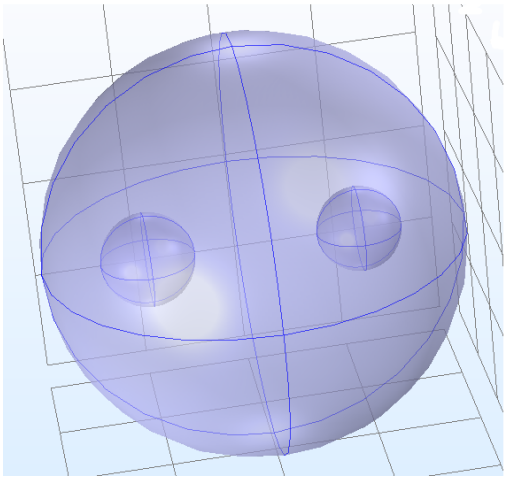

Figure 3.35: Spherical pores - model at 1.6% porosity

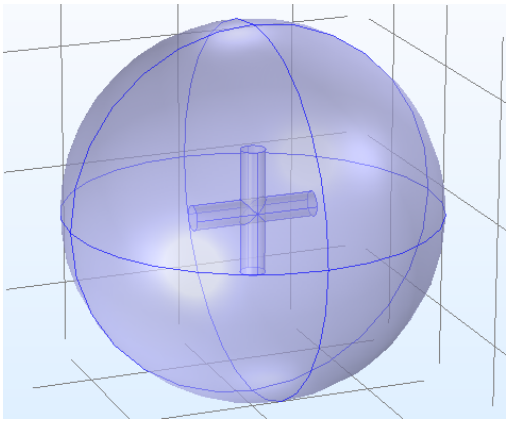

Figure 3.36: Cylindrical pores - model at 0.4% porosity

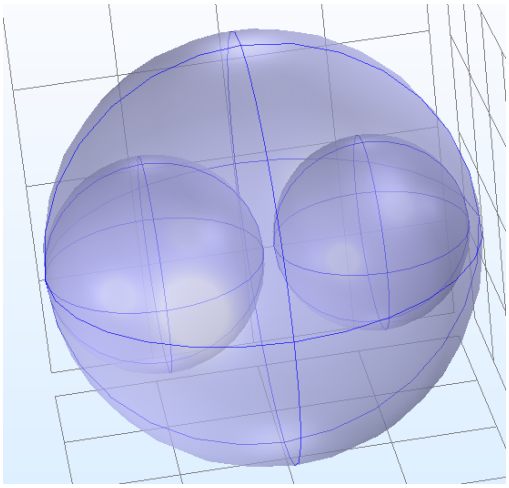

Figure 3.37: Spherical pores - model at 18.2% porosity

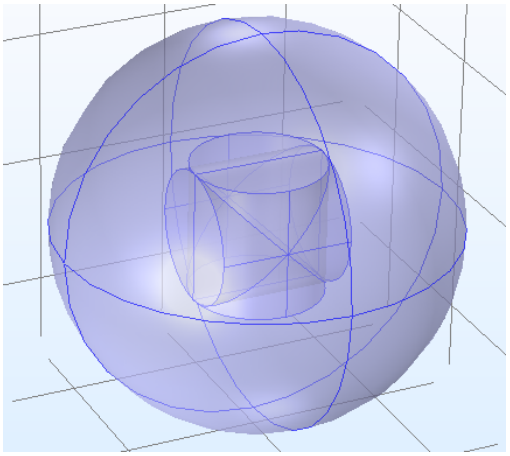

Figure 3.38: Cylindrical pores - model at 6.4% porosity

Figure 3.39: Spherical models with spherical and cylindrical pores - two pores

Figures 3.40 and 3.41 show interesting results for two spherical and two cylindrical pore sets. The plots for the drained bulk modulus show some differences. However, there is very little effect of pore geometry on the undrained bulk moduli. This reveals that, for these particular arrangements, the geometry of the pore space behaves similarly to each other when they are treated as being saturated with fluid (undrained case), and differently when drained of the fluid. This is likely because, for the undrained case, there is less shear around the pores since

the load is being taken by the fluid.

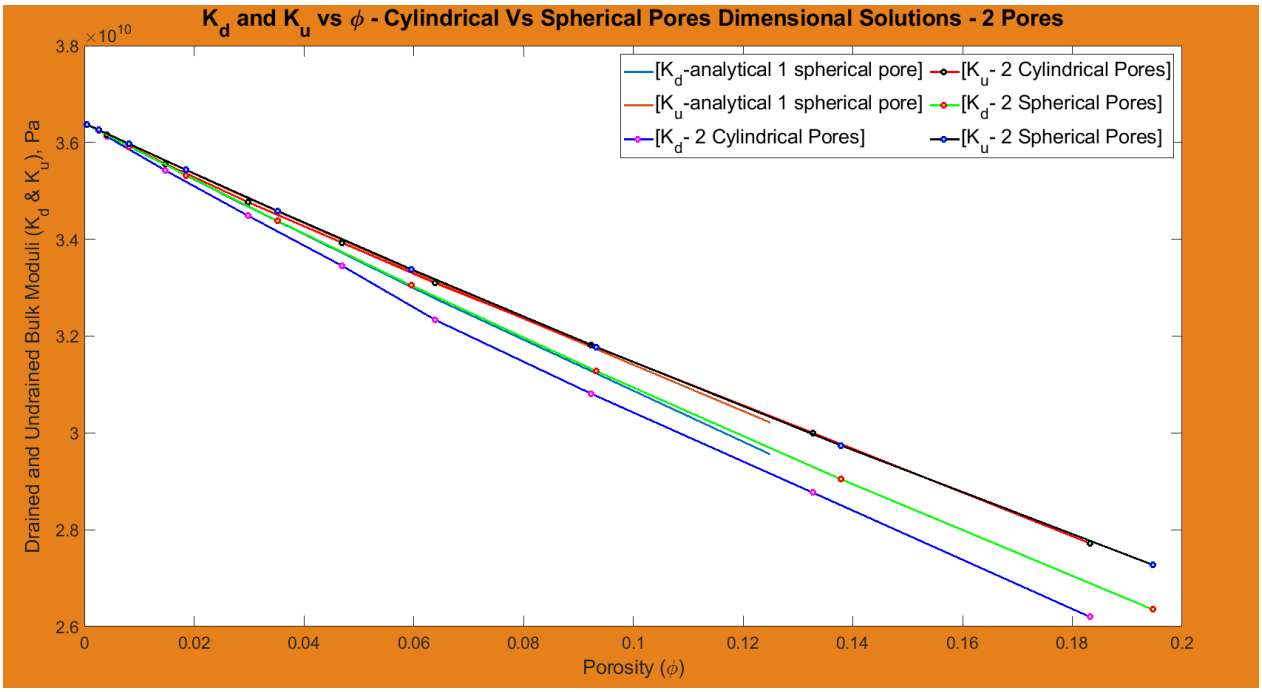

Figure 3.40: Simple spherical and cylindrical pores plots showing comparison of 2 different pore sets for K_d & K_u against ϕ

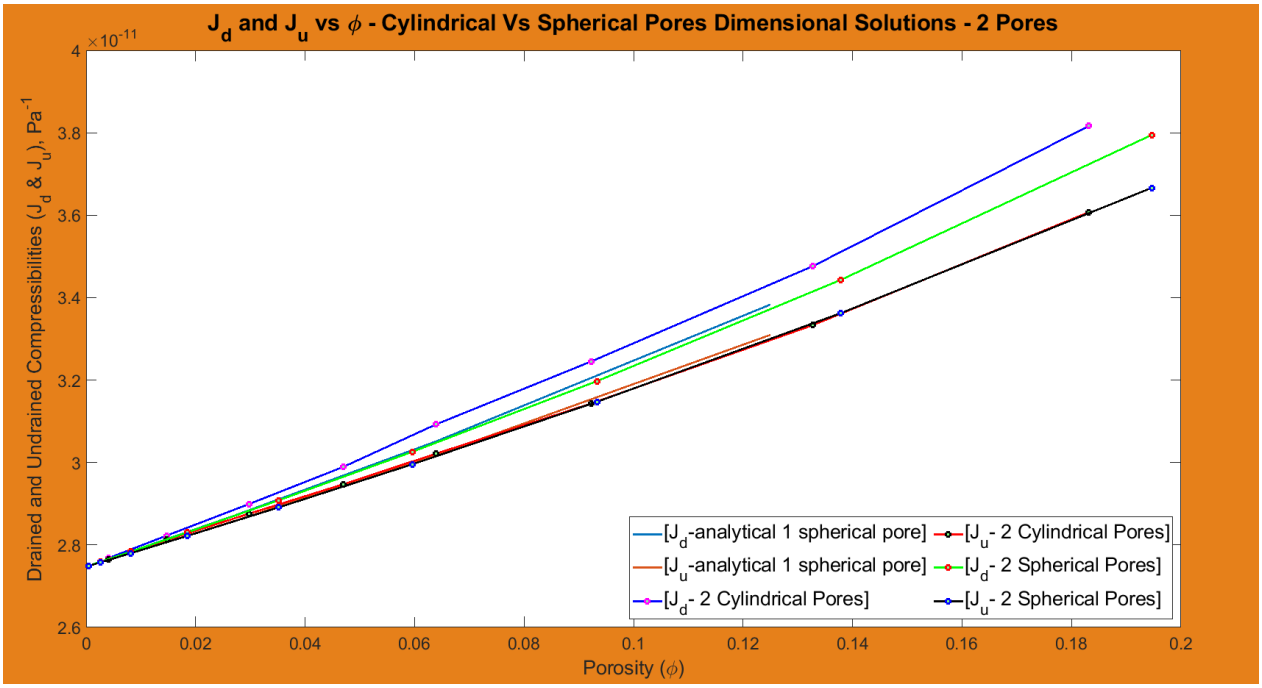

Figure 3.41: J_d & J_u against ϕ - numerical solutions for models in Figure 3.39

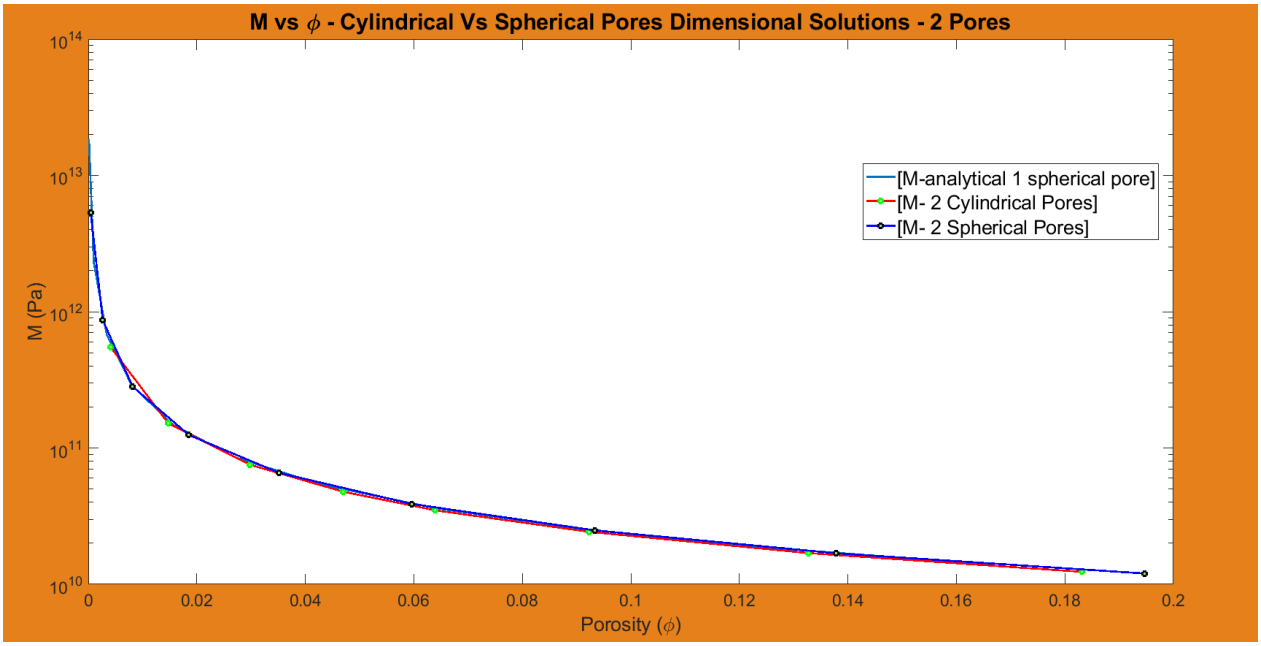

Figure 3.42: M against ϕ - numerical solutions for models in Figure 3.39

Figure 3.42 shows the plot of the pressure M against porosity ϕ for two spherical and two cylindrical pore sets. Here, the pressure remains unchanged, regardless of the difference in geometry. This implies that, to increase the fluid content by a unit value at constant macroscopic dilatation and at the same porosity for both model set-ups, one needs to exert the same amount of pressure on the pore.

3.3.2 Energy Considerations for Models with Various Spherical Pore Sets

In the previous subsection, I had examined the effects of the number of pores on the average solid energy density and discovered that (after normalization with bulk volume) the number of pores added little significance to how the energy is stored in the solid. Therefore, in this subsection, I will take the results from the spherical model with two spherical pores in the previous subsection (see Figure 3.23c) and compare them with those from the spherical model with two cylindrical pores (see Figure 3.24b) to see how the difference in pore geometry influences the average solid energy density.

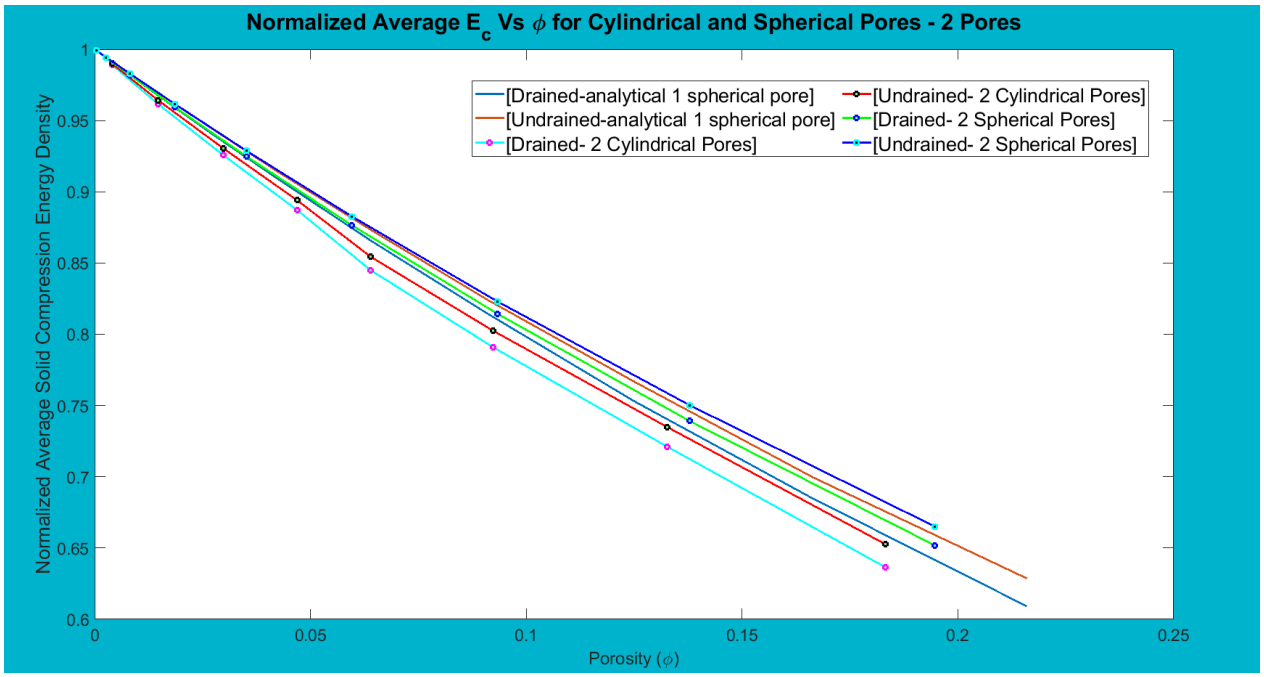

Figure 3.43: E_{c_n} against ϕ - numerical solutions for models in Figure 3.39

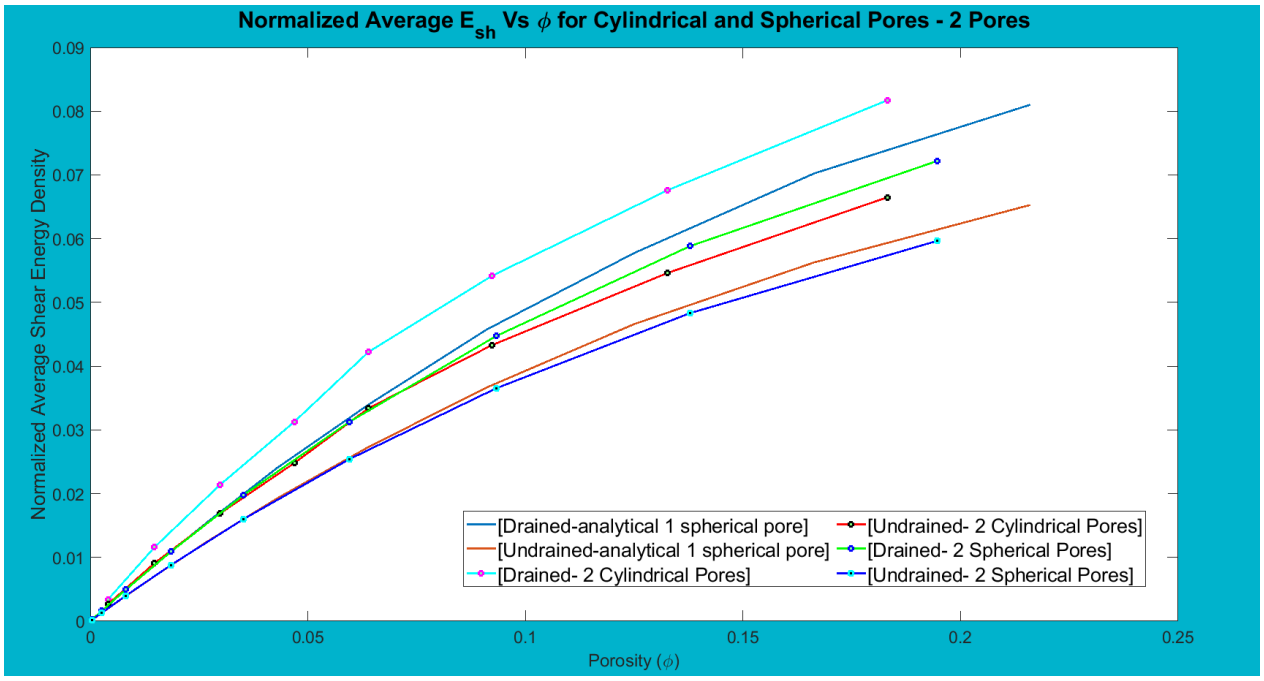

Figure 3.44: E_{sh_n} against ϕ - numerical solutions for models in Figure 3.39

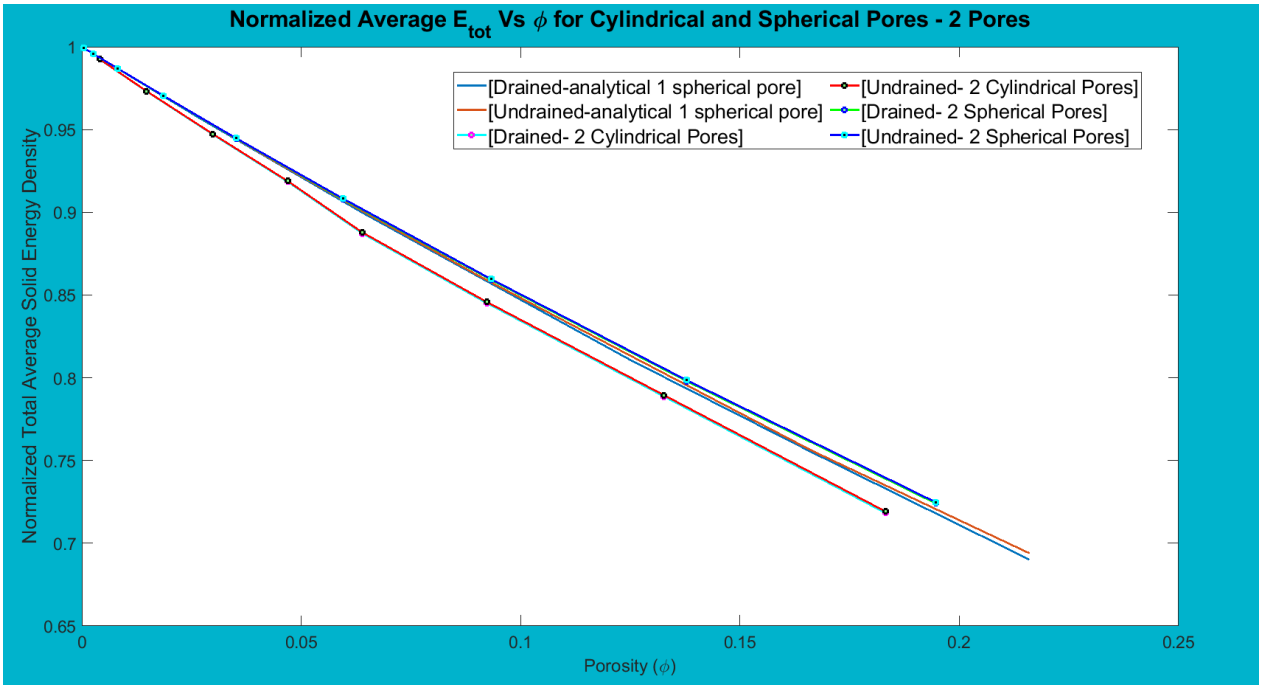

Figure 3.45: E_{tot_n} against ϕ - numerical solutions for models in Figure 3.39

In Figure 3.43, E_{c_n} is plotted against ϕ for the two sets of spheres and cylinders, representing the pore space in a spherical matrix. In Figure 3.44, E_{sh_n} is plotted, and in Figure 3.45, E_{tot_n} is plotted, both against ϕ as in the first figure. Contrary to initial predictions, these results seem to be quite similar to previous ones, indicating that there seems to be very little contribution from the shape of the pores to how the solid energy in the system is being stored. It should be however noted that this similarity is stronger, especially, for lower porosities. But as the pores get bigger, the influence from the pore geometry gradually increases.

3.4 Numerical Solutions for Models with Three Different Cylindrical Pore Sets

Until now, the geometry of the solid matrix of the results being considered were mostly spherical. Here, five different 3D models are considered. The fluid domains have the same cylindrical geometries for all five models, however, the geometries considered for the solid matrices are all different as shown in Figures 3.46 to 3.49, and their dimensions have been chosen arbitrarily. Figures 3.46 and 3.47 show cuboids having dimensions as shown and three

intersecting cylindrical pores, each having a height of 10 m with a radius that ranges from 1 m to 9 m in steps of 1 m. Figure 3.48 shows a cubic model having dimensions as shown and three intersecting cylindrical pores, each having a height of 10 m with a radius that ranges from 1 m to 8 m in steps of 1 m. Figure 3.49 shows a spherical model having a radius as shown and three intersecting cylindrical pores, each having a height of 10 m with a radius that ranges from 1 m to 10 m in steps of 1 m. Figure 3.49 shows a cylindrical model having dimensions as shown and three intersecting cylindrical pores, each having a height of 10 m with a radius that ranges from 1 m to 8 m in steps of 1 m. Figure 3.50 gives a closer look at the intersecting cylindrical pores.

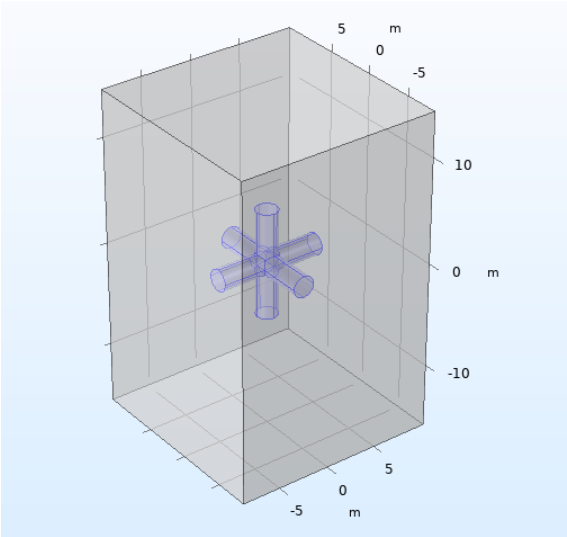

Figure 3.46: Cuboid with only two equal dimensions - 19 x 19 x 30 m

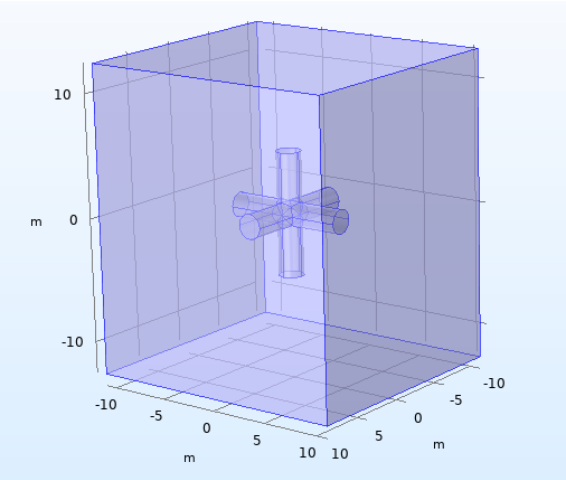

Figure 3.47: Cuboid with unequal dimensions - 20 x 22 x 25 m

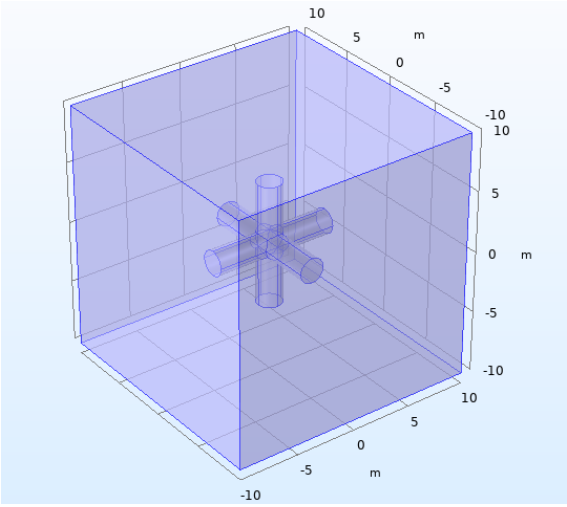

Figure 3.48: Cube - 20 x 20 x 20 m

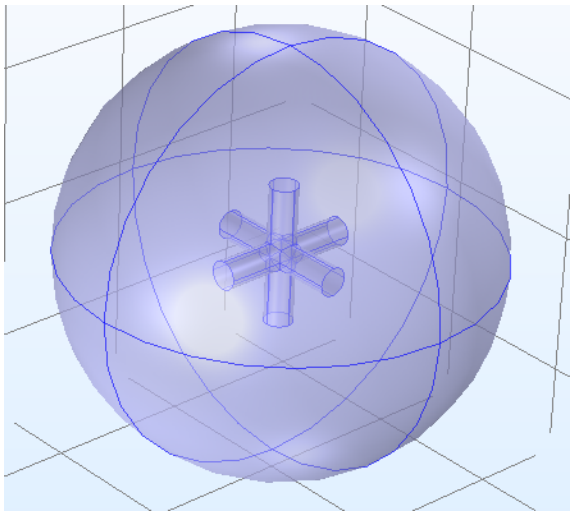

Figure 3.49: Sphere with radius = 15 m

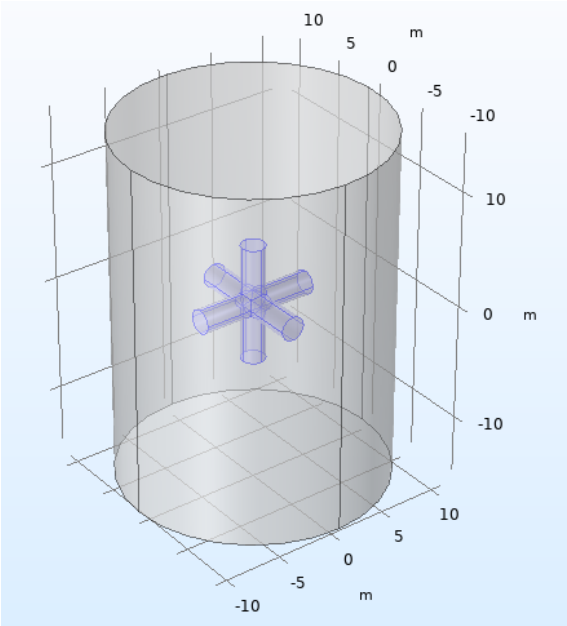

Figure 3.49: Cylinder with radius = 11 m, height = 30 m

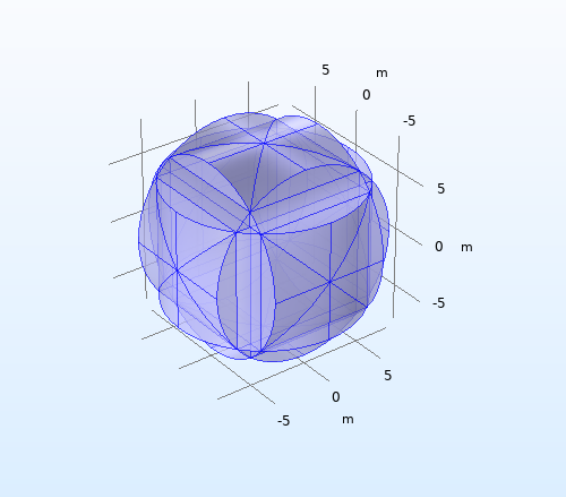

Figure 3.50: Three intersecting cylindrical pores with radius = 10 m, height = 10 m

Figure 3.51: Numerical models with 3 intersecting cylindrical pores and different geometries of solid matrix

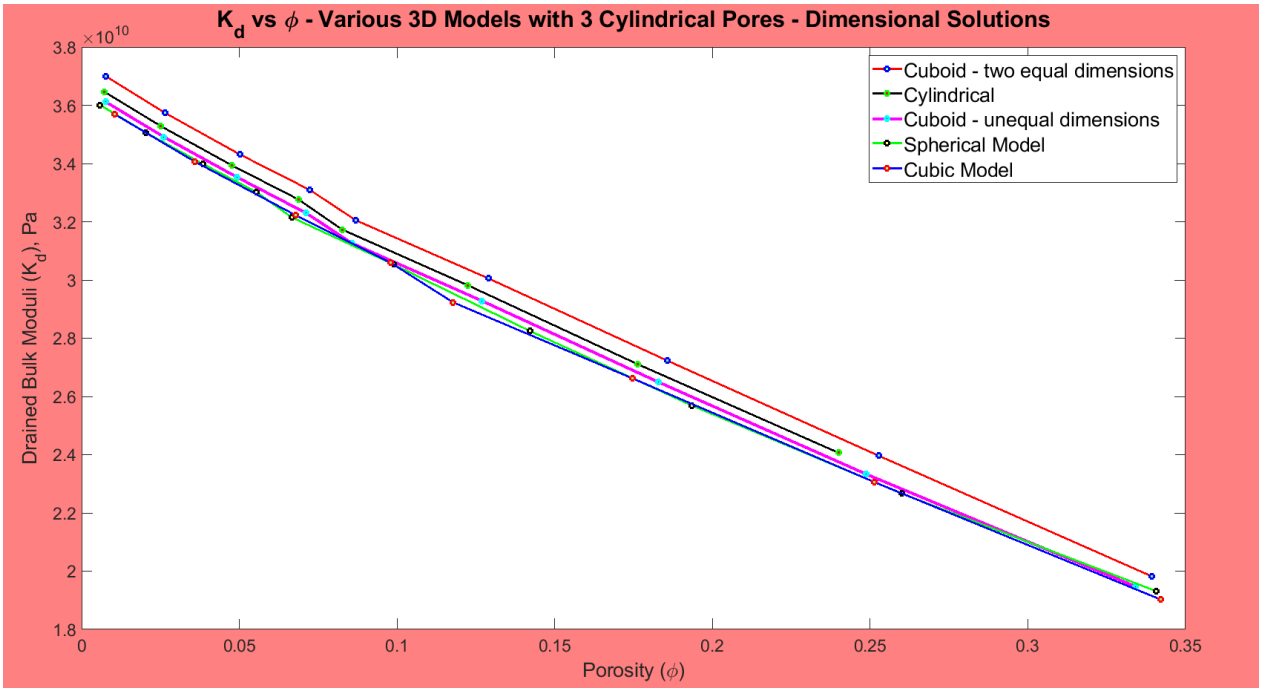

Figure 3.52: K_d vs ϕ

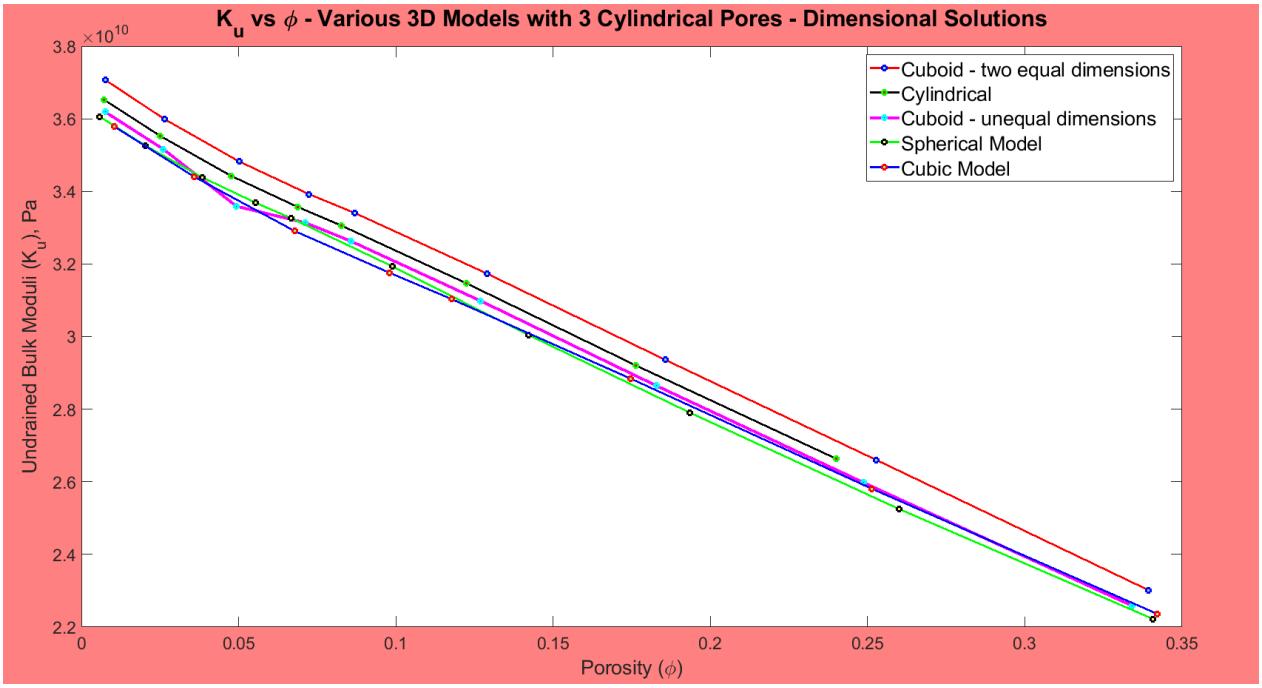

Figure 3.53: K_u vs ϕ

Figure 3.54: Numerical solutions for models in Figure 3.51

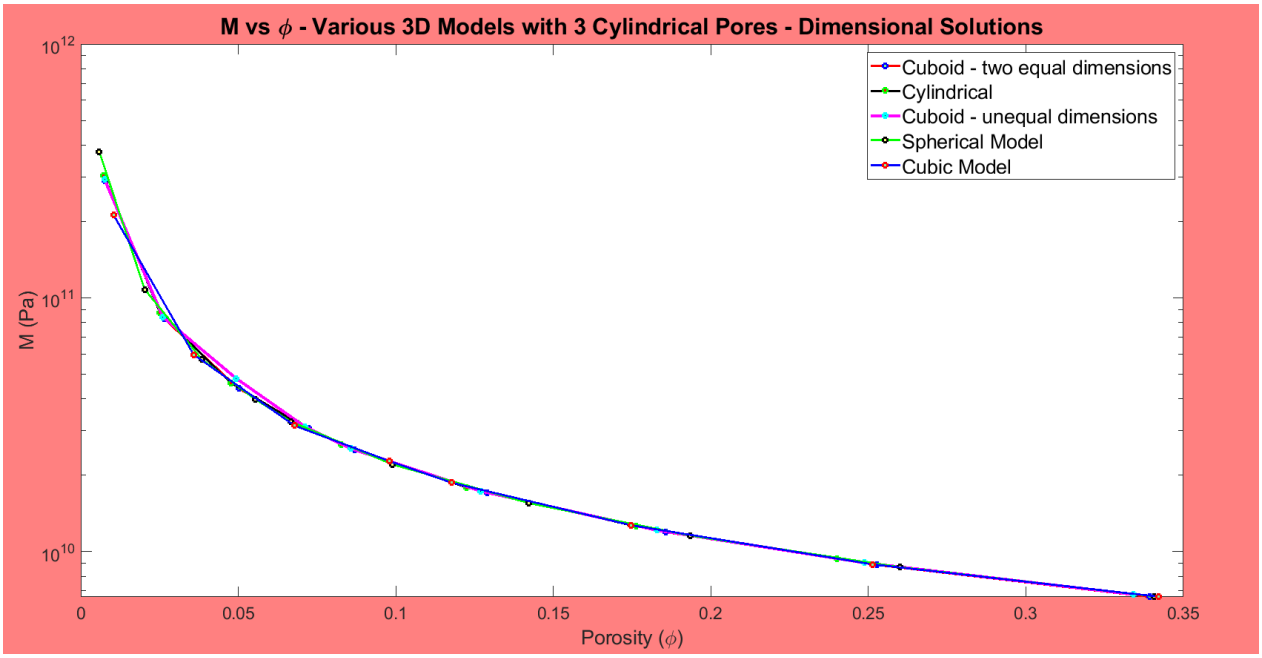

Figure 3.55: M vs ϕ - numerical solutions for models in Figure 3.51

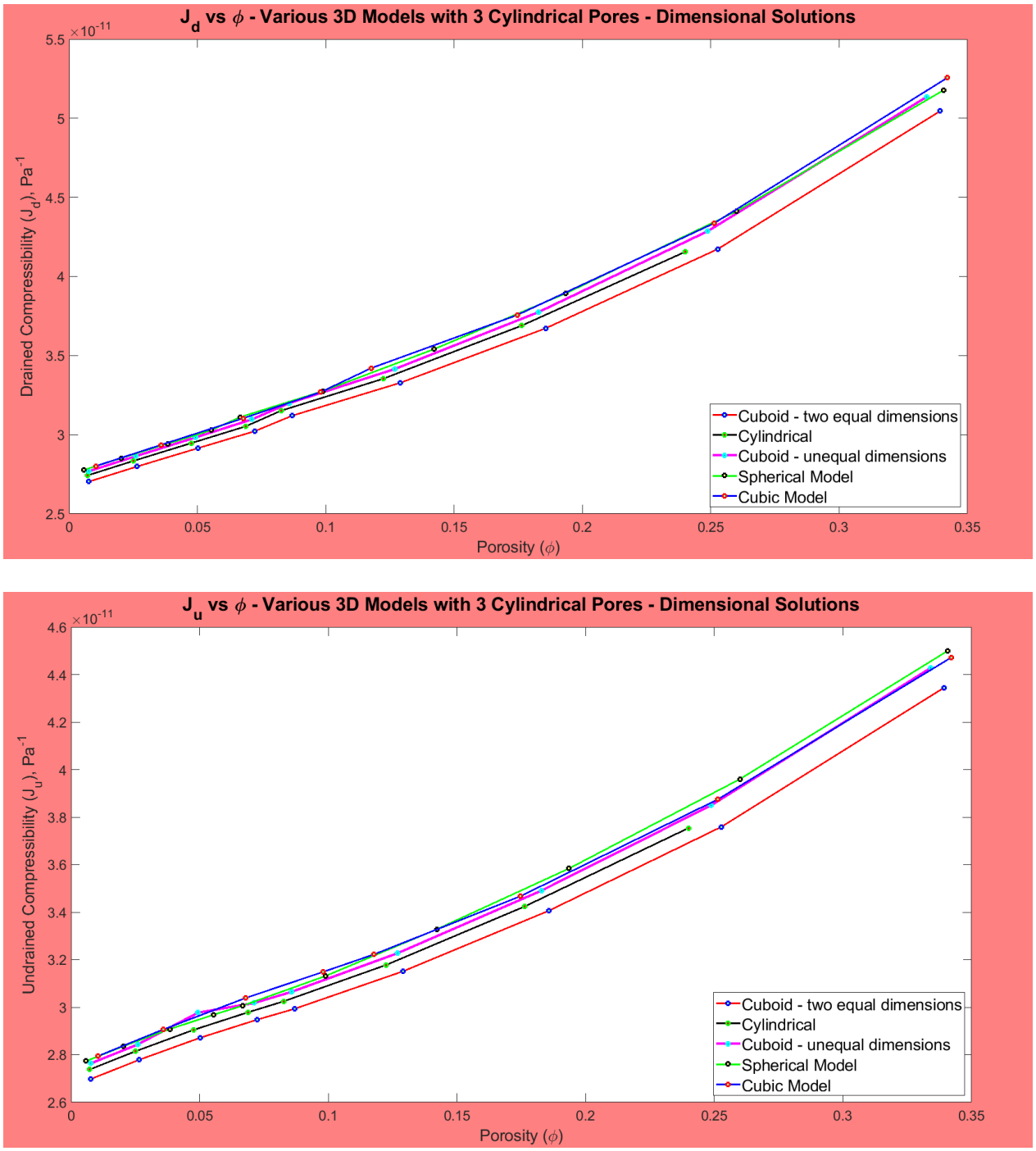

Figure 3.56: Various model plots showing comparison of 3-cylindrical pore sets for different solid geometries - J_d, J_u vs ϕ

The results in Figures 3.54 to 3.56 show some slight differences in the results for different geometries of the solid domain. The cuboid model with two equal dimensions (see Figure

3.46) is stiffer than the other models, followed by the cylindrical model. Also, the dimensions chosen for the cuboid with unequal dimensions are very similar to the cubic model (which is basically a cuboid with equal dimensions), hence, the results from them (as shown in Figures 3.54 to 3.56) are also very similar. Further, results from these latter models are very similar to the ones from the spherical model. From all the above, we can deduce that the models that are closer to having the same dimensions in all directions are closest to being spherical and having results that are most similar to those from the spherical models.

4 RESULTS/DISCUSSION Part 2 – Complex Models

In this chapter, results from models with single spherical pore are compared to those of realistic microstructures from X-ray tomography. The microscopic parameters used in each case correspond to those in Table 2.1. The dimensions of the models are included in their figures while the scale of the image of the pores is 30 x 30 x 30 m for each pore. To implement multiple porosities for the carbonate and sandstone tomography, I simple used each sample's unique porosity. Therefore, in showing the results as a function of porosity, I show three data points for the carbonate samples and two data points for the sandstone samples.

4.1 Simple 3D Case vs Carbonate Models

The spherical model with one spherical pore has a radius of 1 m and the pore radius ranges from 0.4 m to 0.02 m in steps of 0.6 m.

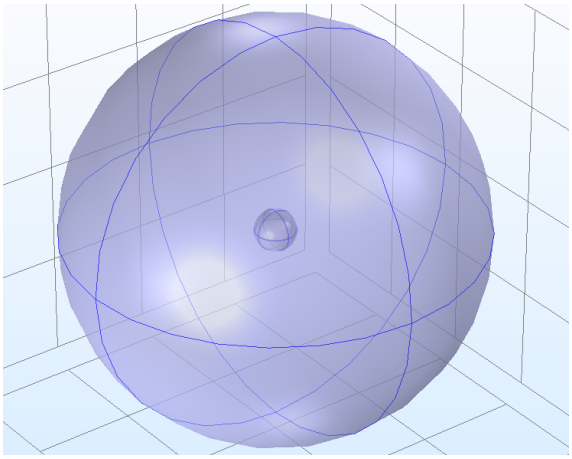

Figure 4.1: Spherical model with a radius of 1 m

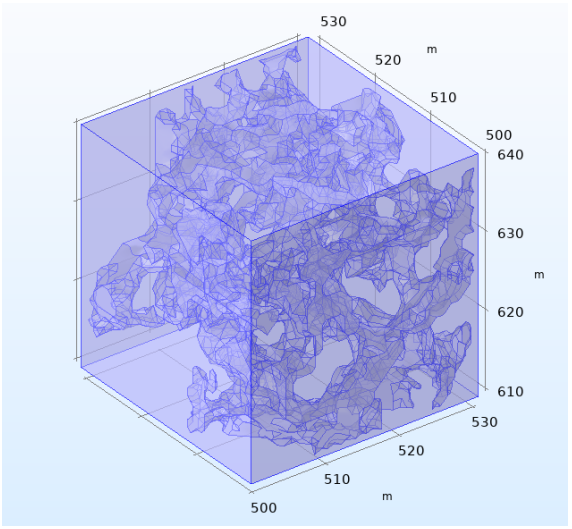

Figure 4.2: Carbonate model 1 with dimensions 30.8 x 30.8 x 30.8 m

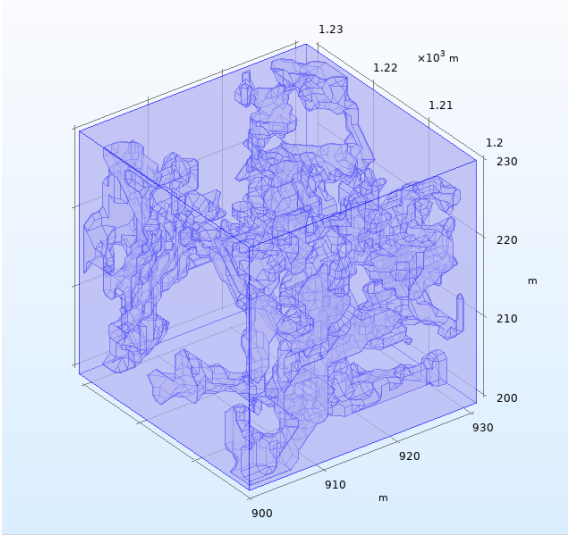

Figure 4.3: Carbonate model 2 with dimensions 30.8 x 30.8 x 30.8 m

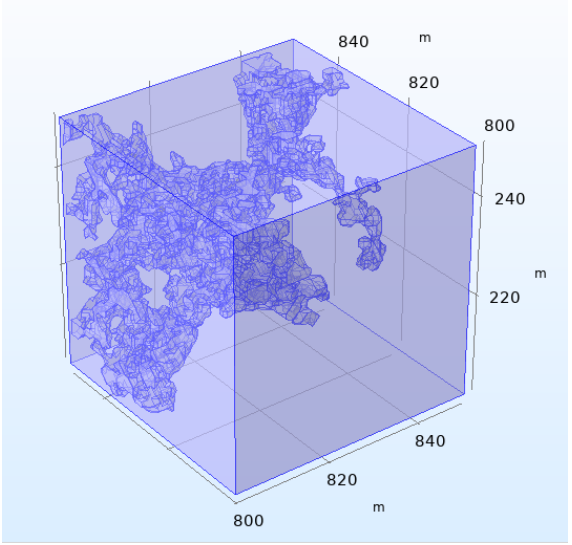

Figure 4.4: Carbonate model 3 with dimensions 50.8 x 50.8 x 50.8 m

Figures 4.5 to 4.8 show the plots of K_d, J_d, K_u, J_u, M, and α against ϕ, for the cases of the carbonate model and one of the simple 3D geometries already discussed in the previous chapter, consisting of a spherical pore and spherical bulk (see Figures 4.1 to 4.4). The plots in Figure 4.5 reveal that the carbonate model is generally softer than the spherical model. This is certainly because the pores in the carbonate models are well interconnected, and there are very small spaces among them. This is also probably why the difference between K_d and

K_u is greater in the carbonate model than in the spherical model. Here again, as in previous considerations, K_d and K_u decrease with increasing porosity in both set-ups, meaning that the rock generally becomes more compressible as the pore space gets larger (see Figure 4.6). Further, in Figure 4.7, M is plotted against ϕ and is very similar in both models. And, even for the complex porosity of the Carbonate, M varies with porosity in a very similar way to those of the simple spherical models. Then in Figure 4.8, α is plotted against ϕ and shows a continuous increase with porosity.

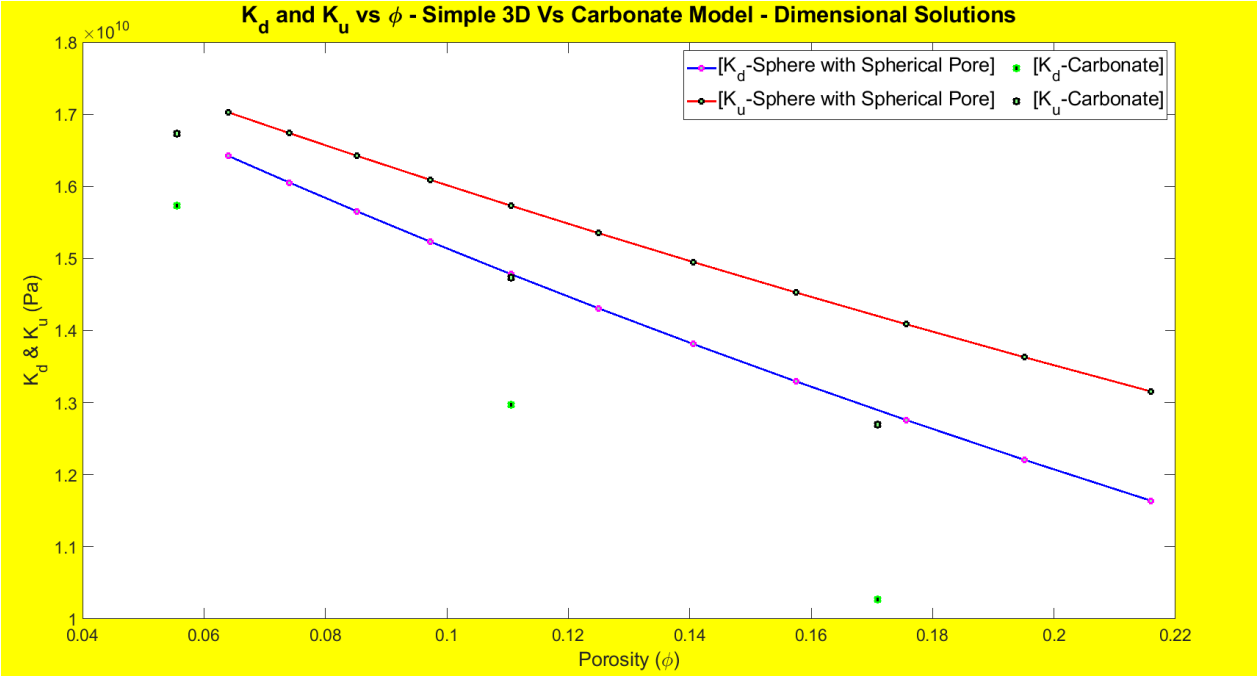

Figure 4.5: K_d & K_u against ϕ

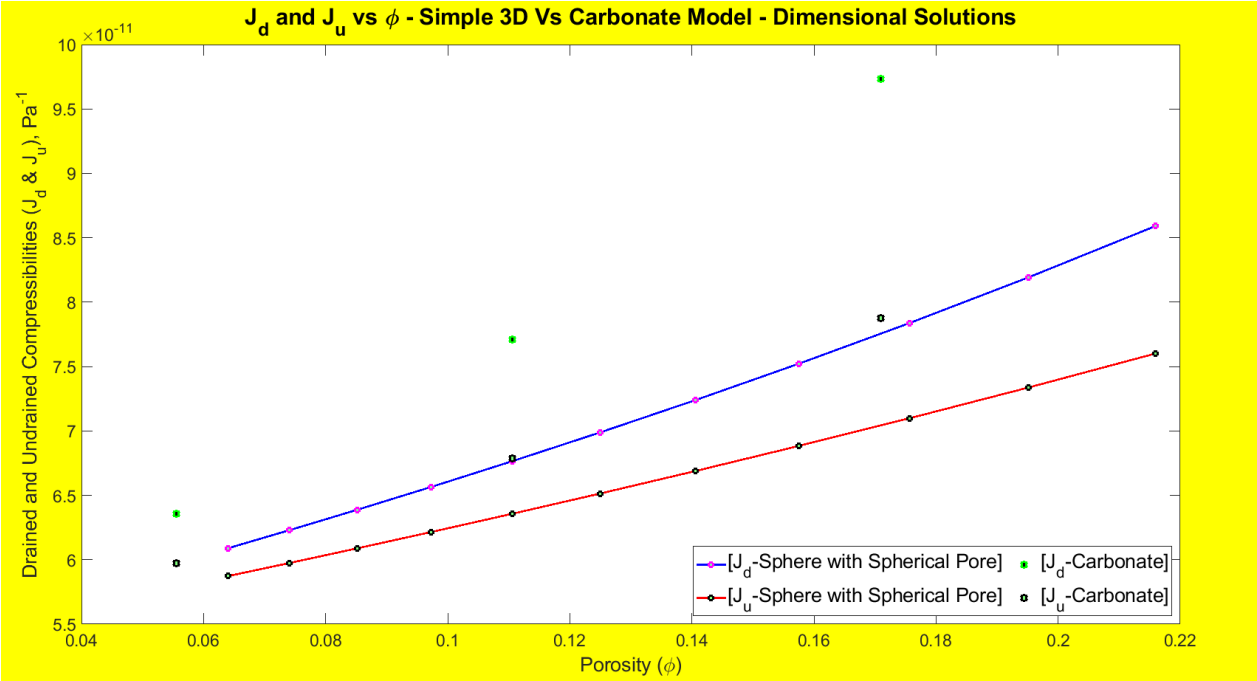

Figure 4.6: J_d & J_u against ϕ

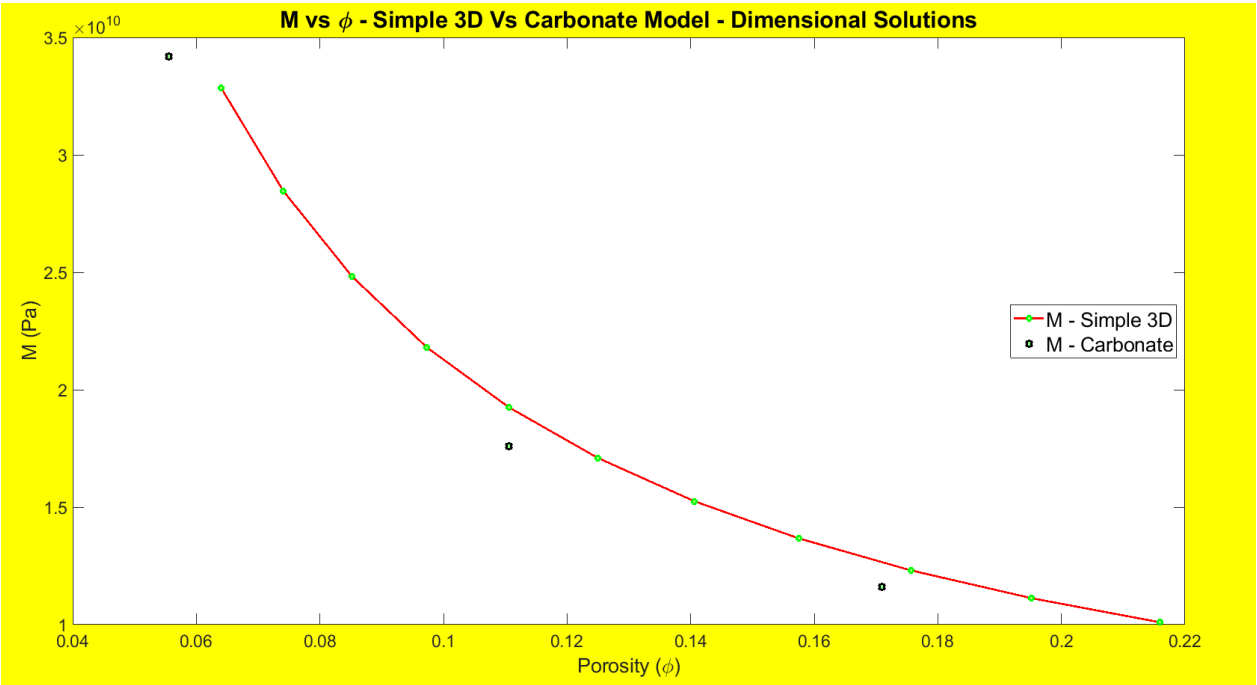

Figure 4.7: M against ϕ

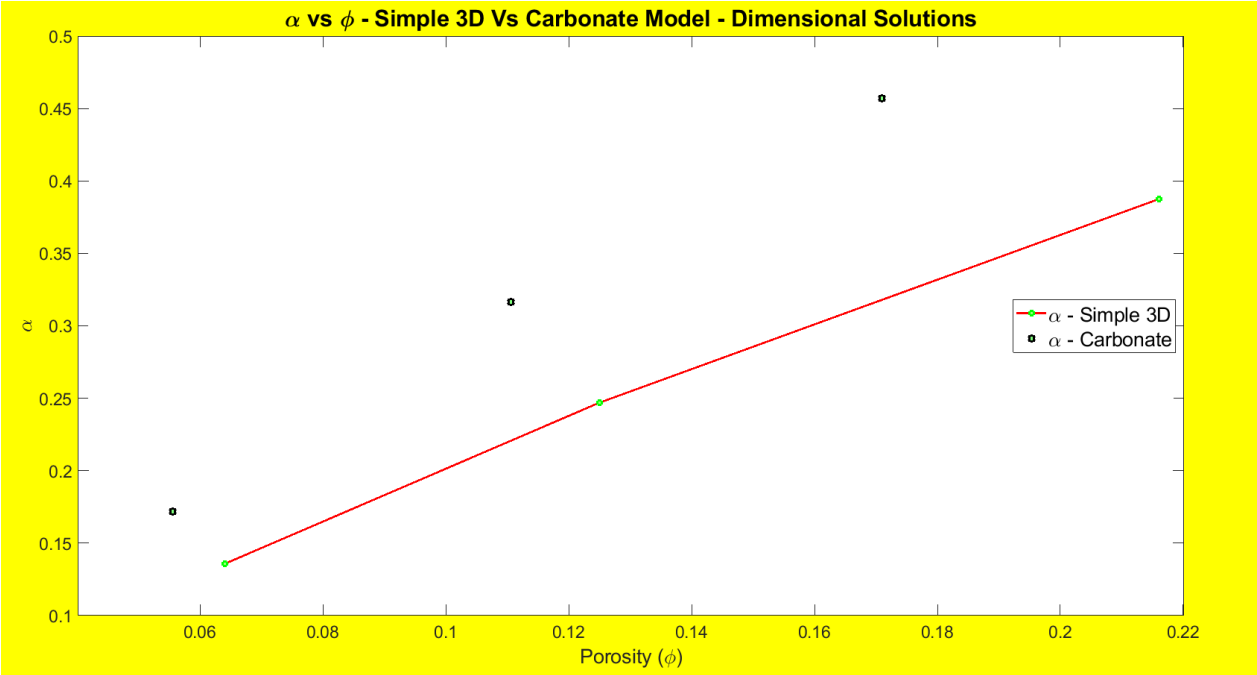

Figure 4.8: α against ϕ

4.1.1 Energy Considerations for 3D vs Carbonate Models

In this subsection, the energy for the simple 3D and complex carbonate models are plotted. Figures 4.9 to 4.12 show the energy signatures (visual representations of the energy) in the models. These show the energy changes or concentration in the rocks. From the simple 3D figures (4.9 and 4.10), it can be observed that the compression energy is mostly constant in the solid and fluid regions with different values in both regions, while the shear energy increases significantly closer to the solid-fluid interface. However, in the complex model figures (4.11 and 4.12), the energy changes are not so visible around the pore walls, most probably because of the complexity of the pore space.

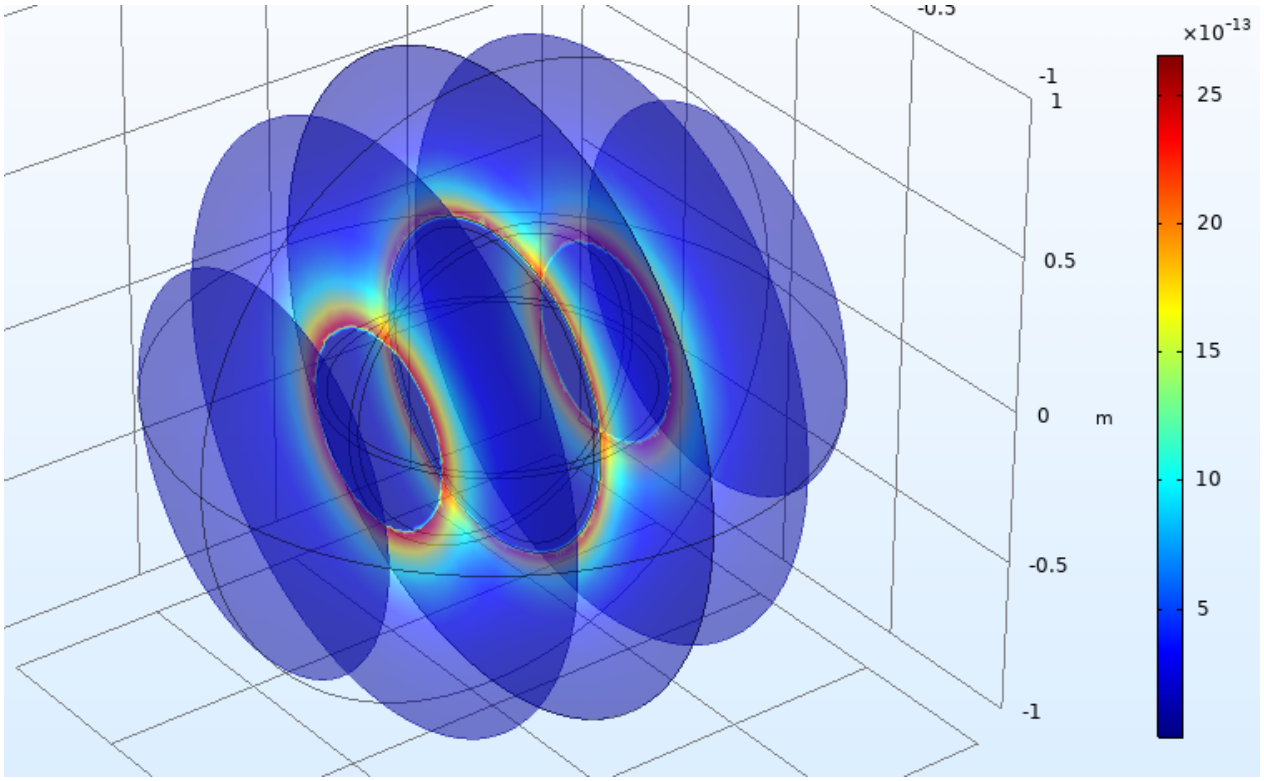

Figure 4.9: Shear Energy

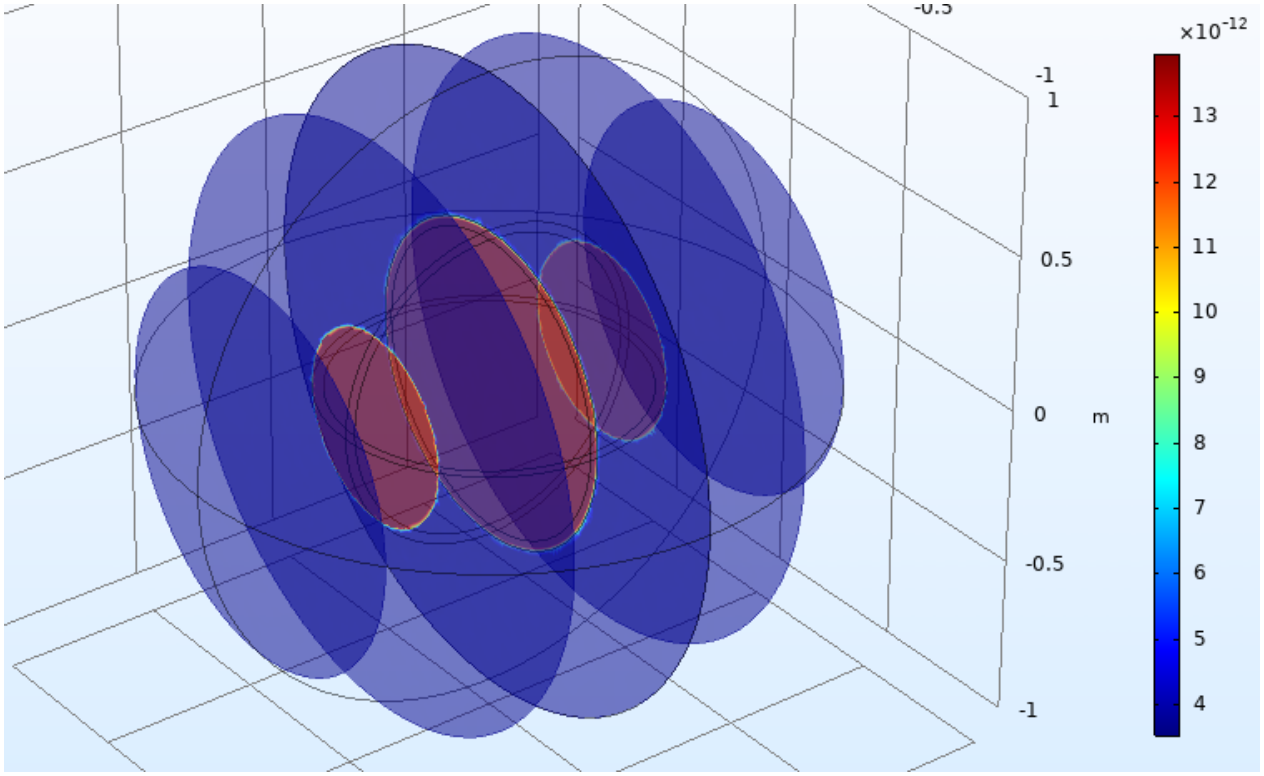

Figure 4.10: Compression Energy

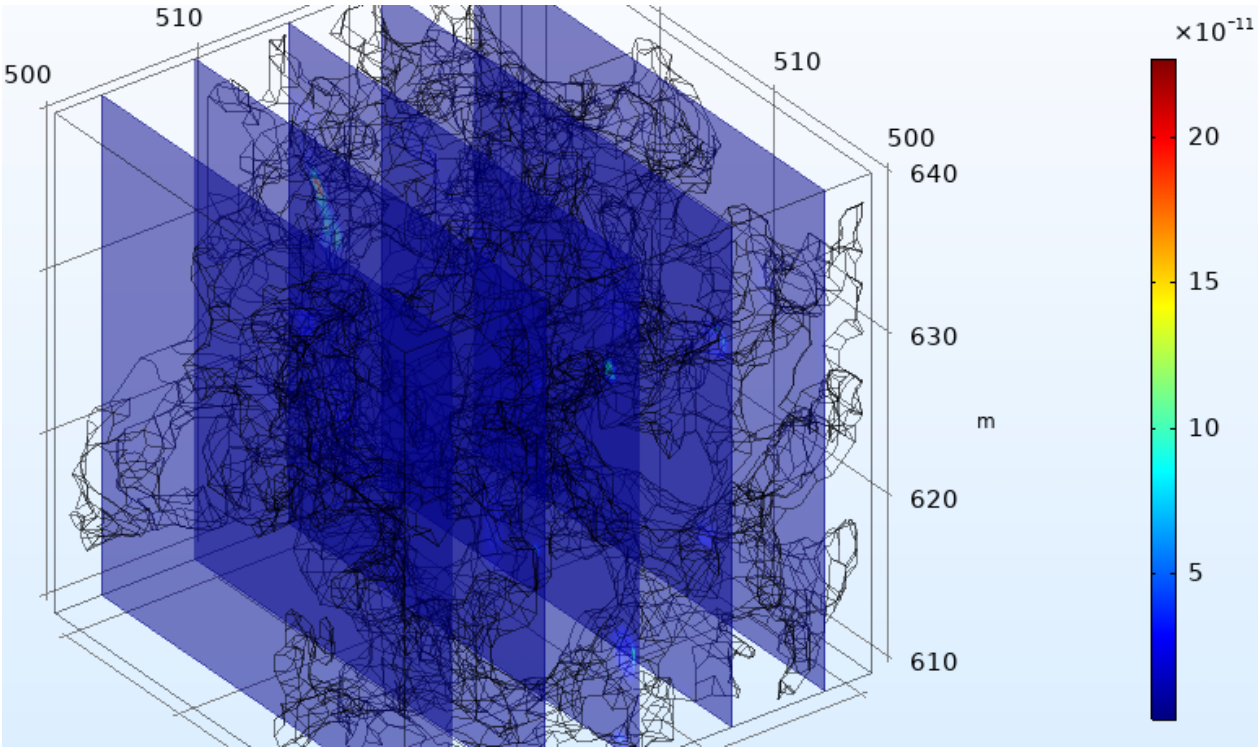

Figure 4.11: Shear Energy

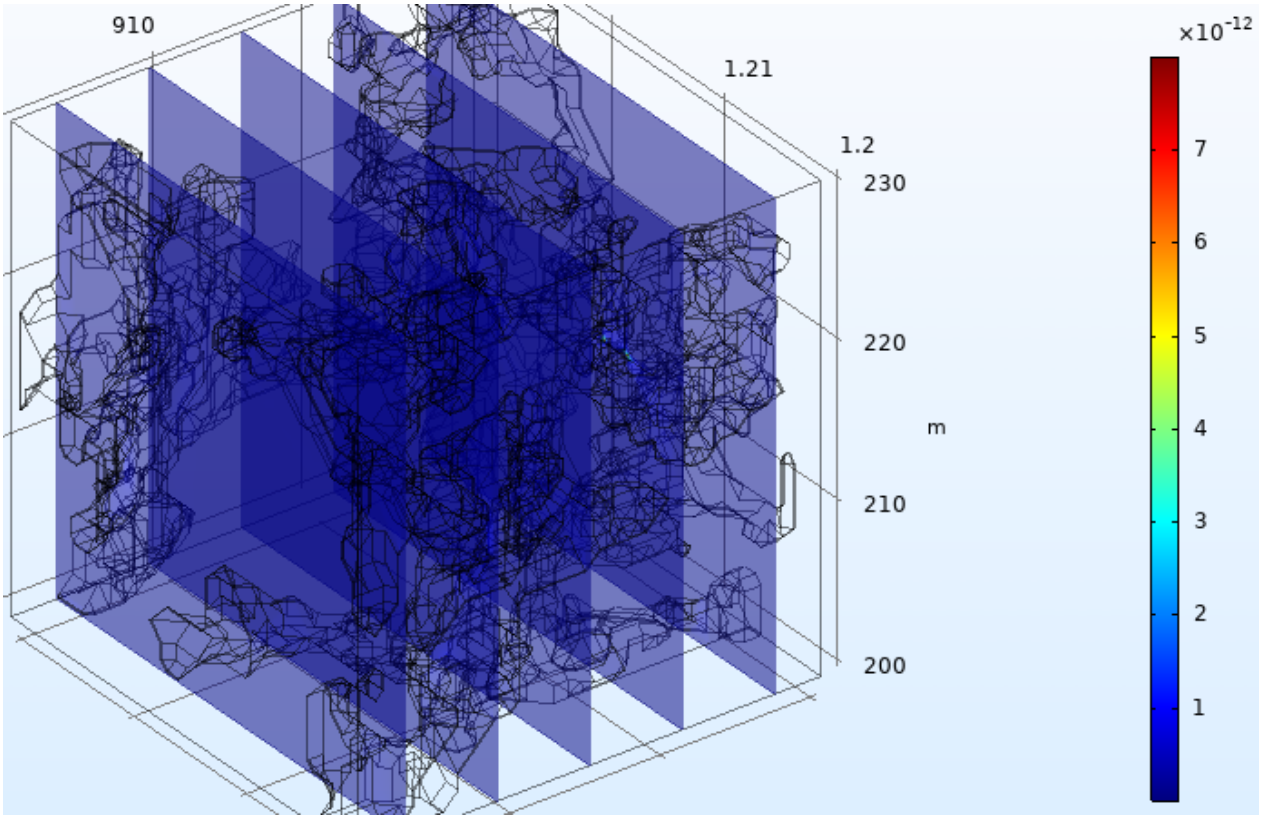

Figure 4.12: Compression Energy

Figures 4.13 to 4.15 show the normalized average energy plots against porosity for both models, including the drained and undrained cases. In Figure 4.15, E_{c_n} is shown as a function of ϕ, and shows that the carbonate models store a lot less energy than the simple models as the porosity increases. This is likely because the pore space in the carbonate models is made up of interconnected pores. To attempt to verify this, I have compared (in Figures 4.16 and 4.17) the energy plots from the interconnecting cylindrical pores with those from the models with non-intersecting spherical pores. A close inspection of these figures reveal that the models with intersecting pores store less energy than the single spherical model. However, the difference is not as distinct as in the case of the comparison between the carbonate and the single spherical pore models. This is because the intersecting cylindrical pore models do not capture the complexity of the carbonate model pore space. This would be worth exploring further in a future work.

Further, Figure 4.14 shows the plot of E_{sh_n} against ϕ. This shows the same trend as already discussed in the previous chapter where the normalized average shear energy is expected to increase with porosity only to a certain point before beginning to decrease (see subsection 3.1.6). Also, we see from equation 2.40 that the shear energy decreases slower than the compression energy by $\frac{1}{r^6}$. Further, it is interesting that the carbonate model stores more shear energy in the drained case than what is stored in the simple 3D. This shows that the deformation around the pores is greater in the carbonate model only when the pores have no fluid in them. However, the deformation is similar for both models when there is fluid present in the pores, especially at lower porosity. Finally, the normalized total solid energy (E_{tot_n}) is plotted against porosity (see Figure 4.15). This also shows similar results between the drained and the undrained cases as a result of the combination of the normalized average compression and shear energies.

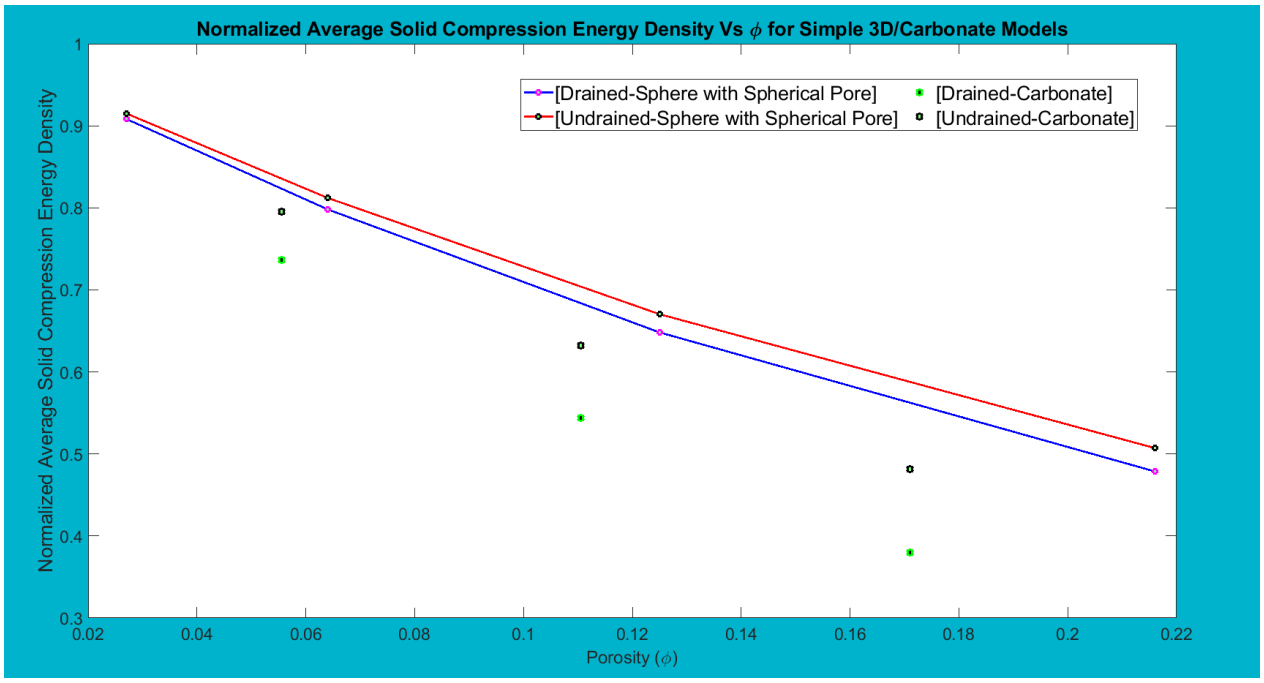

Figure 4.13: E_{c_n} against ϕ

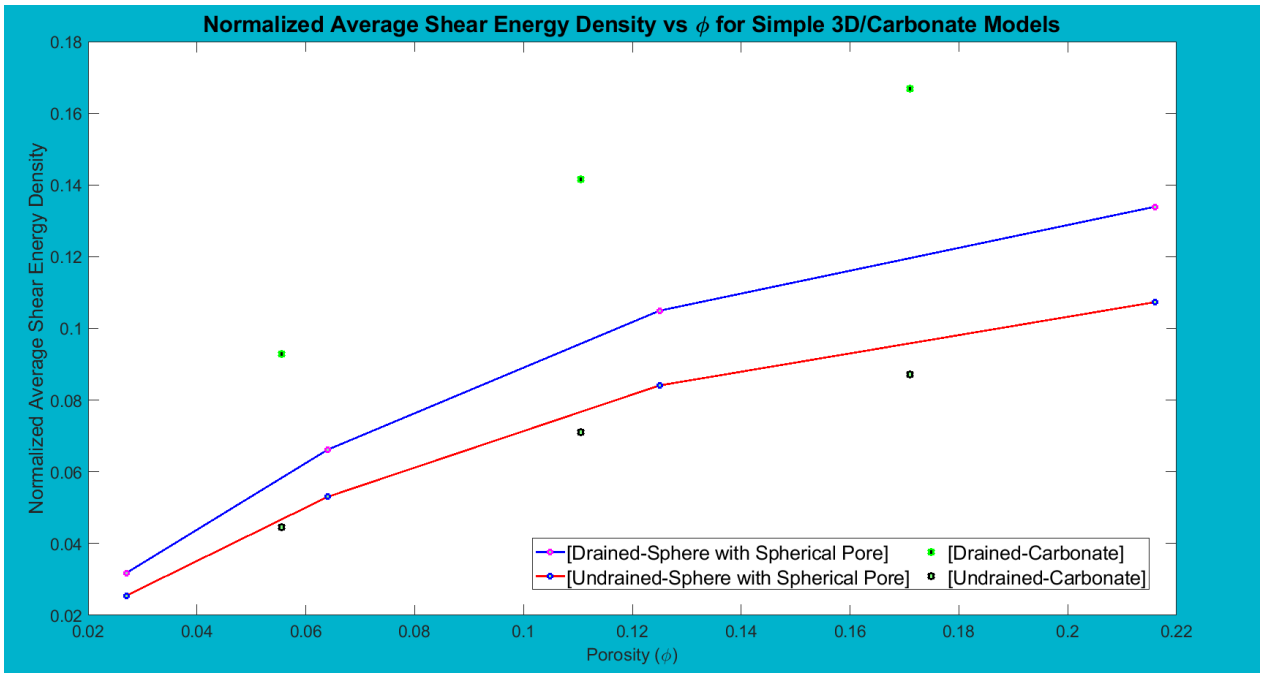

Figure 4.14: E_{sh_n} against ϕ

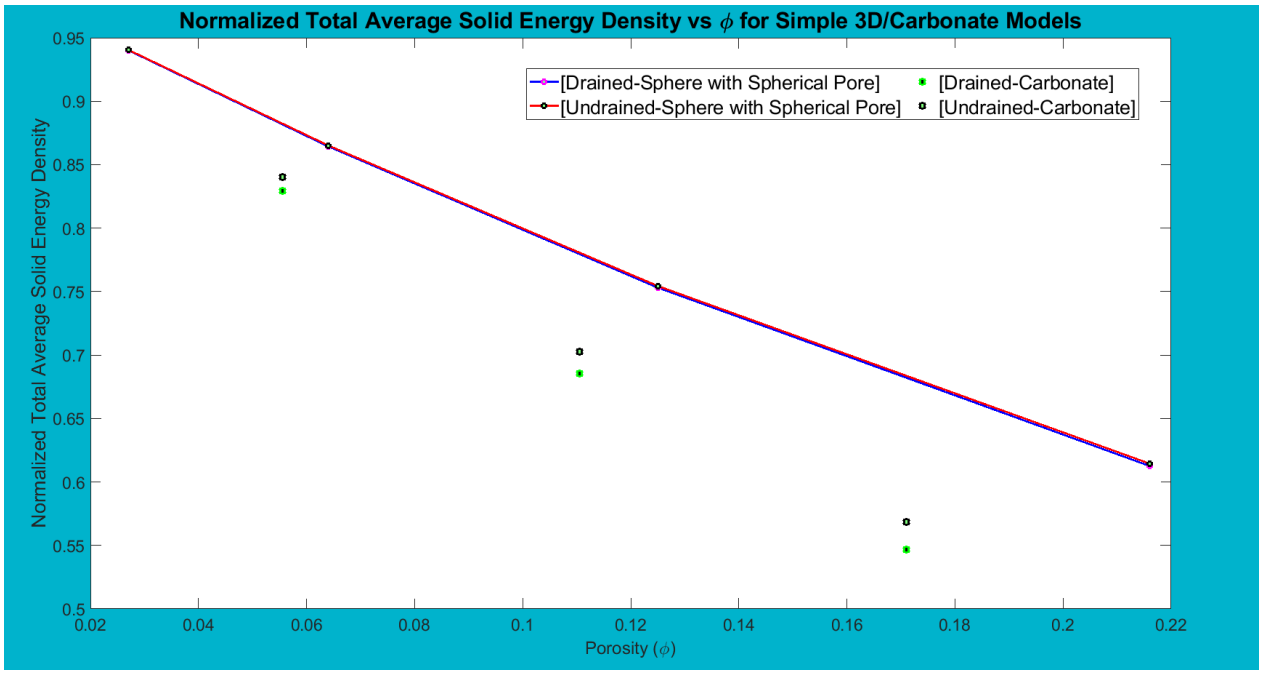

Figure 4.15: $\overline{E_{tot_n}}$ against ϕ

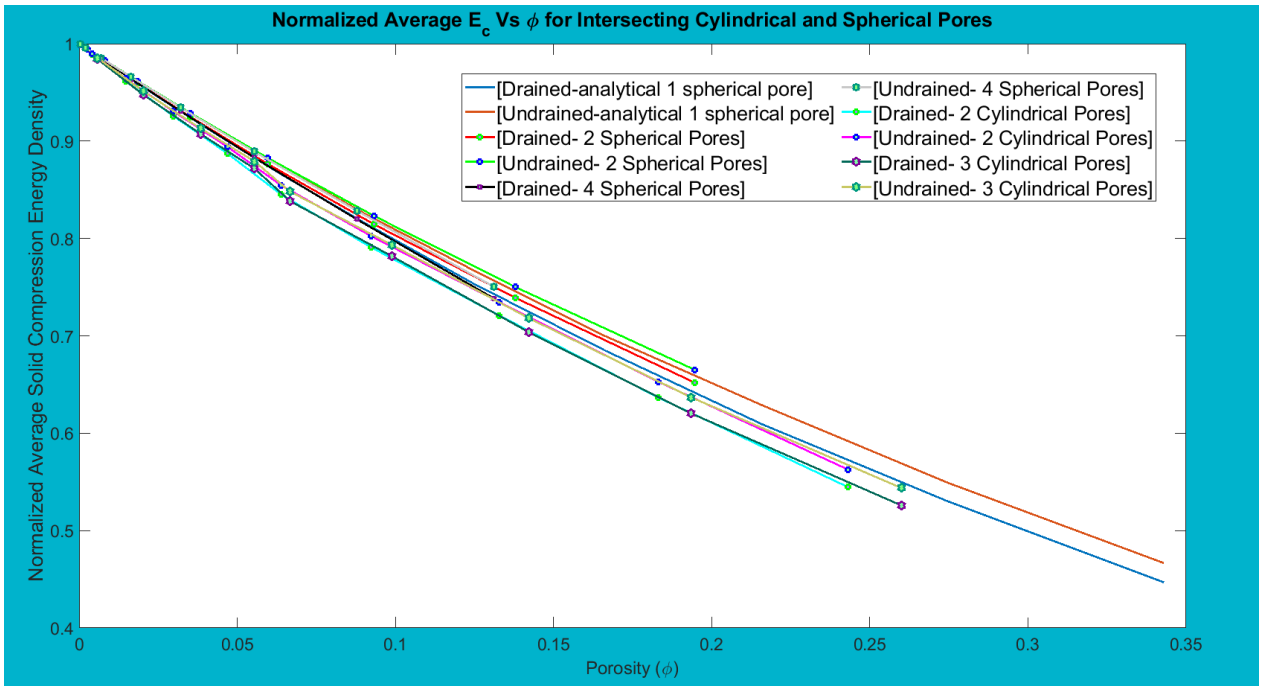

Figure 4.16: E_{c_n} against ϕ

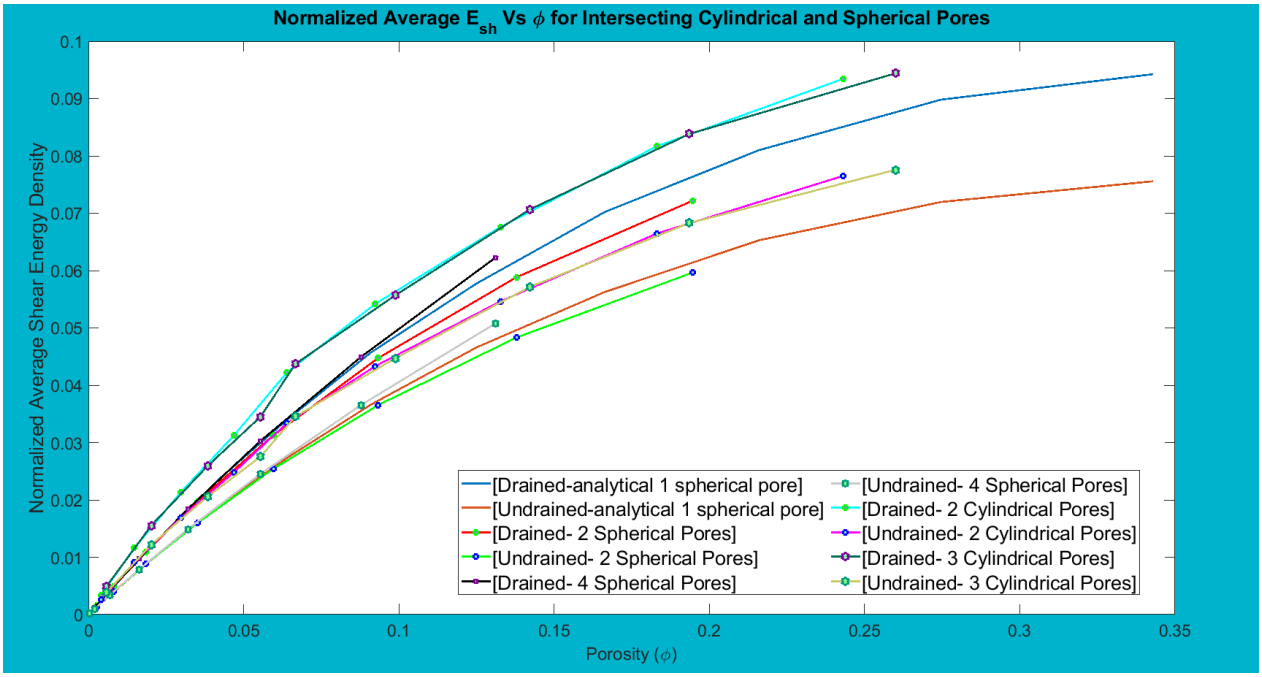

Figure 4.17: E_{sh_n} against ϕ

4.2 Simple 3D Case vs Sandstone Models

The spherical model with one spherical pore has a radius of 1 m and the pore radius ranges from 0.6 m to 0.02 m in steps of 0.9 m.

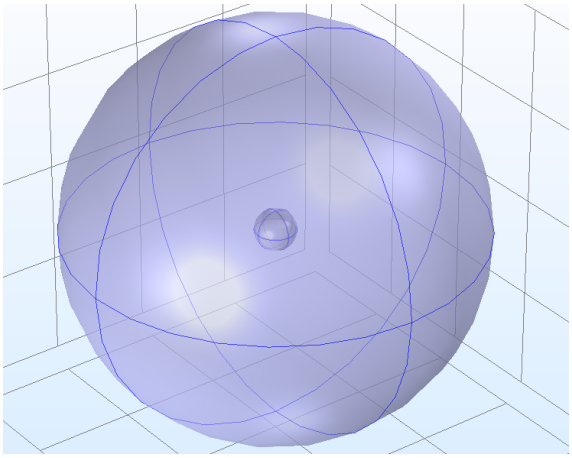

Figure 4.18: Spherical model with a radius of
m

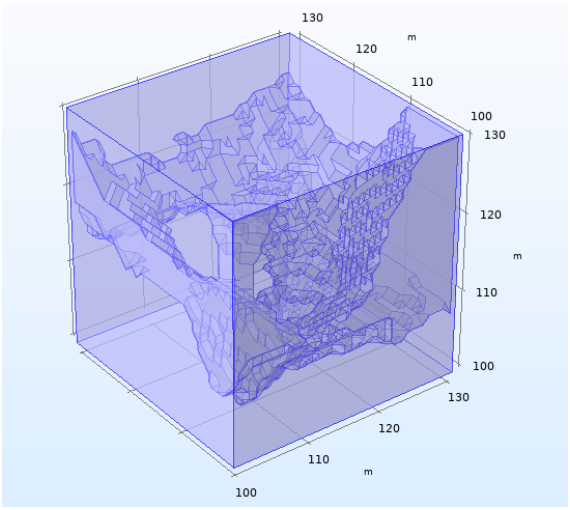

Figure 4.19: Sandstone model 1 with dimensions 30.8 x 30.8 x 30.8 m

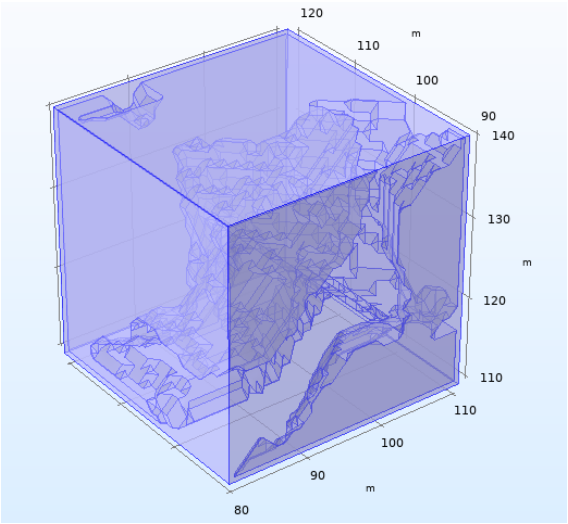

Figure 4.20: Sandstone model 2 with dimensions 30.8 x 30.8 x 30.8 m

Figure 4.21: Simple 3D and Sandstone models considered

Figures 4.22 to 4.25 show the results of K_d, K_u, M, and α plotted against ϕ for the the simple 3D and sandstone models. Again, just like in the comparisons between the spherical pore models and the carbonate models, figures 4.22 and 4.23 show that the sandstone models are softer than the spherical pore ones. This further reinforces the finding that porosity, along with the geometry of the pore space, are all important factors that affect the compressibility

of a porous rock. Further, figure 4.24 shows that the pressure, M, is only influenced by porosity but not the geometry of the pore space. Then, lastly, figure 4.25, just like in the carbonate models (figure 4.8), shows that α is higher in complex pore geometries (carbonate and sandstone models) than in simple ones (spherical pore models).

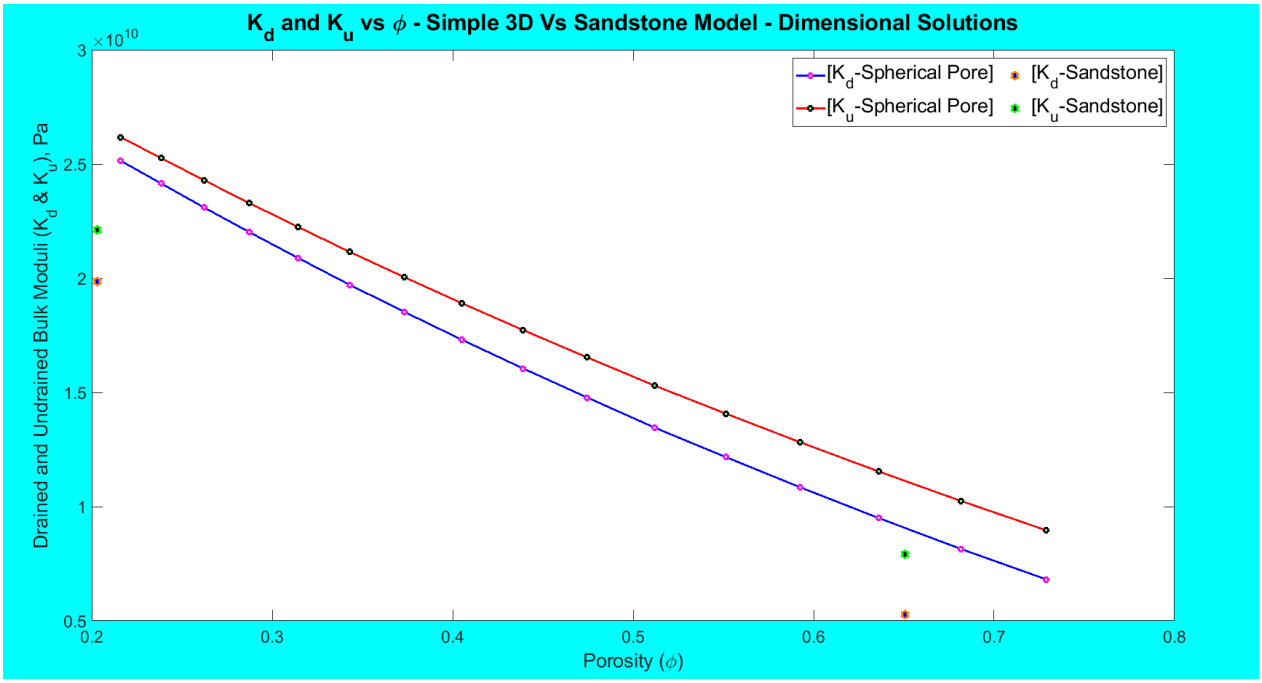

Figure 4.22: K_d & K_u against ϕ

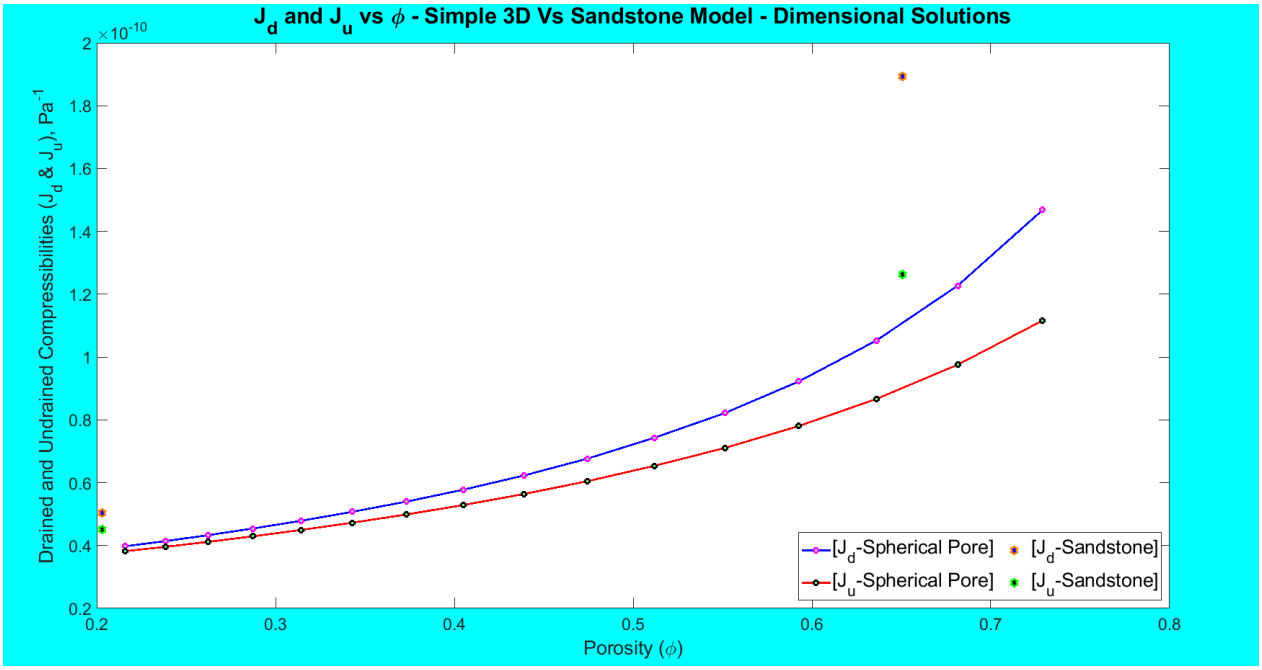

Figure 4.23: J_d & J_u against ϕ

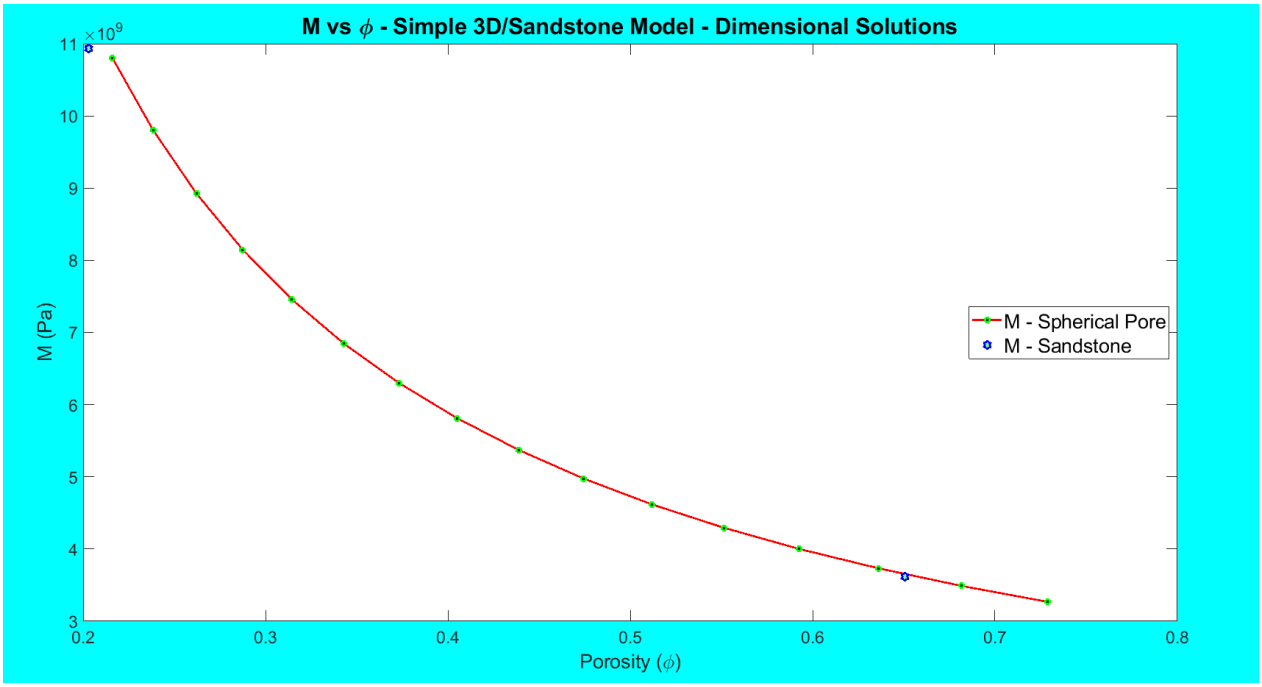

Figure 4.24: M against ϕ

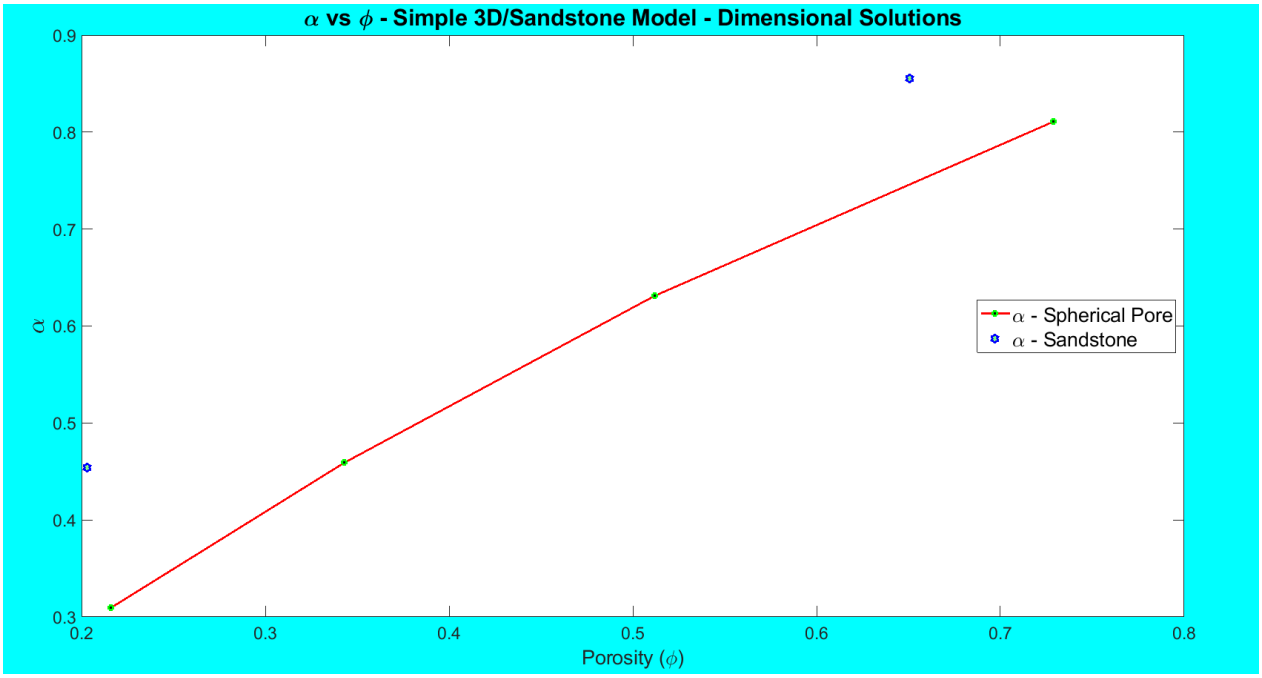

Figure 4.25: α against ϕ

4.2.1 Energy Considerations for 3D vs Sandstone Models

Figures 4.26 to 4.27 show the energy plots for the sandstone models in COMSOL Multiphysics®. Again, the energies (compression and shear) show some faintly visible spots around the pore walls.

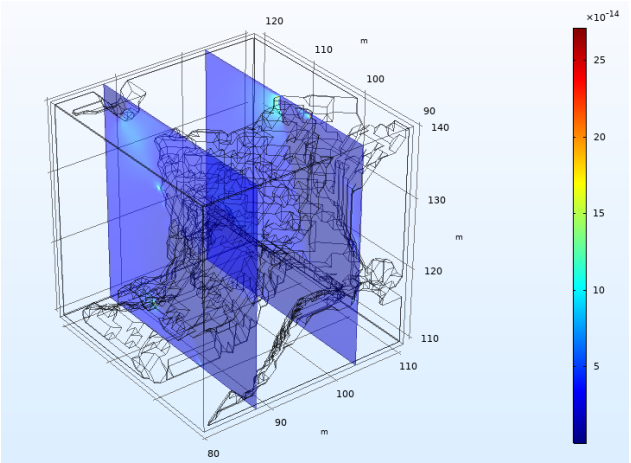

Figure 4.26: Compression Energy

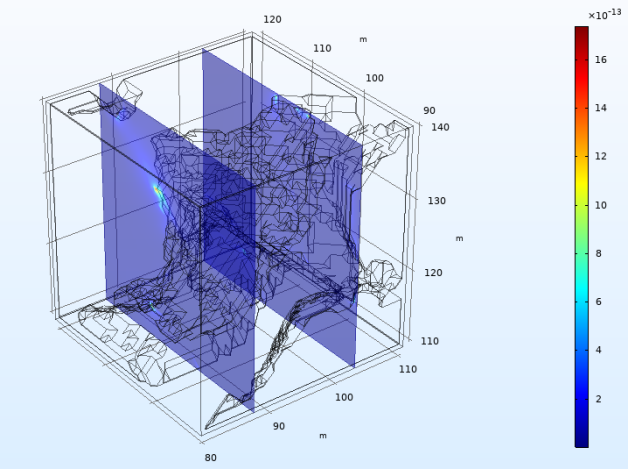

Figure 4.27: Shear Energy

In Figures 4.28 to 4.30, the normalized compression, shear, and total energy densities are plotted against porosity for the simple 3D and sandstone models. In this subsection, as in the previous one, the values from the simple models vary significantly from the sandstone models. And since this is not the case in simple models with different geometries of pore space and rock matrix, the difference here must be as a result of extremely complex pore space.

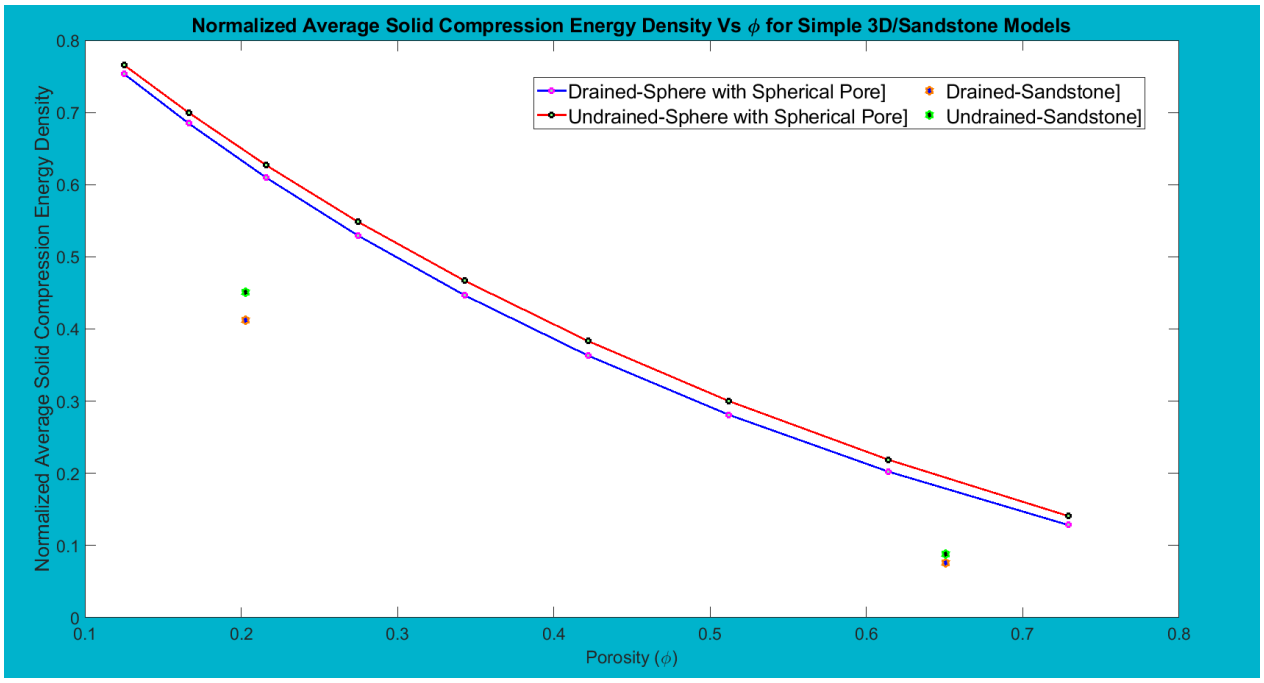

Figure 4.28: E_c against ϕ

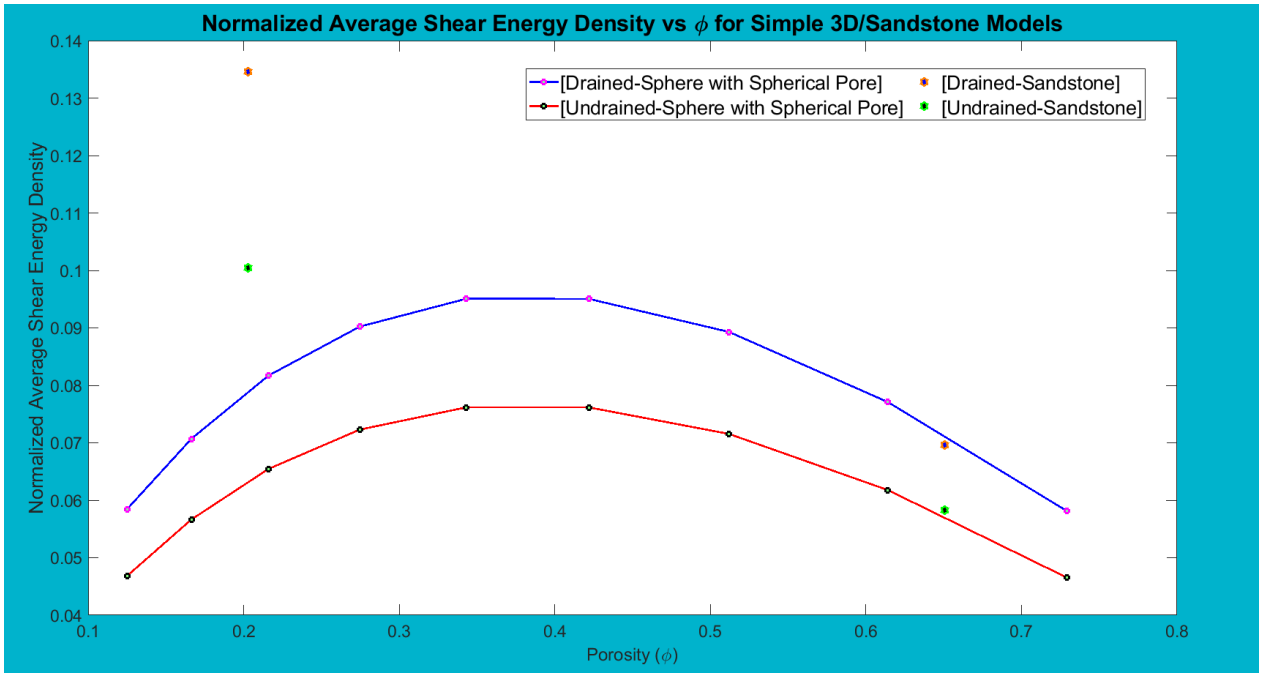

Figure 4.29: E_{sh} against ϕ

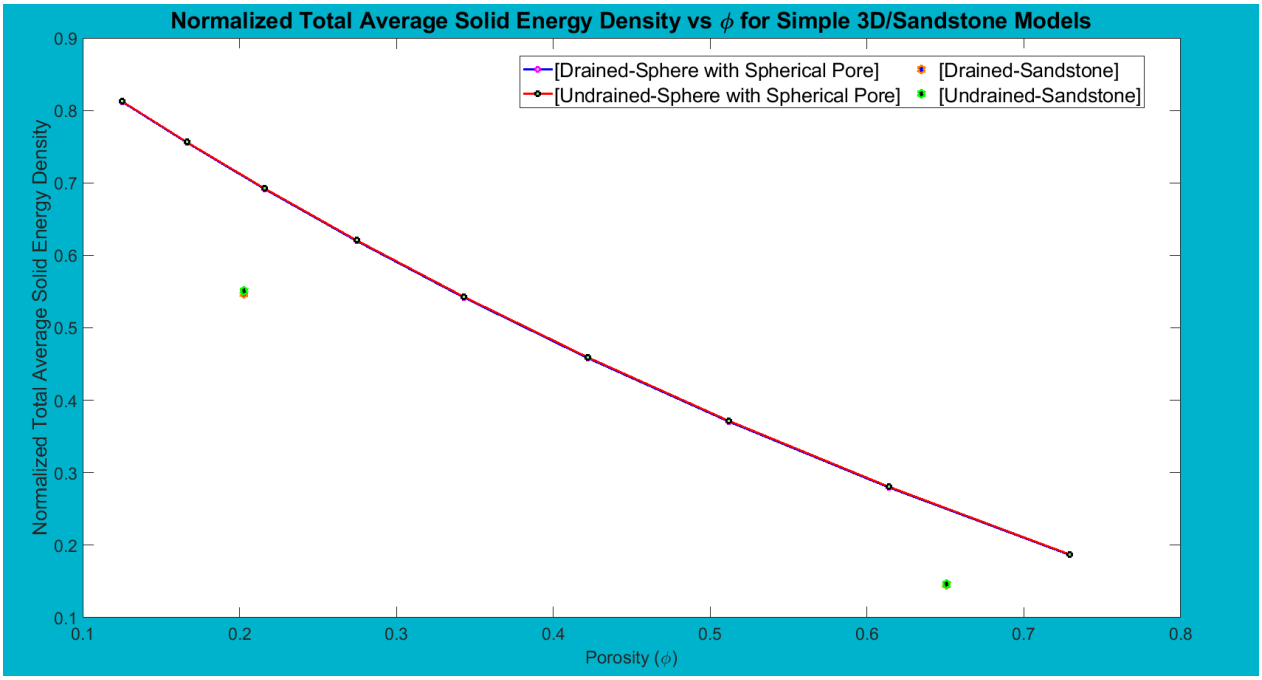

Figure 4.30: $\overline{E_{tot}}$ against ϕ

4.3 Simple vs Carbonate vs Sandstone Models

In this section, the results from both the simple 3D (spherical) and complex (carbonate and sandstone) models above are plotted altogether against porosity.

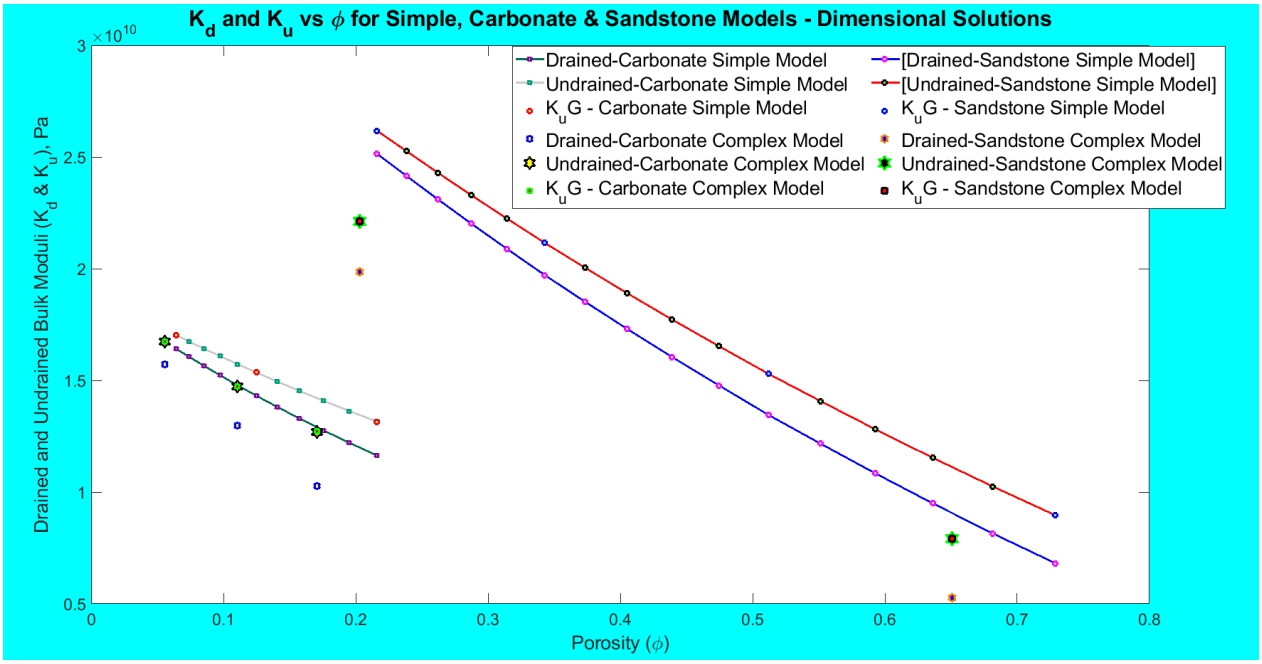

Figure 4.31: K_d & K_u against ϕ

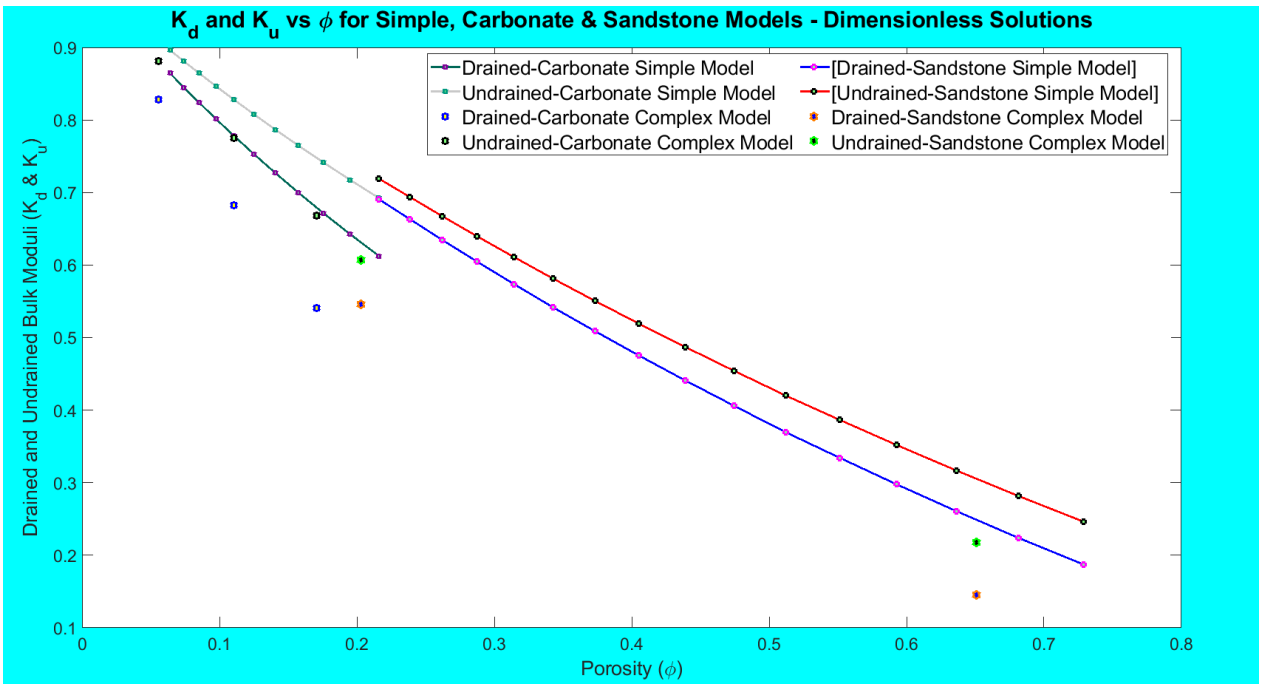

Figure 4.32: K_d & K_u against ϕ

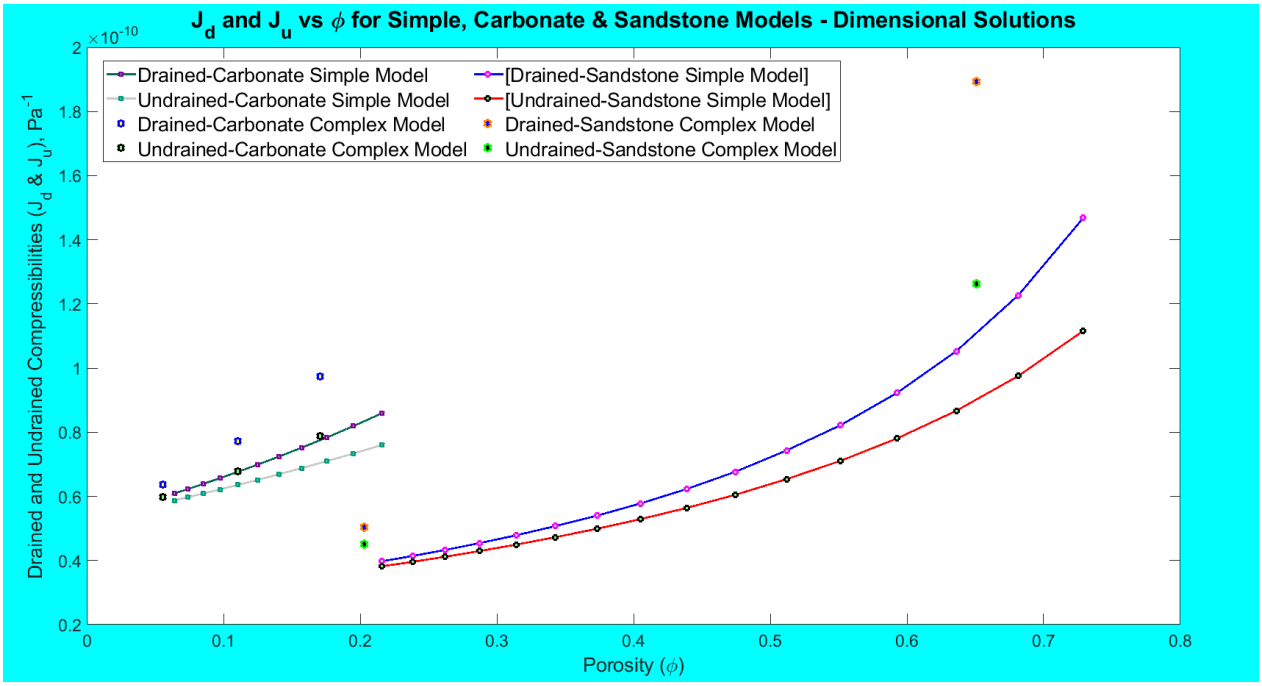

Figure 4.33: K_d & K_u against ϕ

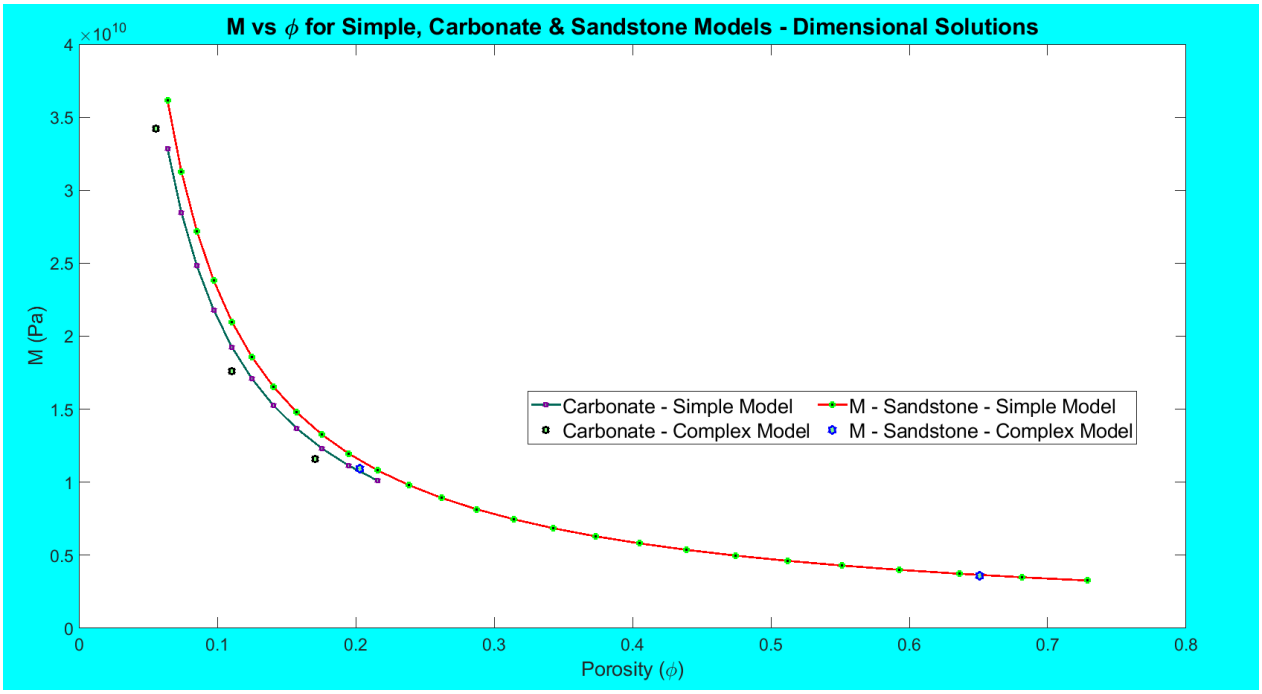

Figure 4.34: M against ϕ

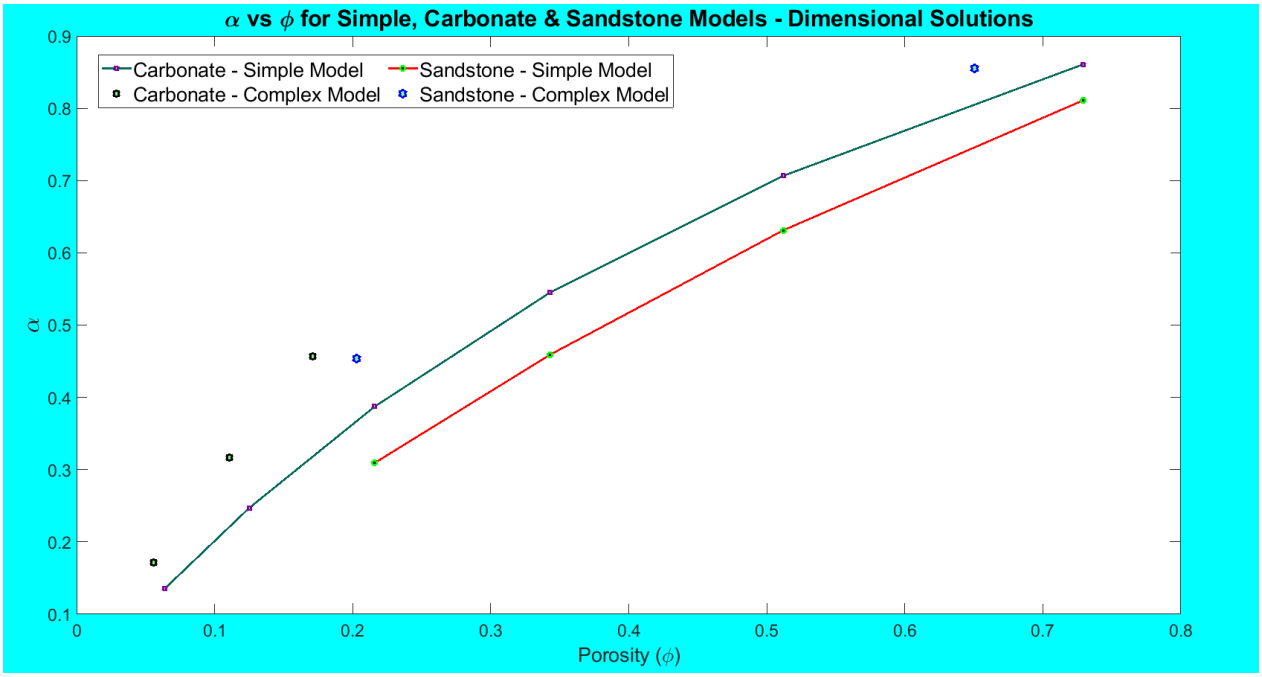

Figure 4.35: α against ϕ

Figures 4.31 and 4.33 compare the results from both types of model for K_d & K_u, and J_d & J_u against porosity. (Figure 4.32 shows the dimensionless values of K_d & K_u.) Figure 4.31 shows agreement with Gassmann's undrained bulk modulus, K_uG. Again, to calculate K_uG, I inserted the values of K_d obtained from my numerical simulations, the microscopic parameters, K_s and K_f, and porosity, ϕ, into equation 1.79. Further, as expected, the carbonate models are generally softer than the sandstone models because of their smaller microscopic bulk modulus, K_s. Recall that they have different values (see Table 2.1). In Figure 4.34, the carbonate and sandstone models show only a slight difference for M plotted against porosity. This again implies that M is not very sensitive to the geometry of the pore or the microscopic parameters. Figure 4.35 compares α to the porosity in both models. Interestingly, this shows very similar results between the carbonate and sandstone models. To understand the physical meaning of this, recall that α is the coefficient that quantifies how much apparent dilatation (Δ) there is in the system as a result of changes in the fluid content. Following this, my result then implies that this value is greater in the carbonate models, however, M is much more similar for all models, regardless of how complex the pore geometry might be.

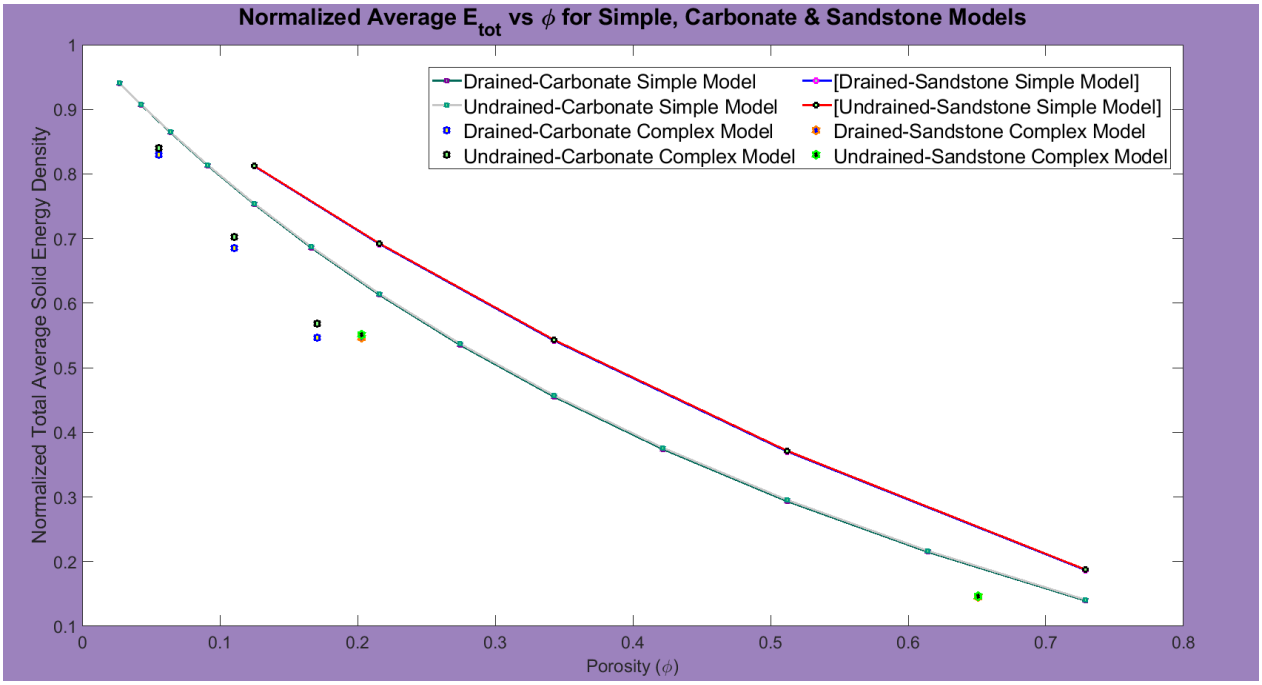

Figure 4.36: E_{tot_n} against ϕ

Figure 4.36 shows the plot for the normalized total average solid energy density, E_{tot_n}, for the carbonate and sandstone models, plotted against porosity. This shows that E_{tot_n} is changing at a very similar rate in both models. The plots also reveal that the sandstone models store slightly more solid energy than the carbonate models.

4.4 Comparing the Models with the Same Set of Parameters

In this section, I compare the carbonate and sandstone models with the same microscopic bulk and shear moduli. That is, I modelled the sandstone rock with the parameters of the carbonate rock. This way, I examine, purely, the effect of the difference in pore geometry.

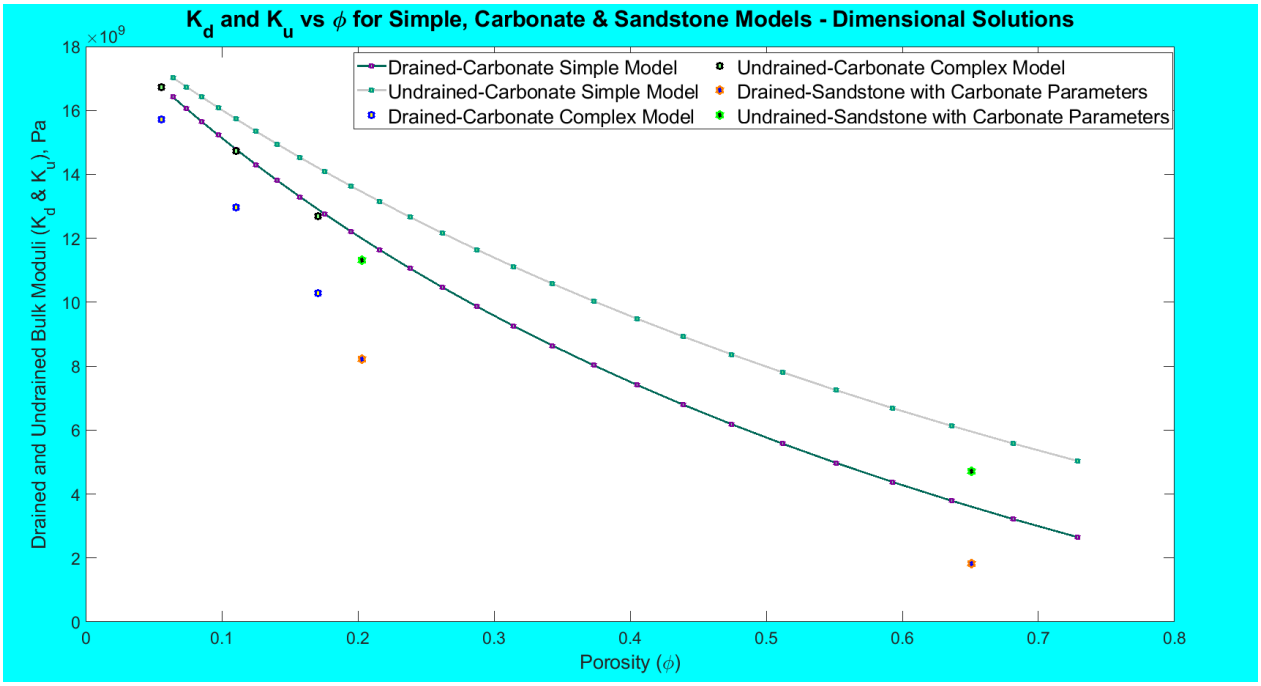

Figure 4.37: K_d & K_u against ϕ

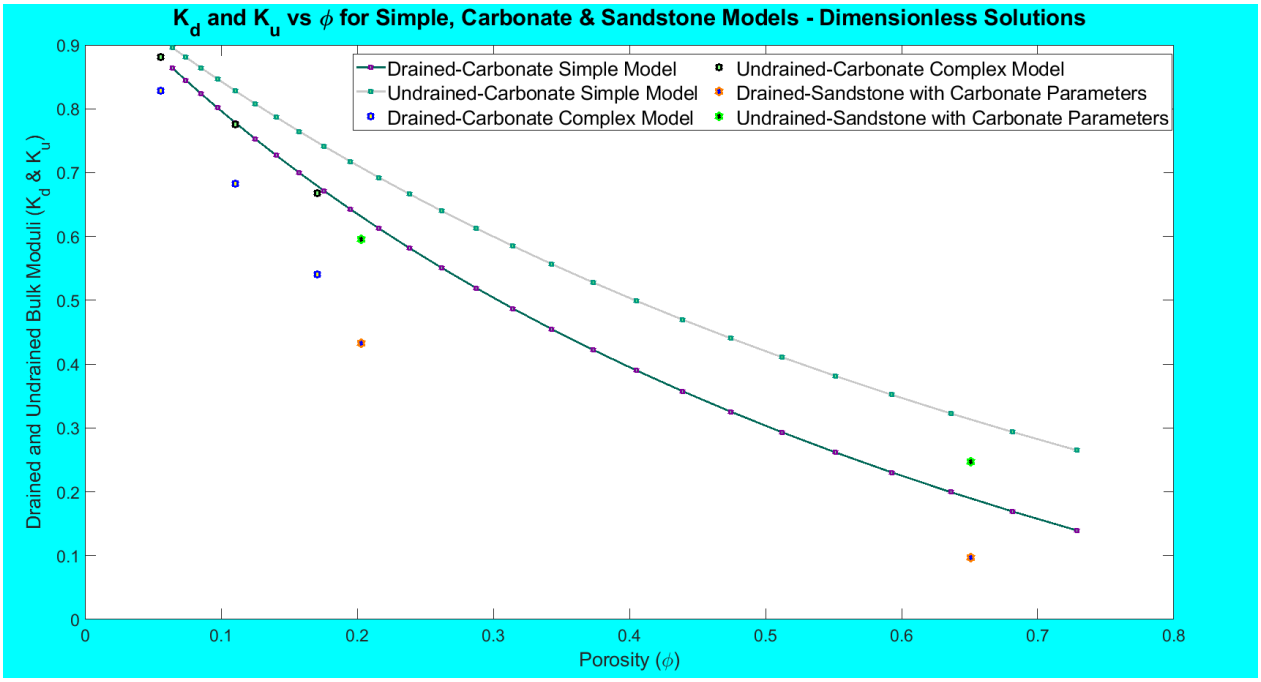

Figure 4.38: K_d & K_u against ϕ

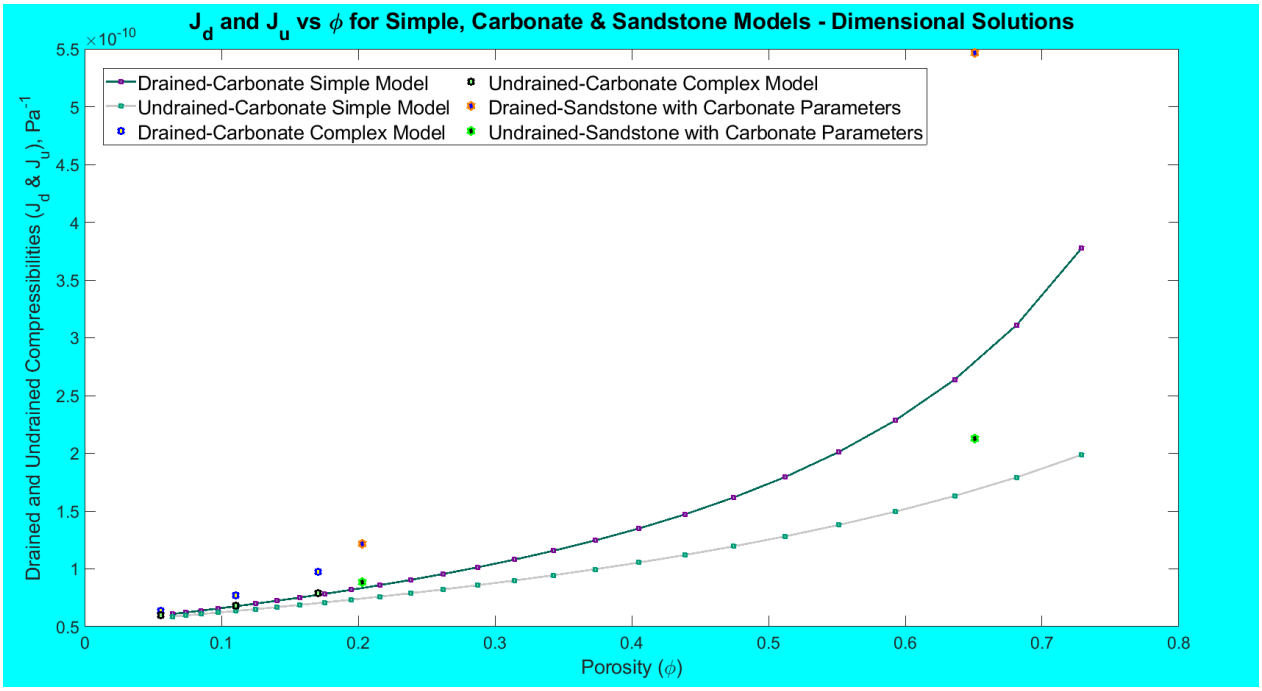

Figure 4.39: K_d & K_u against ϕ

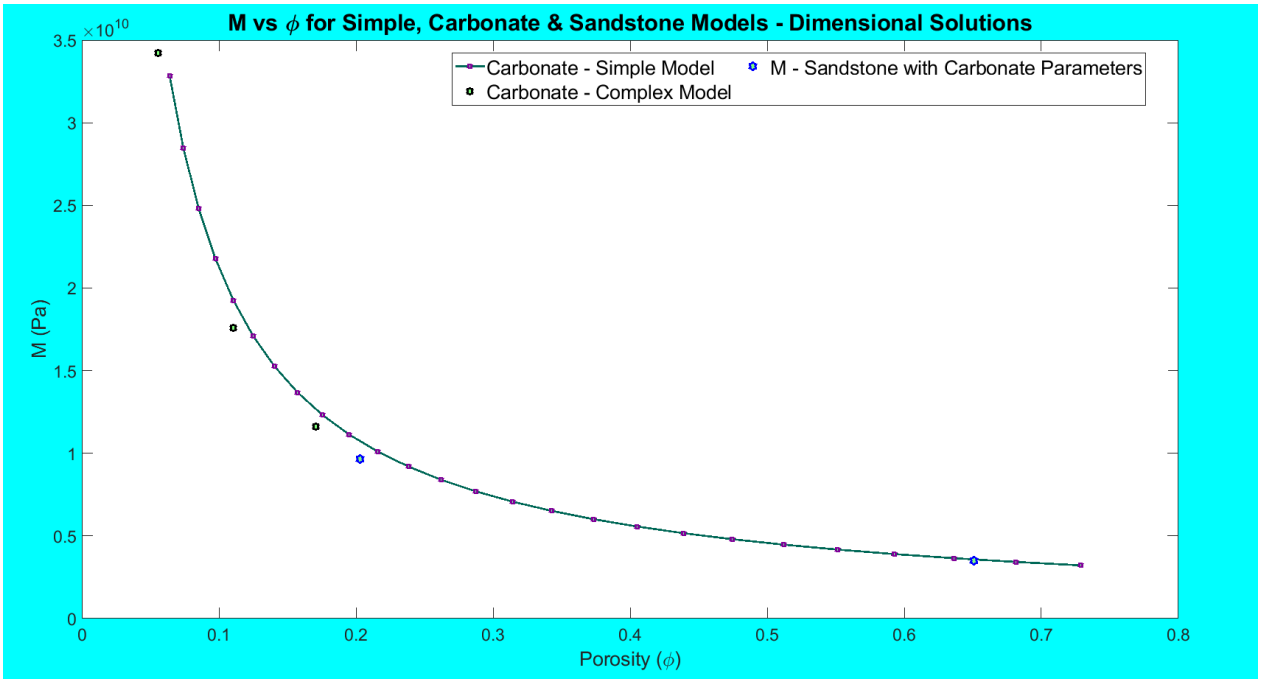

Figure 4.40: M against ϕ

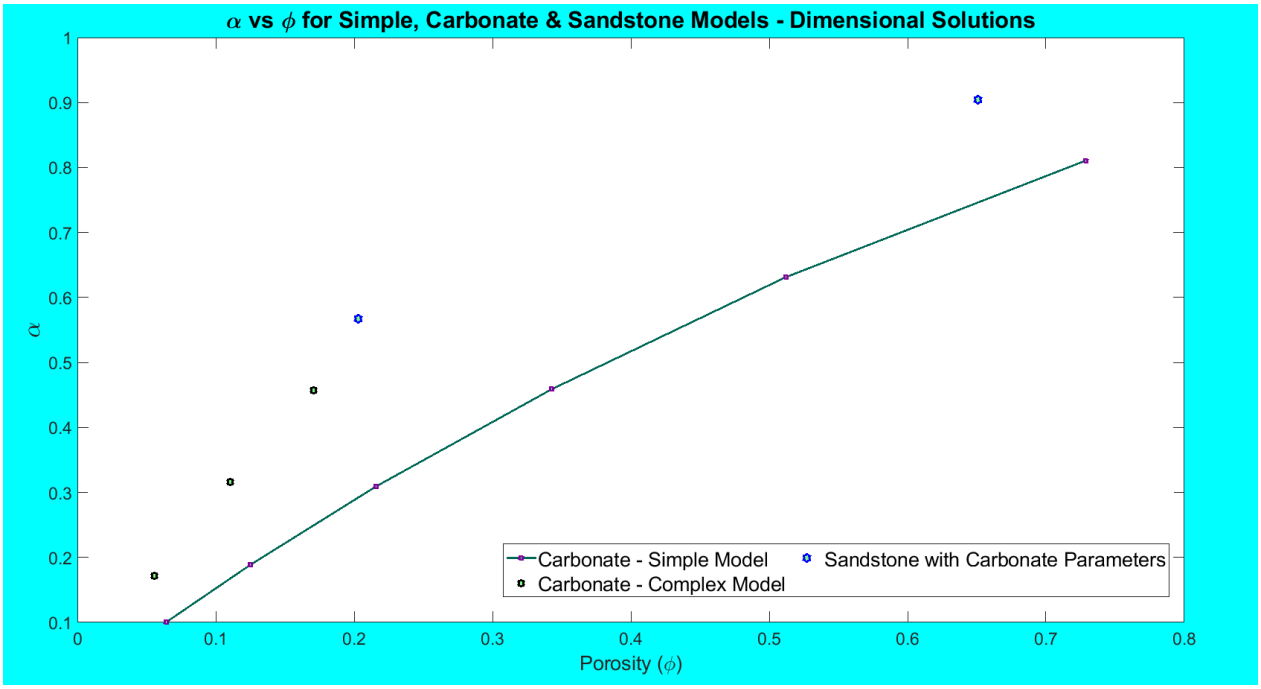

Figure 4.41: α against ϕ

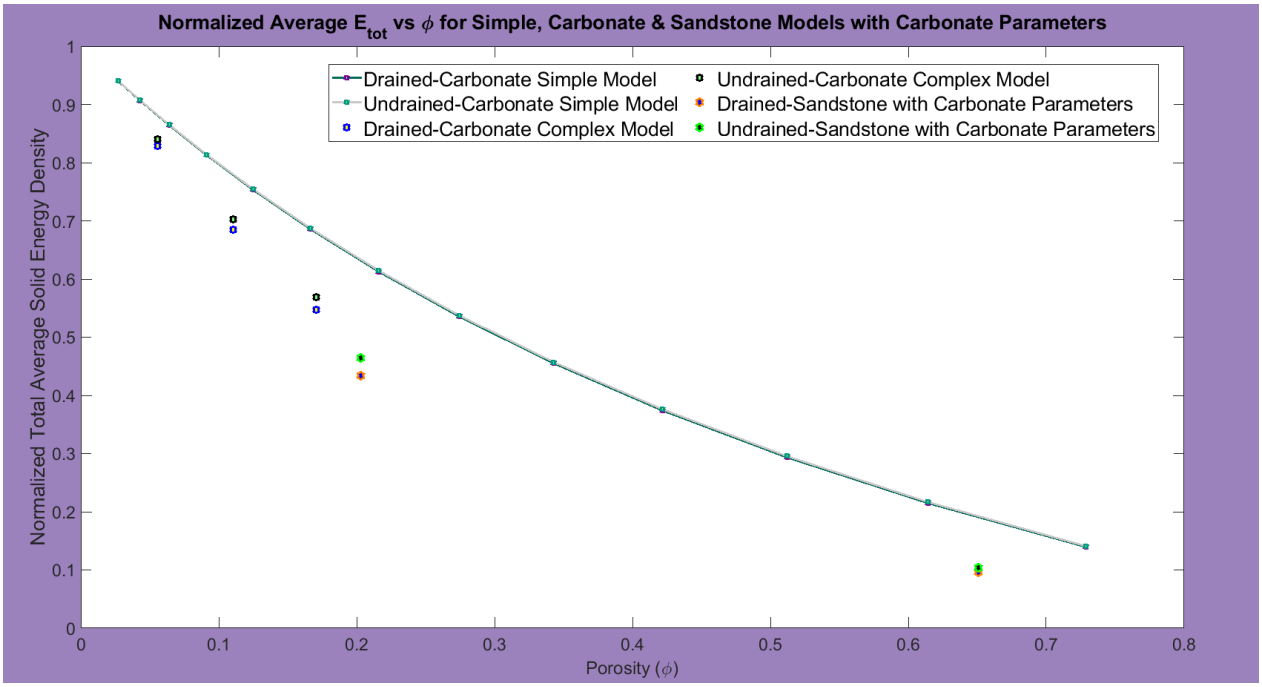

Figure 4.42: E_{tot_n} against ϕ

Figures 4.37 to 4.42 show similar trends as already discussed in previous cases. However, from Figures 4.37 to 4.39, we see that the sandstone models have pore geometries that are slightly

softer than those of the carbonate models. This difference is similar to those of Figures 3.29 to 3.30 and 3.40 to 3.41. While considering the effect of the number of cylindrical pores, we saw that, for the drained case, the incompressibility of the two and three cylindrical pores was the same but different for the one cylindrical pore (3.29), even at the same porosity. Then, for the undrained case, they all had different values (3.30). Also, while comparing the two spherical and two cylindrical pores, their incompressibility (3.40) or compressibility (3.41) was the same for the undrained case, but different for the drained case at the same porosity. We also observed these differences while comparing the complex and simple pore geometries. The carbonate and sandstone models each had the same parameters with their spherical pore counterparts but with different results. Further, the pressure, M (in Figure 4.40), remains largely unaffected by the pore geometry. Then, α (in Figure 4.41), is slightly different for the complex pore geometries, while, in Figure 4.42, we see that the sandstone pore geometry allows for slightly lower storage of energy than its carbonate counterpart.

It is not immediately clear why the pore geometries of the sandstones with the same porosity as the carbonates make them more compressible than the carbonates. And there is probably no one definitive answer (it will be an interesting investigation for a future research). However, one fact is certain: the pore geometry plays a vital role in a rock's response to deformation.

5 Conclusions and Recommendations

This chapter contains general conclusions drawn from the numerical experiments and analytical models in Chapters Three and Four and some recommendations for future research.

5.1 Conclusions

In this project, the macroscopic parameters of various porous rocks have been computed numerically, and in some cases, analytically, using the stress-strain relationships. These (numerical) computations were done by subjecting the rocks to some stresses on the outer boundaries without fluid being present (as in the open system or drained condition), and sometimes, introducing some fluid pressure in the pore (the closed system or undrained condition). And these results, together with the total dilatation and fluid content, were used to evaluate the $\boldsymbol{K}$-matrix, which contains Biot's parameters, namely, the undrained bulk modulus, K_u, the pressure, M, and the coefficient α. From the $\boldsymbol{K}$-matrix, the drained bulk modulus, K_d, was derived. In all cases, the Biot-Gassmann model was capable of describing the system. Further, the average solid compression and shear energy densities (normalized over the bulk volume) were also analyzed. From the numerical simulations in Chapter Three, the following conclusions are drawn.

Firstly, as expected, all the results showed a general continuous decrease in the values of the macroscopic parameters listed above, as well as the stored solid energy as porosity increased, except for the coefficient α and the average shear energy density. Also, the rock geometry or volume seemed to contribute little to the value of the macroscopic parameters. That is, how much bulk (macroscopic) resistance to compression which the system offers is not necessarily influenced by the geometry or volume of the porous rock (see Figures 3.54 and 3.56). Another finding is that, when the pore space was made up of separated spheres (as opposed to

interconnected ones), K_d & K_u, for the drained and undrained cases, respectively, remained the same in each case, regardless of how many pores were present (see Figures 3.25 and 3.26). This is because, when the pore sets are not intersecting, the pore space is not complex enough to cause significant changes in the bulk resistance for each case of the drained and undrained experiments. However, when the pore space was made up of intersecting cylinders, the resulting K_d remained unchanged in any case involving different numbers of cylinders, because of the absence of fluid in the pores; whereas K_u was the same for the various numbers of cylinders only at small porosities of less than 5%, but diverged as the pores got bigger (see Figures 3.29 and 3.30). Further, when the complex models are compared to the simple models in one plot, the results for K_d & K_u (Figure 4.31) further reinforces the observation that, the more complex the pore space, the more different the values of K_d & K_u, will be. Also, K_u and K_d seem to decrease with complexity.

Another interesting observation is that the parameter M is only influenced by porosity, but, otherwise, remains fairly constant regardless of the number of pores present, the complexity of the pore space, the geometry of the rock matrix, or the bulk volume (see Figures 3.27, 3.31, 3.42, & 3.55), and only shows a slight variation for different microscopic parameters (see Figure 4.34). The physical meaning of this is that, to increase the fluid content at constant volumetric strain in a porous medium, one can exert the same amount of pressure on the fluid each time, regardless of the complexity of the pore space or the material properties of the rock, and provided the porosity is the same. Similarly, the coefficient α was found to be the same for systems with the same material properties (see Figure 3.28) but different for systems with different material properties and pore geometries (see Figure 4.35).

Finally, it was observed that the value of the compression and total average energy densities of the solid (normalized over the bulk volume) is similar for rocks of the same porosity, which have pores of the same geometry and volume (see Figures 3.32 and 3.34), but different when the pores are of different shapes (see Figures 3.43 and 3.45). This shows that the geometry of the pore space plays an important role in how the energy is stored in the rock solid. The average shear energy density, however, shows an interestingly different pattern as

it immediately changes when the number of pores present changes and/or the geometry of the pore space changes (see Figures 3.33 and 3.44). It also takes a different direction from the other energy densities as it initially increases with increasing porosity before dropping. This is because, as the pore size gets bigger, the shear around the pore also increases, but then the solid region where the shear energy is stored continues to grow smaller, such that, even though the shear around the pore is increasing, the model begins to run out of storage space (solid region) for the shear energy, storing only less and less of it as the pore size gets bigger.

5.2 Recommendations for Future Work

In a future work, it would be nice to study another property, like tortuosity, and investigate whether this contributes to the influence of pore geometry in poroelastic deformations. There is abundant literature on how to calculate the tortuosity parameter - Berryman (1980), Boudreau (1996), etc. - depending on the case considered. However, assuming the fluid is allowed to flow in our models, it might be possible to calculate the tortuosity parameter as a function of the kinetic energy density of the poroelastic model as shown below (Morozov & Deng, 2016):

$$E_{kin} = \frac{a}{2\phi}\rho_f v^2 \tag{5.1}$$

where E_{kin} is the kinetic energy density of the entire sample, $a \geq 1$ is the effective tortuosity of the pore space, v is the average flow velocity of the pore fluid, ρ_f is the density of the pore fluid. One can then analyze the dependence on tortuosity which might explain why my sandstone model geometry is softer than the carbonate.

A more useful future project would be to simulate numerically triaxial shear tests by imposing different stresses in different directions and compare these with laboratory triaxial shear test (as described in Chapter One).

The drained and undrained shear strength could also be calculated from the simulation of

a triaxial test with only two equal stresses, which will add an extra parameter to Biot's parameters. To show this, we take the different between the first component of stress from equation (1.57) and either of the other two to get

$$\sigma_{zz} - \sigma_{xx} = 2\mu\big(\varepsilon_{zz} - \varepsilon_{xx}\big) \tag{5.2}$$

To represent this in the K matrix, we have

$$\begin{bmatrix} \sigma \\ p \\ \sigma_{zz} - \sigma_{xx} \end{bmatrix} = \begin{bmatrix} K_u & \alpha M & 0 \\ \alpha M & M & 0 \\ 0 & 0 & 2\mu \end{bmatrix} \begin{bmatrix} \Delta \\ \zeta \\ \varepsilon_{zz} - \varepsilon_{xx}; \end{bmatrix} \tag{5.3}$$

where σ now represents the average normal stress, and the shear modulus μ is not included in the first equation from the K matrix because it cancels out when the normal components of stress are added. This shear modulus, which is now the fourth parameter, can be obtained from just one numerical experiment since it is independent of the other Biot parameters.

The results from this study can also be used to check the phenomenon known as the Mendel-Cryer effect. It is a phenomenon where the pore pressure in a triaxial or spherical rock sample increases beyond the loading on the outer walls. With time dependence, my model could be used to check Cryer's analytical solutions.

Further, the surface area to volume ratio of the pore geometries considered in this thesis can be determined and the information used to understand the porosity of each model, whether it is made up of small or big pores. This might also reveal a pattern among the models.

Also, it would be interesting to model a pore space of intersecting pores in order to better understand how this contributes to the stored elastic energy. For instance, one could set up a model that has a pore space similar to the one in Figure 5.1.

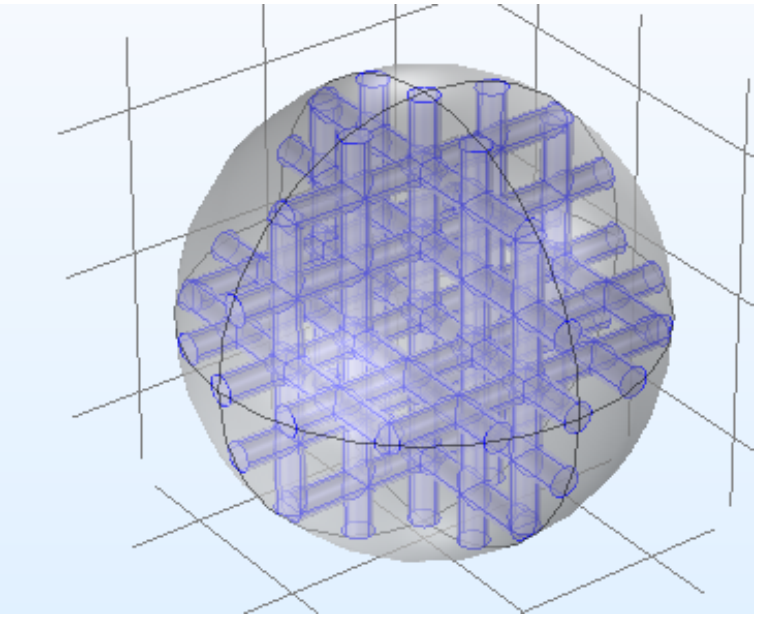

Figure 5.1: Digital Rock Model with Intersecting Pores

Finally, it would be very beneficial to a future work to have more X-ray tomographic images of rock samples and more efficient super computers to run them. Some of the carbonate and sandstone samples used in this research took large amounts of computer memory and prompted me to use the University of Saskatchewan's cluster computers of about 1 terabyte memory to run them. And even at that, some of the rock samples (not included in this research) required more memory than the cloud computing could manage. This was certainly a limitation for me and one that can be better managed in the future.

References

ASTM. (2002). Standard Test Method for Compressive Strength and Elastic Moduli of Intact Rock Core Specimens under Varying States of Stress and Temperatures. *Astm*, *04*(C), 1–6. doi: 10.1520/D7012-10.1

Berryman, J. G. (1980). Confirmation of Biot's theory. *Appl. Phys. Lett*, *37*, 382. Retrieved from `https://doi.org/10.1063/1.91951` doi: 10.1063/1.91951

Biot, M. A. (1935). Le problem de la consolidation des matieres argileuses sous une charge. *Annaies de la Societe Scientifique de Bruxelles*, 110–113. Retrieved from `https://ci.nii.ac.jp/naid/10007808764/`

Biot, M. A. (1941, feb). General Theory of Three-Dimensional Consolidation. *Journal of Applied Physics*, *12*(2), 155–164. Retrieved from `http://aip.scitation.org/doi/10.1063/1.1712886` doi: 10.1063/1.1712886

Biot, M. A. (1962, apr). Mechanics of Deformation and Acoustic Propagation in Porous Media. *Journal of Applied Physics*, *33*(4), 1482–1498. Retrieved from `http://aip.scitation.org/doi/10.1063/1.1728759` doi: 10.1063/1.1728759

Biot, M. A., & Willis, D. G. (1957). The Elastic Coefficients of the Theory of Consolidation. *Journal of Applied Mechanics*, *79*, 594–601. Retrieved from `https://pdfs.semanticscholar.org/19f3/031f724d31b37ad38a0ae67bdace1e539488.pdf`

Bird, M. (2013). *Numerical Calculation of Transport Properties of Rock with Geometry Obtained Using Synchrotron X-Ray Computed Microtomography* (Unpublished doctoral dissertation). University of Saskatchewan.

Boudreau, B. P. (1996). *The diffusive tortuosity of fine-grained unlithified sediments* (Vol. 60; Tech. Rep. No. 16).

Bourbie, T., Coussy, O., & Zinszner, B. (1987). *Acoustics of Porous Media*. Houston: Gulf Publ. Co.

Bower, A. F. (2009). *Applied mechanics of solids*. CRC Press. Retrieved from http://solidmechanics.org/text/Chapter4{_}1/Chapter4{_}1.htm

Fridtjov, I. (2008). *Continuum mechanics*. Springer-Verlag Berlin Heidelberg.

Handoyo, H., Fatkhan, F., Suharno, & Fourier, D. (2017). Introduction to Digital Rock Physics and Predictive Rock Properties of Reservoir Sandstone. *IOP Conference Series: Earth and Environmental Science*, *62*(1), 12022. Retrieved from https://iopscience.iop.org/article/10.1088/1755-1315/62/1/012022/pdf

Ingram, W. T. (2006, apr). A brief historical view of continuum theory. *Topology and its Applications*, *153*(10 SPEC. ISS.), 1530–1539. doi: 10.1016/j.topol.2004.08.024

McLellan, P. J. (1996). Assessing the risk of wellbore instability in horizontal and inclined wells. *Journal of Canadian Petroleum Technology*, *35*(5), 21–32. doi: 10.2118/96-05-02

Morozov, I. B., & Deng, W. (2016). Macroscopic framework for viscoelasticity, poroelasticity, and wave-induced fluid flows — Part 1: General Linear Solid. *Society of Exploration Geophysicists*, *81*(1), L1–L13. Retrieved from https://library.seg.org/doi/abs/10.1190/geo2014-0171.1 doi: 10.1190/geo2014-0404.1

Pan, E. (1999). *Green's Functions in Layered Poroelastic Half-Spaces* (Vol. 23; Tech. Rep.). Retrieved from https://blogs.uakron.edu/ernianpan/files/2014/09/038{_}1999IJNAMGPanLayPoro.pdf

Quintal, B., Rubino, J. G., Caspari, E., & Holliger, K. (2016). A simple hydromechanical approach for simulating squirt-type flow. *Geophysics*, *81*(4), D335–D344. Retrieved from http://library.seg.org/doi/10.1190/geo2015-0383.1 doi: 10.1190/geo2015-0383.1

Reza Saberi, M., & Jenson, F. (2018). Determining dynamic biot's coefficient for unconventionals. *Hart's E and P*(August). Retrieved from https://www.hartenergy.com/exclusives/determining-dynamic-biots-coefficient-unconventionals-177102

Sungkorn, R., Morcote, A., Carpio, G., Davalos, G., Mu, Y., Grader, A., ... Toelke, J. (2015). Multi-Scale and Upscaling of Digital Rock Physics With a Machine That Can Learn About Rocks. In *International symposium of the society of core analysts* (pp. 16–21).

Terzaghi, K. (1923, apr). Die Berechnung der Durchlassigkeitsziffer des Tones aus Dem Verlauf der Hidrodynamichen Span-nungserscheinungen Akademie der Wissenschaften in Wien. *Mathematish-Naturwissen-Schaftiliche Klasse*, *2a*(132), 105–124. Retrieved from `http://www.scirp.org/journal/doi.aspx?DOI=10.4236/am.2013.44099` doi: 10.4236/am.2013.44099

Turcotte, D. L., & Schubert, G. (2002). *Geodynamics* (2nd ed.). Cambridge University Press.

Appendix A

Circular 2D vs Spherical 3D Models

The purpose of this section is to show some results from the comparison between the 2D and 3D cases which are not discussed in Chapter Three. The 2D and 3D models both share the same material properties shown in Table 2.1.

A.1 One-Pore Case

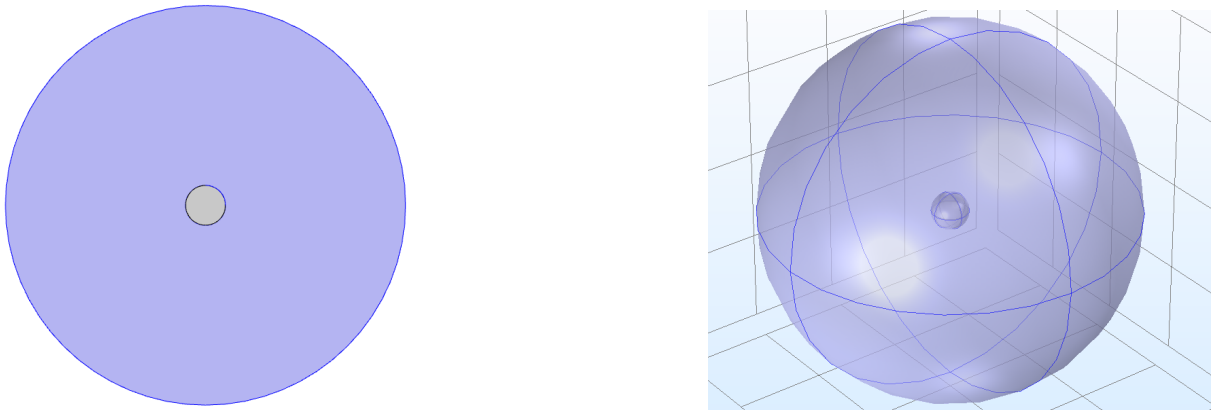

Figure A.1: Simple 2D & 3D models with only 1 spherical pore (at low porosity)

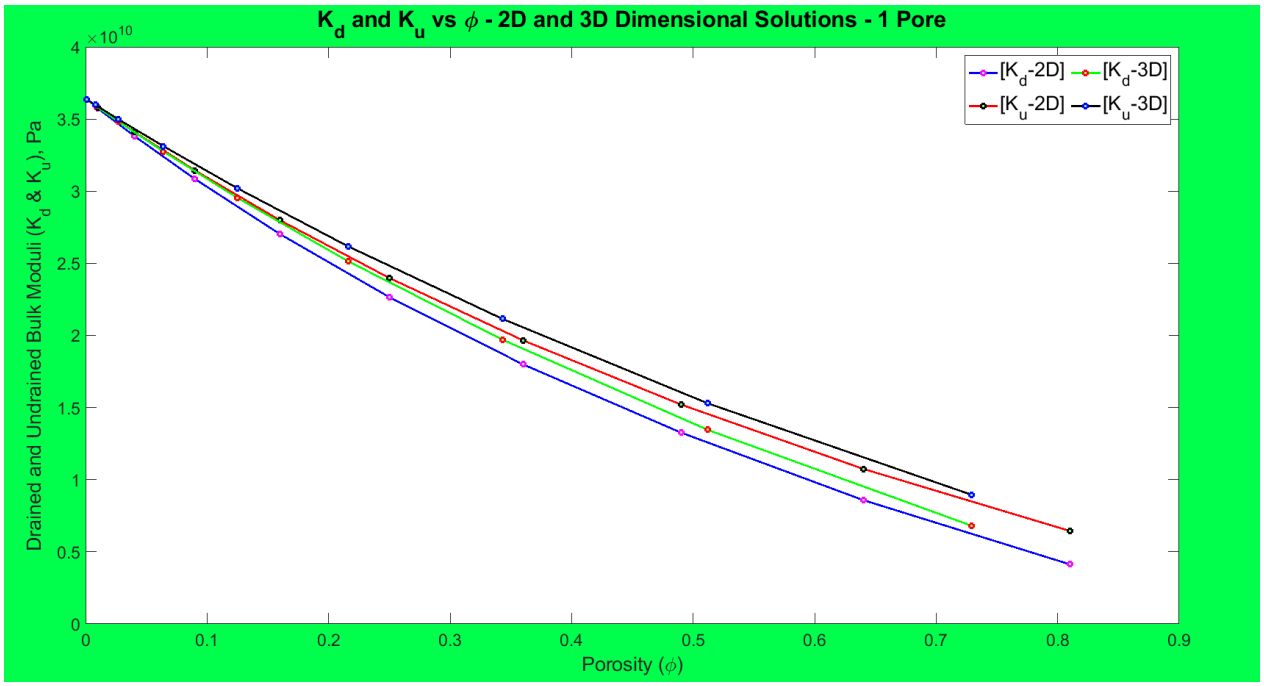

Figure A.2: 2D, 3D plots showing results for K_d and K_u against ϕ (for 1 spherical pore)

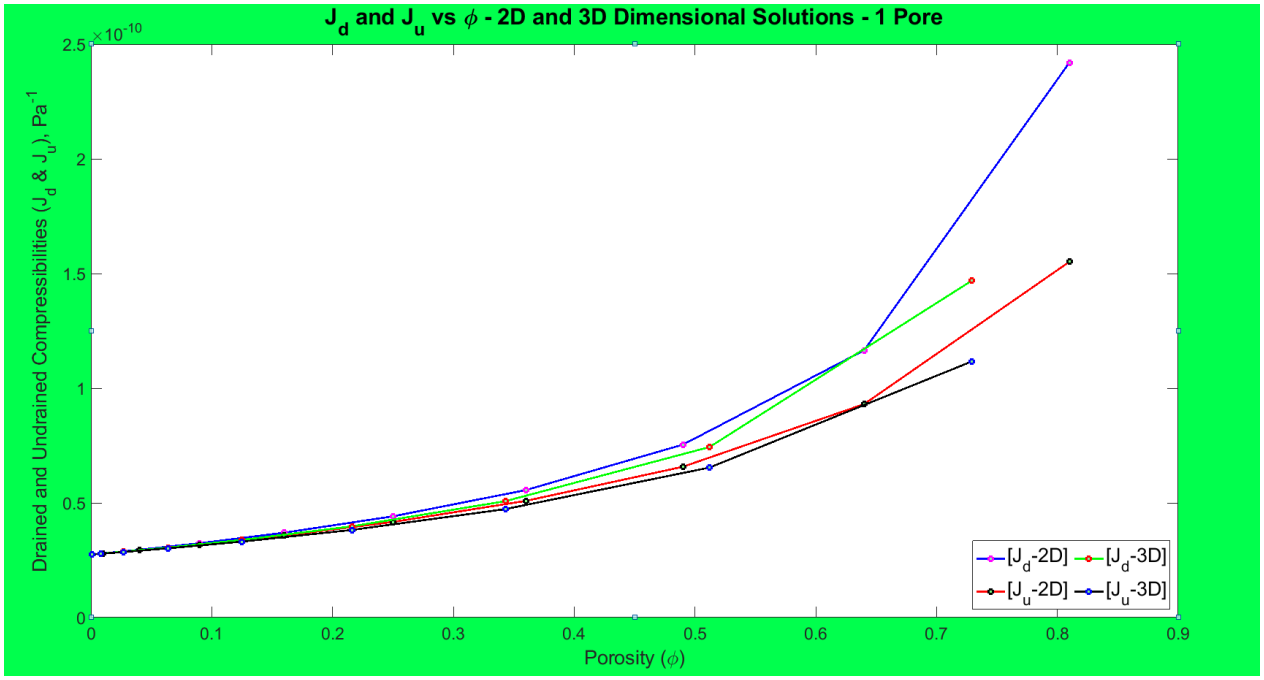

Figure A.3: 2D, 3D plots showing results for J_d and J_u against ϕ (for 1 spherical pore)

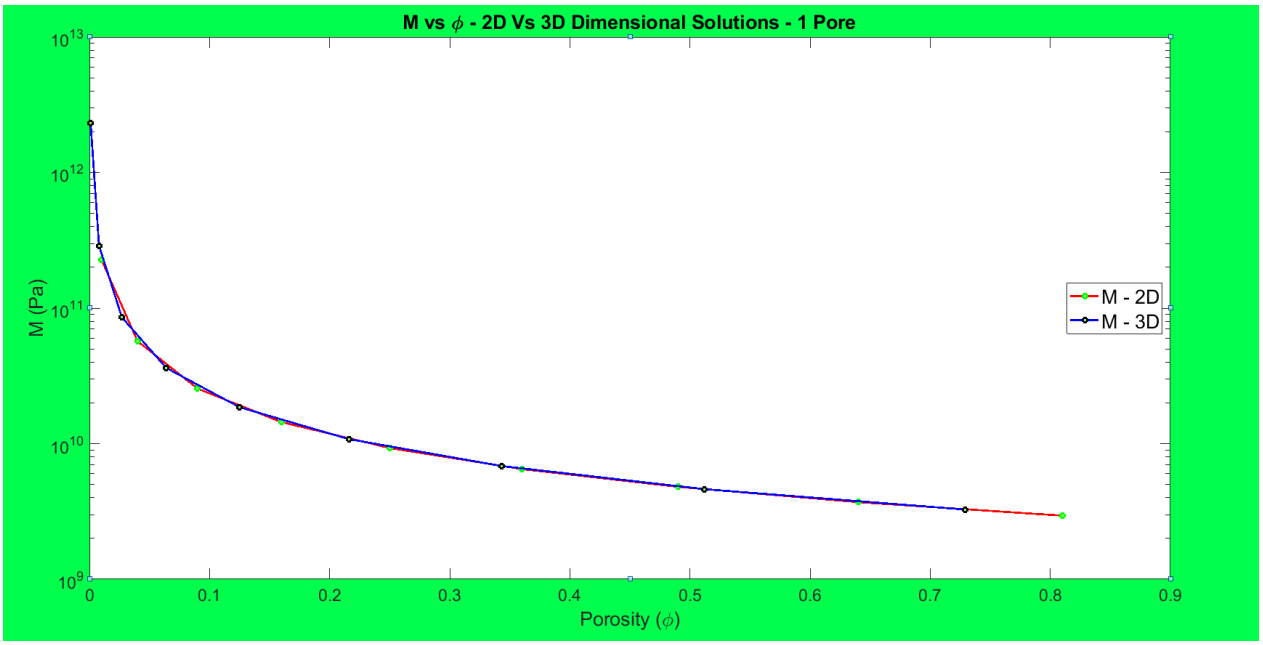

Figure A.4: 2D, 3D plots showing results for M against ϕ (for 1 spherical pore)

A.2 Two-Pore Case

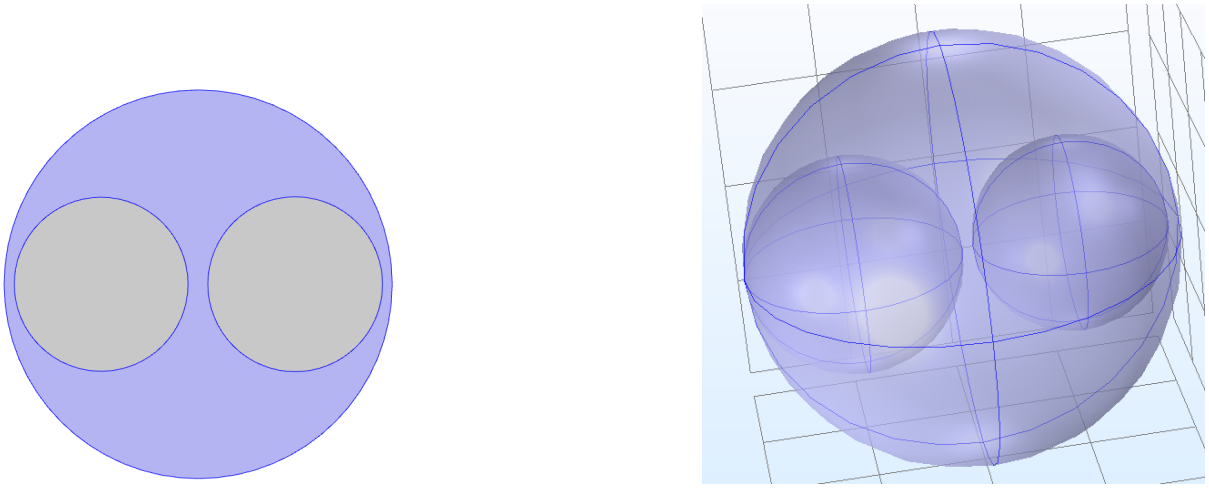

Figure A.5: Simple 2D & 3D models with 2 spherical pores (at high porosity)

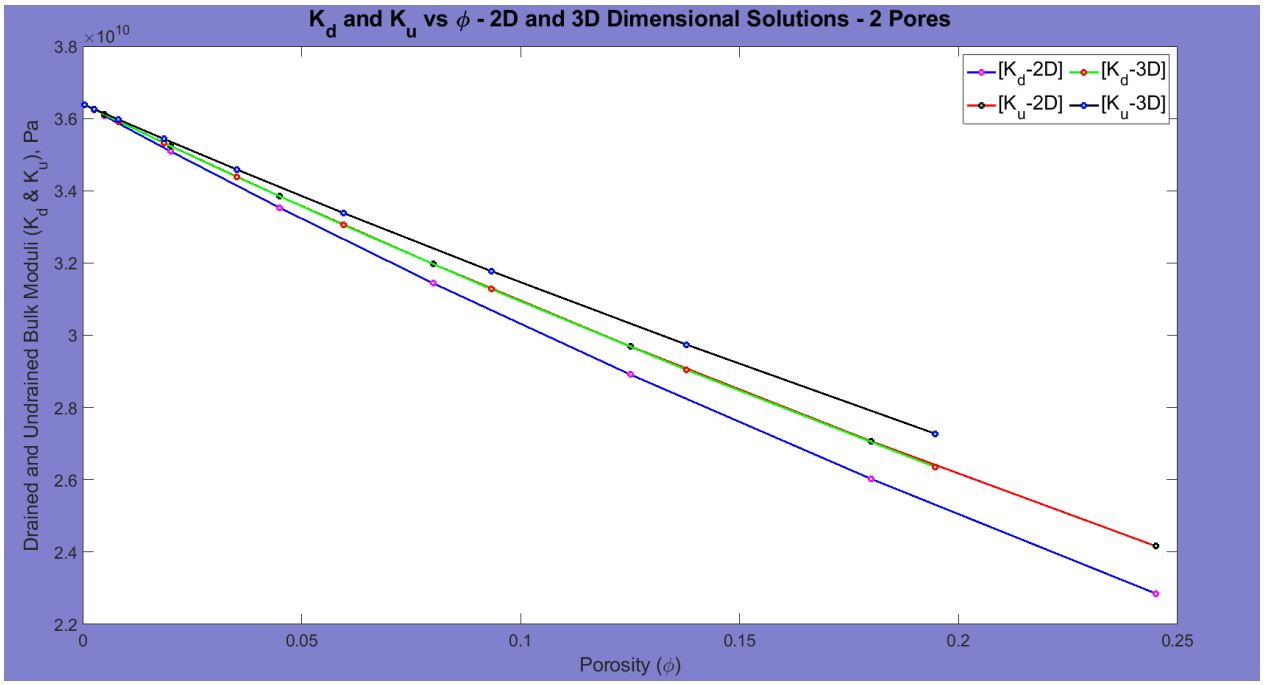

Figure A.6: 2D, 3D plots showing results for K_d and K_u against ϕ (for 2 spherical pores)

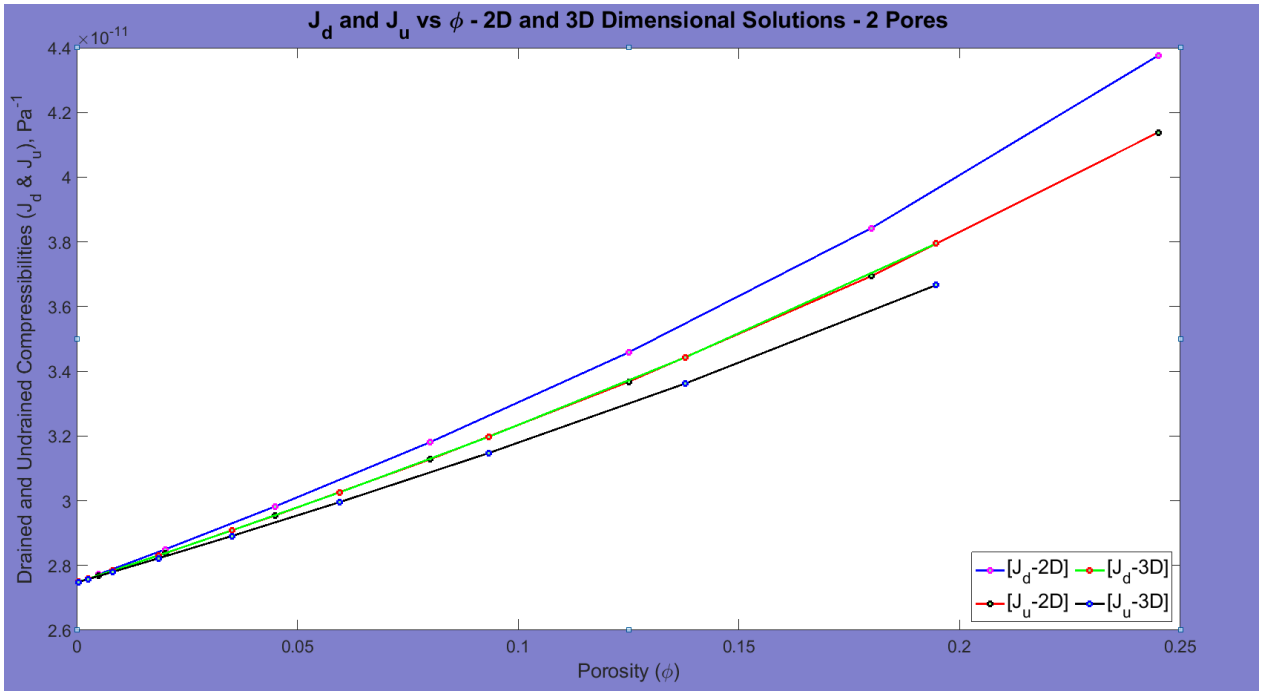

Figure A.7: 2D, 3D plots showing results for J_d and J_u against ϕ (for 2 spherical pores)

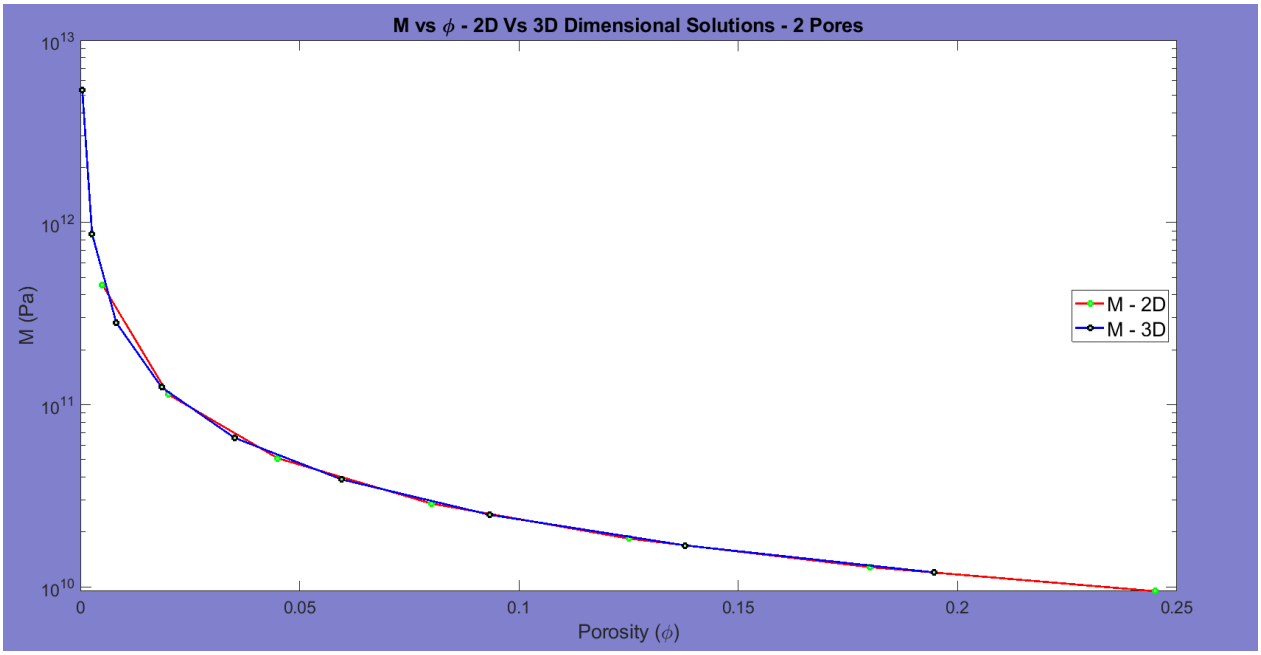

Figure A.8: 2D, 3D plots showing results for M against ϕ (for 2 spherical pores)

A.3 Four-Pore Case

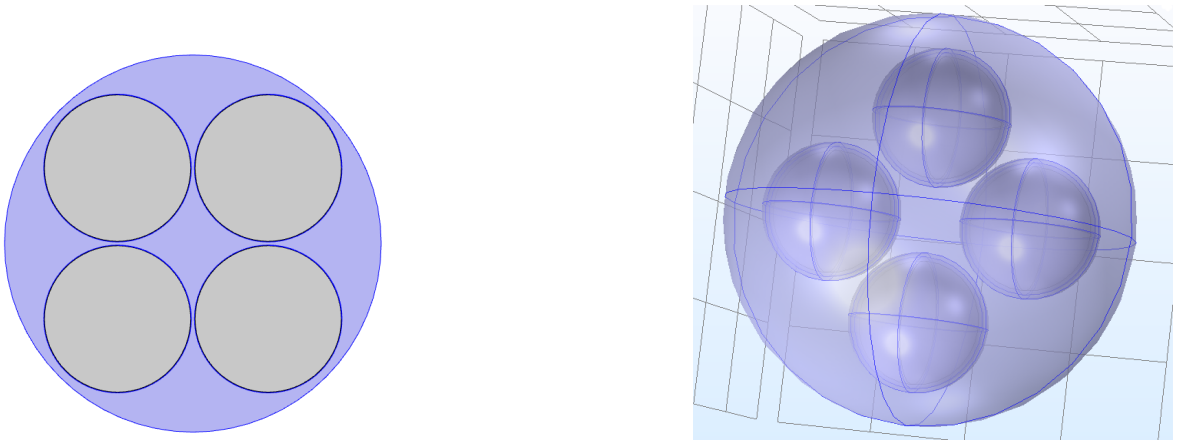

Figure A.9: Simple 2D & 3D models with 4 pores (at high porosity)

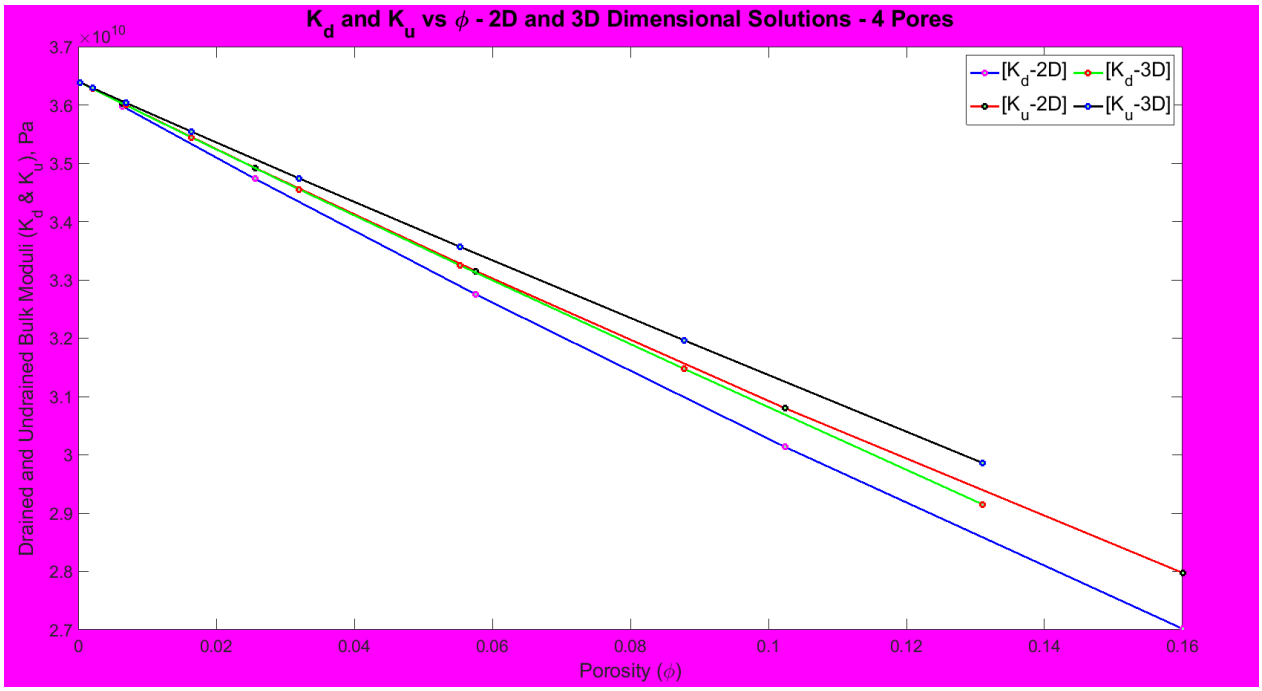

Figure A.10: 2D, 3D plots showing results for K_d and K_u against ϕ (for 4 spherical pores)

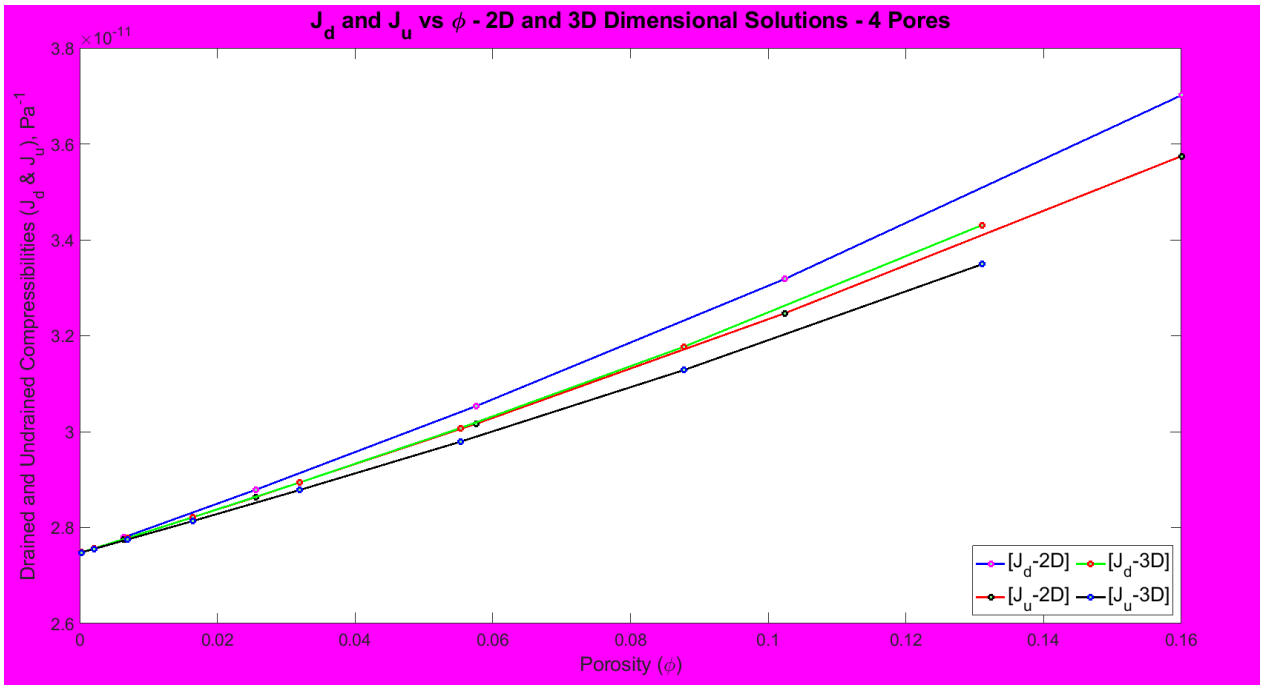

Figure A.11: 2D, 3D plots showing results for J_d and J_u against ϕ (for 4 spherical pores)

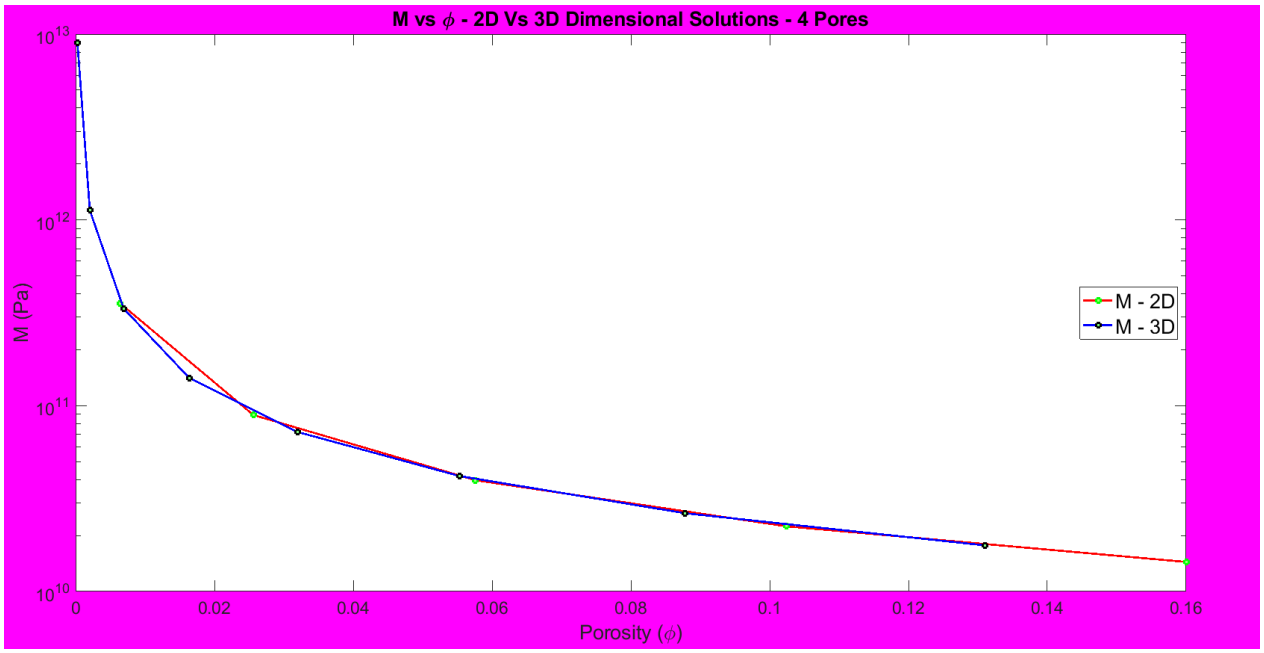

Figure A.12: 2D, 3D plots showing results for M against ϕ (for 4 spherical pores)

Appendix B

Spherical 3D Models - Spherical vs Cylindrical Pores

The purpose of this section is to show some results from spherical and cylindrical pores in a spherical model which are not discussed in Chapter Three.

B.1 One-Pore Case

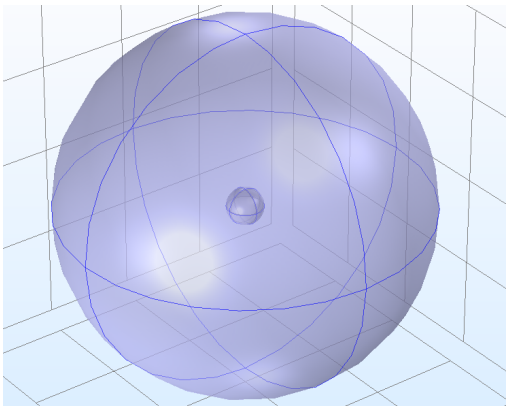

Figure B.1: Spherical pore

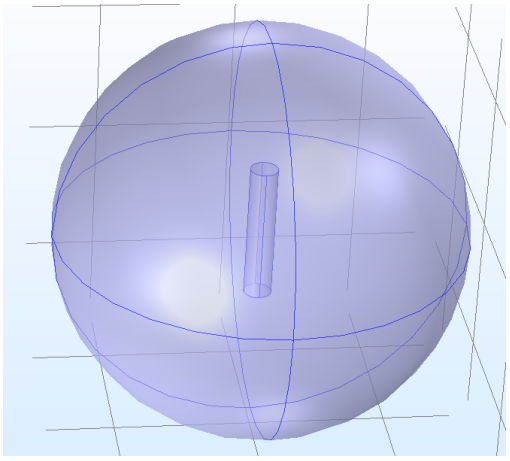

Figure B.2: Cylindrical pore

Figure B.3: Simple spherical and cylindrical pores - 1 pore at low porosity

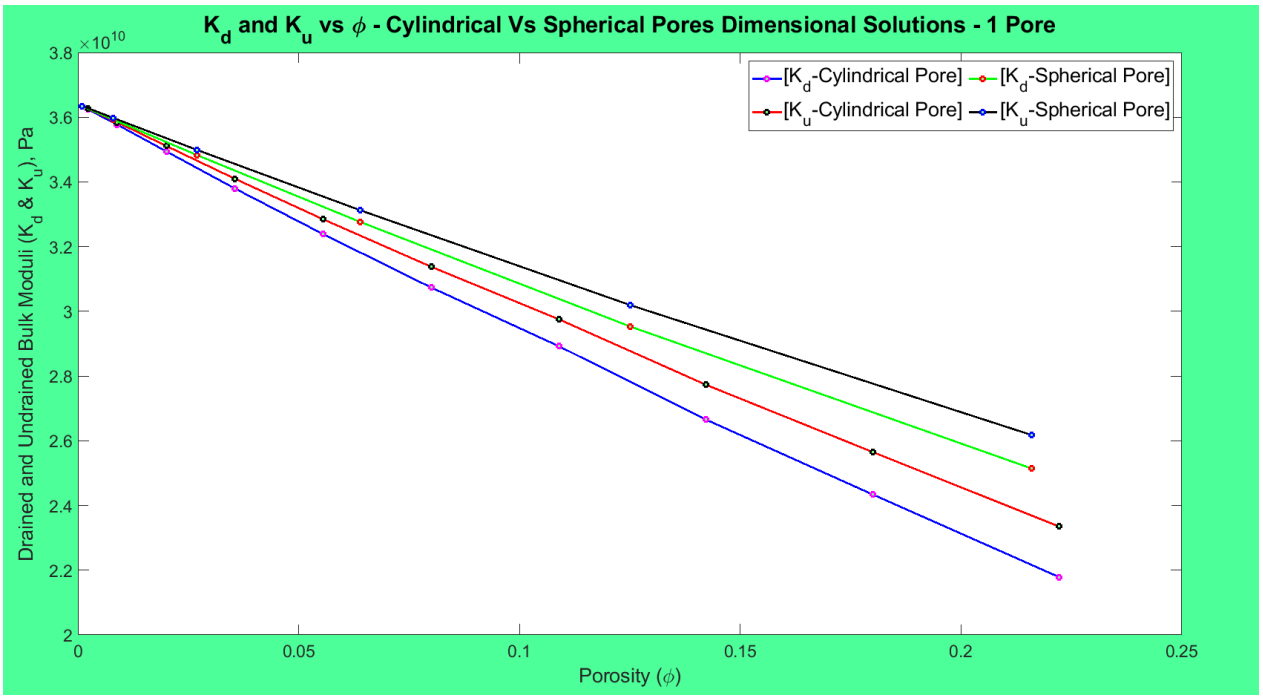

Figure B.4: Spherical 3D plots showing comparison of single pores for K_d & K_u against ϕ

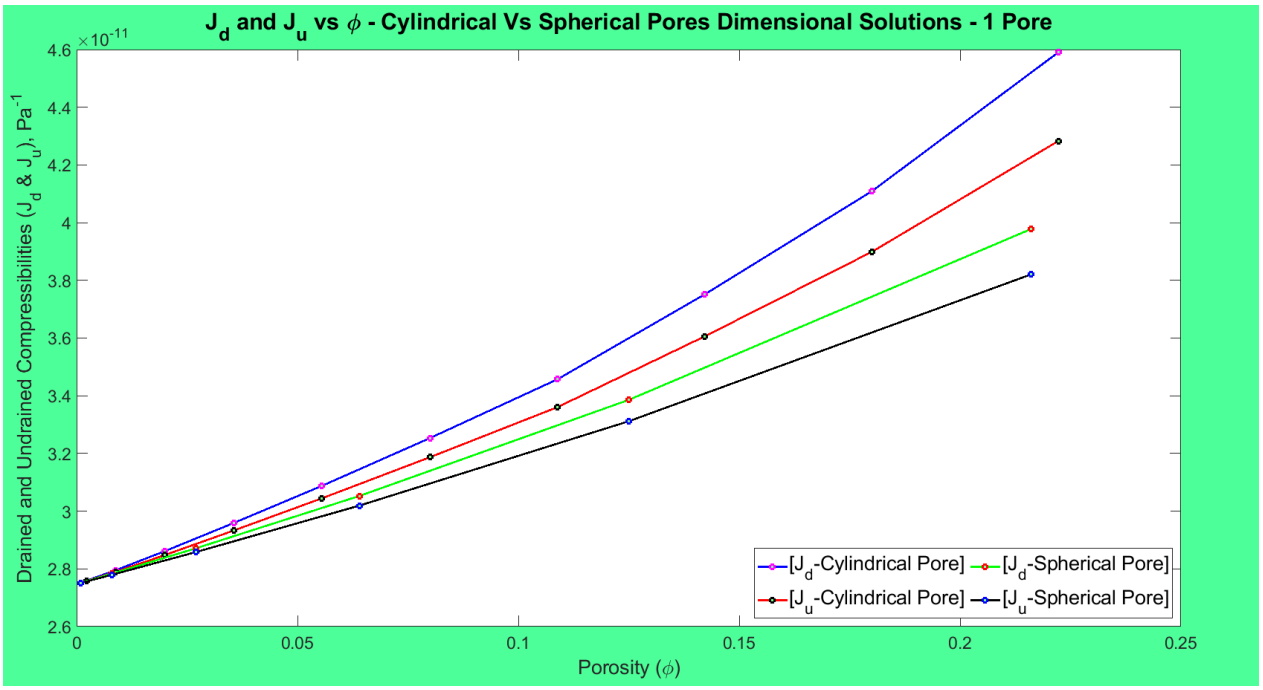

Figure B.5: Spherical 3D plots showing comparison of single pores for J_d & J_u against ϕ

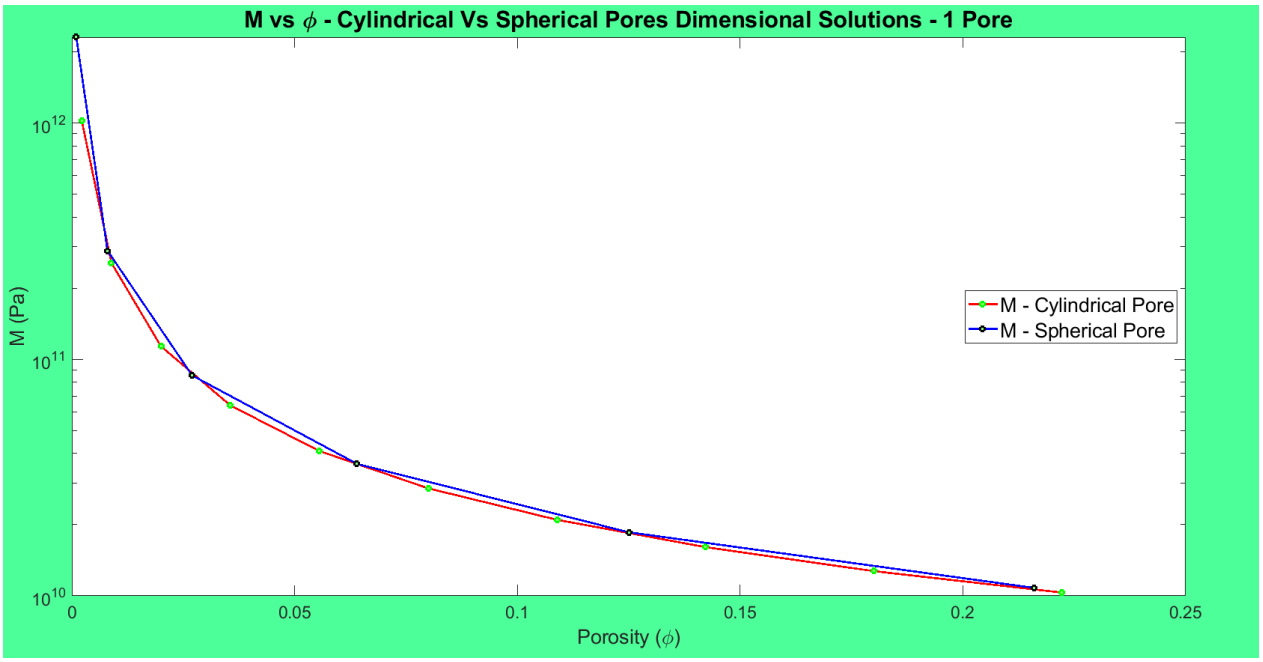

Figure B.6: Spherical 3D plots showing comparison of single pores for M against ϕ

B.2 Two-Pore vs One-Pore Cases

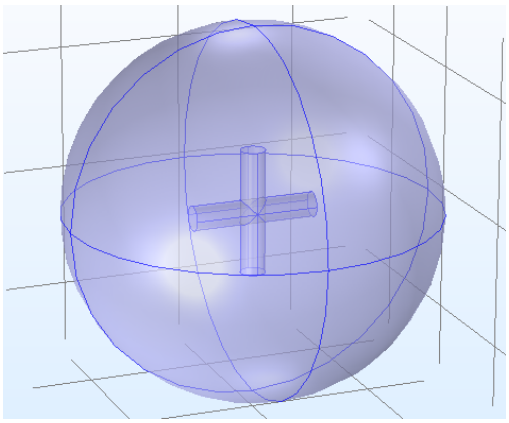

Figure B.7: Simple spherical solid with cylindrical pores

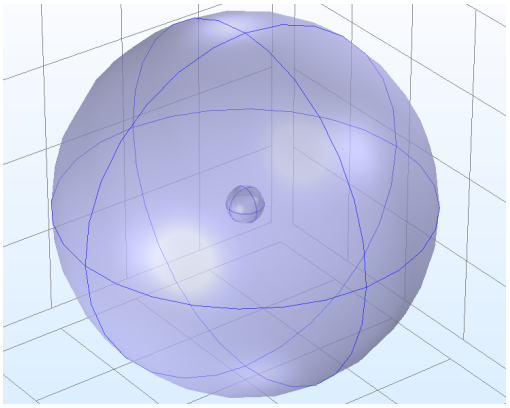

Figure B.8: Simple spherical solid with spherical pores

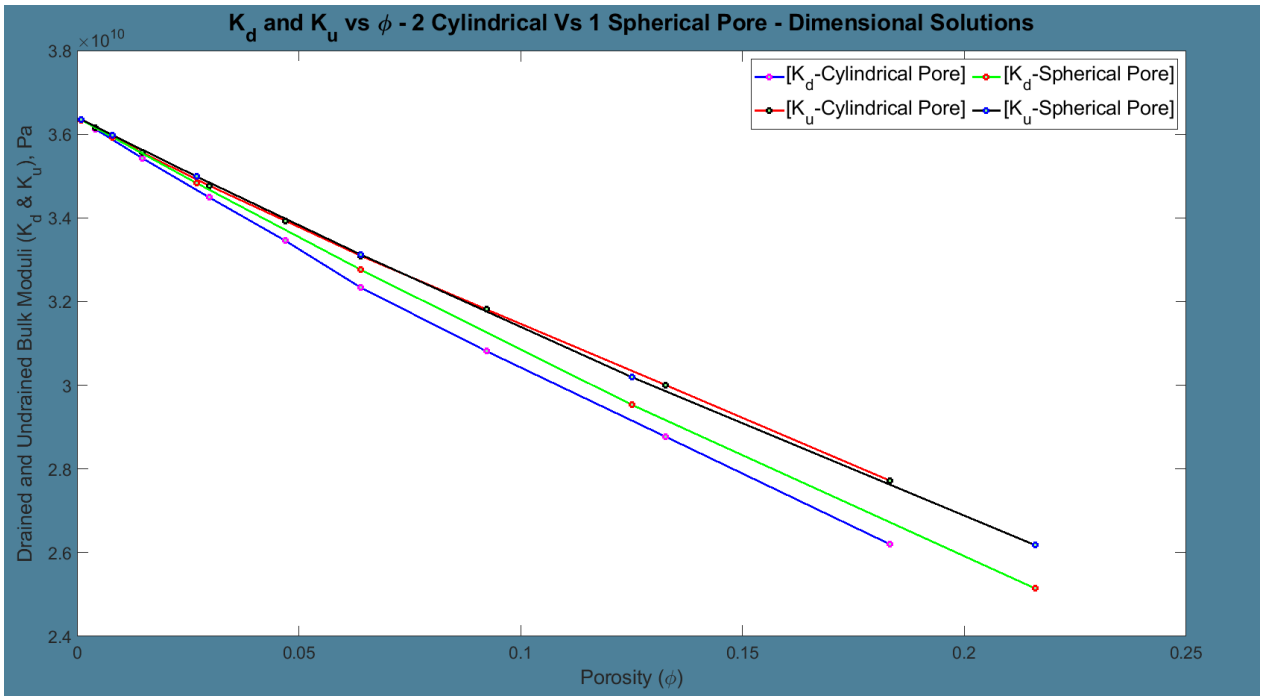

Figure B.9: Simple spherical and cylindrical pores plots showing comparison of 2 different pore sets for K_d & K_u against ϕ

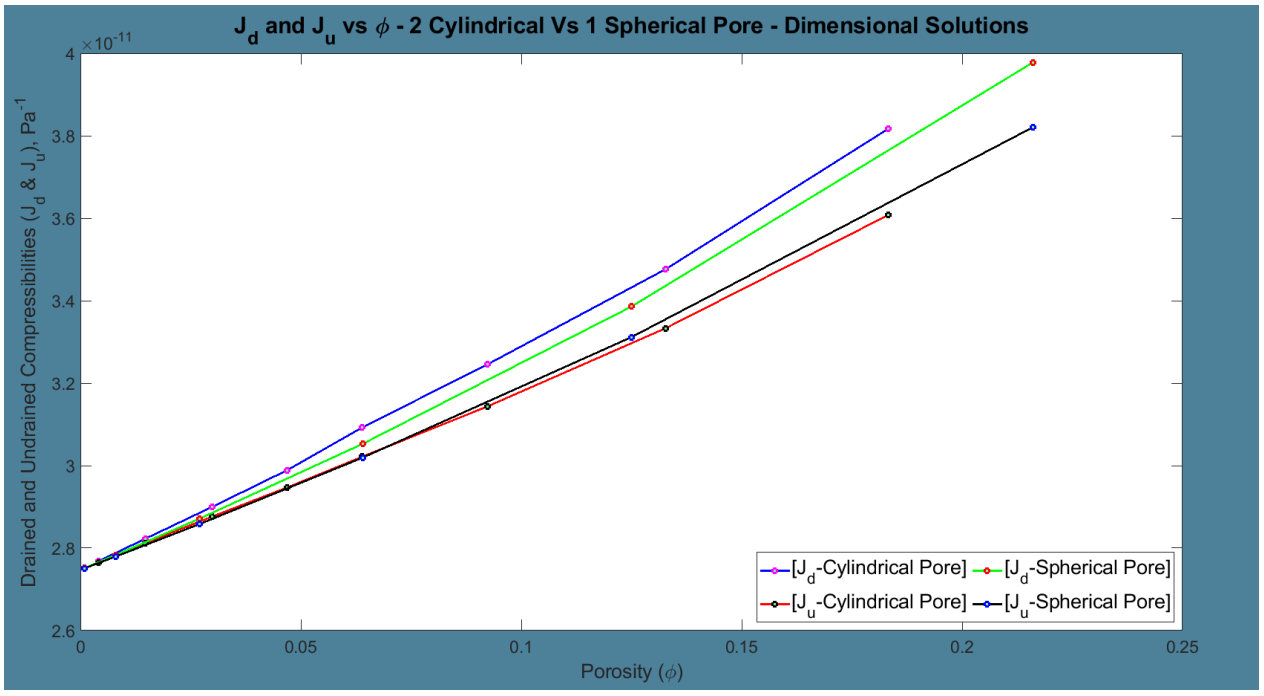

Figure B.10: Simple spherical and cylindrical pores plots showing comparison of 2 different pore sets for J_d & J_u against ϕ

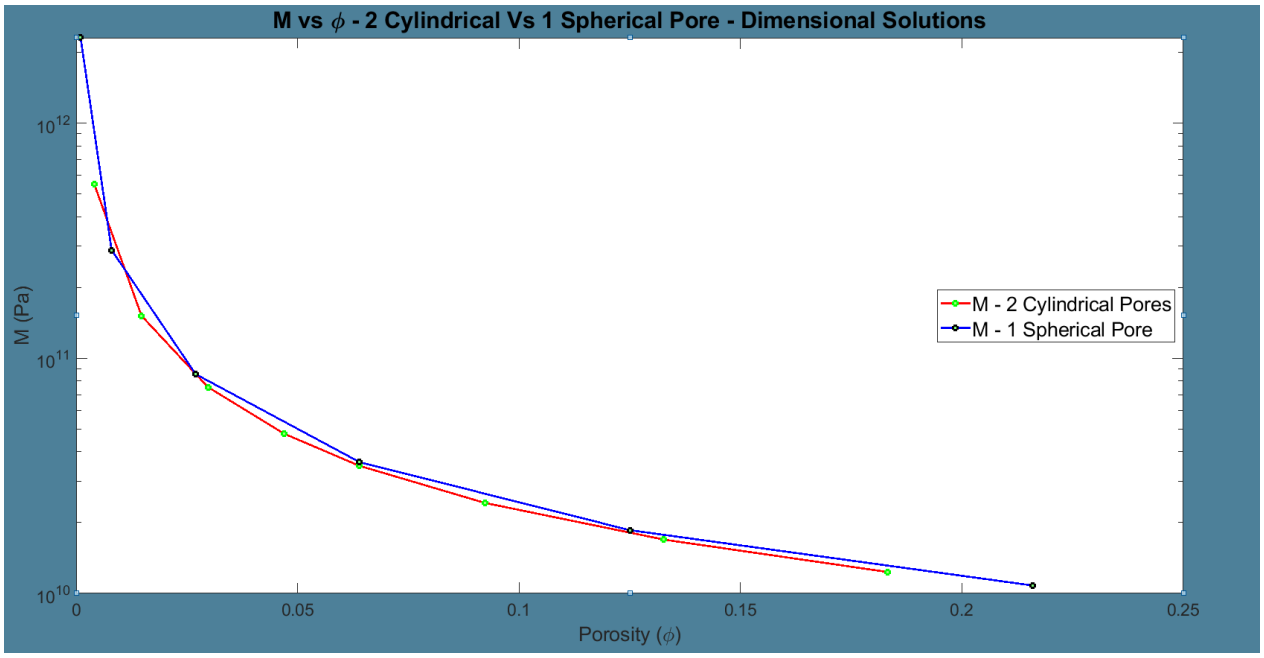

Figure B.11: Simple spherical and cylindrical pores plots showing comparison of 2 different pore sets for M against ϕ

Appendix C

Analytical Proof for $E_{tot_d} = E_{tot_u}$

Here I show analytically, how the total energy stored in the drained case, E_{tot_d}, is equal to the total energy stored in the undrained case, E_{tot_u}.

Recall that the total energy stored in the system (regardless of which) is given by

$$E_{tot} = \frac{2\pi}{(1-\phi)R_o^3}\left[3K_s\Big(R_o^2u_o - R_i^2u_i\Big)^2 + \frac{4\mu}{\phi}\Big(R_i^2u_i - \phi R_o^2u_o\Big)^2\right] \tag{C.1}$$

$$E_{tot} = B\left[3K_sC^2 + \frac{4\mu}{\phi}D^2\right] \tag{C.2}$$

For the drained case,

$$u_o = \frac{\big(3K_s\phi + 4\mu\big)R_o}{12K_s\mu\big(1-\phi\big)}\sigma = AR_o\sigma\big(3K_s\phi + 4\mu\big), \tag{C.3}$$

$$u_i = \frac{\big(3K_s + 4\mu\big)R_i}{12K_s\mu\big(1-\phi\big)}\sigma = AR_i\sigma\big(3K_s + 4\mu\big). \tag{C.4}$$

For the undrained case,

$$u_o = \frac{\big(3K_s\phi + 4\mu\big)R_o\sigma - \big(3K_s + 4\mu\big)R_o\phi p}{12K_s\mu\big(1-\phi\big)} = AR_o\sigma\big(3K_s\phi + 4\mu\big) - AR_o\phi p\big(3K_s + 4\mu\big), \tag{C.5}$$

$$u_o = \frac{\big(3K_s + 4\mu\big)R_i\sigma - \big(3K_s + 4\mu\phi\big)R_ip}{12K_s\mu\big(1-\phi\big)} = AR_i\sigma\big(3K_s + 4\mu\big) - AR_ip\big(3K_s + 4\mu\phi\big). \tag{C.6}$$

where,

$$A = \frac{1}{12K_s\mu\big(1-\phi\big)}, \tag{C.7}$$

$$B = \frac{2\pi}{\big(1-\phi\big)R_o^3}, \tag{C.8}$$

$$C = R_o^2u_o - R_i^2u_i, \tag{C.9}$$

$$D = R_i^2u_i - \phi R_o^2u_o. \tag{C.10}$$

Then,

$$C^2 = R_o^4 u_o^2 - 2R_o^2 R_i^2 u_o u_i + R_i^4 u_i^2, \tag{C.11}$$
$$D^2 = R_i^4 u_i^2 - 2\phi R_o^2 R_i^2 u_o u_i + \phi^2 R_o^4 u_o^2. \tag{C.12}$$

For the drained case,

$$u_o^2 = A^2 R_o^2 \sigma^2 \Big(9K_s^2\phi^2 + 24K_s\mu\phi + 16\mu^2\Big), \tag{C.13}$$
$$u_i^2 = A^2 R_i^2 \sigma^2 \Big(9K_s^2 + 24K_s\mu + 16\mu^2\Big), \tag{C.14}$$
$$u_o u_i = A^2 R_o R_i \sigma^2 \Big(9K_s^2\phi + 12K_s\mu\phi + 12K_s\mu + 16\mu^2\Big). \tag{C.15}$$

For the undrained case,

$$u_o^2 = A^2 R_o^2 \Bigg[\sigma^2 \Big(9K_s^2\phi^2 + 24K_s\mu\phi + 16\mu^2\Big) - 2\phi\sigma p \Big(9K_s^2\phi + 12K_s\mu\phi + 12K_s\mu + 16\mu^2\Big) + \phi^2 p^2 \Big(9K_s^2 + 24K_s\mu + 16\mu^2\Big)\Bigg], \tag{C.16}$$

$$u_i^2 = A^2 R_i^2 \Bigg[\sigma^2 \Big(9K_s^2 + 24K_s\mu + 16\mu^2\Big) - 2\sigma p \Big(9K_s^2 + 12K_s\mu\phi + 12K_s\mu + 16\mu^2\phi\Big) + p^2 \Big(9K_s^2 + 24K_s\mu\phi + 16\mu^2\phi^2\Big)\Bigg], \tag{C.17}$$

$$u_o u_i = A^2 R_o R_i \Bigg[\sigma^2 \Big(9K_s^2\phi + 12K_s\mu\phi + 12K_s\mu + 16\mu^2\Big) - \sigma p \Big(9K_s^2\phi + 12K_s\mu\phi^2 + 12K_s\mu + 16\mu^2\phi\Big) - \phi\sigma p \Big(9K_s^2 + 24K_s\mu + 16\mu^2\Big) + \phi p^2 \Big(9K_s^2 + 12K_s\mu\phi + 12K_s\mu + 16\mu^2\phi\Big)\Bigg]. \tag{C.18}$$

For the drained case,

$$C^2 = A^2\sigma^2\Bigg[R_o^6\Big(9K_s^2\phi^2 + 24K_s\mu\phi + 16\mu^2\Big) - 2R_o^3R_i^3\Big(9K_s^2\phi + 12K_s\mu\phi + 12K_s\mu + 16\mu^2\Big) + R_i^6\Big(9K_s^2 + 24K_s\mu + 16\mu^2\Big)\Bigg], \tag{C.19}$$

$$D^2 = A^2\sigma^2\Bigg[R_i^6\Big(9K_s^2 + 24K_s\mu + 16\mu^2\Big) - 2\phi R_o^3R_i^3\Big(9K_s^2\phi + 12K_s\mu\phi + 12K_s\mu + 16\mu^2\Big) + \phi^2R_o^6\Big(9K_s^2\phi^2 + 24K_s\mu\phi + 16\mu^2\Big)\Bigg]. \tag{C.20}$$

For the undrained case,

$$\begin{aligned} C^2 = A^2\Bigg[&R_o^6\sigma^2\Big(9K_s^2\phi^2 + 24K_s\mu\phi + 16\mu^2\Big) - 2\phi R_o^6\sigma p\Big(9K_s^2\phi + 12K_s\mu\phi + 12K_s\mu + 16\mu^2\Big) \\ &+ \phi^2R_o^6p^2\Big(9K_s^2 + 24K_s\mu + 16\mu^2\Big) - 2R_o^3R_i^3\sigma^2\Big(9K_s^2\phi + 12K_s\mu\phi + 12K_s\mu + 16\mu^2\Big) \\ &+ 2R_o^3R_i^3\sigma p\Big(9K_s^2\phi + 12K_s\mu\phi^2 + 12K_s\mu + 16\mu^2\phi\Big) + 2R_o^3R_i^3\phi\sigma p\Big(9K_s^2 + 24K_s\mu \\ &+ 16\mu^2\Big) - 2R_o^3R_i^3\phi p^2\Big(9K_s^2 + 12K_s\mu\phi + 12K_s\mu + 16\mu^2\phi\Big) + R_i^6\sigma^2\Big(9K_s^2 \\ &+ 24K_s\mu + 16\mu^2\Big) - 2R_i^6\sigma p\Big(9K_s^2 + 12K_s\mu\phi + 12K_s\mu + 16\mu^2\phi\Big) \\ &+ R_i^6p^2\Big(9K_s^2 + 24K_s\mu\phi + 16\mu^2\phi^2\Big)\Bigg], \end{aligned} \tag{C.21}$$

$$\begin{aligned} D^2 = A^2\Bigg[&R_i^6\sigma^2\Big(9K_s^2 + 24K_s\mu + 16\mu^2\Big) - 2R_i^6\sigma p\Big(9K_s^2 + 12K_s\mu\phi + 12K_s\mu + 16\mu^2\phi\Big) \\ &+ R_i^6p^2\Big(9K_s^2 + 24K_s\mu\phi + 16\mu^2\phi^2\Big) - 2\phi R_o^3R_i^3\sigma^2\Big(9K_s^2\phi + 12K_s\mu\phi + 12K_s\mu \\ &+ 16\mu^2\Big) + 2\phi R_o^3R_i^3\sigma p\Big(9K_s^2\phi + 12K_s\phi^2\mu + 12K_s\mu + 16\mu^2\phi\Big) + 2R_o^3R_i^3\phi^2\sigma p\Big(9K_s^2 \\ &+ 24K_s\mu + 16\mu^2\Big) - 2R_o^3R_i^3\phi^2p^2\Big(9K_s^2 + 12K_s\mu\phi + 12K_s\mu + 16\mu^2\phi\Big) \\ &+ \phi^2R_o^6\sigma^2\Big(9K_s^2\phi^2 + 24K_s\mu\phi + 16\mu^2\Big) - 2\phi^3R_o^6\sigma p\Big(9K_s^2\phi + 12K_s\mu\phi + 12K_s\mu + 16\mu^2\Big) \\ &+ \phi^4R_o^6p^2\Big(9K_s^2 + 24K_s\mu + 16\mu^2\Big)\Bigg]. \end{aligned} \tag{C.22}$$

To make the expressions a bit tidier, let

$$F = 9K_s^2\phi^2 + 24K_s\mu\phi + 16\mu^2 \tag{C.23}$$
$$H = 9K_s^2\phi + 12K_s\mu\phi + 12K_s\mu + 16\mu^2 \tag{C.24}$$
$$J = 9K_s^2 + 24K_s\mu + 16\mu^2 \tag{C.25}$$
$$N = 9K_s^2\phi + 12K_s\mu\phi^2 + 12K_s\mu + 16\mu^2\phi \tag{C.26}$$
$$Q = 9K_s^2 + 12K_s\mu\phi + 12K_s\mu + 16\mu^2\phi \tag{C.27}$$
$$T = 9K_s^2 + 24K_s\mu\phi + 16\mu^2\phi^2 \tag{C.28}$$

Therefore, for the drained case,

$$C^2 = A^2R_o^6\sigma^2\Big(F - 2\phi H + \phi^2 J\Big), \tag{C.29}$$
$$D^2 = A^2\phi^2R_o^6\sigma^2\Big(F - 2H + J\Big). \tag{C.30}$$

Then, for the undrained case,

$$C^2 = A^2R_o^6\Big(\sigma^2F - 2\phi\sigma pH + \phi^2p^2J - 2\phi\sigma^2H + 2\phi\sigma pN + 2\phi^2\sigma pJ - 2\phi^2p^2Q + \phi^2\sigma^2J - 2\phi^2\sigma pQ + \phi^2p^2T\Big) \tag{C.31}$$

$$D^2 = A^2\phi^2R_o^6\Big(\sigma^2J - 2\sigma pQ + p^2T - 2\sigma^2H + 2\sigma pN + 2\phi\sigma pJ - 2\phi p^2Q + \sigma^2F - 2\phi\sigma pH + \phi^2p^2J\Big). \tag{C.32}$$

Finally, the total energy stored in the drained and the undrained cases becomes

$$E_{tot_d} = A^2BR_o^6\sigma^2\Big[3K_s\Big(F - 2\phi H + J\Big) + 4\mu\phi\Big(F - 2H + J\Big)\Big]; \tag{C.33}$$

$$\begin{aligned} E_{tot_u} = A^2BR_o^6\Big[3K_s\Big(&\sigma^2F - 2\phi\sigma pH + \phi^2p^2J - 2\phi\sigma^2H + 2\phi\sigma pN + 2\phi^2\sigma pJ - 2\phi^2p^2Q + \phi^2\sigma^2J - 2\phi^2\sigma pQ \\ &+ \phi^2p^2T\Big) + 4\mu\phi\Big(\sigma^2J - 2\sigma pQ + p^2T - 2\sigma^2H + 2\sigma pN + 2\phi\sigma pJ - 2\phi p^2Q + \sigma^2F - 2\phi\sigma pH \\ &+ \phi^2p^2J\Big)\Big]. \end{aligned} \tag{C.34}$$

The next section illustrates how E_{tot_d} and E_{tot_u} are equal to each other.

C.1 Case Study of a Spherical Rock with One Spherical Pore

To demonstrate, analytically, that $E_{tot_d} = E_{tot_u}$, let us consider a spherical rock with one spherical pore, having these parameters:

$$K_s = 36.4\text{GPa}, \tag{C.35}$$
$$\mu = 44\text{GPa}, \tag{C.36}$$
$$R_i = 0.5m, \tag{C.37}$$
$$R_o = 1m, \tag{C.38}$$
$$\phi = \frac{R_i^3}{R_o^3} = 0.125 \tag{C.39}$$

Substituting these parameters into the expressions for A through T, we have that

$$A^2 = 3.54 \text{ x } 10^{-45} \text{ Pa}^{-4}, \tag{C.40}$$
$$B = 7.18\text{m}^{-3}, \tag{C.41}$$
$$F = 3.6 \text{ x } 10^{22} \text{ Pa}^2, \tag{C.42}$$
$$H = 5.4 \text{ x } 10^{22} \text{ Pa}^2, \tag{C.43}$$
$$J = 8.13 \text{ x } 10^{22} \text{ Pa}^2, \tag{C.44}$$
$$N = 2.49 \text{ x } 10^{22} \text{ Pa}^2, \tag{C.45}$$
$$Q = 3.74 \text{ x } 10^{22} \text{ Pa}^2, \tag{C.46}$$
$$T = 1.72 \text{ x } 10^{22} \text{ Pa}^2. \tag{C.47}$$

Inserting these into equations C.33 and C.34 in terms of σ and p, we have

$$E_{tot_d} = 7.08 \text{ x } 10^{-11}\sigma^2 \text{ Joules}, \qquad \text{and} \tag{C.48}$$
$$E_{tot_u} = 7.09 \text{ x } 10^{-11}\sigma^2 + 6.13 \text{ x } 10^{-12}p^2 - 2.66 \text{ x } 10^{-11}\sigma p \text{ Joules} \tag{C.49}$$

For the drained case,

$$\sigma = -8.8714 \text{ x } 10^4 \text{ Pa}, \tag{C.50}$$
$$p = 0 \text{ Pa}; \tag{C.51}$$

And for the undrained case,

$$\sigma = -9.0680 \text{ x } 10^4 \text{ Pa}, \tag{C.52}$$
$$p = -1.0479 \text{ x } 10^4 \text{ Pa}. \tag{C.53}$$

These give

$$E_{tot_d} = 0.5577 \text{ Joules}, \qquad \text{and} \tag{C.54}$$

$$E_{tot_u} = 0.5580 \text{ Joules}. \tag{C.55}$$

From equations C.54 and C.55, we can conclude that $E_{tot_d} = E_{tot_u}$.